A STUDY OF REACTIVE PRECIPITATION PROCESSES USING COMPUTATIONAL FLUID DYNAMICS

By

Mohsen Hassan Jaber Al-Rashed
B.Eng. (Hons) - Chemical Engineering (UCL) 1994

A Thesis Submitted to the
University of London
for the Degree of
Doctor of Philosophy

February 1998

Ramsay Memorial Laboratory
of Chemical Engineering
University College London
Torrington Place
London WC1E 7JE

To Abo-Saleh a.t.f.

ABSTRACT

The objective of this research is to study and model a reactive precipitation process and determine the feasibility of applying the Computational Fluid Dynamics (CFD) technique. The CFX package of AEA Technology is adopted in this procedure. CFD is employed to model the batch gas-liquid reactive precipitation process of calcium carbonate in a 1.357 litre stirred vessel. Two major steps are involved in the modelling scheme, viz. the hydrodynamic model and the chemical kinetics and precipitation process model. Then, a link between these two models is created.

The hydrodynamic model considers the impeller as a momentum source. To predict the turbulence behaviour, the Reynolds differential stress model is implemented because it is more appropriate than the standard k-ε model for swirling flows in stirred tanks. The flow pattern is predicted for two-blade paddle impeller and details of the fluid speed, pressure and turbulent energy are produced. The same procedure is followed in modelling a 45° pitched-blade impeller with six blades, to show the effect of impeller type on the mixing process. Both 2-D and 3-D models are evaluated.

Experimental validation is carried out for the CFD hydrodynamic model using three methods: video recording, still photographs and image analysis of 1 mm diameter beads suspended in the vessel using a white light source. Qualitative measurements of the flow pattern give similar results as the predictions of the 3-D CFD model. In

addition, flow number calculations from both the 2-D and 3-D CFD simulations show good agreement with literature data.

In order to minimise the computation time, the crystallization kinetics and precipitation process simulation is developed for a 2-D problem. The model calculates the extent of reaction, supersaturation, primary nucleation, size-independent crystal growth and the first four moments of the crystal size distribution throughout the vessel. Subsequently, the crystal average-mean size is evaluated. The model predicts an initial thin layer of particles forming in the interfacial region. The crystal slurry then starts to disperse into the bulk of the vessel following the flow pattern of the liquid. This behaviour is qualitatively comparable to the experimental results reported by Wachi and Jones (1991b).

The CFD model predictions are compared with those of the film and penetration theories for the same time range. The film theory shows a minor change in the mean size which indicates that it is a nucleation dominated process, i.e. high local supersaturation. Penetration theory predicts higher mean sizes, i.e. a growth dominated process with lower local supersaturation. The CFD simulation on the other hand, adopts an intermediate behaviour highlighting the role of the hydrodynamics in the process.

Thus, the model illustrates the feasibility of CFD to tackle the transient reactive precipitation process sufficiently. The main problem currently is excessive computational time.

ACKNOWLEDGEMENTS

Praise and eulogy is for Allah for the blessing and bounties which He has bestowed.

I would like to thank the following:

Professor Alan G. Jones for his supervision, support and encouragement throughout the project.

Timothy P. Elson for his precious discussion.

Crystallization group for their invaluable friendship and support.

Technical staff for their assistance especially Martyn Vale.

SPS and CFDS at the AEA Technology for funding this project.

Crystallization Panel of SPS for their constructive suggestions at the six-monthly progress meetings during the project.

The Overseas Research Students Award Scheme for the financial support.

IUS founders, trustees, EC and members who made my university life distinctive, enjoyable and fruitful.

All My Friends.

I also would like to thank my parents, brothers, sisters and my wife and son for the encouragement, enthusiasm and especially their prayers.

"KNOWLEDGE ENABLES ITS POSSESSOR TO DISTINGUISH WHAT IS FORBIDDEN FROM WHAT IS NOT; LIGHTS THE WAY TO HEAVEN; IT IS OUR FRIEND IN THE DESERT, OUR COMPANION IN SOLITUDE, OUR COMPANION, WHEN BEREFT OF FRIENDS; IT GUIDES US TO HAPPINESS; IT SUSTAINS US IN MISERY; IT IS OUR ORNAMENT IN THE COMPANY OF FRIENDS; IT SERVES AS AN ARMOUR AGAINST THE ENEMIES. WITH KNOWLEDGE THE CREATURES OF ALLAH RISES TO THE HEIGHTS OF GOODNESS AND TO NOBLE POSITION, ASSOCIATES WITH THE SOVEREIGNS IN THIS WORLD AND ATTAINS THE PERFECTION OF HAPPINESS IN THE NEXT."

AL-MUSTAFA S.A.W.

(6TH/7TH CENTURY)

"KNOWLEDGE ENABLES ITS POSSESSOR TO DISTINGUISH WHAT IS FORBIDDEN FROM WHAT IS NOT; LIGHTS THE WAY TO HEAVEN; IT IS OUR FRIEND IN THE DESERT, OUR COMPANION IN SOLITUDE, OUR COMPANION, WHEN BEREFT OF FRIENDS; IT GUIDES US TO HAPPINESS; IT SUSTAINS US IN MISERY; IT IS OUR ORNAMENT IN THE COMPANY OF FRIENDS; IT SERVES AS AN ARMOUR AGAINST THE ENEMIES. WITH KNOWLEDGE THE CREATURES OF ALLAH RISES TO THE HEIGHTS OF GOODNESS AND TO NOBLE POSITION, ASSOCIATES WITH THE SOVEREIGNS IN THIS WORLD AND ATTAINS THE PERFECTION OF HAPPINESS IN THE NEXT."

AL-MUSTAFA S.A.W.

(6TH/7TH CENTURY)

CONTENTS

LIST OF FIGURES

LIST OF TABLES

1

LITERATURE SURVEY

1. LITERATURE SURVEY

1.1 Crystallization

The formation of a crystal can be characterised by two steps; the birth of a new particle and its growth to macroscopic scale. The first step is known as nucleation. The interaction of the rates of nucleation and crystal growth and the overall process determines the crystal size distribution (CSD) in a crystallizer. The driving force for both rates is supersaturation, and neither of the two steps can be achieved in a saturated or under saturated solution, McCabe and Smith (1976). Thus, the first step to consider is supersaturation.

1.1.1. Supersaturation

Supersaturation is defined rigorously as the deviation from thermodynamic equilibrium, which is the difference between the chemical potential of the solute at the existing conditions of the system μ and the chemical potential of the solute equilibrated at the system conditions μ^*, Rousseau (1993).

Four methods may produce a supersaturation, viz., cooling, evaporation, salting-out and reaction. If the solubility increases significantly with temperature, then cooling method is usually used. Evaporation is employed when the solubility is not affected by

temperature. The salting-out method is applied when the other two processes are not desired. In the third method a third component is added forming a homogeneous mixture with the solvent in which the solute solubility is sharply reduced. However, if a precipitation is required, the new solute may be created chemically by adding a third component that will react with the original solute and form an insoluble substance, McCabe and Smith (1976) and Söhnel and Mullin (1982).

Supersaturation can be expressed, with greater or lesser accuracy, in any of the following formulations:

1. The difference between the chemical potential of the system and the chemical potential at saturation, μ-μ^*, where $\mu = \mu(T, c)$.
2. The difference between solute concentration and the concentration at equilibrium, c-c*.
3. The difference between the temperature at equilibrium and the actual temperature, T*-T.
4. The relative saturation, $\frac{c}{c^*}$.
5. The relative supersaturation, $s = \frac{(c - c^*)}{c^*}$.

The first formulation is the most fundamental, the second is particularly useful in calculating the yield of a crystallizer, the third is usually employed in the control of a crystallizer, and the fifth is often used in relating the dependence of nucleation and growth kinetics on supersaturation as an approximation to the first.

1.1.2. Nucleation

The molecular rearrangement which leads to the development of a new ordered solid phase from a liquid or amorphous phase, and the thermodynamic and kinetic principles that initiate such arrangement, is called crystal nucleation (Zettlemoyer, 1969).

Nucleation mechanisms are classified into two types; homogenous and heterogeneous. In the former collisions on the molecular scale generate nuclei and in the later solid surfaces catalyse the nucleation process, Mersmann and Kind (1988).

Nucleation is a very important process in relating crystallizer design and operation to CSDs. Hence, it sets the character of the crystallization process. Homogeneous and heterogeneous mechanisms are the bases of classical nucleation theory and are referred to as primary nucleation. To explain primary nucleation, consider a hypothetical experiment in the context of the solubility data in Figure (1.1). Starting from point A on the figure where the solution is undersaturated at the corresponding concentration and temperature. Thus, any crystals present in the solution would dissolve. As the concentration increases at constant temperature (e.g., evaporation) the path followed leads to point B, at which the solution becomes saturated. Due to any concentration increase, supersaturated solution would result and any crystals present in the system would grow. However, nucleation cannot be initiated until the system concentration reaches point C, which defines the "metastable limit".

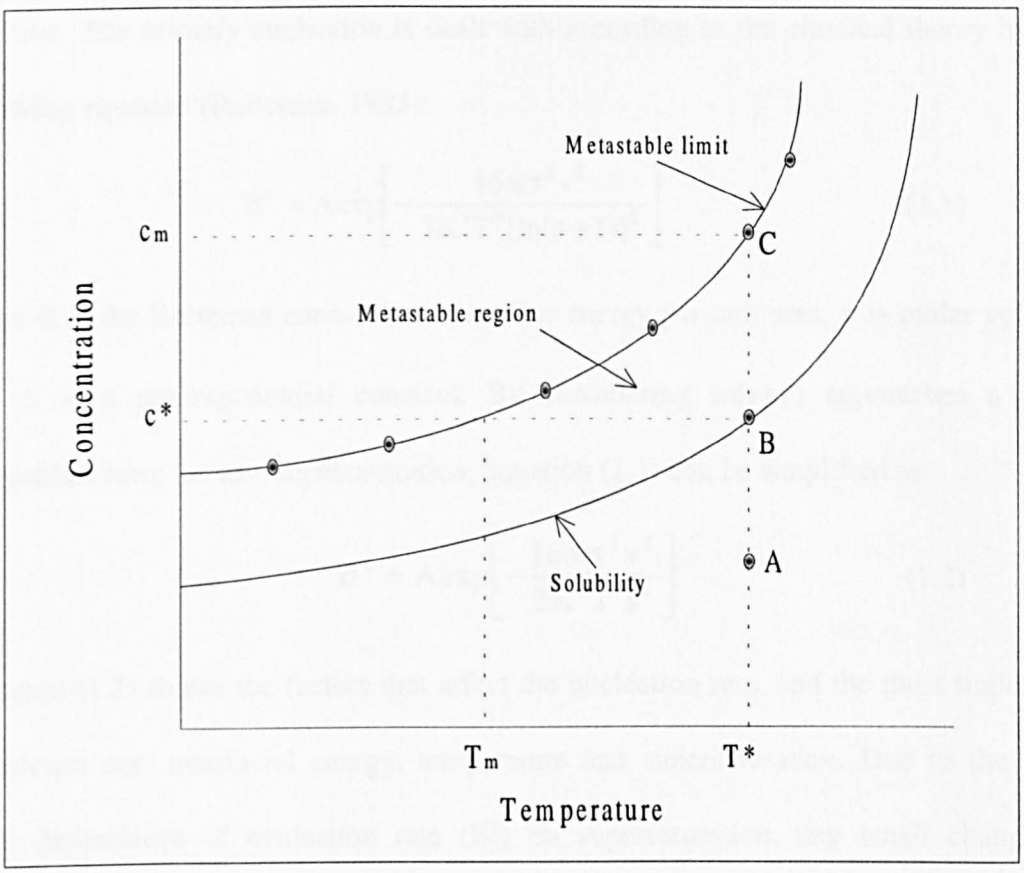

Figure (1.1): Solubility and primary nucleation in a hypothetical experiment.

The metastable curve can be drawn by repeating the same procedure at different temperatures as illustrated in the figure. The width of the metastable zone corresponds to c_m -c* or T*-T_m, which is a characteristic of the substance used, in this zone only crystal growth but not nucleation will occur. Moreover, many factors affect the zone width of the same substance, such as the presence of impurities which alter interfacial tension.

A relatively high supersaturation is needed to induce homogeneous and heterogeneous mechanisms, since they have a high order dependence on supersaturation. This results in numerous fine crystals in systems where the primary mechanisms are

effective. The primary nucleation is dealt with according to the classical theory by the following equation (Rousseau, 1993):

$$B^{\circ} = A\exp\left[-\frac{16\pi\sigma^3 v^2}{3K^3T^3[\ln(s+1)]^2}\right] \qquad (1.1)$$

where K is the Boltzman constant, σ is surface energy per unit area, v is molar volume and A is a pre-exponential constant. By considering ln(s+1) approaches s as s approaches zero, i.e. low supersaturation, equation (1.1) can be simplified as:

$$B^{\circ} = A\exp\left[-\frac{16\pi\sigma^3 v^2}{3K^3T^3s^2}\right] \qquad (1.2)$$

Equation (1.2) shows the factors that affect the nucleation rate, and the most important parameters are: interfacial energy, temperature and supersaturation. Due to the high order dependence of nucleation rate (B°) on supersaturation, any small change in supersaturation may cause the nucleation rate to change dramatically. This explains the phenomenon observed of a clear liquor transformed to a slurry of fine crystals as a result of a slight change in supersaturation, e.g. by temperature drop.

In heterogeneous systems, the catalytic effect of solid particles is employed to reduce the energy barrier to formation of a new phase, i.e. reduce the interfacial energy (σ) significantly. The metastable limit can be obtained through experimentation, and may be used to provide an empirical approach to model primary nucleation.

Empirically the nucleation rate is given as:

$$B^{\circ} = k(c - c^*)^n \qquad (1.3)$$

where the parameters k and n must be found experimentally.

There is another type of nucleation called secondary nucleation. This is a crystal formation through mechanisms involving the solute crystal. Thus, in order to have secondary nucleation, solute crystals must already be present.

Secondary nucleation has special features which make it more important than primary nucleation in many industrial crystallizers. Primary nucleation, however, is thought to be the dominant mechanism during precipitation processes. The secondary nucleation features include: first, continuous and seeded batch crystallizers have crystals in the magma that can participate in the secondary nucleation mechanism. Second, employing the requirements for secondary nucleation is applicable in most industrial crystallizers. Finally, it is more favourable for most industrial crystallizers than primary nucleation, because those industrial crystallizers are operated at a low supersaturation which support secondary nucleation but not primary nucleation. A low supersaturation regime improves yield and enhances product purity and crystal morphology.

Secondary nucleation can be obtained following one of the identified mechanisms in selected systems.

1. Initial breeding: this mechanism is important especially in seeded batch crystallization. It results from immersion of seed crystals in a supersaturated solution. It is also proposed that it is a result of dislodging extremely small crystals that were formed on the surface of larger crystals during drying.
2. Contact nucleation: results from collisions of crystals with one another, and/or crystallizer internals, and/or an impeller in an agitator or circulation pump. The

required energy for contact nucleation is small and does not result in macroscopic degradation (breakage) of the contacted crystals.

3. Shear breeding: when a supersaturated solution flows by a crystal surface and carries with it crystal precursors believed formed in the region of growing crystal surface.

Many studies have investigated factors affecting contact nucleation. The number of crystals generated by a controlled impact of a particle with a seed crystal depends on energy of impact, supersaturation at impact, supersaturation at which crystals developed, hardness of the impacting particle, area of impact, angle of impact, and system temperature. It is impossible to quantify all of these variables, but some generalisations can be set from studying such nucleation mechanism.

For constant supersaturation systems, the following equation was proposed on experimental basis, Rousseau *et al.* (1976):

$$B^\circ = k_N \exp(E - E_t) \qquad (1.4)$$

It was also suggested that a relation of impact energy, E, to crystallizer variables must include the mass of the impacting crystal m_c , the rotational velocity of the impeller providing mixing ω, and the fraction of the available energy actually transmitted to the crystal ε:

$$E = f(\omega, \varepsilon, m_c) \qquad (1.5)$$

Although it has been found that supersaturation affects contact nucleation, this mechanism is not clear. Also, it has been shown that the effect of supersaturation on contact nucleation must consider the reduction of interfacial supersaturation due to the

resistance to diffusion or convective mass transfer. Furthermore, supersaturation affects the solution structure and causes the formation of clusters of solute molecules. These clusters may participate in nucleation, but again the mechanism of this is not clear. The contact nucleation mechanism dominates in many industrial operations, because of the ease with which nuclei can be produced by this mechanism, Rousseau (1993).

1.1.3. Crystal Growth

Growth kinetics are governed by at least two types of resistance. The first, resistance related to integration or incorporation of the crystalline unit into the crystal surface. The second, molecular or bulk transport of the unit from the surrounding solution to the crystal face, Smallwood (1977) and Nancollas and Reddy (1971). The former is of a prime concern here.

Various growth models have been suggested to describe surface reaction kinetics, including models that assume crystals grow by layers and others that propose growth to occur by the movement of a continuous step. Thus, each model gives a particular relationship between growth rate and supersaturation, but none is applicable for a *priori* predictions of growth kinetics.

Models employed to describe the growth of crystals by layers follow a two-step process: (1) formation of a two-dimensional nucleus on the surface and (2) spreading of the solute from the two-dimensional nucleus across the surface. The mononuclear two-

dimensional nucleation (MTDN) theory and the polynuclear two-dimensional nucleation (PTDN) theory are generated from the relative rates at which those two steps occur. The MTDN theory assumes that the surface nucleation step occurs at a finite rate, but the spreading across the surface is assumed to occur at an infinite rate. Whereas for the PTDN theory, the reverse is true. The MTDN theory relates growth to supersaturation as follows:

$$G = C_1 hA\sqrt{\ln(1+s)}\exp\left[-\frac{C_2}{T^2\ln(1+s)}\right] \qquad (1.6)$$

where the parameters C_1 and C_2 are system-dependent constants, h is the height of nucleus, A is the surface area, s is the relative supersaturation and T is the system temperature. The PTDN theory results in the following relationship:

$$G = \left(\frac{C_3}{T^2[\ln(1+s)]^{3/2}}\right)\exp\left[-\frac{C_2}{T^2\ln(1+s)}\right] \qquad (1.7)$$

where C_3 is a system-dependent constant. Finally, if both formation of the two-dimensional nucleus and spreading of the surface layer are important in predicting the growth rate, the following derivation can be obtained:

$$G = C_4 s^{2/3}[\ln(1+s)]^{1/6}\exp\left[-\frac{C_2}{3T^2\ln(1+s)}\right] \qquad (1.8)$$

where C_4 is a system-dependent constant.

Since the quantity s is much less than 1, equations (1.6) to (1.8) can be simplified. The term, ln(1+s), may be approximated to s. Consequently, the MTDN theory becomes:

$$G = C_1 hAs^{1/2}\exp\left[-\frac{C_2}{T^2 s}\right] \qquad (1.9)$$

For the PTDN theory:

$$G = \left(\frac{C_3}{T^2 s^{3/2}}\right)\exp\left[-\frac{C_2}{T^2 s}\right] \tag{1.10}$$

and for both steps occurring at similar rates:

$$G = C_4 s^{5/6}\exp\left[-\frac{C_2}{3T^2 s}\right] \tag{1.11}$$

The screw dislocation or BCF theory (Burton, Cabrera and Frank, 1951), shows that the relationship between growth and supersaturation changes from a parabolic to linear as the supersaturation varies from low to high values, respectively. The growth rate is given by the BCF theory as:

$$G = C\left(\frac{\varepsilon s^2}{\sigma_1'}\right)\tanh\left[\frac{\sigma_1'}{\varepsilon s}\right] \tag{1.12}$$

where ε is screw dislocation activity and σ_1' is a system-dependent quantity that is $\sigma_1' \propto (1/T)$. An empirical approach is also obtainable to relate growth kinetics to supersaturation with a power-law function of the form:

$$G = k_G s^g \tag{1.13}$$

where k_G and g are constants determined by fitting the equation to growth-rate data. However, such type of approaches is valid for a small ranges of supersaturation.

In the models described above, the temperature of the system has a pronounced effect on the growth rate. The relation between growth kinetics and temperature is often given by Arrhenius expression, Mersmann (1995):

$$k_G = k_G^{\circ}\exp\left[-\frac{\Delta E_G}{RT}\right] \tag{1.14}$$

where k_G is a growth rate coefficient of the type required in equation (1.13), k_G^o is a constant and E_G is an activation energy. Different effects are expected from both supersaturation and temperature. These effects influence the growth rates of different faces of the same crystal.

Impurities usually cause a reduction in the growth rates of crystalline materials, therefore obtaining smaller crystals than required is a common problem which is related to contamination of the feed solution. Certain operating conditions must be employed to minimise the possibility of such problems. Monitoring the composition of recycle streams can be advantageous in predicting the possible accumulation of impurities.

Two sets of factors are often attributed due to the outcome of a solvent in growth rates. One deals with the effects of solvent on mass transfer of the solute through adjustments in viscosity, density and diffusivity. The second considers the structure of the interface between crystal and solvent. It is concluded that a solute-solvent system with a higher solubility is likely to produce a rough interface and concomitantly large crystal growth rates.

The studies of magma with multicrystal cover examination of the rate of change of characteristic dimension or the rate of change of mass of crystals. The characteristic dimension, however, depends on the method applied in the determination of the size, e.g. sieve analysis gives the second largest dimension, but both electronic-zone-sensing and laser-light-scattering instruments estimate an equivalent spherical diameter.

The rate of change of a crystal mass dM/dt is related to the rate of change in crystal characteristic dimension by the equation:

$$\frac{dM}{dt} = \frac{d(\rho_c k_v L^3)}{dt} = 3\rho_c k_v L^2 \frac{dL}{dt} \qquad (1.15)$$

where ρ_c is the crystal density and k_v is the volume shape factor. Since an area shape factor, k_a may be defined by the equation:

$$k_a = \frac{A_c}{L^2} \qquad (1.16)$$

and G is defined as dL/dt, therefore:

$$\frac{dM_c}{dt} = 3\rho_c (\frac{k_v}{k_a}) A_c G \qquad (1.17)$$

The definition of growth rate, as the rate of change of the characteristic dimension, is needed for the formulation of a population balance:

$$G = \frac{dL}{dt} \qquad (1.18)$$

and the resulting differential population balance has a solution which requires a knowledge of the relationship between growth rate and size of the growing crystals. In the mean time, this relationship can often be derived from the form of population density data. One of the special cases is that when all crystals in the magma have the same growth rate. If the crystals of the same size have different growth rates in the same environment, they are said to exhibit anomalous growth.

Anomalous growth means that growth rates of crystals in a magma are not the same or that the mass of crystals is not constant. There are two theories explaining anomalous growth: (1) size-dependent growth and (2) growth rate dispersion. Both

affect the form of the population density function that results from perfectly mixed continuous crystallizers, but this behaviour is inefficient to differentiate between the two theories, since they have the same qualitative effects on population density.

Correlating the apparent effect of crystal size on growth rate is attempted by many empirical expressions. The most commonly used correlation is:

$$G = G^{\circ}(1 + \gamma L)^{b}; b < 1 \qquad (1.19)$$

Three parameters are involved in it; G°, γ and b and they are determined from experimental data. Although several theories have been suggested to explain the size-dependent growth kinetics, none has been substantiated by direct observation or used to determine the onset of such behaviour. One explanation shows some applicability, that is: large crystals have higher frequency and energy than smaller crystals during the impact with impellers and other crystallizer internals. Thus, the larger crystals are recipients of more surface breaks and irregularities that lead to higher growth rates. This theory proposes different crystal growth rates in a magma, although they may have identical sizes and the same conditions are employed.

There is experimental support for two different mechanisms describing growth dispersion. One assumes that all crystals have identical time-averaged growth rate, while individual crystals have fluctuating growth rates about some mean value. The other suggests that the formation of crystals is linked with a characteristic distribution of growth rates, but individual crystals retain a constant rate throughout their residence in a crystallizer.

The major factor in both mechanisms of growth rate dispersion is surface integration. The number, sign and location of screw dislocations on the surface of a growing crystal influence the growth rate, this is illustrated by the BCF theory. Changes in the dislocation network occur as a result of a number of reasons: (1) collision of crystals with each other and crystallizer internals and (2) imperfect growth of crystal faces. The first leads to random fluctuations of growth rates. The varying dislocation networks and densities among nuclei and seed crystals, produce the distribution of growth rates.

Two different mechanisms are proposed for incorporating both mechanisms of growth rate dispersion into descriptions of crystal population: the first is a random growth rate and the second is the growth rate distributions. In order to clarify the relative influences of the two mechanisms on CSDs from batch and continuous crystallizers, both mechanisms can be included in a population balance.

1.4. Agglomeration

As mentioned earlier, agglomeration occurs just after nucleation, where small particles in liquid suspension have a tendency to cluster together. If the particles are small enough for the van der Waal forces to exceed the gravitational forces, then the interparticle collision may result in a stable new larger particle. The above constraint is applicable for sizes < 1 μm.

The required time to halve the number of particles in monodisperse system is called the half-time t*, which is given by the expression, Smoluchowski (1918):

$$t^* = [\frac{n_t}{(n_o - n_t)}]t \qquad (1.20)$$

where n_t and n_o are the numbers of particles at t = t and t = 0, respectively. If an arbitrary agglomerated system is defined as one in which more than 10% of particles have agglomerated in less than 1000 s, then aqueous systems containing less than 10^7 cm^{-3}. However, agglomeration is quite common in systems that have nucleated homogeneously when n often exceeds 10^7 cm^{-3}. In general, not all interparticle collisions result in permanent contact, and charge stabilisation in lyophopic systems has a major influence in decreasing the rate of agglomeration.

Two types of agglomeration are reported for colloidal particles in suspension, Smoluchowski (1918):

1. Perikinetic (static fluid, particles in Brownian motion)
2. Orthokinetic (agitated dispersion, fluid shear)

Precipitation processes involve both modes, but orthokinetic agglomeration dominates in a stirred precipitator. The relationship between agglomerate size and time t can be given by:

$$D^3(t) = A_1 + B_1 t \qquad \text{(Perikinetic)} \qquad (1.21)$$

and

$$\log D(t) = A_2 + B_2 t \qquad \text{(Orthokinetic)} \qquad (1.22)$$

where A and B are particle-fluid system constants. These two equations are strictly applicable only to the early stages of agglomeration, because they imply an unlimited

increase of agglomerate size with time, which is unrealistic. In fact, after a certain time, an upper limiting agglomerate size D_{max} is often reached which in many cases may be comparable with the Kolmogoroff microscale of turbulence (typically around 25-50 μm in stirred vessels). Moreover, D_{max} is a function of the mixing intensity and often satisfies an expression of the form:

$$D_{max} \propto N^{-n} \qquad (1.23)$$

where N is the stirrer speed and exponent n has a value of 0 or 3 for viscous or inertial forces respectively, however, in the transition region n has some intermediate value, Mullin (1993).

1.1.5. Ageing

1.1.5a. Ripening

There is a tendency of smaller particles in a saturated solution to dissolve and the solute to be deposited subsequently on the larger particles. Therefore, the large particles become larger and the smaller disappear. Theoretical works suggest that particle size distribution changes towards that of monosized dispersion. This is because the solid phase in the systems tends to adjust itself to obtain a minimum total surface free energy. This particle coarsening process is called "Ostwald ripening".

The solubility difference between small and large particles is the driving force for ripening as given by the size-solubility (Gibbs-Thomson) relationship, Mullin (1993):

$$\ln\left[\frac{c(r)}{c^*}\right] = \frac{2M\gamma}{\nu RTr\rho} \qquad (1.24)$$

where c(r) is the solubility of (small) particles of size (radius) r, c* is the normal equilibrium solubility of the substance (as $r \rightarrow \infty$), R is the gas constant, T is the absolute temperature, ρ is the density of the solid, M is the molecular weight of the solid in solution, γ is the interfacial tension of the solid in contact with the solution and ν represents the number of ions formed from one mole of electrolyte, for a non-electrolyte $\nu=1$.

Equation (1.24) can be written for the present purpose as:

$$\ln\left[\frac{c(r)}{c^*}\right] = \frac{2\gamma v}{\nu RTr} \qquad (1.25)$$

where v is the molecular volume of the solute. A significant increase in solubility occurs when $r < 1\mu m$. By expanding the logarithmic in equation (1.25) for $c(r) / c^* \sim 1$ (i.e. ripening takes place at very low supersaturation), the following expression can be obtained:

$$c(r) - c^* \approx \frac{2\gamma v c^*}{\nu RTr} \qquad (1.26)$$

If it is possible to have mass transport between the particles in a polydisperse precipitate, then the large will grow at the expense of the small. If the growth kinetics involved are first order, diffusion controlled, the particle radius changes with time as:

$$\frac{dr}{dt} = \frac{Dv[c - c(r)]}{r} \qquad (1.27)$$

where c is the average bulk solution concentration and from equation (1.26):

$$\frac{dr}{dt} = \frac{Dv}{r}\left[(c - c^*) - \frac{2\gamma v c^*}{vRTr}\right] \tag{1.28}$$

where (c-c*) > 0 during precipitation. By setting equation (1.28) equal to zero, all particles of size:

$$r = \frac{2\gamma v c^*}{vRT(c - c^*)} \tag{1.29}$$

are in equilibrium with the bulk solution (dr/dt = 0). All particles smaller than this will dissolve (dr/dt < 0), and all particles larger will grow (dr/dt > 0).

Ripening speed depends on the particle size and solubility. For diffusion controlled growth kinetics, the linear growth velocity is approximated to:

$$\frac{dr}{dt} \approx \frac{\gamma v^2 D c^*}{3vRTr^2} \tag{1.30}$$

by integration:

$$t \approx \frac{vRTr^3}{\gamma v^2 D c^*} \tag{1.31}$$

Therefore, the ripening process is faster for smaller particles or for higher solubility. On the other hand, at low supersaturation, the ripening process is more likely to be controlled by a surface reaction than a diffusion process, thus ripening may be retarded. The linear growth velocity for surface reaction growth kinetics, follows an expression such as:

$$\frac{dr}{dt} = k(c - c^*)^n \tag{1.32}$$

where k is a growth rate constant. If n has an assumed value of 2, then

$$t = \left[\frac{vRT}{\gamma v c^*}\right]^2 \frac{r^3}{k} \tag{1.33}$$

Therefore, from equation (1.31): [$t = t_D$] and equation (1.33): [$t = t_R$],

$$t_R \approx \left(\frac{\nu R T D}{\gamma k c^*} \right) t_D \qquad (1.34)$$

Ripening process is influenced to a large extent by the interfacial reaction. However, suspension stability can be achieved by an additive to the system, which slows down the surface reaction step, and automatically retard the ripening process.

Although particle size distribution of a precipitate can be affected by ripening over a period of time, even in an isothermal system, controlled temperature fluctuations can accelerate this change. This behaviour is called "temperature cycling", has been introduced to alter the physical characteristics of organic and inorganic precipitates, Mullin (1993).

1.1.5b. Phase Transformation

Ostwald ripening is considered as an important ageing process for a precipitate that remains in contact with it's mother liquor, specially for small primary crystals (<1μm). But it is not the only ageing process, nor it is always the most important one.

There is another stage that is the first precipitation of a metastable phase followed by a phase transformation to the final product. The metastable phase may have different forms such as; an amorphous precipitate, a polymorph of the final product, a hydrated species or some system contaminated substance, Mullin (1993).

1.1.6. Crystal Size Distribution (CSD)

Although good yield and high purity are very important aspects in crystallization, the appearance and size range of the crystalline product are significant as well. The individual crystals of the final product, for marketing purposes, must be strong, nonaggregated, uniform in size and noncaking in the package. Consequently, controlling CSD is the prime objective in the design and operation of crystallization processes, McCabe and Smith (1976).

This first general recognition of the importance of the CSD was studied in depth by Randolph and Larson who presented the interrelationships between the CSD and the crystallizer design criteria, and operating problems, Tavare (1986).

Söhnel *et al.* (1991) reviewed the CSD "schools". Three different schools were reported. The Japanese, which is based on kinetic considerations, the European which adopted crystal mass and number balances analysis and the Northern American which used the population balance. These different approaches result in similar design equations, but not fully identical.

CSD is usually expressed as a population (number) distribution or as a mass (weight) distribution. The former shows how the number of crystals at each size is distributed over the size domain, and the later relates the mass to the size range. The two distributions are related and they affect many areas such as, crystal processing and

properties including appearance, solid-liquid separation, purity, reactions, dissolution and other properties involving surface area.

Population density (n) is very important in the discussion of CSD. It has dimensions of [number/(volume)(length)], which means that it is a function of the characteristic crystal dimension, L, i.e. independent of the magnitude of the system. If the total population density is used, it is given the symbol $\bar{n}$ with units (number/length). Population density can be defined in mathematical terms as the number of crystals per unit system volume (ΔN) in a size range from L to L+ΔL, thus

$$n = \lim_{\Delta L \to 0} \frac{\Delta N}{\Delta L} \tag{1.35}$$

Since n is based on the system volume, this volume must be defined in order to have a meaningful population density function, it can be for instance, the volume of the slurry or the volume of the clear liquor in the system.

The function N in equation (1.35) is a cumulative number distribution representing the number of crystals per unit volume in the distribution that have a characteristic dimension less than L' which implies:

$$N(L') = \int_0^{L'} n\,dL \tag{1.36}$$

and the fraction of the crystals, of a size less than L', in the distribution $F(L')$ can be obtained by:

$$F(L') = \frac{N(L')}{N_{tot}} \tag{1.37}$$

By analogue to population density, the mass (weight) density function is given the symbol m with units [mass/(volume)(length)], also letting ΔM to be the mass of crystals per unit system volume in the size range L to L+ΔL, therefore:

$$m = \lim_{\Delta L \to 0} \frac{\Delta M}{\Delta L} \tag{1.38}$$

A simple shape factor can be introduced relating the two density functions. Let the mass of a single crystal to be M_c with a characteristic dimension L. Assuming that the crystal is from a population with a shape independent on size, therefore, the mass of any crystal from that population is related to characteristic dimension by a volume shape factor (k_v):

$$M_c = k_v \rho_c L^3 \tag{1.39}$$

where ρ_c is the crystal density. Since the mass of a sample is the product of the number of crystals in this sample and the mass of a single crystal, mass and population densities may be related as follows:

$$\Delta M = k_v \rho_c L^3 \Delta N \tag{1.40}$$

Dividing by ΔL as this expression approaches to zero:

$$m = k_v \rho_c n L^3 \tag{1.41}$$

M is cumulative mass distribution function which shows the mass of crystals having a characteristic dimension less than L′. Thus, the total mass of crystals per unit system volume can be related to population density as:

$$M_T = k_v \rho_c \int_0^\infty n L^3 dL \tag{1.42}$$

which is called "magma density" or solids concentration. Crystals with a size less than L′ have a cumulative mass fraction defined as:

$$W(L') = \frac{M(L')}{M_T} = \frac{k_v \rho_c \int_0^{L'} n(L) L^3 dL}{M_T} \qquad (1.43)$$

In order to characterise a particulate matter, moments of a distribution are introduced to provide such information. The jth moment, of the population density function, is defined as:

$$m_j = \int_0^{\infty} L^j n dL \qquad (1.44)$$

It can be shown that the values of zero, first, second and third moments of the population density function, are related to the total number of crystals, the total length, the total area and the total volume of crystals, all in a unit volume of system volume. Another parameter which is often used as a particle characteristic, is the coefficient of variation (cv) of a distribution. It is a measure of the spread of the distribution about some characteristic size, and is related to the dominant size to characterise crystal populations through the equation:

$$cv = \frac{\sigma}{L_D} \qquad (1.45)$$

where σ is the standard deviation of the distribution. cv of the mass density function about the dominant crystal size is given by:

$$cv = \sqrt{\frac{m_0 m_2}{m_j^2} - 1} \qquad (1.46)$$

The most favoured size distribution is one that is monodisperse, i.e., all crystals have the same size, so that the rate at which crystals dissolve and taken up by the body is known and reproducible, Rousseau (1993).

1.1.7. Population Balances and CSDs

Process variables can be related to the CSD, produced by a crystallizer, by using population balances and crystallization kinetics, Zumstein and Rousseau (1987). These balances are coupled with mass and energy balances. Population distribution is proposed as a continuous function and a characteristic dimension L is given to describe crystal size, surface area and volume. Also, it is assumed that area and volume shape factors have constant values, that means there is no change in the crystal morphology with size.

If a crystal size range is assumed, say L_1 to L_2 , then a balance can be carried out around a control volume V_T on the number of the crystals in the assumed range. This balance should account for crystals that enter and leave the size range by both convection flow and crystal growth. In the following analysis, primary nucleation is assumed to be predominant and agglomeration, secondary nucleation and attrition are neglected. The crystal growth rate (G) can be defined here as the rate of change of the characteristic dimension (L) of the crystal, i.e. $G = dL/dt$.

If a well mixed crystallizer Figure (1.2) is considered with a constant slurry volume V_T, it is possible to derive the following partial differential population balance, Randolph and Larson (1988):

$$\frac{\partial(nG)}{\partial L} + \frac{Q_o n}{V_T} - \frac{Q_i n_i}{V_T} = -\frac{\partial n}{\partial t} \qquad (1.47)$$

In order to simplify this equation, some assumptions can be incorporated: (a) clear feed ($n_i = 0$), (b) steady state ($\partial n/\partial t = 0$), (c) G is invariant and (d) a mean residence time τ is defined as V_T/Q_o then:

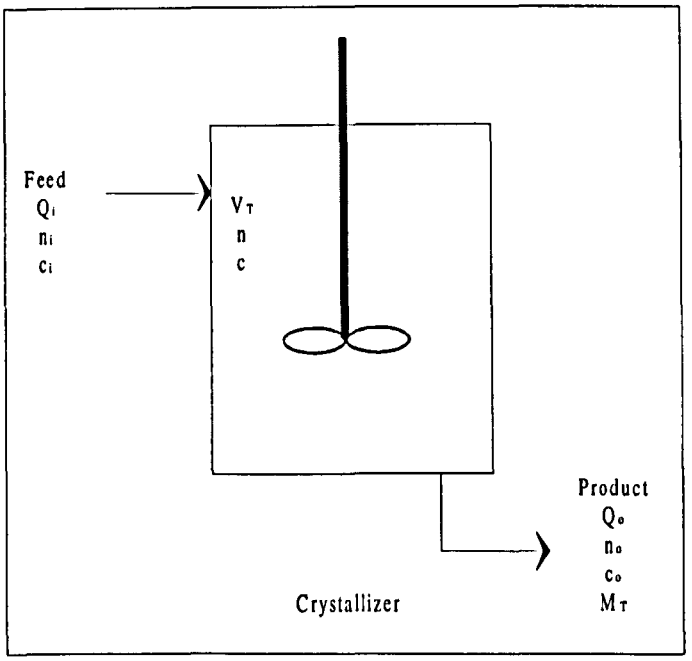

Figure (1.2): Schematic diagram of a simple, perfectly mixed crystallizer.

$$G\frac{dn}{dL} + \frac{n}{\tau} = 0 \qquad (1.48)$$

τ is also known as the drawdown time, i.e. the time needed to empty the crystallizer contents when the feed is set to zero. By applying the boundary condition, $n = n^o$ at L=0, equation (1.48) can be written as:

$$n(L) = n_o exp\left[-\frac{L}{G\tau}\right] \tag{1.49}$$

If the volume of the magma V_T, is not constant, then equation (1.47) becomes:

$$\frac{\partial n}{\partial t} + \frac{\partial (nG)}{\partial L} + n\frac{\partial (\ln V_T)}{\partial t} + \frac{Q_o n}{V_T} = 0 \tag{1.50}$$

Equations (1.49) and (1.50) are based on a crystallizer model which is referred to as the mixed-suspension, mixed-product removal (MSMPR) crystallizer, Randolph and Larson (1988). A more general form of the population balance can be given as:

$$\frac{\partial n}{\partial t} + \nabla \cdot \mathbf{v}_e n + \mathbf{V} \cdot \mathbf{v}_i n = B - D \tag{1.51}$$

where $\mathbf{v}_e$ and $\mathbf{v}_i$ are the external (spatial) and internal particle velocity vectors, respectively and the particle birth and death functions are represented by B and D, respectively. This general form highlights the mathematical similarity with the mass continuity equation (see section 1.3.3) and it is beneficial for spatially distributed systems, as here.

1.1.8. Precipitation Techniques:

In this section, three techniques will be reviewed:

1.1.8a. Precipitation by direct mixing

One of the main standard methods, used in various chemical industries, is the precipitation as a result of chemical reaction between gases and /or liquids. This type of

precipitation happens because the gaseous or liquid phase becomes supersaturated with respect to the solid precipitate. Thus, a crystallization process can be obtained by controlling the degree of supersaturation of a crude precipitation.

Mixing two solutions together as quickly as possible is a common method used to produce a precipitate. A complex analysis, however, may be introduced in some systems. One of the difficulties incorporated in precipitation processes (i.e., highly supersaturated systems) is to obtain uniform conditions throughout the reaction vessel. Consequently, the choice of method of mixing the reactants is of a critical importance to avoid any possible development of excessive supersaturation zones. Also, the development of local pockets of reactants in non-stoichiometric ratios, undesirable pH levels, and so on, can have profound effects.

Primary nucleation occurrence depends on high levels of supersaturation. Thus, a possible time lag (induction period) is expected after the mixing stage. Induction period is influenced by a number of factors such as: temperature, supersaturation, efficiency of mixing, state of agitation, presence of impurities, and so on, before nuclei appear. Although the growth of nuclei is the predominant process when a rapid desupersaturation ensues, some time after the induction period, primary (homogeneous and heterogeneous) and possibly secondary nucleation can occur together. Subsequent particle coarsening may result by particle agglomeration followed by ageing processes (e.g., ripening).

1.1.8b. Precipitation From Homogeneous Solution (PFHS)

In general, when gravimetric analysis is aimed, precipitation must be carried out slowly from dilute solution, since an efficient separation of precipitate from liquid is necessary to be affected. Extremely high dilutions and excessively long times, however, are needed for some substances (e.g., hydroxides and basic salts of aluminium, iron and tin) in order to produce dense particles. This method is called "precipitation from homogeneous solution" (PFHS), where coarse precipitates are produced in relatively short times.

PFHS technique can be described as slowly generating the precipitation agent homogeneously within the solution by chemical reaction means. Since the supersaturation levels are under control, undesirable concentration influences are eliminated, a dense granular precipitate is produced and co-precipitation is minimised.

PFHS is one of the major methods in analytical chemistry. Furthermore, it is also used in studies of co-precipitation and nucleation phenomena, since a close equilibrium between the solid and the solution can be achieved by the slow controlled precipitation. Although industrial scale of PFHS applications is limited, the PFHS technique appears to be promising. For example, PFHS improves on fractional precipitation methods and it has also been employed in the difficult separation of radium and barium, for the production of carriers for radioactive materials and for the preparation of monodisperse suspension of pigments and polishing agents.

1.1.8c. Salting-out

This term is assigned for processes where supersaturated solution is obtained with respect to a given solute, by adding a substance that reduces the solubility of the solute in the solvent. The added substance is called "precipitant". The process itself, however, has a variety of other terms such as: watering out, quenching, solventing out, and so on, depending on the operation involved.

A liquid precipitant needs to be miscible with the solvent of the original solution, at least over the ranges of concentration encountered that the solute be relatively insoluble in it. At the same time, the final solvent-precipitant mixture can be separated (e.g., by distillation), if comprising valuable components.

Various advantages may be obtained by employing the salting-out technique. For example, a solution can be highly concentrated initially by dissolving an impure crystalline material in a suitable solvent. If the miscibility of the solute in the given solvent is high then the dissolution may be affected at low temperatures, and this is advantageous for the processing of heat-sensitive substances. Solute recovery yield may be increased by the proper choice of precipitant. Moreover, purification achieved from applying salting-out is better than that obtained from straight forward crystallization operation because the original solvent has less ability to retain the undesirable impurities than the mixed mother liquor. On the other hand, salting-out technique needs a separation unit, if the solvent and precipitant have to be recovered, which is a disadvantage.

Excessive nucleation, in the regions of primary contact, can be avoided by a slight dilution of the salting-out agent with the system solvent. Supersaturation levels (and hence nucleation rates) may also be reduced by the use of diluted precipitant. If the precipitant is a volatile organic liquid, then the procedure can be arranged quite easily.

Not only liquids can be used as precipitant, but also gases and solids, as long as they are miscible in the original solvent without reacting with the solute to be precipitated. Salts can precipitate from solutions by the addition of other crystalline salts, the formation of a stable salt pair is an example of that, Mullin (1993).

1.1.9. Determination of Crystallization Kinetics

In a continuous well-mixed crystallizer under steady state conditions, crystal production rate is identical to the rate of nucleation B^0, therefore:

$$B^\circ = \frac{1}{\tau}\int_0^\infty n\,dL \qquad (1.52)$$

For an MSMPR crystallizer with constant V_T:

$$B^\circ = n^\circ G \qquad (1.53)$$

Combining equations (1.49) and (1.53):

$$n = \frac{B^\circ}{G}\exp\left[-\frac{L}{G\tau}\right] \qquad (1.54)$$

Equation (1.54) gives the opportunity to evaluate nucleation and growth rates at the system conditions, by taking a single sample either from the magma (inside the crystallizer) or from the product stream. A plot of population density as a function of

characteristic size, L, on a semi-log paper, gives a straight line with a slope of $-\frac{1}{G\tau}$ and an interception of $n^o = B^o/G$ thereby facilitating simultaneous determination of G and B^o.

Since many industrial crystallizers operate in a well-mixed or nearly well-mixed manner, the equations described above can be used to predict their performance. A general correlation of nucleation and growth kinetics, can be obtained by performing a series of runs at different operating conditions. In addition, this correlation can be used to guide either crystallizer scale-up or the development of an operating strategy for an existing crystallizer. Nucleation and growth are influenced by a number of variables such as: temperature, supersaturation, magma density and external stimuli (e.g., agitation or circulation rate of the magma). Usually, empirical power-law functions are used in correlating nucleation and growth rates, but independent variables choice can be obtained from a mechanistic perspective. The following power-law functions are used quite frequently:

$$B^o = k_1 s^b M_T^j \tag{1.55}$$

$$G = k_2 s^g \tag{1.56}$$

Supersaturation measurements are usually difficult, especially if the growth rates are high. Although supersaturation can be neglected in the mass balance of the solute because it is so small in such systems, it is significant in predicting nucleation and growth rates. Therefore, it is then preferable to substitute growth rate for supersaturation by combining equations (1.55) and (1.56) to obtain:

$$B^{\circ} = k_n G^i M_T^j \qquad (1.57)$$

where k_n is a coefficient, which may depend on process variables such as temperature, rate of agitation or circulation, presence of impurities, and other variables. The system-specific constants i and j can be obtained using experimental data and may be incorporated in scale-up, but noting that j may vary with mixing conditions.

1.1.10. Mass balance constraints

From Figure (1.2), a mass balance on solute can be written as:

$$Q_i c_i = Q_o c_o + Q_o M_T \qquad (1.58)$$

where c_o is determined by system kinetics and constrained by solid-liquid equilibrium (solubility) relationship, which gives the equilibrium concentration c* at the system conditions. The system is characterised by the supersaturation magnitude (i.e. c_o - c*) remaining in the product stream. If the system is closed, where c* is substituted for c_o, then the system is called a fast-growth or class II system. On the other hand, if the system is not closed, it is said to be class I (slow-growth) system, where $c_o > c^*$ and

$$M_T = \frac{Q_i}{Q_o} c_i - c_o \qquad (1.59)$$

c* is not influenced by process variables, thus, M_T is constant over modest ranges of operating conditions, Rousseau (1993).

1.1.11. Moments of crystal size distribution

In this section, the moments equations are derived with a reference to the CSD section.

The number of crystals, N, up to size L, can be written as:

$$N = \int_0^L n\,dL \tag{1.60}$$

From equation (1.49):

$$N = \int_0^L n_o \exp\left[-\frac{L}{G\tau}\right] dL$$

$$N = n_o G\tau\left(1-\exp\left[-\frac{L}{G\tau}\right]\right) \tag{1.61}$$

This equation is the zeroth moment of the distribution, and as L approaches ∞, it reduced to the total number of crystals in the system:

$$N_T = n_o G\tau \tag{1.62}$$

The first moment of the distribution represents the comulative length (all the crystals laid side by side), but it is not of a critical importance:

$$L = \int_0^L nL\,dL$$

$$= \int_0^L n_o L \exp\left[-\frac{L}{G\tau}\right] dL$$

$$= n_o(G\tau)^2\left(1-\exp\left[-\frac{L}{G\tau}\right]-L\exp\left[-\frac{L}{G\tau}\right]\right) \qquad (1.63)$$

For $L \rightarrow \infty$: $$L_T = n_o(G\tau)^2 \qquad (1.64)$$

The second moment gives the surface area:

$$A = k_a \int_0^L nL^2 dL \qquad (1.65)$$

where k_a is a surface shape factor. For $L \rightarrow \infty$:

$$A_T = 2k_a n_o (G\tau)^3 \qquad (1.66)$$

The third moment gives the mass:

$$M = k_v \rho_c \int_0^L nL^3 dL \qquad (1.67)$$

where k_v is a volume shape factor and ρ_c is the crystal density. For $L \rightarrow \infty$:

$$M_T = 6k_v \rho_c n_o (G\tau)^4 \qquad (1.68)$$

Dimensionless correlations can be obtained as a single representation of the above equations using a relative size by putting $X=L/G\tau$, i.e., the ratio of crystal size to the size of a crystal that needs a period equals to the residence time τ.

$$\frac{N}{N_T} = N(X) = 1-\exp(-X) \qquad (1.69)$$

$$\frac{L}{L_T} = L(X) = 1-(1+X)\exp(-X) \qquad (1.70)$$

$$\frac{A}{A_T} = A(X) = 1-(1+X+\frac{X^2}{2})\exp(-X) \qquad (1.71)$$

$$\frac{M}{M_T} = M(X) = 1-(1+X+\frac{X^2}{2}+\frac{X^3}{6})\exp(-X) \qquad (1.72)$$

The use of the relative size X simplifies the CSD analysis. The CSD can be carried out by applying the relative size X, without a reference to the dependence of growth rate on supersaturation. The differential mass distribution is given by:

$$\frac{dM(X)}{dX} = \frac{1}{6}X^3\exp(-X) \qquad (1.73)$$

(see e.g. Mullin, 1993).

1.1.12. Mass and Energy Balances

Many texts (e.g. Rousseau, 1993) have dealt with the procedures followed in the formulation of mass and energy balances. If the maximum rate of crystal production from a crystallizer, P_{max}, operating at temperature T_2 with an inlet stream of a saturated solution at temperature T_1, P_{max} depends on T_2 and is given by:

$$P_{max} = Fx_F - Lx_L \qquad (1.74)$$

where F is the feed rate, L is the mother liquor flow rate and x_F and x_L are mass fractions of solute in the feed and the mother liquor, respectively. The solute balance can be represented as:

$$x_c P_{max} = Fx_F - Lx_L \qquad (1.75)$$

where x_c is mass fraction of solute in the crystal.

The rate of heat removal from such a crystallizer can be evaluated from an energy balance:

$$F\hat{H}_F = P\hat{H}_c + L\hat{H}_L + Q \qquad (1.76)$$

where $\hat{H}$ is the specific enthalpy of the stream corresponding to the subscript, viz., the feed, the crystals and the mother liquor, respectively, and Q is the required rate of heat transfer. By evaluating F, P and L from mass balance, Q can be calculated using methods of estimating specific enthalpies.

Enthalpy data can be obtained either from literature or from estimation where a number of steps must be specified. First, reference states for both solvent and solute are defined. The most common reference states are: pure solvent and crystalline solute at a reference temperature corresponds to that at which the heat of crystallization $\Delta\hat{H}_c$ of the solute is known. The heat of crystallization $\hat{H}_c$ is approximately equal to the negative of the heat of the solution. If the temperature T_{ref} is the temperature at which the heat of crystallization is known, then reference conditions are reasonably taken to be the solute as a solid and the solvent as a liquid both at T_{ref}. Thus, evaluation of the enthalpies is now possible:

$$\hat{H}_F = x_F \Delta\hat{H}_c + C_{PF}(T - T_{ref}) \qquad (1.77)$$

$$\hat{H}_c = C_{Pc}(T - T_{ref}) \qquad (1.78)$$

$$\hat{H}_L = x_L \Delta\hat{H}_c + C_{PL}(T - T_{ref}) \qquad (1.79)$$

where C_{PF}, C_{Pc} and C_{PL} are heat capacities of the solute in the feed, the crystals and the mother liquor, respectively. The values of these heat capacities can be found experimentally, and then used to calculate the rate of heat transfer.

Assume that some of the solvent is evaporated in the crystallizer, Figure (1.3). Total mass and solute balances can be written independently as:

$$F = V + L + P \tag{1.80}$$

$$x_F F = x_L L + x_c P \tag{1.81}$$

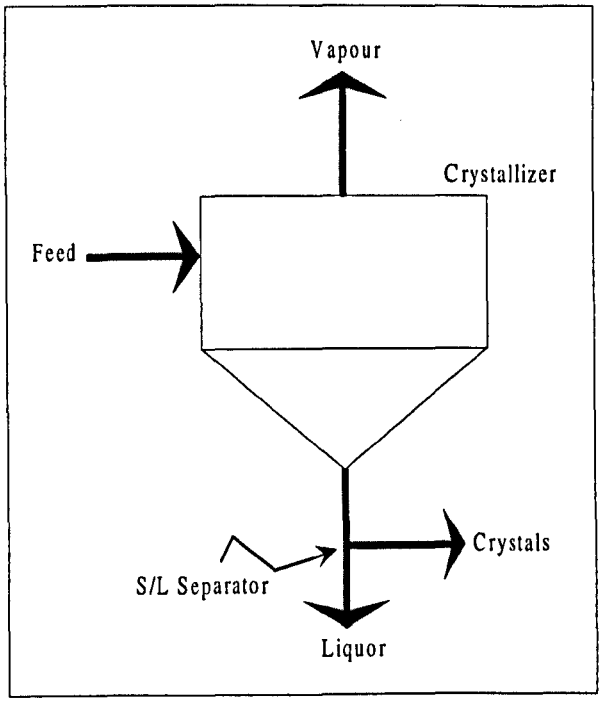

Figure (1.3): Schematic diagram of a simple crystallizer.

There is an equilibrium equation relating x_L, x_c and temperature or pressure at which the operation is conducted. Also, satisfying the energy balance is a necessity:

$$F\hat{H}_F + Q = V\hat{H}_V + L\hat{H}_L + P\hat{H}_c \tag{1.82}$$

1.1.13. Driving Force for Mass Transfer

A variety of possible driving force choices can be made for a mass transfer process. In some cases, such as high mass flux conditions, the choice is crucial. For low

mass flux mass transfer from a single sphere to an extensive fluid, the expression (see e.g. Mullin, 1993):

$$Sh = 2 + 0.72Re_p^{1/2}Sc^{1/3} \qquad (1.83)$$

may be employed in the range: $20 < Re_p < 2000$.

The mass transfer coefficient in the Sherwood number may be defined by:

$$R = K_c(c_o - c_\infty) \qquad (1.84)$$

$$= K_c(\rho_o\omega_o - \rho_\infty\omega_\infty) \qquad (1.85)$$

$$= \rho_c K_c(\omega_o - \omega_\infty) \qquad (1.86)$$

where $\rho_o \approx \rho_\infty \approx \rho_s$, for low mass flux. Also, there are other definitions of mass transfer coefficient, including:

$$R = K_\omega(\omega_o - \omega_\infty) \qquad (1.87)$$

$$= K_y(Y_o - Y_\infty) \qquad (1.88)$$

$$= K_b B \qquad (1.89)$$

where R = mass flux, c = solution concentration, K = mass transfer coefficient, (K_c = m/s, K_ω= kg/(m^{2}s$\Delta\omega$), K_y = kg/(m^{2}sΔY), K_b = kg/(m^{2}sB), ρ_s = solution density (kg/m^3), ω = mass fraction of solute in solution (dimensionless) and Y is the mass ratio of solute to solvent in the solution. The subscripts o and ∞ refer to the interfacial and bulk solution conditions, respectively.

The dimensionless driving force for mass transfer, B, is defined as:

$$B = \frac{\omega_o - \omega_\infty}{\omega_i - \omega_o} \qquad (1.90)$$

where ω_t is mass fraction of the solute in the transferred solid substance, e.g. for single component $\omega_t = 1$. Also, $\omega_t = 1$ for hydrate solute provided that the mass fractions are given as mass of hydrate per unit mass of solution.

Equation (1.83) predicts the dissolution of solid solute into a solvent or its own solution, and either K_c or K_ω can be involved since $Sh = K_c d/D = K_\omega d/\rho_s D$. If solute solubility is high, the procedure becomes complicated. Two possible causes for such cases: (1) the physical properties depend significantly on the concentration, and (2) the mass flux from the surface alters the concentration gradient at the surface compared with that obtained under otherwise identical conditions of low mass flux.

1.1.14. Residence Time Distribution (RTD)

This term is of a great importance in chemical reaction engineering where sophisticated situations can be simplified in process vessels, and design procedures become manageable to a certain extent. RTD is a characteristic feature of macromixing. It represents a pioneering combination of theory and practice in minimising the complexities of modelling physical situations for both flow and mixing to a tractable form without losing their identity.

The term "particle" may represent any conserved entity, e.g. molecule, Brownian particle, elementary volume of fluid or clump. To describe the history of a particle, a simple system can be taken. For instant, in a steady-state continuous-flow system, the

particle enters the system and stays in it for some particular (deterministic or probabilistic) time; and eventually leaves. Once the particle enters the system, there may be a number of possible exits and consequently reenterances, but it is necessary to have a first entrance and an absolute final exit. The age of a particle can be presented to relate the particle to time, taking the time when the particle enters the system to be zero age and when the particle leaves the last exit from the system to be the residence time of the particle. The normalised density function gives the distribution of the residence times of the particle leaving the system. This function is the dimensionless RTD.

If there is not enough information about the flow and mixing within the vessel, RTD analysis can be useful, bearing in mind that it is not fully adequate to describe the flow configuration completely. RTD can be obtained experimentally, however. A useful experimental technique called a stimulus-response (input signal) may be employed, where a tracer material is induced in the flow such as pulse, step or periodic injections. It is possible to predict the state of the system and the behaviour of the flow, from the amount and the concentration of the tracer material. Another useful feature of the stimulus-response is that it is very effective in predicting the equipment performance, provided that the rate for a process is linear in an intensive property of a particle.

In multiphase process configurations, the RTD analysis is introduced for each phase in order to achieve better modelling. RTD studies play a major role in determining a mathematical model of a system representing the behaviour of flow and mixing realistically enough to make appreciable contribution towards the design and analysis of the system.

1.2. Mixing and Precipitation Processes Interactions

1.2.1. Introduction

Mixing phenomenon is usually introduced to overcome the non-uniformities or gradients (i.e. changes in composition, properties or temperature) of the fluid(s) in the bulk. It is achieved by the movement of fluid(s) between different parts of the whole mass in the vessel. The movement of the fluids combines a set of the following mechanisms: laminar and turbulent bulk flow regimes and eddy and molecular diffusion.

The most common mixing operation is when different molecular species are brought together to initiate and facilitate a chemical reaction. Mixing systems components can be (1) miscible liquids, (2) immiscible liquids, (3) solid particles and a liquid, (4) a gas and a liquid, (5) a gas and solid particles or (6) two gases. Since the fluid inertia exerts a resisting force if there is a directional or velocity changes, external forces are needed to overcome the resisting forces. In the case of a two-phase system, inertia and shear forces cause the reduction of the dispersed-phase particle size, i.e., increase in interfacial area, Uhl and Gray (1966).

Mixing process can be identified by two distinguishable elements, macro- and micro-mixing. These two elements are independent of each other. Macromixing is characterised by the residence time distribution (RTD) of the elementary volume

whereas micromixing (i.e. mixing at the fine scale level by molecular diffusion, Bourne and Dell'ava, 1987) clarifies the interrelationship between elementary volumes. The scale of mixing is the main pronounced difference between them. Furthermore, while macromixing defines the RTD and is influenced by agitator speed, vessel geometry, etc., micromixing covers all other mixing aspects and is influenced by fluid physical properties and local conditions, Tavare (1986).

Precipitation is one of the common and widely used techniques in the chemical industry (Mullin, 1993). As a result of chemical and physical changes in a solution, an amorphous or crystalline solid is formed and separated often as a very low solubility and very small mean crystal size. Controlling a precipitation process is often not a straight forward procedure with respect to crystal size, shape, agglomeration and encrustation. On the other hand, crystallization processes are more easily controllable for highly soluble products (Mersmann and Kind, 1988). Precipitation is used not only for production but also for purification of a wide range of substances and treatment of various media and waste liquors.

Two terms are used quite frequently in this area viz., crystallization and precipitation. As far as supersaturation is concerned, crystallization usually represents low levels of supersaturation ($S < 2$) which leads to large crystals and secondary nucleation. Precipitation, however, is often initiated at high levels of supersaturation ($S > 10$). Therefore primary nucleation predominates giving a smaller mean product crystal size, Söhnel *et al.* (1991). In addition, precipitation can be considered as a fast crystallization, and implies an irreversible process. Although there are generally three

main steps in both processes, two subsequent secondary steps influence the final crystalline product, namely, agglomeration and ageing. The former occurs just after nucleation and the later represents all irreversible changes taking place in the formed precipitate, Mullin (1993).

Identification of the intermediate micromixing or partial segregation for a reactive precipitation system is important (Danckwerts, 1953; Becker and Larson, 1969; Garside and Tavare, 1984 and 1985 and Tavare 1986 and 1989). A model to characterise micromixing level has been the aim of many authors. Pohoreki and Baldyga (1983) proposed a single-parameter model based on mass transfer between a point and its environment to outline the molecular dissipation zone as originally suggested in Interaction by Exchange with the Mean (IEM) model by Costa and Trevissoi (1972). Tavare (1992) investigated the IEM micromixing model of a reactive precipitation system. It was found that the reaction and crystallization performance characteristics are affected significantly by two cases of the feed conditions; premixed and unpremixed feeds. The sensitivity of these two conditions was examined and found that premixed feeds case was better in presenting almost segregated configuration.

David and Marcant (1994) reported a quantitative prediction of micromixing effects on precipitation in single-jet batch and semibatch precipitators. The suggested model presented some general rules for calcium oxalate monohydrate:

- Avoiding the effects of micromixing and keeping the number of moles of reactants constant.
- Accentuation of mixing effects due to initial volume increase.

- The small volume available for micromixing counterbalances the high nucleation rates due to the high intermediate local supersaturation.
- Changing the location of the feed point has more influence on the crystal number and sizes than agitator speed modifications.

The mixing process has a great influence on the precipitation processes, (Garside, 1991 and Mersmann *et al.*, 1994). Precipitation kinetics are usually determined by a series of processes (Seckler, *et al.*, 1995) affecting the CSD, RTD, etc. When two reactants are mixed together supersaturation which represents the driving force for nucleation, results in crystal growth and agglomeration. Also, the precipitated crystals are affected by shear stresses and collisions with each other and crystallizer internals, consequently larger agglomerates or smaller crystals will be obtained.

A number of mass transfer models (at a phase boundary) is reported in literature (e.g. Sherwood *et al.*, 1975 and Bird *et al.*, 1960). These models have been adopted to explore the rule of the mixing on the precipitation process. In the following sections, a brief review of these models is introduced.

1.2.2. Mass Transfer with Chemical Reaction and Precipitation

When two phases are not at chemical equilibrium with one another, are brought into contact, a phenomenon arises called mass transfer with chemical reaction. Four main steps are involved in such phenomenon:

1. Diffusion of reactants from the bulk of phase 1 to the interface between the two phases. At the interface, physical equilibrium can be proposed, i.e. if the reactants concentrations in one phase are finite, then they are finite in the other.
2. Diffusion of the reactants from the interface towards the bulk of phase 2.
3. Chemical reaction within phase 2 and possibly subsequent precipitation.
4. Diffusion of products away from the reaction zone.

Steps (2, 3 and 4) take place simultaneously and mutually interfere. The process is said to be not affected by the chemical reaction and considered as simple mass transfer process, if step (1) is controlling (Levenspiel, 1972).

1.2.2a. Film Theory

The film theory model was proposed (by Nernst, 1904) for the investigation of the transport processes and shaped the principles of "two-film theory of gas absorption" of Whitman in 1923 (Whitman, 1923; Lewis and Whitman, 1924). This hydrodynamic model suggests that all resistance to mass transfer is accumulated in a film of thickness δ and considers this film to be stagnant where mass transfer can only take place by simple molecular diffusion. Also, the conditions in the bulk of the considered phase are assumed constant.

The absorption rate per unit surface, N_A, can be evaluated for a process of liquid-side controlled absorption, by the film-theory model as:

$$N_A = -D_A\left(\frac{\partial c}{\partial x}\right)_{x=0} + (u_x c_x)_{x=0} \qquad (1.91)$$

where D_A is the molecular diffusivity of the absorbing component in the liquid, c is the concentration of the absorbing component in the liquid phase, x is the distance from the interface and u_x is the velocity of the component normal to the gas-liquid interface. Assuming:

$$u_x = 0 \qquad (1.92)$$

and the concentration gradient being constant within the stagnant film, if no reaction is occurring:

$$-\left(\frac{\partial c}{\partial x}\right)_{x=0} = \frac{c_{Ai} - c_{Ao}}{\delta} \qquad (1.93)$$

where c_{Ai} and c_{Ao} are the concentrations at the interface and in the bulk of the liquid phase, respectively. The absorption coefficient for physical absorption, K_L^o, can be defined as:

$$K_L^o = \frac{N_A}{c_{Ai} - c_{Ao}} \qquad (1.94)$$

and is thus expressed by:

$$K_L^o = \frac{D_A}{\delta} \qquad (1.95)$$

Equation (1.95), however, does not provide any useful hydrodynamic meaning about the process under consideration. One suggestion is that the hydrodynamic conditions of the liquid phase only influence the value of δ. Therefore, under constant hydrodynamic conditions

$$K_L^o \propto D_A \tag{1.96}$$

One of the empirical correlations for the absorption coefficient in the liquid-side controlled absorption is, (Treybal., 1980):

$$\frac{K_L^o}{u_L} = a_1 \left(\frac{L u_L}{\nu_L} \right)^{a_2} \left(\frac{\nu_L}{D_A} \right)^{a_3} \tag{1.97}$$

where u_L is a characteristic velocity of the liquid, L is a characteristic linear dimension, ν_L is the liquid kinematic viscosity and a_1, a_2 and a_3 are numerical constants. The value of a_3 introduces some uncertainty, however, the best estimate is $a_3 = -0.5$, thus:

$$K_L^o \propto \sqrt{D_A} \tag{1.98}$$

If the liquid phase is in contact with either a solid or a more viscous liquid phase, then:

$$K_L^o \propto D_A^{2/3} \tag{1.99}$$

Equations (1.96) to (1.99) show that the film theory contradicts the experimental results. The film-theory, however, provides a reasonable first estimate for the difficult mathematical problems in the field of chemical absorption, Astarita (1967).

Wachi and Jones (1991 a) provided a numerical solution of the coupled equations of gas-liquid mass transfer with chemical reaction for the film theory and the mass and population balances of the precipitation process of calcium carbonate system. They predicted a smaller mean crystal size for a lower mass transfer coefficient because of the enhancement of the nucleation rate by the local accumulation of high supersaturation at the gas-liquid interface. Experimental observations (cloud starts near interface, Wachi and Jones, 1991a and b) and confrontation of model with data (Jones *et al.*, 1992) are reported as well.

1.2.2b. Surface Renewal Models

In the film theory, it is proposed that a steady-state film is developed at an interface, where diffusive mass transfer is taking place. On the other hand, surface renewal suggests that the fluid at the interface consists of elements which are replaced at intervals by fresh fluid arriving from the bulk and having the local mean bulk composition.

Thus, there are now two types of diffusive mass transfer, one is the capacity depth of the film which governs mass transfer (Film theory), and the other is taking place through each individual element (Surface renewal theories) (Secor and Beutler, 1967 and Glasscock and Rochelle, 1989). In the later, it is the exposure time of each element to the interface that is important. Thus, it can be concluded that surface renewal theories are unsteady-state in nature.

Surface Renewal Theories

- Higbie (1935): Proposed that the exposure time t_c, to the interface, is identical for each fluid element before replacing it by another element from the bulk.

$$t_c = \text{constant} \qquad (1.100a)$$

- Danckwerts (1951): Assumed an independent relationship between the exposure time of a fluid element and its probability to be replaced by a fresh fluid.

$$t_c = \text{random} \qquad (1.100b)$$

Danckwerts' model means that there is a fraction f(θ) of the surface which at any instant is exposed to the surface for a period between t and t+dt, and this is called the distribution of surface ages and given by:

$$f(\theta) = se^{-st}dt \tag{1.101}$$

where s is the fraction of surface renewed in unit time.

Unsteady-State Diffusion:

$$c = c(x,t) \tag{1.102}$$

By analogue of unsteady heat conduction

$$D_A \frac{\partial^2 c_A}{\partial x^2} = \frac{\partial c_A}{\partial t} \tag{1.103}$$

Surface Renewal Model:

First, initial and boundary conditions must be determined:

For the initial condition: $x \geq 0, \quad t \leq 0 \Rightarrow c_A = c_o$ (1.104)

For boundary conditions: 1. $x = 0, \quad t > 0 \Rightarrow c_A = c_{Ai}$ (1.105)

2. $x \to \infty \quad t > 0 \Rightarrow c_A = c_{Ao}$ (1.106)

Thus, concentration profile can be written as:

$$\frac{c_A - c_{Ao}}{c_{Ai} - c_{Ao}} = 1 - \text{erf}\left(\frac{x}{2\sqrt{D_A t}}\right) \tag{1.107}$$

or

$$\frac{c_A - c_{Ao}}{c_{Ai} - c_{Ao}} = \text{erf}_c\left(\frac{x}{2\sqrt{D_A t}}\right) \tag{1.108}$$

where

$$\text{erf}(y) = \frac{2}{\pi}\int_0^y e^{-z^2}dz \tag{1.109}$$

and $$erf_C = 1 - erf \qquad (1.110)$$

Error function values can be found from tables (e.g., U. S. National Bureau of Standards, 1954).

Penetration Distance x_p:

Penetration distance is the position at which:

$$erf\left(\frac{x_p}{2\sqrt{D_A t}}\right) = 0.99 \qquad (1.111)$$

i.e., $\frac{x_p}{2\sqrt{D_A t}} = 1.82$, from tables,

or simply $$x_p \approx 4\sqrt{D_A t} \qquad (1.112)$$

Mass Flux:

Instantaneous $$N_A = -D_A\left(\frac{\partial c_A}{\partial x}\right)_{x=0} \qquad (1.113)$$

From diffusion equation $$N_A = \sqrt{\frac{D_A}{\pi t}}(c_{Ai} - c_{Ao}) \qquad (1.114)$$

Time average rate absorption $$\overline{N}_A = \frac{1}{t}\int_0^t N_A dt \qquad (1.115)$$

Higbie Model:

$$t = t_c$$

$$\Rightarrow \qquad \overline{N}_A = 2\sqrt{\frac{D_A}{\pi t_c}}(c_{Ai} - c_{Ao}) \qquad (1.116)$$

i.e., $K_L \propto D_A^{1/2}$ (t_c is unknown)

Danckwerts Model:

Random surface age distribution:

$$\int_0^\infty se^{-st}dt = 1 \qquad (1.117)$$

where s is the surface renewal rate and its reciprocal (i.e., 1/s) is the average life of a surface element. Therefore, the average rate of absorption:

$$\overline{N}_A = \int_0^\infty (c_{Ai} - c_{Ao})\sqrt{\frac{D_A}{\pi t_c}} \cdot se^{-st}dt \qquad (1.118)$$

❶ ❷

❶ Instantaneous mass transfer rate.

❷ Fraction of surface of age t.

$$\Rightarrow \qquad \overline{N}_A = (c_{Ai} - c_{Ao})\sqrt{D_A s} \qquad (1.119)$$

i.e., $K_L \propto \sqrt{D_A s}$ (s is unknown)

Therefore, surface renewal theory implies that $K_L \propto D_A^{1/2}$, i.e. closer to the empirical observations than film theory.

Hostomský and Jones (1995) based their analysis of the gas-liquid reactive precipitation of calcium carbonate system on the coupled equations of the penetration model with those of precipitation. These coupled equations involve gas-liquid mass transfer, solution chemistry and the distributed dynamic mass and population balances applied to the crystallization step. They predicted the nucleation rate in a region close to the gas-liquid interface to increase with decreasing gas-liquid mass transfer rate. Nucleation rates at very low mass transfer, however, was impeded by the depletion of

calcium ions. It was found that, under low mass transfer rates conditions, nucleation proceeded predominantly in the interfacial region rather than the bulk solution. Nucleation rate, particle number density and mean particle size were predicted to have a maximum with position away from the gas-liquid interface.

1.2.2c. Empirical Models: -Frossling equation-

Generally:

$$Sh = A + BRe^{1/2}Sc^{1/3 \rightarrow 1/2} \tag{1.120}$$

i.e.,

$$\frac{K_L d}{D} \propto \left(\frac{\mu}{\rho D}\right)^{1/3 \rightarrow 1/2} \tag{1.121}$$

i.e.,

$$K_L \propto D^{1/2 \rightarrow 2/3} \tag{1.122}$$

Although this model supports surface-renewal theory, film theory is often used because of its simplicity and convenience. Both (film and penetration) theories have their limitations due to the underlying assumptions of mass transfer with fluid flow.

In the next section, the use of computational fluid dynamics (CFD) to model complex flows is reviewed.

1.3. Computational Fluid Dynamics

1.3.1. Introduction to Computational Fluid Dynamics

Computational Fluid Dynamics (CFD) technology is applied in industry to facilitate scale-up, commissioning, design of experiments, developments of new processes and plant upgrade. CFD is a computationally intensive modelling technique. It solves the basic equations that describe the motion of fluids by the use of computers, Sharratt (1990). CFD embraces a wide range of technologies such as: mathematics, computer science, engineering and physics, which are brought together to assist the process of modelling fluids flow, Shaw (1992).

The first consideration of CFD as an engineering tool was in the 1970s. The early applications of CFD were in the nuclear and aerospace industries. The main problem faced CFD was the high cost of the computing facilities. This cost declined in the early 1980s which made CFD become attractive to chemical and oil companies. CFD was still available, however, to a narrow range of process engineers.

Since then, CFD has been improved tremendously, technically and practically, where it becomes a handy tool for "ordinary" engineer, Sharratt (1990).

1.3.2. Fluids in Motion

It is essential that everyone dealing with CFD must have some understanding of the physical phenomena that CFD can predict and analyse for a particular fluid flow. It must be realised, therefore, that the computer hardware and software are merely tools to simplify the understanding of the fluids flow and the interactions between this flow and the object (e.g., vessel, pipe, free surface, etc.) under consideration, Shaw (1992).

There are various ways of describing the motion of fluids. The problem, however, is that we need some way of completely describing the state of the fluid. One trivial way is to have a description of the velocity of the fluid at all points in space and time. This method, however, still does not adequately describe the state of fluid, as there is a need for other properties in addition to the velocity. The most important properties that can be employed are:

- normal shear stress or pressure (i.e., force per unit area normal to a surface).
- viscosity which leads to find the tangential shear stress (i.e., viscous shear stress).
- density.

Mathematical relationships must then be determined to govern the interactions between these properties.

1.3.3. Equations of Fluid Dynamics

As stated earlier, it is very important for the CFD analyst to have an understanding of the flow features together with the fluid governing equations. By employing this, numerical solutions can be obtained which enables the CFD software to predict the fluid flow in a given situation. Conservation laws, i.e., mass and momentum, are used to derive the equations that govern the fluid flow. It then becomes a straightforward process to calculate the numerical predictions of all flows. On the other hand, a lot of problems are usually associated with this process. One of the main concerns is the physics of the flow and the way of modelling the turbulence where almost all points in flow are affected randomly by this phenomenon.

1.3.3a. The Equation of Continuity

If we consider a stationary volume element $\Delta x\Delta y\Delta z$ through which the fluid is flowing, see Figure (1.4), and apply a mass balance over it:

Rate of Mass ACCUMULATION = Rate of Mass IN - Rate of Mass OUT (1.123)

Faces perpendicular to the x-axis:

The rate of mass in through the face at x is: $(\rho v_x)|_x \Delta y\Delta z$

The rate of mass out through the face at $x+\Delta x$ is: $(\rho v_x)|_{x+\Delta x} \Delta y\Delta z$

The other two pairs of faces have similar expressions. The LHS of equation (1.123) is given as $(\Delta x \Delta y \Delta z)(\partial \rho / \partial t)$, therefore the mass balance becomes:

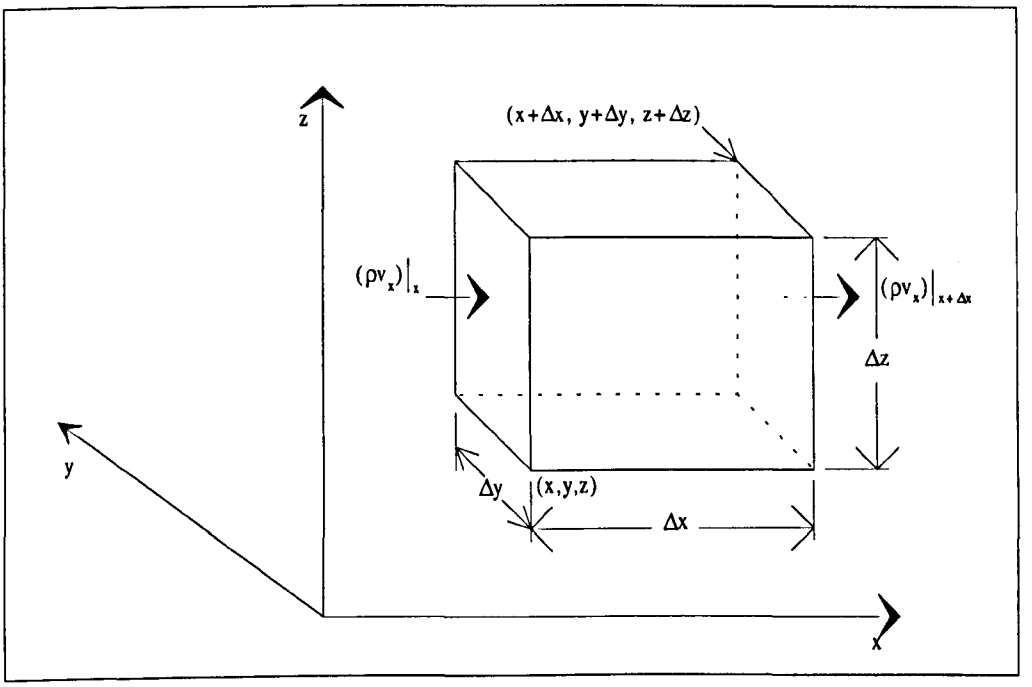

Figure (1.4): Region of volume $\Delta x \Delta y \Delta z$ fixed in space through which a fluid is flowing.

$$(\Delta x \Delta y \Delta z)(\frac{\partial \rho}{\partial t}) = \Delta y \Delta z\left[(\rho v_x)|_x - (\rho v_x)|_{x+\Delta x}\right]$$

$$+\Delta x \Delta z\left[(\rho v_y)|_y - (\rho v_y)|_{y+\Delta y}\right]$$

$$+\Delta x \Delta y\left[(\rho v_z)|_z - (\rho v_z)|_{z+\Delta z}\right] \qquad (1.124)$$

Dividing equation (1.124) by $(\Delta x \Delta y \Delta z)$ and taking the limit as these dimensions approaches zero, we obtain:

$$\frac{\partial \rho}{\partial t} = -\left(\frac{\partial}{\partial x}\rho v_x + \frac{\partial}{\partial y}\rho v_y + \frac{\partial}{\partial z}\rho v_z\right) \qquad (125)$$

This equation expresses the rate of change of density at a fixed point resulting from the changes in mass vector $\rho \mathbf{v}$, and it is called the **equation of continuity**.

The divergence operator (∇) of $\rho\mathbf{v}$ can be used in equation (1.125) to give:

$$\frac{\partial \rho}{\partial t} = -(\nabla . \rho \mathbf{v}) \qquad (1.126)$$

which implies that the rate of increase of the density within a small volume element fixed in space is equal to the net rate of mass influx to the element divided by its volume. Equation (1.125) can be modified and rearranged as:

$$\frac{\partial \rho}{\partial t} + v_x \frac{\partial \rho}{\partial x} + v_y \frac{\partial \rho}{\partial y} + v_z \frac{\partial \rho}{\partial z} = -\rho \left(\frac{\partial v_x}{\partial x} + \frac{\partial v_y}{\partial y} + \frac{\partial v_z}{\partial z} \right) \qquad (1.127)$$

where the LHS is the substantial derivative of density, i.e., the time derivative for a path following the fluid motion. An abbreviation may be used for equation (1.127) as:

$$\frac{D\rho}{Dt} = -\rho(\nabla . \mathbf{v}) \qquad (1.128)$$

This expression of the equation of continuity indicates the rate of change of density as seen by an observer "moving along" with the fluid. There is a special case for the equation of continuity and that is for incompressible (i.e. constant density) fluids:

$$(\nabla . \mathbf{v}) = 0 \qquad (1.129)$$

This assumption is often employed in engineering practice for liquids.

1.3.3b. The Equations of Motion

A momentum balance can be made for a volume element $\Delta x \Delta y \Delta z$, Figure (1.4) as:

Rate of Momentum ACCUMULATION = Rate of Momentum IN
- Rate of Momentum OUT
+ Sum of forces Acting on System (1.130)

Two important considerations are involved in the solution procedure:

- unsteady-state behaviour
- the fluid moves through all six faces of the volume element in an arbitrary direction.

Also, for simplicity, x-component of each term in equation (1.130) will be given as a first attempt and then by analogue the other two components may be handled.

From Figure (1.5), momentum flows into and out of the volume element by two different mechanisms:

I. Convection - as a result of the bulk fluid flow -

II. Molecular transfer - as a result of the velocity gradients -

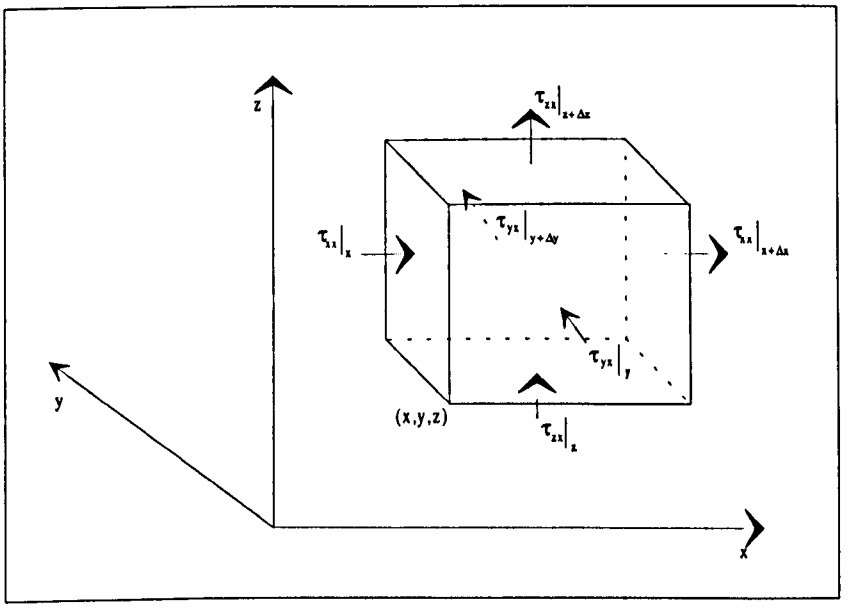

Figure (1.5): Volume element $\Delta x \Delta y \Delta z$ with arrows indicating the direction in which the x-component of momentum is transported through the surfaces.

Convective x-momentum flow:

The rate at which it enters the face at x is: $\rho v_x v_x|_x \, \Delta y \Delta z$

The rate at which it leaves at x+Δx is: $\rho v_x v_x|_{x+\Delta x} \, \Delta y \Delta z$

The rate at which it enters at y is: $\rho v_y v_x|_y \, \Delta x \Delta z$

The rate at which it leaves at y+Δy is: $\rho v_y v_x|_{y+\Delta y} \, \Delta x \Delta z$

The rate at which it enters at z is: $\rho v_z v_x|_z \, \Delta x \Delta y$

The rate at which it leaves at z+Δz is: $\rho v_z v_x|_{z+\Delta z} \, \Delta x \Delta y$

Hence, the net convective x-momentum flow into the volume element is:

$$\Delta y \Delta z\left(\rho v_x v_x|_x - \rho v_x v_x|_{x+\Delta x}\right) + \Delta x \Delta z\left(\rho v_y v_x|_y - \rho v_y v_x|_{y+\Delta y}\right) + \Delta x \Delta y\left(\rho v_z v_x|_z - \rho v_z v_x|_{z+\Delta z}\right) \qquad (1.131)$$

The molecular transfer of x-momentum can be constructed in the same manner to give the following expression:

$$\Delta y \Delta z\left(\tau_{xx}|_x - \tau_{xx}|_{x+\Delta x}\right) + \Delta x \Delta z\left(\tau_{yx}|_y - \tau_{yx}|_{y+\Delta y}\right) + \Delta x \Delta y\left(\tau_{zx}|_z - \tau_{zx}|_{z+\Delta z}\right) \qquad (1.132)$$

where τ_{yx} and τ_{zx} are the fluxes of x-momentum through a face perpendicular to the y- and z-axis, respectively. They are also the x-directed tangential (or shear) stresses on the y- and z-face, respectively, resulting from viscous forces. Whereas τ_{xx} is the normal stress on the x-face. Fluid pressure and gravitational force per unit mass are the important forces that have to be included in the overall equation of motion. The resultant of these two forces in the x-direction may be written as:

$$\Delta y \Delta z\left(p|_x - p|_{x+\Delta x}\right) + \rho g_x \Delta x \Delta y \Delta z \qquad (1.133)$$

Keeping in mind that the pressure (in a moving fluid) is a scalar quantity as it is defined by the equation of state p = p(ρ,T)

Finally, the LHS of equation (1.130) is given as: $\Delta x \Delta y \Delta z \left(\frac{\partial (\rho v_x)}{\partial t} \right)$

Then, substituting all the expressions in equation (1.130) and:

- Dividing both sides by ΔxΔyΔz.
- Taking limits as Δx, Δy and Δz approach zero.

This yields the x-component of the equation of motion:

$$\frac{\partial}{\partial t}\rho v_x = -\left(\frac{\partial}{\partial x}\rho v_x v_x + \frac{\partial}{\partial y}\rho v_y v_x + \frac{\partial}{\partial z}\rho v_z v_x\right)$$

$$-\left(\frac{\partial}{\partial x}\tau_{xx} + \frac{\partial}{\partial y}\tau_{yx} + \frac{\partial}{\partial z}\tau_{zx}\right) - \frac{\partial p}{\partial x} + \rho g_x \qquad (1.134)$$

Similarly, y- and z-components may be given as:

$$\frac{\partial}{\partial t}\rho v_y = -\left(\frac{\partial}{\partial x}\rho v_x v_y + \frac{\partial}{\partial y}\rho v_y v_y + \frac{\partial}{\partial z}\rho v_z v_y\right)$$

$$-\left(\frac{\partial}{\partial x}\tau_{xy} + \frac{\partial}{\partial y}\tau_{yy} + \frac{\partial}{\partial z}\tau_{zy}\right) - \frac{\partial p}{\partial y} + \rho g_y \qquad (1.135)$$

$$\frac{\partial}{\partial t}\rho v_z = -\left(\frac{\partial}{\partial x}\rho v_x v_z + \frac{\partial}{\partial y}\rho v_y v_z + \frac{\partial}{\partial z}\rho v_z v_z\right)$$

$$-\left(\frac{\partial}{\partial x}\tau_{xz} + \frac{\partial}{\partial y}\tau_{yz} + \frac{\partial}{\partial z}\tau_{zz}\right) - \frac{\partial p}{\partial z} + \rho g_z \qquad (1.136)$$

A more convenient form of the equation of motion can be written as a single vector equation:

$$\frac{\partial}{\partial t}(\rho \mathbf{v}) = -[\nabla . \rho \mathbf{v}\mathbf{v}] - \nabla p - [\nabla \tau] + \rho \mathbf{g} \qquad (1.137)$$

It must be noticed that ρvv and τ have a tensorial nature, i.e., each has nine components. Therefore, [∇.ρvv] and [∇τ] are not simple divergences. The physical meaning of the terms (∇.ρv) and (∇.ρvv) is that they represent the rate of loss of mass (a scalar) and momentum (a vector) per unit volume by fluid, respectively. Equation (1.134) may be rearranged to give:

$$\rho \frac{Dv_x}{Dt} = \frac{\partial p}{\partial x} - \left(\frac{\partial \tau_{xx}}{\partial x} + \frac{\partial \tau_{yx}}{\partial y} + \frac{\partial \tau_{zx}}{\partial z} \right) + \rho g_x \qquad (138)$$

Similarly, equation (1.137) can be written as:

$$\rho \frac{D\mathbf{v}}{Dt} = -\nabla p - [\nabla \tau] + \rho \mathbf{g} \qquad (139)$$

This momentum balance completely satisfies Newtonian's second law of motion, i.e., (mass) * (acceleration) = (sum of forces). The same interpretation given earlier for the equation of continuity, may be applied on the equation of motion and that is:

- Equation (1.137) describes a balance over a volume element fixed in space.
- Equation (1.139) predicts the changes that are taking place in a volume element following the fluid motion.

Stress terms need to be calculated as a function of velocity gradients and fluid properties, and this enables us to solve equations (1.134) to (1.139). For Newtonian fluids, these terms can be given as:

$$\tau_{xx} = -2\mu \frac{\partial v_x}{\partial x} + \frac{2}{3}\mu(\nabla . \mathbf{v}) \qquad (1.140)$$

$$\tau_{yy} = -2\mu \frac{\partial v_y}{\partial y} + \frac{2}{3}\mu(\nabla . \mathbf{v}) \qquad (1.141)$$

$$\tau_{zz} = -2\mu\frac{\partial v_z}{\partial z} + \frac{2}{3}\mu(\nabla.\mathbf{v}) \tag{1.142}$$

$$\tau_{xy} = \tau_{yx} = -\mu\left(\frac{\partial v_x}{\partial y} + \frac{\partial v_y}{\partial x}\right) \tag{1.143}$$

$$\tau_{yz} = \tau_{zy} = -\mu\left(\frac{\partial v_y}{\partial z} + \frac{\partial v_z}{\partial y}\right) \tag{1.144}$$

$$\tau_{zx} = \tau_{xz} = -\mu\left(\frac{\partial v_z}{\partial x} + \frac{\partial v_x}{\partial z}\right) \tag{1.145}$$

If we have a fluid flowing in the x-direction between two plates perpendicular to the y-direction, then:

- $v_x = f(y)$, i.e., v_x is a function of y alone.
- $\tau_{xx} = \tau_{yy} = \tau_{zz} = \tau_{yz} = \tau_{xz} = 0$.
- $\tau_{yx} = -\mu(dv_x/dy)$.

Substituting equations (1.140) to (1.145) into equation (1.138), and similarly for y- and z-equations, produces the general equations for a Newtonian fluid with varying density and viscosity:

$$\rho\frac{Dv_x}{Dt} = -\frac{\partial p}{\partial x} + \frac{\partial}{\partial x}\left[2\mu\frac{\partial v_x}{\partial x} - \frac{2}{3}\mu(\nabla.\mathbf{v})\right]$$

$$+\frac{\partial}{\partial y}\left[\mu\left(\frac{\partial v_x}{\partial y} + \frac{\partial v_y}{\partial x}\right)\right] + \frac{\partial}{\partial z}\left[\mu\left(\frac{\partial v_z}{\partial x} + \frac{\partial v_x}{\partial z}\right)\right] + \rho g_x \tag{1.146}$$

$$\rho\frac{Dv_y}{Dt} = -\frac{\partial p}{\partial y} + \frac{\partial}{\partial x}\left[\mu\left(\frac{\partial v_y}{\partial x} + \frac{\partial v_x}{\partial y}\right)\right]$$

$$+\frac{\partial}{\partial y}\left[2\mu\frac{\partial v_y}{\partial y} - \frac{2}{3}\mu(\nabla.\mathbf{v})\right] + \frac{\partial}{\partial z}\left[\mu\left(\frac{\partial v_z}{\partial y} + \frac{\partial v_y}{\partial z}\right)\right] + \rho g_y \tag{1.147}$$

$$\rho\frac{Dv_z}{Dt}=-\frac{\partial p}{\partial z}+\frac{\partial}{\partial x}\left[\mu\left(\frac{\partial v_z}{\partial x}+\frac{\partial v_x}{\partial z}\right)\right]$$

$$+\frac{\partial}{\partial y}\left[\mu\left(\frac{\partial v_x}{\partial y}+\frac{\partial v_y}{\partial z}\right)\right]+\frac{\partial}{\partial z}\left[2\mu\frac{\partial v_z}{\partial z}-\frac{2}{3}\mu(\nabla.\mathbf{v})\right]+\rho g_z \qquad (1.148)$$

Pressure, density and velocity components, in a flowing isothermal fluid, therefore can be totally described by:

A. equation of continuity.

B. equation of motion.

C. equation of state p = p(ρ).

D. dependence of density on viscosity μ = μ(ρ).

E. boundary conditions.

These general forms are usually simplified such as:

1. for constant ρ and constant μ, equations (1.146) to (1.148) can be written as:

$$\rho\frac{D\mathbf{v}}{Dt}=-\nabla p+\mu\nabla^2\mathbf{v}+\rho\mathbf{g} \qquad (1.149)$$

where the special case of the equation of continuity [(∇.**v**)=0] is used. This equation is called *Navier-Stokes* equation.

2. For [∇.τ] = 0, equation (1.139) may be simplified as:

$$\rho\frac{D\mathbf{v}}{Dt}=-\nabla p+\rho\mathbf{g} \qquad (1.150)$$

This equation is called *Euler equation* in which the viscous effects are relatively insignificant, Bird *et al.* (1960).

1.3.4. Turbulence Modelling

Viscosity has a stabilising effect on all fluids giving rise, at small velocities, to disorderly randomly phenomenon called *turbulence* (White, 1994 and Werner and Mersmann, 1994). In stirred tanks, the turbulence of the flow can be estimated by calculating the impeller Reynolds number as follows:

$$\mathrm{Re} = \frac{D^2 N \rho}{\mu} \qquad (1.151)$$

When the impeller Reynolds number in a stirred tank $\leq$ 10,000, the flow is said to be fully developed laminar. In the laminar region, the flow resistance to impeller rotation is mainly viscous resistance. When Reynolds number $\geq$ 10,000, the flow is considered to be fully developed turbulent. The region between the fully developed laminar and fully developed turbulent is called the transition region where laminar and turbulent flow coexist. This region is not well defined in the present CFD codes because of the complexities involved in the mathematical derivations.

Due to the swirling flows in the stirred tanks, the turbulence is anisotropic to a large extent. The standard k-ε model assumes turbulence isotropy, therefore it is less favoured compared with the Differential Reynolds-stress model. The later model is employed here for modelling the turbulent transport of momentum.

1.3.4a. k-ε model

For the turbulence, an eddy-viscosity hypothesis is employed in the k-ε model. The continuity and momentum equations are:

$$\frac{\partial \rho}{\partial t} + \nabla \cdot (\rho \mathbf{U}) = 0 \tag{1.152}$$

and

$$\frac{\partial \rho \mathbf{U}}{\partial t} + \nabla \cdot (\rho \mathbf{U} \otimes \mathbf{U}) - \nabla \cdot (\mu_{eff} \nabla \mathbf{U}) = -p' + \nabla \cdot (\mu_{eff} (\nabla \mathbf{U})^T + \mathbf{B} \tag{1.153}$$

ρ and **U** are presented here as mean fluid density and velocity, respectively, μ_{eff} is the effective viscosity which can be given as:

$$\mu_{eff} = \mu + \mu_T \tag{1.154}$$

where μ_T is the turbulent viscosity, and **B** is the body force.

In k-ε model, the μ_T value is estimated from the following expression:

$$\mu_T = C_\mu \rho \frac{k^2}{\varepsilon} \tag{1.155}$$

The turbulent kinetic energy (k) and turbulence dissipation rate (ε) are given by:

$$\frac{\partial \rho k}{\partial t} + \nabla \cdot (\rho \mathbf{U} k) - \nabla \cdot ((\mu + \frac{\mu_T}{\sigma_k}) \nabla k) = \mathbf{P} + \mathbf{G} - \rho \varepsilon \tag{1.156}$$

and

$$\frac{\partial \rho \varepsilon}{\partial t} + \nabla \cdot (\rho \mathbf{U} \varepsilon) - \nabla \cdot ((\mu + \frac{\mu_T}{\sigma_\varepsilon}) \nabla \varepsilon) = C_1 \frac{\varepsilon}{k} (\mathbf{P} + C_3 max(\mathbf{G}, 0)) - C_2 \rho \frac{\varepsilon^2}{k} \tag{1.157}$$

respectively, where **P** is the shear production defined by:

$$\mathbf{P} = \mu_{eff}\nabla\mathbf{U}\cdot(\nabla\mathbf{U}+(\nabla\mathbf{U})^T)-\frac{2}{3}\nabla\cdot\mathbf{U}(\mu_{eff}\nabla\cdot\mathbf{U}+\rho k) \quad (1.158)$$

The second term is only non-zero for compressible flows. **G** is production due to the body force is given by:

$$\mathbf{G} = \mathbf{G}_{buoy} + \mathbf{G}_{rot} + \mathbf{G}_{res} \quad (1.159)$$

where the $\mathbf{G}_{buoy}$, $\mathbf{G}_{rot}$ and $\mathbf{G}_{res}$ are production due to buoyancy, rotation and resistance, respectively. However, $\mathbf{G}_{rot} = 0$ and $\mathbf{G}_{res}$ is included in the code. Thus, $\mathbf{G} = \mathbf{G}_{buoy}$ which is defined by:

$$\mathbf{G} = -\frac{\mu_{eff}}{\rho\sigma_\rho}\mathbf{g}\cdot\nabla\rho \quad (1.160)$$

which, with the Boussinesq buoyancy approximation, can be written as:

$$\mathbf{G} = \frac{\mu_{eff}}{\sigma_T}\beta\mathbf{g}\cdot\nabla T - \frac{\mu_{eff}}{\sigma_Y}\alpha\mathbf{g}\cdot\nabla Y \quad (1.161)$$

where α and β are coefficients of expansion.

1.3.4b. Reynolds Stress Model

In the differential Reynolds stress model, the eddy-viscosity hypothesis is not invoked. The model does not propose that the turbulent viscosity is isotropic. However, equations are solved for the individual Reynolds stress components. The differential equations for the transport of $\overline{\mathbf{u}\otimes\mathbf{u}}$ are solved by the model by solving:

- Four equations in a 2-D flow (without swirl) for $\overline{u_1u_1}, \overline{u_2u_2}, \overline{u_3u_3}, \overline{u_1u_2}$, or
- Six equations in a 3-D flow for $\overline{u_1u_1}, \overline{u_2u_2}, \overline{u_3u_3}, \overline{u_1u_2}, \overline{u_2u_3}, \overline{u_1u_3}$.

The equation $\overline{\mathbf{u}\otimes\mathbf{u}}$ satisfies the following equation:

$$\underset{\text{❶}}{\frac{\partial \rho \overline{\mathbf{u} \otimes \mathbf{u}}}{\partial t}} + \underset{\text{❷}}{\nabla \cdot (\rho \overline{\mathbf{u} \otimes \mathbf{u}} \otimes U)} - \underset{\text{❸}}{\nabla \cdot (\rho \frac{C_s}{\sigma_{DS}} \frac{k}{\varepsilon} \overline{\mathbf{u} \otimes \mathbf{u}} (\nabla \overline{u \otimes u})^T} = \mathbf{P} + \mathbf{G} + \phi - \underset{\text{❹}}{\frac{2}{3} \rho \varepsilon \mathbf{I}} \qquad (1.162)$$

❶transient **❷advection** **❸diffusion** **❹dissipation**

P is the shear stress production term

G is the buoyancy stress production term

ϕ is the pressure-strain correlation term

Three terms, namely ❸, ❹ and ϕ, are modelled. For the dissipation term (❹), local isotropic turbulence is assumed.

Shear stress production term (**P**) is presented by:

$$\mathbf{P} = -\rho(\overline{\mathbf{u} \otimes \mathbf{u}}(\nabla \mathbf{U})^T + (\nabla \mathbf{U})\overline{\mathbf{u} \otimes \mathbf{u}}) \qquad (1.163)$$

If a rotating system is employed, an additional dissipation term ($\mathbf{P}_{rot}$) arises which is defined by:

$$\mathbf{P}_{rot} = -2\rho\omega \otimes \overline{\mathbf{u} \otimes \mathbf{u}} \qquad (1.164)$$

where ω is the constant angular velocity of the reference frame of the rotating body about a fixed axis. $\mathbf{P}_{rot}$ is split into two halves, one is added to the shear production (**P**), therefore:

$$\mathbf{P} = -\rho(\overline{\mathbf{u} \otimes \mathbf{u}}(\nabla \mathbf{U})^T + (\nabla \mathbf{U})\overline{\mathbf{u} \otimes \mathbf{u}}) - \rho\omega \otimes \overline{\mathbf{u} \otimes \mathbf{u}} \qquad (1.165)$$

and the other is effectively added to LHS of the transport equation for $\overline{\mathbf{u} \otimes \mathbf{u}}$.

Variations in the density of a buoyant flow are presented in terms of temperature or scalar concentrations variations. If Boussinesq approximation (Clarke and Wilkes, 1989) is used for incompressible flows, the buoyancy stress production term is given as:

$$\mathbf{G} = -\rho\beta(\mathbf{g} \otimes \overline{\mathbf{u}h} + (\mathbf{g} \otimes \overline{\mathbf{u}h})^T) + \rho\alpha(\mathbf{g} \otimes \overline{\mathbf{u}s} + (\mathbf{g} \otimes \overline{\mathbf{u}s})^T) \qquad (1.166)$$

Whereas the density for compressible flow is calculated using the equation-of-state such as:

$$\frac{1}{\rho} = a_h H_s + a_s S + b \qquad (1.167)$$

therefore, **G** can be written as:

$$\mathbf{G} = -a_h(\rho\overline{\mathbf{u}h}(\nabla p)^T + \rho\overline{\mathbf{u}h}^T\nabla p) - a_s(\rho\overline{\mathbf{u}s}(\nabla p)^T + \rho\overline{\mathbf{u}s}^T\nabla p) \qquad (1.168)$$

The pressure-strain (ϕ) correlation is given by:

$$\phi = \phi_1 + \phi_2 + \phi_3 \qquad (1.169)$$

where:

$$\phi_1 = -\rho C_{1s}\frac{\varepsilon}{k}(\overline{\mathbf{u} \otimes \mathbf{u}} - \frac{2}{3}k\mathbf{I}) \qquad (1.170)$$

$$\phi_2 = -C_{2s}(\mathbf{P} - \frac{2}{3}P\mathbf{I}) \qquad (1.171)$$

$$\phi_3 = -C_{3s}(\mathbf{G} - \frac{2}{3}G\mathbf{I}) \qquad (1.172)$$

P and G are the shear and buoyancy production of turbulence kinetic energy, respectively, they are defined as follows:

$$P = \frac{1}{2} trace(\mathbf{P}) = -\rho \overline{\mathbf{u} \otimes \mathbf{u}} \cdot \nabla \mathbf{U} \tag{1.173}$$

and

$$\mathrm{G} = \frac{1}{2} \mathrm{trace}(\mathbf{G})$$

$$= \begin{cases} (1) - \rho\beta \mathbf{g} \cdot \overline{\mathbf{uh}} + \rho\alpha \mathbf{g} \cdot \overline{\mathbf{us}} \\ (2) - \mathrm{a_h} \rho \overline{\mathbf{u}h} \cdot \nabla p - a_s \rho \overline{\mathbf{u}s} \cdot \nabla p \end{cases} \tag{1.174}$$

where (1) and (2) are for incompressible and compressible flows, respectively.

Approximations are applied for the unknown Reynolds fluxes $\overline{\mathbf{u}h}$ and $\overline{\mathbf{u}s}$ in equations (1.166), (1.168) and (1.174):

$$\overline{\mathbf{u}h} = C_S \frac{k}{\varepsilon} \overline{\mathbf{u} \otimes \mathbf{u}} (\nabla H)^T \tag{1.175}$$

and

$$\overline{\mathbf{u}s} = C_S \frac{k}{\varepsilon} \overline{\mathbf{u} \otimes \mathbf{u}} (\nabla S)^T \tag{1.176}$$

An equation for ε is needed because the dissipation appears in the individual stress equations, this can be given as:

$$\frac{\partial \rho \varepsilon}{\partial t} + \nabla \cdot (\rho \mathbf{U} \varepsilon) + \nabla \cdot (\rho \frac{C_S}{\sigma_\varepsilon} \frac{k}{\varepsilon} \overline{\mathbf{u} \otimes \mathbf{u}} \nabla \varepsilon) = C_1 \frac{\varepsilon}{k} (P + C_3 \max(G,0)) - C_2 \rho \frac{\varepsilon^2}{k} \tag{1.177}$$

(a) (b) (c) (d)

where: the terms (a), (b), (c) and (d) are advection, diffusion, production and dissipation, respectively.

No transport equation is needed for k in the differential stress model. k is calculated as half the trace of the normal Reynolds stresses.

1.3.5. Numerical Solutions to Partial Differential Equations

The equations that we obtained for the fluids in motion, are made up of combinations of the flow variables, e.g., velocity components and fluid pressure, and their derivatives. In order to use digital computers to solve these partial differential equations, numerical transformation for these equations are needed, since the computer is only able to predict and process binary data, i.e., zeros and ones. The transformation of partial differential equation to a numerical analogue is called *numerical discretisation.* There are many techniques may be used to perform such a numerical discretisation. Although, the underlying principles of these techniques are different, there are several conjoint features among them.

Three main numerical discretisation techniques, viz., the finite difference method, the finite element method and the finite volume method, will be discussed.

1.3.6. Numerical Discretisation Techniques

1.3.6a. Finite Difference Method

This technique uses Taylor series as an essential tool to construct a library of equations. These equations describe the derivatives of a variable in terms of the differences between values of the variable at some points which are functions of time and position. The partial differential equations of the flow problems as discussed earlier, give two types of variables, namely, dependent variables such as the velocity components or the fluid pressure, and independent variables which are represented by the time and the spatial coordinates, Shaw (1992).

Suppose that a reference value is given as a known dependent variable where all of it's derivatives are defined with respect to one independent variable. Next, Taylor series expansions are employed to obtain the value of the dependent variable at a value of the independent variable a small distance from the reference value. Figure (1.6) demonstrates this assumption where U, the dependent variable, varies with x the independent variable. A small distance h can be taken at both sides of the central point, i.e., at (x + h) and (x - h) along the x-axis. Therefore, Taylor series expansions for the variable U at the two points are:

$$U(x+h) = U(x) + h\frac{dU}{dx} + \frac{1}{2}h^2\frac{d^2U}{dx^2} + \frac{1}{6}h^3\frac{d^3U}{dx^3} + \cdots \qquad (1.178)$$

and

$$U(x-h) = U(x) - h\frac{dU}{dx} + \frac{1}{2}h^2\frac{d^2U}{dx^2} - \frac{1}{6}h^3\frac{d^3U}{dx^3} + \cdots \qquad (1.179)$$

where h is the small displacement in the x-direction, and the derivatives of the function U are taken at x.

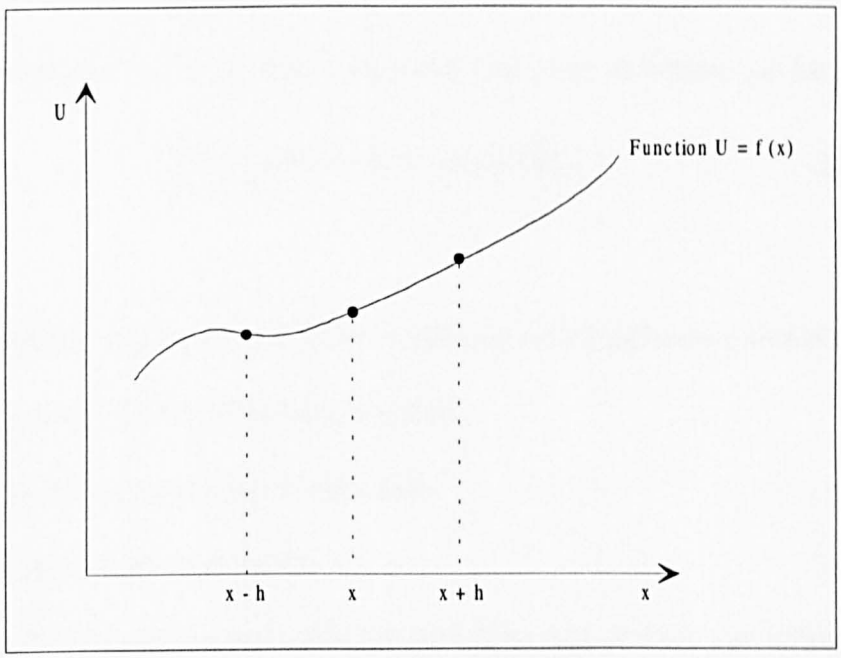

Figure (1.6): Location of points for Taylor series.

If these two equations are solved (by addition or subtraction), the resultant equations will be functions of the first and second derivatives at x, respectively. These derivatives are:

$$\frac{d^2U}{dx^2} = \frac{1}{h^2}(U(x+h) - 2U(x) + U(x-h)) + O(h^2) \qquad (1.180)$$

and

$$\frac{dU}{dx} = \frac{1}{2h}(U(x+h) + U(x-h)) + O(h^2) \qquad (1.181)$$

where $O(h^n)$ refers to the existence of order n or higher-order terms. If h is very small, these terms can be neglected, however, this yields a source of error in the numerical calculations as equations (1.180) and (1.181) are truncated. Other forms of derivatives

may be obtained if each of equations (1.178) and (1.179) is considered in separate. The first order derivative from equation (1.178) can be written as:

$$\frac{dU}{dx} = \frac{1}{h}(U(x+h) - U(x)) + O(h) \qquad (1.182)$$

and from equation (1.179), another form of the first order derivative can be given as:

$$\frac{dU}{dx} = \frac{1}{h}(U(x) - U(x-h)) + O(h) \qquad (1.183)$$

These four equations (1.180) to (1.183) are called *difference formulae*. There are two classifications for the difference formulae:

1. The geometrical relationship of the points.
2. The accuracy of the expressions.

According to this classification, equations (1.180) and (1.181) are central difference formulae and are second order accurate. On the other hand, equations (1.182) and (1.183) are forward and backward difference formulae, respectively, and both are first order accurate.

These difference formulae are basic tools for the numerical analyst, where each term in the differential equation can have a numerical analogue. This may be demonstrated as follows:

I. Placing points within the domain of the problem.

II. Replacing the derivatives at each point by the appropriate difference formula.

III. An equation will be obtained, which consists solely of the values of variables at the given point and it's neighbours.

If this procedure is repeated for all other points and resultant equations are solved, then a numerical solution will be achieved. Two important remarks can be made:

1. The domain may include a time direction in addition to the spatial directions.
2. The partial differential equation that is valid for the entire domain, i.e., at an infinite number of points, can be translated into a finite number of equations and therefore, a finite set of points in the domain representing the relationship between the variables.

1.3.6b. Finite Element Method

This is the second technique in which the partial differential equations are applied over a finite number of sub-domains called "elements". It is proposed that the dependent variable varies in a simple manner over each element. Consequently, a general description of the variable behaviour can be obtained over the whole domain. On the other hand, the discretisation process is more complicated than the finite difference method (Reddy; 1984, Zienkiewicz and Taylor, 1989; Shaw, 1992).

The continuous development of this utility makes it a powerful technique to solve various physical problems, i.e. different groups of partial differential equations. To illustrate how the finite element method is employed to transform a partial differential equation into its numerical analogue, an element is considered as shown in Figure (1.7). The variable U is presumed to change in a simple manner. In this Figure, the change is linear, nevertheless it could be of any higher order, e.g., quadratic, cubic, etc. As shown in Figure (1.7), the variable, U, is a function of its values at the end-points of the

element and the length along the element x. The end-points of the element are needed as reference positions on the element and known as the nodes of the element. It must be noticed that the number of the required nodes depends on the order of the function (e.g., three nodes are needed for a quadratic variation).

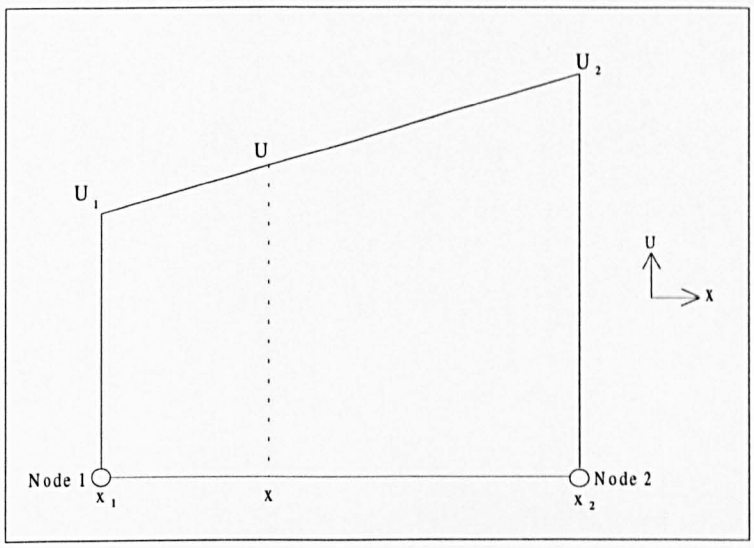

Figure (1.7): A two-noded linear element.

Figure (1.7) shows a linear variation, therefore the first derivative of U with respect to x is constant. Hence, the second derivative is not defined. Since many partial differential equations include second derivative, then high order-derivatives, in general, must be transformed into low-order derivatives. This can be done as follows:

a) Multiplying the partial differential equation by an unknown function.

b) Integrating the new expression over the domain in which it applies.

c) Integrating by parts the terms which their derivatives need to reduced to lower orders.

1.3.6c. Finite Volume Method

The finite difference method was the basis of the finite volume method's primary development. The later method is being commercially widely used for various CFD codes, such as CFX™, PHOENICS™, FLUENT™ and STAR-CD™. The algorithm has three main numerical steps (Versteeg and Malalasekera, 1995). It starts with integration of fluid flow governing equations over the domain of all finite control volumes which is a characteristic of this method. Then, a discretisation is performed to obtain a system of algebraic equations. Finally, an iterative procedure is adopted to solve these equations.

The control volume integration concept distinguishes the finite volume method from the other techniques where the *exact* conservation of relevant properties can be determined for each finite size cell. This demonstrates the main attraction of the finite volume method because it shows a clear relationship between the numerical algorithm and the underlying physical conservation principle. Also, this relationship makes its concepts much more simple to understand by engineers than the other discretisation techniques.

The governing equations for the finite volume method from the general form of the transport equation:

Rate of Increase of ϕ of Fluid Element + **Net Rate of flow of ϕ out of Fluid Element**

$$= \textbf{Rate of Increase of } \phi \textbf{ due to Diffusion} + \textbf{Rate of Increase of } \phi \textbf{ due to Sources} \qquad (1.184)$$

$$\frac{\partial(\rho\phi)}{\partial t} + div(\rho\phi\mathbf{u}) = div(D_c grad\phi) + S_\phi \qquad (1.185)$$

can be derived using a simple transport process such as steady state pure diffusion problem and this takes the following form:

$$div(D_c grad\phi) + S_\phi \qquad (1.186)$$

The control volume integration which is the main characteristic of this discretisation method gives:

$$\int_{CV} div(D_c grad\phi)dV + \int_{CV} S_\phi dV = \int_A n\cdot(D_c grad\phi)dA + \int S_\phi dV = 0 \qquad (1.187)$$

One-Dimensional Steady State Diffusion

Figure (1.8) demonstrates a control volume of a defined boundary one-dimensional steady state diffusion problem for a property ϕ. The process can be described by the following expression:

$$\frac{d}{dx}(D_c\frac{d\phi}{dx}) + S = 0 \qquad (1.188)$$

where D_c and S are the diffusion coefficient and source term, respectively. A typical example of this problem is a one-dimensional heat conduction in a rod.

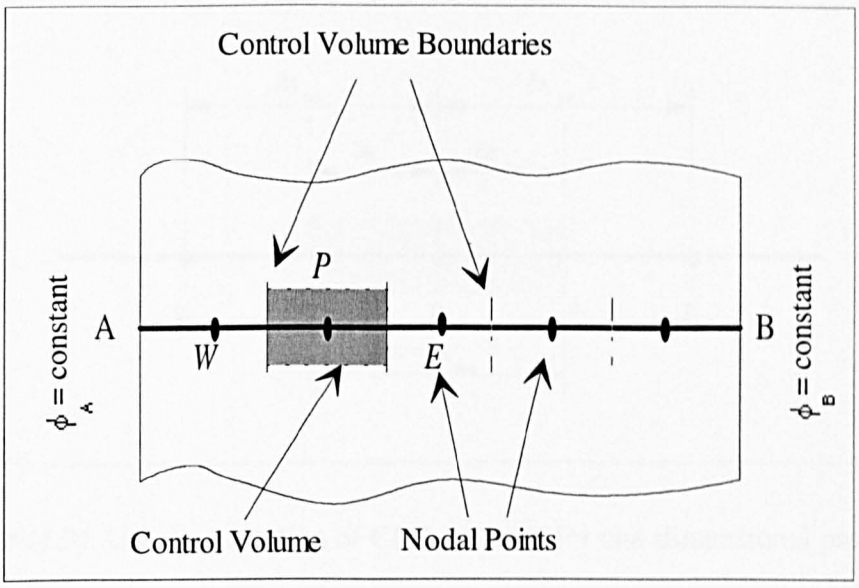

Figure (1.8): One-dimensional steady state diffusion problem.

Grid Generation: The domain should be divided first into discrete control volumes. For this problem, a number of nodal points is located between points A and B. Then, the boundaries of the control volume are placed mid-way between adjacent nodes. Therefore, there is a control volume surrounding every node in the domain under consideration. At the same time, control volumes can be set up close to the edge of the domain so that the physical boundaries coincide with the control volume boundaries.

Figure (1.9) shows a sample nodal point (P) and its neighbours (points E and W) and the related distance notations.

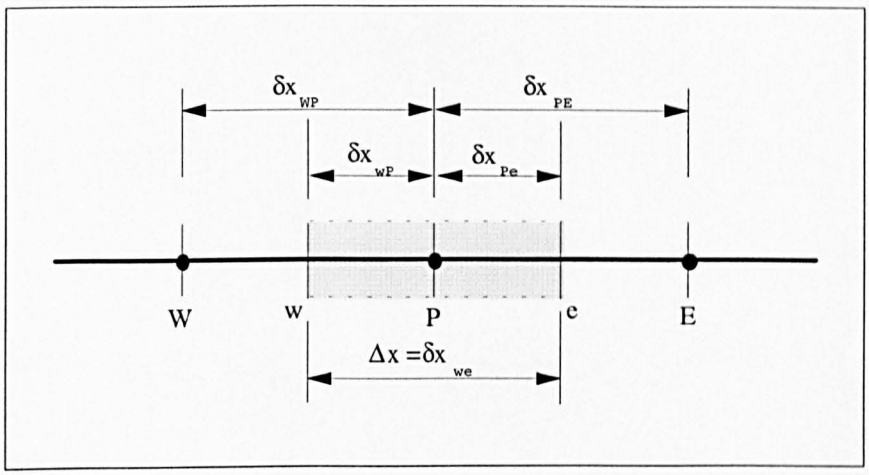

Figure (1.9): Usual convention of CFD methods for one-dimensional problem.

Discretisation: For the above control volume, Figure (1.9), the integration can take the following form:

$$\int_{\Delta V}\frac{d}{dx}\left(D_c\frac{d\phi}{dx}\right)dV+\int_{\Delta V}SdV=\left(D_cA\frac{d\phi}{dx}\right)_e-\left(D_cA\frac{d\phi}{dx}\right)_w+\overline{S}\Delta V=0 \quad (1.189)$$

where A is the cross-sectional area of the control volume face, ΔV is the volume and $\overline{S}$ is the average value of source S over the control volume. Equation (1.189) states clearly the ability of the finite volume method to observe the physical interpretation. The interface diffusion coefficient and the gradient $\frac{d\phi}{dx}$ at both ends (e and w) of the control volume are needed in order to obtain useful forms of the discretised equations. One possible option to calculate these terms is a linear approximation of properties between nodal points, and this is called central differencing. Therefore, the values of $D_{c\,e}$ and $D_{c\,w}$ can be written as:

$$D_{cw}=\frac{D_{cW}+D_{cP}}{2} \quad (1.190)$$

$$D_{ce} = \frac{D_{cP} + D_{cE}}{2} \tag{1.191}$$

and the diffusive terms as:

$$\left(D_c A \frac{d\phi}{dx}\right)_e = D_{ce} A_e \left(\frac{\phi_E - \phi_P}{\delta x_{PE}}\right) \tag{1.192}$$

$$\left(D_c A \frac{d\phi}{dx}\right)_w = D_{cw} A_w \left(\frac{\phi_P - \phi_W}{\delta x_{WP}}\right) \tag{1.193}$$

The source term S, which may be a function of the dependent variable, is approximated by means of a linear form as:

$$\overline{S}\Delta V = S_u + S_P \phi_P \tag{1.194}$$

Substituting equations (1.192-194) into equation (1.189):

$$D_{ce} A_e \left(\frac{\phi_E - \phi_P}{\delta x_{PE}}\right) - D_{cw} A_w \left(\frac{\phi_P - \phi_W}{\delta x_{WP}}\right) + \left(S_u + S_P \phi_P\right) = 0 \tag{1.195}$$

which can be re-arranges as:

$$\left(\frac{D_{ce}}{\delta x_{PE}} A_e + \frac{D_{cw}}{\delta x_{WP}} A_w - S_P\right)\phi_P = \left(\frac{D_{cw}}{\delta x_{WP}} A_w\right)\phi_W + \left(\frac{D_{ce}}{\delta x_{PE}} A_e\right)\phi_E + S_u \tag{1.196}$$

The latest equation can be written, for interior nodes, in another form as:

$$a_P \phi_P = a_W \phi_W + a_E \phi_E + S_u \tag{1.197}$$

where $a_W = \frac{D_{cw}}{\delta x_{WP}} A_w$, $a_E = \frac{D_{ce}}{\delta x_{PE}} A_w$ and $a_P = a_W + a_E - S_P$

The values of S_u and S_p can be calculated from equation (1.197). The discretised form of equation (1.184) thus is given by equations (1.194 and 1.197).

Solution of Equations: The solution of the discretised equations of the equation (1.197) form needs to be set at every nodal point in the domain. However, in order to

include the boundary conditions, a modified version of equation (1.197) is required. Finally, a set of linear algebraic equations is achieved and its solution will be given to the distribution of the property ϕ at nodal points.

Finite Volume Method for Two-Dimensional Diffusion Problems

The two-dimensional steady state diffusion equation is given by:

$$\frac{\partial}{\partial x}\left(D_c \frac{\partial \phi}{\partial x}\right)+\frac{\partial}{\partial y}\left(D_c \frac{\partial \phi}{\partial y}\right)+S=0 \qquad (1.198)$$

Following the same procedure of the one-dimensional problem, the integration of equation (1.198) yields, Figure (1.10):

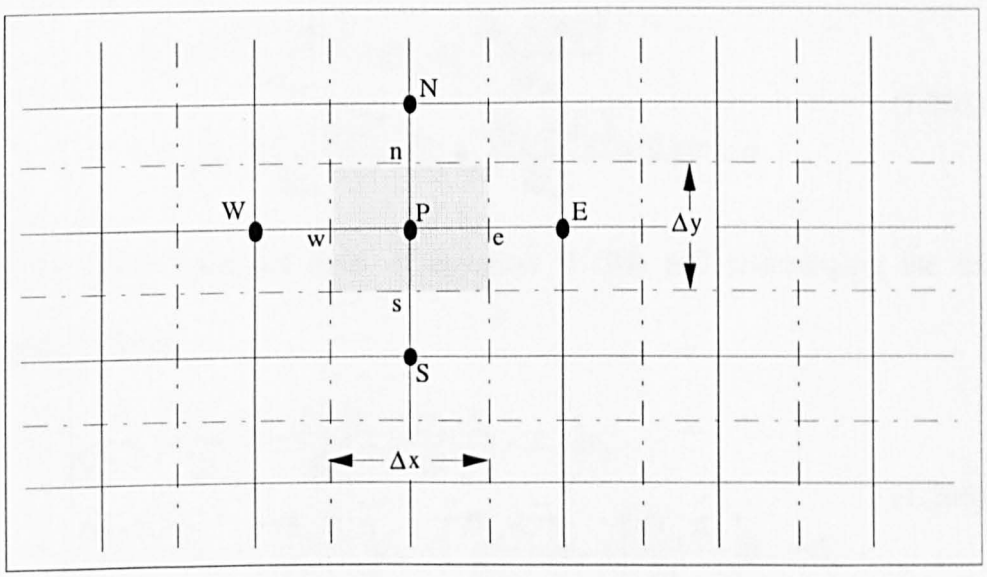

Figure (1.10): Two-dimensional grid convention.

$$\int_{\Delta V}\frac{\partial}{\partial x}\left(D_c \frac{\partial \phi}{\partial x}\right)dx\cdot dy+\int_{\Delta V}\frac{\partial}{\partial y}\left(D_c \frac{\partial \phi}{\partial x}\right)dx\cdot dy+\int S_\phi dV=0 \qquad (1.199)$$

since $A_e = A_w = \Delta y$ and $A_n = A_s = \Delta x$, Figure (1.10), then:

$$\left[D_{ce}A_e\left(\frac{\partial\phi}{\partial x}\right)_e - D_{cw}A_w\left(\frac{\partial\phi}{\partial x}\right)_w + D_{cn}A_n\left(\frac{\partial\phi}{\partial y}\right)_n - D_{cs}A_s\left(\frac{\partial\phi}{\partial y}\right)_s\right] + \bar{S}\Delta V = 0 \quad (1.200)$$

Employing the same linear central differencing approximation method from the one-dimensional example, the flux through control volume faces may be given as:

$$\text{Flux across W face} = D_{cw}A_w\left.\frac{\partial\phi}{\partial x}\right|_w = D_{cw}A_w\frac{(\phi_P - \phi_W)}{\delta x_{WP}} \quad (1.201)$$

$$\text{Flux across E face} = D_{ce}A_e\left.\frac{\partial\phi}{\partial x}\right|_e = D_{ce}A_e\frac{(\phi_E - \phi_P)}{\delta x_{PE}} \quad (1.202)$$

$$\text{Flux across S face} = D_{cs}A_s\left.\frac{\partial\phi}{\partial y}\right|_s = D_{cs}A_s\frac{(\phi_P - \phi_S)}{\delta y_{SP}} \quad (1.203)$$

$$\text{Flux across N face} = D_{cn}A_n\left.\frac{\partial\phi}{\partial x}\right|_n = D_{cn}A_n\frac{(\phi_N - \phi_P)}{\delta y_{PN}} \quad (1.204)$$

Substituting equations (1.201) to (1.204) and re-writing equation (1.200):

$$\begin{aligned} &D_{ce}A_e\frac{(\phi_E - \phi_P)}{\delta x_{PE}} - D_{cw}A_w\frac{(\phi_P - \phi_W)}{\delta x_{WP}} \\ &+D_{cn}A_n\frac{(\phi_N - \phi_P)}{\delta y_{PN}} - D_{cs}A_s\frac{(\phi_P - \phi_S)}{\delta y_{SP}} + \bar{S}\Delta V = 0 \end{aligned} \quad (1.205)$$

taking the same linearised form of equation (1.194) and re-arranging the resultant expression to give:

$$\begin{aligned} &\left(\frac{D_{cw}A_w}{\delta x_{WP}} + \frac{D_{ce}A_e}{\delta x_{PE}} + \frac{D_{cs}A_s}{\delta y_{SP}} + \frac{D_{cn}A_n}{\delta y_{PN}} - S_P\right)\phi_P \\ &= \left(\frac{D_{cw}A_w}{\delta x_{WP}}\right)\phi_w + \left(\frac{D_{ce}A_e}{\delta x_{PE}}\right)\phi_E + \left(\frac{D_{cs}A_s}{\delta y_{SP}}\right)\phi_S + \left(\frac{D_{cn}A_n}{\delta y_{PN}}\right)\phi_N + S_u \end{aligned} \quad (1.206)$$

which can be written, for interior nodes, as:

$$a_P\phi_P = a_W\phi_W + a_E\phi_E + a_S\phi_S + a_N\phi_N + S_u \quad (1.207)$$

where $a_W = \frac{D_{cw}A_w}{\delta x_{WP}}$, $a_E = \frac{D_{ce}A_e}{\delta x_{PE}}$, $a_S = \frac{D_{cs}A_s}{\delta y_{SP}}$, $a_N = \frac{D_{cn}A_n}{\delta y_{PN}}$ and $a_P = a_W + a_E + a_S + a_N - S_P$. This two-dimensional analysis has the following face areas: $A_w=A_e=\Delta y$ and $A_n=A_s=\Delta x$.

In order to get the two-dimensional distribution of the property ϕ, discretised equations of the form shown in equation (1.207) should be applied at each grid node in the subdivided domain. Also, the discretised equations at the boundaries are adjusted to account for the boundary conditions.

Finite Volume Method for Three-Dimensional Diffusion Problems

The governing equation for three-dimensional steady state diffusion is:

$$\frac{\partial}{\partial x}\left(D_c\frac{\partial\phi}{\partial x}\right)+\frac{\partial}{\partial y}\left(D_c\frac{\partial\phi}{\partial y}\right)+\frac{\partial}{\partial z}\left(D_c\frac{\partial\phi}{\partial z}\right)+S=0 \qquad (1.208)$$

The Integration of the above equation can be evaluated similar to the last two cases, one- and two-dimensional, as follows, see Figure (1.11):

$$\left[D_{ce}A_e\left(\frac{\partial\phi}{\partial x}\right)_e - D_{cw}A_w\left(\frac{\partial\phi}{\partial x}\right)_w\right]+\left[D_{cn}A_n\left(\frac{\partial\phi}{\partial y}\right)_n - D_{cs}A_s\left(\frac{\partial\phi}{\partial y}\right)_s\right] + \left[D_{ct}A_t\left(\frac{\partial\phi}{\partial z}\right)_t - D_{cb}A_b\left(\frac{\partial\phi}{\partial z}\right)_b\right]+\bar{S}\Delta V=0 \qquad (1.209)$$

which gives, after discretisation:

$$\left[D_{ce}\frac{(\phi_E-\phi_P)A_e}{\delta x_{PE}}-D_{cw}\frac{(\phi_P-\phi_W)A_w}{\delta x_{WP}}\right]$$
$$+\left[D_{cn}\frac{(\phi_N-\phi_P)A_n}{\delta y_{PN}}-D_{cs}\frac{(\phi_P-\phi_S)A_s}{\delta y_{SP}}\right] \qquad (1.210)$$
$$+\left[D_{ct}\frac{(\phi_T-\phi_P)A_t}{\delta z_{PT}}-D_{cb}\frac{(\phi_P-\phi_B)A_b}{\delta z_{BP}}\right]+(S_u+S_P\phi_P)=0$$

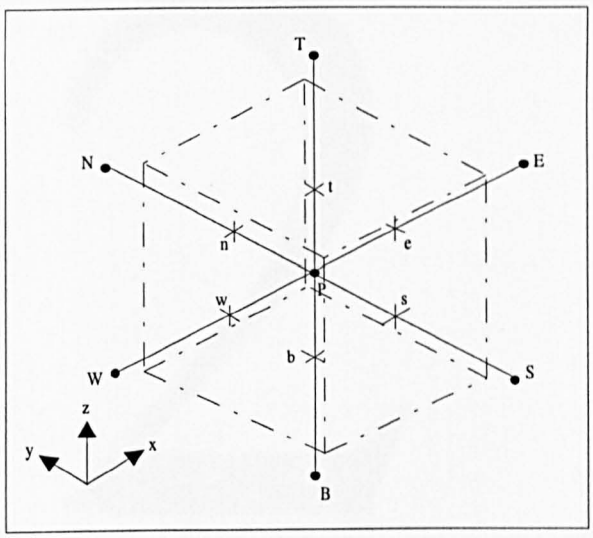

Figure (1.11): A cell in three-dimensions and its neighbouring nodes.

For interior nodes equation (1.210) can be rewritten as:

$$a_P\phi_P=a_W\phi_W+a_E\phi_E+a_S\phi_S+a_N\phi_N+a_B\phi_B+a_T\phi_T+S_u \qquad (1.211)$$

where $a_W=\frac{D_{cw}A_w}{\delta x_{WP}}$, $a_E=\frac{D_{ce}A_e}{\delta x_{PE}}$, $a_S=\frac{D_{cs}A_s}{\delta y_{SP}}$, $a_N=\frac{D_{cn}A_n}{\delta y_{PN}}$, $a_B=\frac{D_{cb}A_b}{\delta z_{BP}}$,

$a_T=\frac{D_{ct}A_t}{\delta z_{PT}}$ and $a_P=a_W+a_E+a_S+a_N+a_B+a_T-S_P$. To incorporate the boundary conditions, links with the suitable face(s), should be cut and the source term should be altered accordingly.

2

CFD, MIXING AND PRECIPITATION

2. CFD, MIXING AND PRECIPITATION

Multi-phase problems in CFD have attracted the attention of many industrial processes (Bode, 1994; Weetman, 1994 and Foumeny and Sandhu, 1995). The most difficult cases of such problems are the ones which involve the formation of new phase(s). It is always recommended in CFD problems to start with the simplest possible case by employing one parameter at a time and then examining the interactions between those parameters. This procedure is followed not only in complicated processes but also in simple cases. Precipitation processes, however, involve a large collection of parameters, i.e. supersaturation, nucleation (primary and secondary), crystal growth, agglomeration, breakage and attrition, etc. (Randolph, 1969). To realise the complexity of the modelling procedure, consider the interactions between the parameters themselves and between these parameters and the mixing process (Mersmann, 1988). Therefore, to model a precipitation process a number of steps must be taken into account: mixing process (i.e., crystallizer geometry, type and speed of impeller, baffles, feed and off-take locations, etc.), chemical reaction, diffusion, mass transfer, supersaturation, nucleation, crystal growth, ageing, agglomeration, etc.

The application of CFD in precipitation processes is a new field and only few workers have recently investigated this area. However, there is no relevant CFD multi-phase model known to the author that would be able to describe the production of a new phase. On the other hand, many reports in the literature discussed the modelling of

mixing processes using CFD, e.g. Hallas and Hannan (1990); Murthy *et al.* (1994); Foumeny and Sandhu (1995); Bakker *et al.* (1996 and 1997).

Seckler *et al.* (1993) described the precipitation of calcium phosphate in a 2-D jet mixer representation. Another work, Seckler *et al.* (1995) developed a mathematical model, for the same previous system, which predicts the local supersaturation, local moments of the particle size distribution and product properties. They only encountered, however, primary nucleation and crystal growth. The later study showed that only a small fraction of the reactor volume is effectively used for nucleation and crystal growth. k-ε CFD model was used to predict the turbulence behaviour in a double-jet continuous reactor.

Van Leeuwen *et al.* (1996) studied the precipitation of barium sulphate in a rectangular flat reactor with jet mixing. Their steady-state 2-D CFD model estimated the effect of changing the inlet velocity ratio while keeping the residence time and species concentration in the reactor constant. The k-ε turbulence model was used in the CFD simulation. A good agreement was found between the CFD model and the experimental studies.

Wei and Garside (1997) used a coaxial flow pipeline in their steady-state CFD model of a continuous precipitation of $BaSO_4$ system. They studied the influence of the positions and orientation of two inlet streams and the length of a jet mixer on the mixing and precipitation processes. Primary nucleation and crystal growth kinetics and k-ε

turbulence model were used in the CFD model. The mixing obtained by the tee-junction mixer was predicted to have a better mixing than in the coaxial mixer. They also found an optimal jet-to-pipe diameter ratio, in the tee-junction mixer, to obtain specific precipitate properties.

Garside and Wei (1997) were the first to explore the precipitation process in a stirred tank which is a useful method for studying the effect of mixing on precipitation processes and for the design of precipitating devices. They applied CFD on both pumped jet mixers and stirred tanks. One of their most important findings was that the MSMPR model can be a source of error when employed to predict the behaviour of precipitation processes due to the hydrodynamic influence.

Each previous study investigated different aspects of the application of the CFD technique on the precipitation processes. The common aspects between these pioneering researches can be summarised as follows:

☆ Continuous steady-state operations.

☆ Liquid-liquid systems.

☆ Supersaturation, primary nucleation and size-independent crystal growth kinetics only were modelled.

☆ Instantaneous reactions were assumed, i.e. the chemical (micro-mixing) kinetics were neglected.

☆ k-ε turbulence model was employed.

This study, however, focuses on the following:

- ☆ Steady-state hydrodynamics and transient chemical kinetics and precipitation process.
- ☆ Gas-liquid system with a single (liquid) phase assumption.
- ☆ Supersaturation, primary nucleation and size-independent crystal growth kinetics only were modelled, similar to the above models.
- ☆ Chemical kinetics are considered in the modelling procedure.
- ☆ Reynolds differential stress model is applied to model the turbulence in the mixing vessel.

The next chapter will investigate the precipitation kinetics and simulation conditions followed by a chapter about the CFD hydrodynamic simulation and then the chemical kinetics and precipitation process simulation will be presented.

3

PRECIPITATION KINETICS AND SIMULATION CONDITIONS

3. PRECIPITATION KINETICS AND SIMULATION CONDITIONS

Gas-Liquid Precipitation System Industrial Importance

Industrial processes for particle preparation may be operated in combination of gas and liquid. Precipitation represents the formation of sparingly soluble products induced by liquid phase chemical reaction. The industrial applications of precipitation, of solids enhanced by gas-liquid reactions, are various and embrace different fields such as fine chemicals, biotechnology and gas cleaning. There is an increasing industrial demand on many gas-liquid reaction systems, including the following (Söhnel and Garside, 1992 and Wachi and Jones, 1995).

Ammonium phosphate is produced by reaction of ammonia with phosphoric acid resulting in the formation of the mono or di-basic salts. The mono salts tends to produce needles while the di-basic salt results in more granular crystals. Ammonium phosphate finds applications as a fertiliser.

Barium carbonate (Yagi, 1988 and Kubota *et al.*, 1990) can be prepared by the carbonation of either barium hydroxide or barium sulphate. The product crystals are employed as a component raw material for optical glass, fibre-glass, Braun tubes, electric condensers, barium ferrite, etc.

Calcium carbonate (Al-Khayat and Garside; 1990; Wachi and Jones, 1991b; Garside, 1991 and Hostomský and Jones, 1993 and 1995) precipitation, which is the

proposed system for this project, has various markets including the chemical industries, building, refractory, agricultural and highway construction. The reaction details will be given in details later.

Gypsum (calcium sulphate) (Sada *et al.*, 1977) formed from the gas-liquid reaction between sulphur dioxide and calcium hydroxide, is of a commercial use for plaster, cement or fertiliser. For the purpose of pollution control in the burning of high sulphur coal, sulphur dioxide present in stack gases is removed by absorption into lime water with the formation of calcium sulphate/sulphite mixtures.

Geothite is produced by air oxidation of alkaline suspension of ferrous hydroxide (Sada *et al.*, 1988). As a starting material for ferrous oxide, the preparation of fine particles with prescribed size, size distribution and shape is required in its application to magnetic materials for recording tapes and disks.

Terephthalic acid is made by air oxidation of *p*-xylene in acetic acid with cobalt manganese salt of metal bromide at 200 °C and 400 psi. The crude terephthalic acid is cooled and crystallized. A subsequent recrystallization is needed to achieved a 99.9 % purification for polyester grade.

Sodium bicarbonate is made by the carbonation of salt and ammonia in a carbonation tower (Solvay process). The sodium bicarbonate produced is heated to 175 °C in rotary dryers to give light soda ash. Holes are left in the crystals obtained, as the carbon dioxide is liberated. Dense soda ash, used by the glass industry, is manufactured from the light ash by adding water and drying

Chemicals production, e.g. fermentation processes and effluent treatment.

Calcium Carbonate Precipitation

A batch calcium carbonate precipitation in a gas-liquid cell is chosen for the model because of its well-defined geometry which allows many simplifications in CFD modelling. The gas-liquid interface between the carbon dioxide and the aqueous solution of calcium hydroxide, eliminates the complexity of the feed/off-take positions which would dramatically affect the crystal size distribution (David and Marcant, 1994). Implementing this reaction (which mainly takes place at the interfacial region) also enables to avoid the multi-phase CFD modelling which is difficult to handle.

The reaction scheme can be described as follows:

$$CO_2\,(g) \rightarrow CO_2\,(aq) \qquad (3.1)$$

$$CO_2\,(aq) + OH^- \rightarrow HCO_3^- \qquad (3.2)$$

$$HCO_3^- + OH^- \rightarrow CO_3^{2-} + H_2O \qquad (3.3)$$

$$Ca^{2+} + CO_3^{2-} \rightarrow CaCO_3\,(s) \qquad (3.4)$$

Equation (3.1) represents a mass transfer step at the interface which can be expressed in terms of Henry's law:

$$[CO_2] = \frac{P_{CO_2}}{H_{CO_2}} \qquad (3.5)$$

Where p_{CO_2} and H_{CO_2} are the partial pressure and the Henry's constant of carbon dioxide, respectively. This step can be implicitly introduced as a boundary condition of a constant concentration of carbon dioxide in the model. The reaction rates of equations (3.2) and (3.3) are given as follows:

$$R_1 = k_1 ([CO_2][OH^-] - \frac{K_w}{K'}[HCO_3^-]) \quad (3.6)$$

$$R_2 = k_2 ([HCO_3^-][OH^-] - \frac{K_w}{K''}[CO_3^{2-}]) \quad (3.7)$$

where k_1 and k_2, are rate constants for reactions (3.2) and (3.3) respectively, K' and K" are the first and second order dissociation constants of H_2CO_3 respectively and K_w is the equilibrium constant for the reaction $H_2O \rightarrow H^+ + OH^-$. Equation (3.7) demonstrates a very fast ionic reaction, hence the rate constant k_2 can be approximated by a large value, i.e. approximating equilibrium for equation (3.3), Hostomský and Jones (1995).

Finally, equation (3.4) can be illustrated by the number rate of nucleation (B), linear crystal growth rate (G) and mass growth rate (r_D):

$$B = k_n(S)^n \quad (3.8)$$

$$G = k_g(S)^g \quad (3.9)$$

$$r_D = \beta \rho_c M_2 G/2 \quad (3.10)$$

where β is the surface to length shape factor, M_2 is the second moment and S is the supersaturation which is given as:

$$S = \left(\sqrt{[Ca^{2+}][CO_3^{2-}]} - \sqrt{K_{sp}}\right) \quad (3.11)$$

K_{sp} is the solubility product of calcite.

for simplicity and saving computational time, the above reactions reduced to one reaction:

$$CO_2\,(aq) + Ca(OH)_2\,(aq) \longrightarrow H_2O + CaCO_3\,(s) \qquad (3.13)$$

The reaction kinetics are as used by Wachi and Jones (1991 a) and Hostomský and Jones (1995), see Appendix (1).

The CFD simulation also calculates the moments M_0, M_1, M_2 and M_3 as follows:

$$\frac{dM_0}{dt} = B \qquad (3.14)$$

$$\frac{dM_1}{dt} = M_0 G \qquad (3.15)$$

$$\frac{dM_2}{dt} = M_1 G \qquad (3.16)$$

$$\frac{dM_3}{dt} = M_2 G \qquad (3.17)$$

where $G \neq G(L)$ and $B = dN/dt$. The size-independent growth rate assumption is implemented here because a precipitation process is considered, i.e. only small crystal mean sizes occur. On the other hand, the problem of size-dependent growth is more complicated for smaller crystals than larger ones (Söhnel and Garside, 1992). Therefore, it is a common practice in the CFD precipitation modelling to assume size-independent growth which simplifies the derivations of the above equations. Equally, there is no evidence of size-dependent growth rate of $CaCO_3$ crystals.

Then, the level of supersaturation can be estimated as a balance between the production of solute due to chemical reaction, R, and its consumption due to both nucleation and crystal growth, as follows:

$$\frac{dc}{dt} = R - \alpha\ L_0^3 \rho_c B - r_D \qquad (3.18)$$

The gas-liquid calcium carbonate precipitation system has also the following advantages:

- The system can be considered initially as a one-phase (liquid) system, and the gas phase at the interface is implicitly introduced in the boundary conditions where the mass transfer at the gas-liquid interface is neglected. This assumption is valid since the critical concentration of the solute (= $[k_G/k_L][D_A/D_B][qp_A]$) for the limiting case (instantaneous reaction) is much larger than its interfacial concentration, i.e. it is a liquid-film controlled process, Danckwerts (1970). The interfacial concentration (proportional to the partial pressure of carbon dioxide in the gas phase) can be kept constant throughout the experiment.
- There is no feed or off-take which in turn eliminates the complexities of the positions and the rates of charging and discharging.
- Theoretical and experimental results are also available (Wachi and Jones, 1991a and b; Jones *et al.*, 1992) to provide a reliable base to compare with the new CFD simulation model predictions.

The system geometry, see Figure (3.1), is similar to that investigated earlier by Hikita and Ishikawa (1969); Wachi and Morikawa (1986) and Wachi and Jones (1991b). The agitated vessel has an inner diameter and a height of 0.12 m and 0.2 m, respectively.

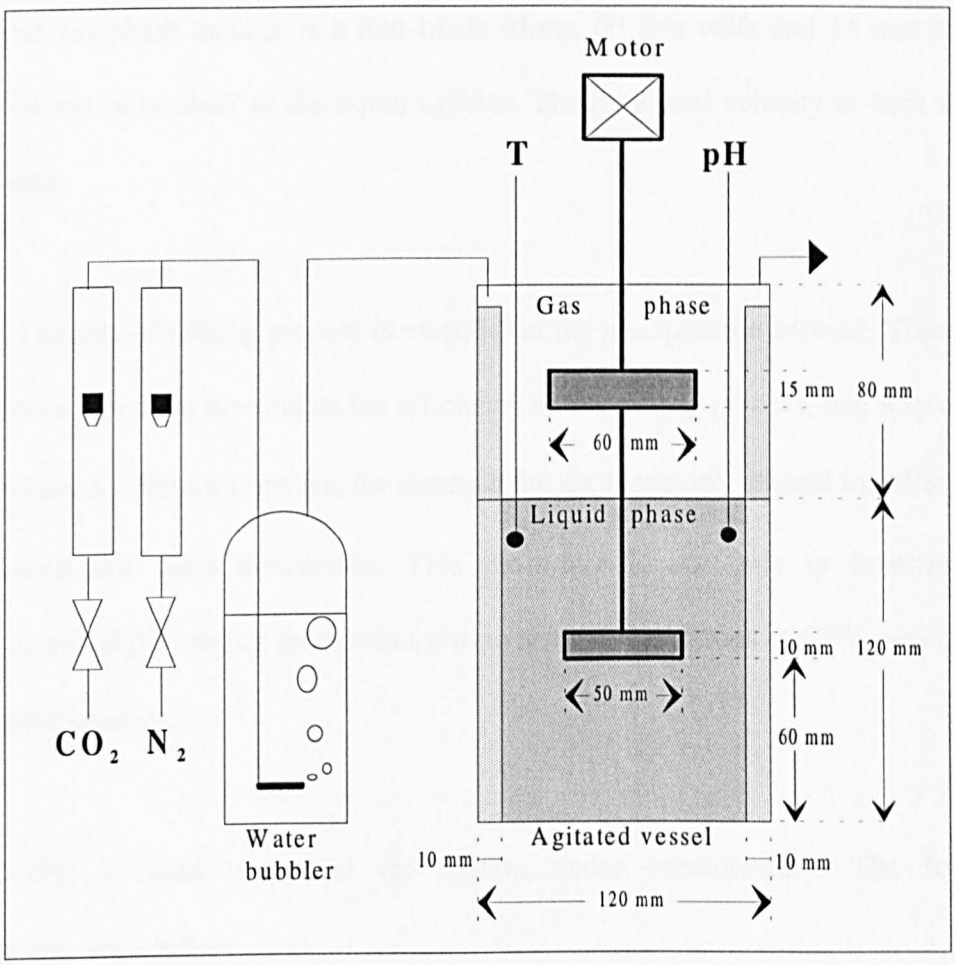

Figure (3.1): Experimental apparatus.

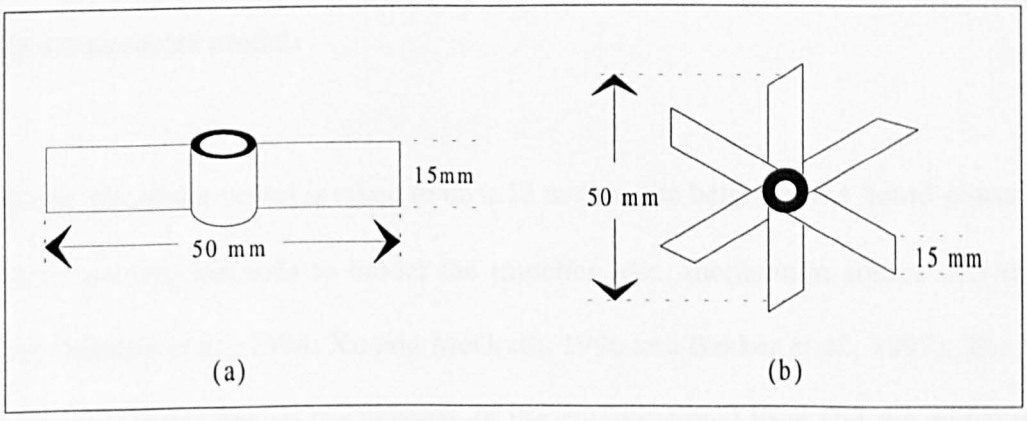

Figure (3.2): (a) Two-blade paddle agitator and (b) six-blade 45° pitched impeller.

The initial liquid depth is 0.12 m. Four vertical baffle plates, 10 mm wide are fitted in the vessel. The liquid phase is mixed by a two-blade paddle agitator, Figure (3.2a), 50 mm wide and 15 mm high, and placed at the centre of the vessel and 60 mm from the base. The gas-phase agitator is a four-blade stirrer, 60 mm wide and 15 mm high and placed on the same shaft as the liquid agitator. The rotational velocity of both agitators is the same.

The role of mixing process is essential in the precipitation scheme. Therefore, it is very momentous to investigate the efficiency of the mixing process, one way of doing this is to use a different impeller, for example the six-blade 45° pitched impeller, Figure (3.2b) with the same dimensions. This procedure is not only to investigate the effectiveness of the mixing process but also to test the predictions of CFX with different momentum sources.

CFX is used to model the system under consideration. The following assumptions are applied:

a. Hydrodynamic model:

- The height of the vessel is taken to be 0.12 m (i.e., the height of the liquid-phase).
- There are two methods to model the impeller, viz., momentum source and sliding grid (Murthy *et al.*, 1994; Xu and McGrath, 1996 and Bakker *et al.*, 1997). The latter is more accurate but on the expense of the computational time and the combination

between the sliding grid and the chemical kinetics subroutine is not possible due to the code limitations. Hence, the former method will be employed.

- No change in the interface level and it is considered as a wall with zero shear stresses.
- Baffles are assumed to be thin surfaces.
- Rectangular and stagnant shaft is modelled.

b. 2-D Chemical kinetics and precipitation model:

The 2-D model geometry represents half of the vessel with a height of 0.12 m and 0.06 m width.

- Single (liquid) phase reactive precipitation process with one polymorph of calcium carbonate, viz. calcite.
- Carbon dioxide is an aqueous solution which is introduced at the interface region with a constant flow rate.
- No change in the overall volume/mass of the vessel.
- Supersaturation, primary nucleation size-independent crystal growth and the first four moments (M_0, M_1, M_2 and M_3) are taken into account in the model.
- No dissolution of particles and no particle settling.
- Initial size of the nuclei is zero.

IBM Power PC (RISC SYSTEM/6000 250) is used to run the CFD simulations.

4

CFD HYDRODYNAMIC SIMULATION

4. CFD HYDRODYNAMIC SIMULATION

In order to solve the present CFD modelling problem, it is divided into four main steps, Sharratt (1990):

1. Grid generation: in which the volume in question is divided into a number of cells. A range of possible geometry representations is available from the simple coordinates (e.g., cylindrical and Cartesian) to the complex e.g., body-fitted coordinates -BFC (Hallas and Hannan, 1990 and Harvey III *et al.*, 1995).
2. Choice of relaxation parameters: since CFD produces a large set of non-linear simultaneous equations, this choice provides an adequate contribution towards both the rate of convergence and the production of a solution.
3. Boundary conditions: which must be defined starting with a simplified case by leaving out unimportant details and irrelevant effects.
4. Verification: Three questions must be considered separately for this step: (a) the numerical methods and solution, (b) the physical models used and (c) the boundary conditions.

The procedures adopted for the definition of the present CFD problem are described below.

Momentum Source -Impeller- Modelling

The time-averaged Navier-Stokes equations are used for the conservation of mass and momentum to model the flow in a cylindrical vessel which is discretised using

a multiblock grid. The flow is considered to be steady, incompressible, turbulent and isothermal. Therefore, the following equations can be applied:

a. continuity equation:

$$\underline{\nabla}.(\underline{U}) = 0 \tag{4.1}$$

b. momentum equation:

$$\underline{\nabla}.(\rho \underline{U} \otimes \underline{U} - \mu \underline{\nabla U}) = \underline{B} + \underline{\nabla} P - \underline{\nabla}.(\overline{\rho \underline{u} \otimes \underline{u}}) \tag{4.2}$$

where $\underline{U} = (U, V, W)$ is the fluid mean velocity and $\overline{\rho \underline{u} \otimes \underline{u}}$ is the turbulence Reynolds stress.

The impeller is modelled as a momentum source where the body forces are employed in the region swept by the impeller. Perry's method is used to calculate these body forces through the power consumption of the impeller (Al-Rashed *et al.*, 1996). Reynolds number is defined as:

$$\mathrm{Re} = \frac{D^2 N \rho}{\mu} \tag{4.3}$$

Power number (N_P) can be given by impeller power correlation curves, Sano and Usui (1987). Then, the power consumption (P) is given as:

$$P = N_P \rho N^3 D^5 \tag{4.4}$$

The power consumption of the impeller is also defined as the product of the angular velocity and the impeller torque (T), therefore,

$$T = \frac{P}{2\pi N} \tag{4.5}$$

By applying the balance of the torque acting on the shaft and the impeller, the momentum source representing the effect of the impeller can be calculated as follows:

$$T = \int_{V_S} rFdV \tag{4.6}$$

$$V = \pi r^2 W \tag{4.7}$$

where V_S is the volume swept by the impeller. The force is assumed to be uniform in the circumferential and axial directions and proportional to the radial distance at which it acts:

$$F = K_F r \tag{4.8}$$

Substituting for V from equation (4.7) and for F from equation (4.8) into equation (4.6):

$$T = \int_{r_1}^{r_2} 2\pi r^3 K_F W dr \tag{4.9}$$

integrating equation (4.8) for K_F:

$$K_F = 2T / [\pi W(r_2^4 - r_1^4)] \tag{4.10}$$

For the present vessel D = 0.05 m, N = 450 rpm (= 7.5 s^{-1}), ρ = 996.6 kgm^{-3} and μ = 8.967*10^{-4} $kgm^{-1}s^{-1}$, so the Reynolds number is 20.8*10^3 (>10*10^3) -equation (4.3)- which means that the flow is turbulent. The power consumption (P) equals to 0.263 W where N_P has a value of 2.0 -equation (4.4)- therefore, the impeller torque (T) is 5.58*10^{-3} Nm -equation (4.5)-. Finally, the value of K_F is calculated using equation (4.10) as 6.06*10^5 Nm^{-4} (5.14*10^5 Nm^{-4} for the pitched impeller system). Therefore, at (x, y) position within the impeller volume, the x and y components of the force are:

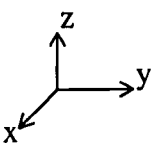

$$F_x = -K_F y \tag{4.11}$$

$$F_y = K_F x \tag{4.12}$$

If the blades are inclined from the vertical, then the axial force may be given as:

$$F_z = K_F \tan\theta \tag{4.13}$$

Hence, the body force vector in equation (4.2) can be written as:

$$\mathbf{B} = (F_x / V, F_y / V, F_z / V) \qquad (4.14)$$

Since the impeller used has flat-blade paddles, then the axial force, F_z, is going to be zero. Equations (4.11) to (4.14) are solved (simultaneously) using an IBM Power PC RISC System / 6000-250. 43,000 cells are used for both systems, and the CPU times are 13.0 and 14.1 hrs for the paddle and 45° pitched impellers, respectively, where they converged after approximately 500 iterations.

CFD Model Computer Code

The outline flow chart of the CFD hydrodynamic simulation is shown in Figure (4.1). The simulation has two main parts:

1. Command file: is written by the author and consists of 65 lines.
2. Fortran file: is a modification of the user body forces subroutine (USRBF). It has 37 added and modified lines comprising 82 lines overall.

Under the terms of the license agreement, the detailed CFD model computer code, and its modifications, remain the property of the licensor (AEA Technology Ltd.)

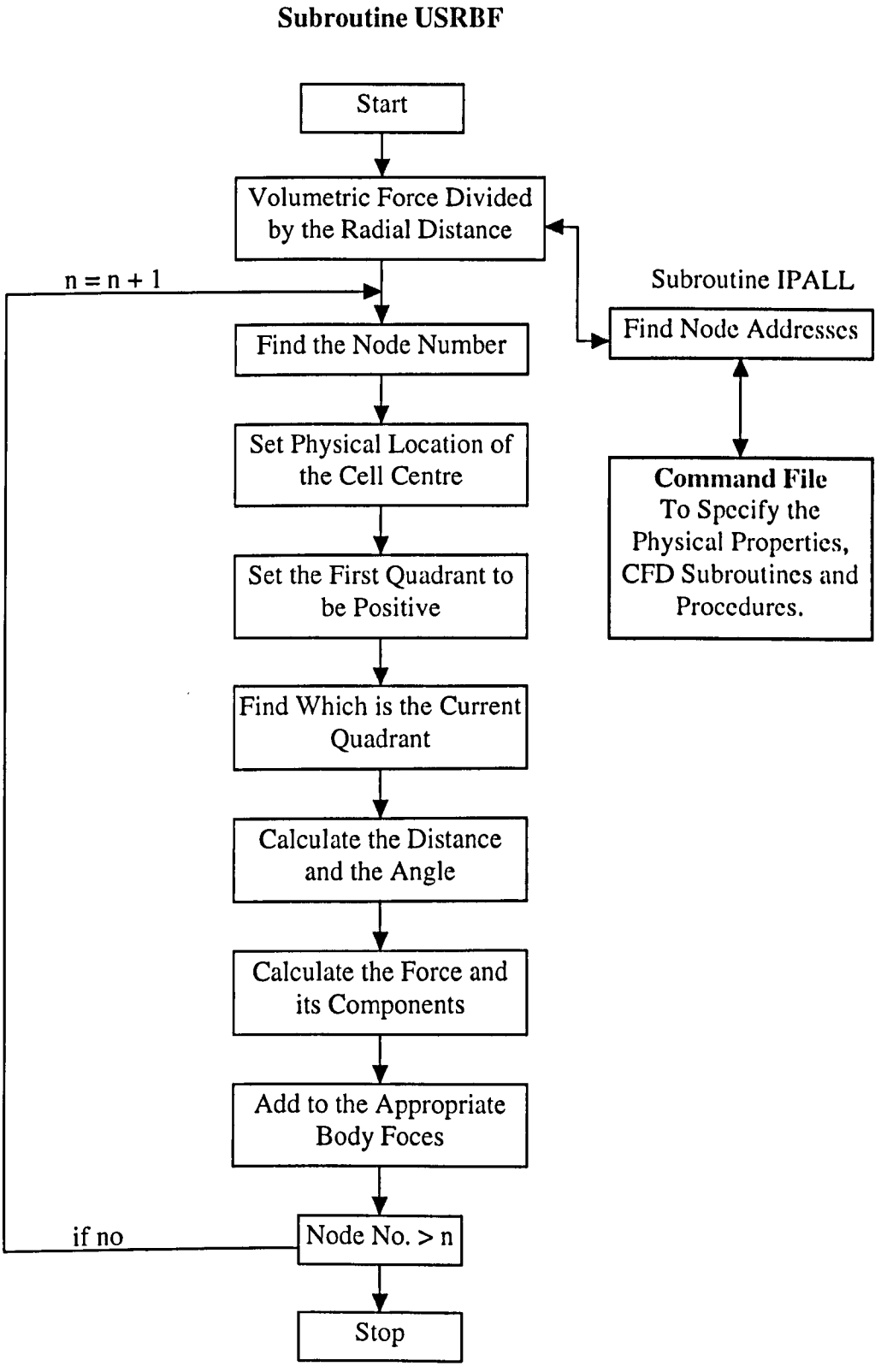

Figure (4.1): CFD Hydrodynamic simulation flow chart.

5

CHEMICAL KINETICS & PRECIPITATION PROCESS MODEL

5. CHEMICAL KINETICS AND PRECIPITATION PROCESS SIMULATION

As shown in the literature survey micromixing plays a major role in reactive processes in mixing vessels. However, for simplicity, some authors tend to neglect it in CFD modelling for precipitation processes, since the reaction is very fast and almost instantaneous in some systems. This project was directed to investigate the effect of the chemical kinetics and therefore of micromixing in the CFD modelling of reactive precipitation processes.

A two-dimensional geometry is applied in the model where it represents one slice of the vessel. The dimensions are 0.12 m length and 0.06 m wide with the assumption that it has one cell thickness. This 2-D model, which symbolises half of the vessel, is chosen to check the practicality of the model and to save on computational time for obvious reasons. Also, the hydrodynamic characteristics of this 2-D model are sufficiently consistent with the 3-D hydrodynamic model which is validated both experimentally and from literature results (see later).

There are two processes involved, namely the hydrodynamic motion which is steady state and the precipitation process which is transient. To overcome the interactions between these two distinct processes, the hydrodynamic steady state process is taken as a background for the model. Therefore, the first run of the simulation considers only a pure mixing process as is usually the case in the experimental

procedures for such systems. Hence, the stirrer is switched on for few minutes (ideally) until a steady flow pattern mixing is observed then the gas will be discharged to the liquid interface to allow the precipitation process to take place. Next, the chemical kinetics and precipitation simulation is run in a transient mode.

The reaction scheme of the calcium carbonate reactive precipitation process can be described as follows:

$$CO_2\,(g) \rightarrow CO_2\,(aq)$$

$$CO_2\,(aq) + OH^- \rightarrow HCO_3^-$$

$$HCO_3^- + OH^- \rightarrow CO_3^{2-} + H_2O$$

$$Ca^{2+} + CO_3^{2-} \rightarrow CaCO_3\,(s)$$

For simplicity it is reduced to only one lumped reaction:

$$CO_2 + Ca(OH)_2 \rightarrow CaCO_3 + H_2O$$

The advantage of this simplification is mainly in the simulation computational time which will be reduced substantially.

The single-phase simulation assumption is justifiable for this system since the produced (solid) particles are very small such that they follow the flow pattern which itself is not affected by their presence. In addition, the mass of these particles is too small compared with the mass of the liquid. Water is defined to be the background fluid in the simulation because the other species concentrations are very small compared with

the water. The background fluid concentration means that it is not calculated from a transport equation but it is obtained however by setting the background fluid mass fraction equal to the difference between unity and the sum of the mass fractions of the other species.

On the other hand, at the interface, the reactant gas (CO_2) is introduced in the boundary conditions as an aqueous state. Thus, the model presumes calcium carbonate initially as a solution and when its concentration reaches the supersaturation region the model starts to calculate various precipitation parameters. Accordingly, the density and viscosity of the fluid in the vessel is taken as the values of water.

The simulation considers reaction, supersaturation, primary nucleation and linear crystal growth kinetics. At the same time, it calculates the zeroth, first, second and third moments representing; the total number, the length, the surface area and the mass of particles, respectively. Hence, the crystal mean size is calculated from the zeroth and first moments as $d_{avg} = \frac{m_1}{m_0}$.

There are two main methods to model a transient problem in CFX. The first permits the user to specify all the time steps and this is called "FIXED TIME STEPPING". Whereas the second method lets the solver to choose the proper time step within a given range and is called "ADAPTIVE TIME STEPPING". Choosing the right method depends on the problem in hand. If the reaction time scale is not well known then it is recommended to use the second method which is the case for this project.

The main adaptive time stepping method parameters (CFX manual) can be listed as follows:

1. **Number of time steps**: to specify how many time steps are to be calculated.
2. **Initial time step**: to set the initial time step.
3. **Minimum time step**: to allow a minimum possible time step.
4. **Maximum time step**: to allow a maximum possible time step.
5. **Multiply time step by**: to set the factor by which the time step is increased when the time step increment interval has been reached.
6. **Divide time step by**: to set the factor by which the time step is divided when a time step fails.
7. **Differencing method**: to set one of the available methods; i.e. backward difference (Euler), central difference, Linear time differencing (first order time stepping) or Quadratic time differencing (second order).
8. **Initial time**: to set the initial time of the problem. It can be taken from a restart file by default.
9. **Maximum time**: to set the maximum time of the problem.

Four different stirrer speeds are implemented in the system under consideration, i.e. 1, 100, 200 and 450 rpm. The Re number for fully developed laminar flow is 10 or less and 10,000 or more for turbulent. However, there is no sharp cut for the behaviour of the flow.

The first stirrer speed (1 rpm ~ Re = 46) is used instead of 0 rpm (i.e., no mixing) for computational reasons. It is stated earlier that CFD can not handle over-

simplified problems and also zero fluid flow motion may cause divergence problems which is the case for the stagnant (0 rpm) system.

The second stirrer speed (100 rpm) is applied in the simulation under both laminar and turbulent conditions. The Re number (= $4.63*10^3$) for this speed is in the transition state of the flow where it is not laminar and not fully developed turbulent flow. Therefore, the simulation is run for both cases to show the effect of turbulence since an intermediate (transition) model is not possible in the code. Moreover, it is going to be a double check on the effect of turbulence on the micromixing which in turn will be reflected on the performance of the precipitation process.

The other two stirrer speeds (200 and 450 rpm) are considered in the simulation to have turbulent behaviour where their Re numbers are $9.26*10^3$ and $2.08*10^4$, respectively. It should be noticed that the Re number represents the impeller region and uniformity of the mixing depends on the geometry of the vessel and type of impeller.

Appendix (2) illustrates the variation of the power and flow numbers with Re number for the two blade paddle.

CFD Model Computer Code

The outline flow chart of the chemical kinetics and precipitation process simulation is shown in Figure (5.1). The simulation has two main parts:

1. Command file: is written by the author and consists of 163 lines.

2. Fortran file: is a modification of the user subroutine (USRTRN). It has 59 added and modified lines comprising 103 lines overall.

Under the terms of the license agreement, the detailed CFD model computer code, and its modifications, remain the property of the licensor (AEA Technology Ltd.).

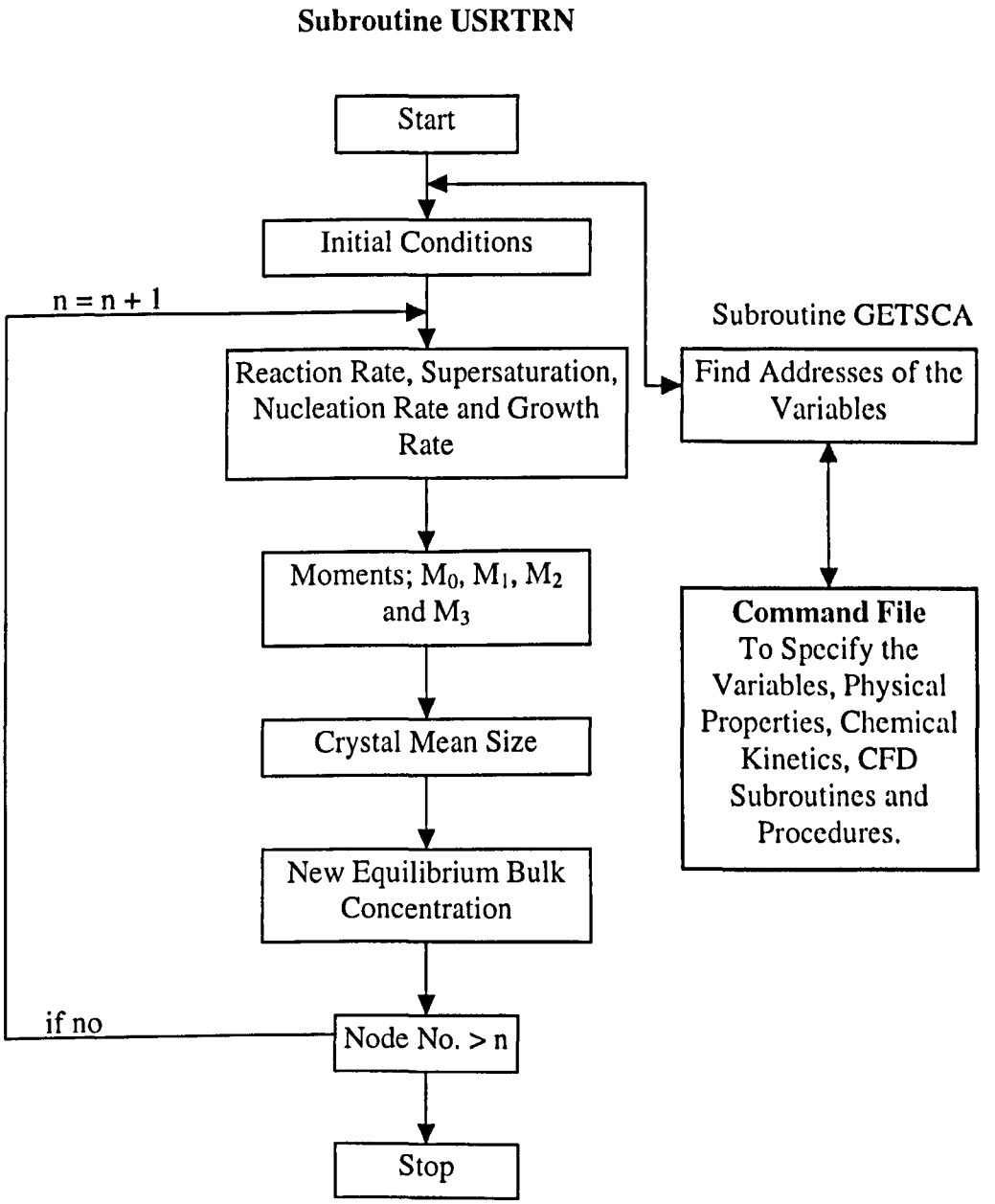

Figure (5.1): Chemical Kinetics and Precipitation process CFD simulation flow chart (for every time step).

6

RESULTS & DISCUSSION

6. RESULTS AND DISCUSSION

6.1. 3-D Hydrodynamic Simulation

The model considers the steady-state flow pattern of a liquid phase. In cylindrical systems, if the flow is crossing the axis, it is recommended to use the Cartesian grid system, because a source of singularity is expected at the central axis of the vessel i.e., r = 0 (Al-Rashed *et al.*, 1996). Therefore, O-grid patched to H-grid, Figure (6.1), is applied here. Figure (6.2) shows a view of the blocks created by the simulation.

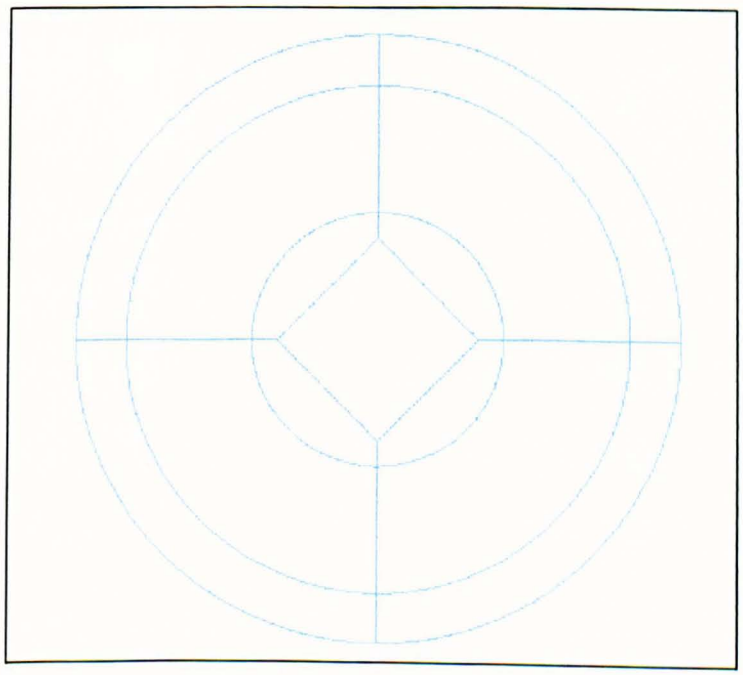

Figure (6.1): O-grid patched to H-grid.

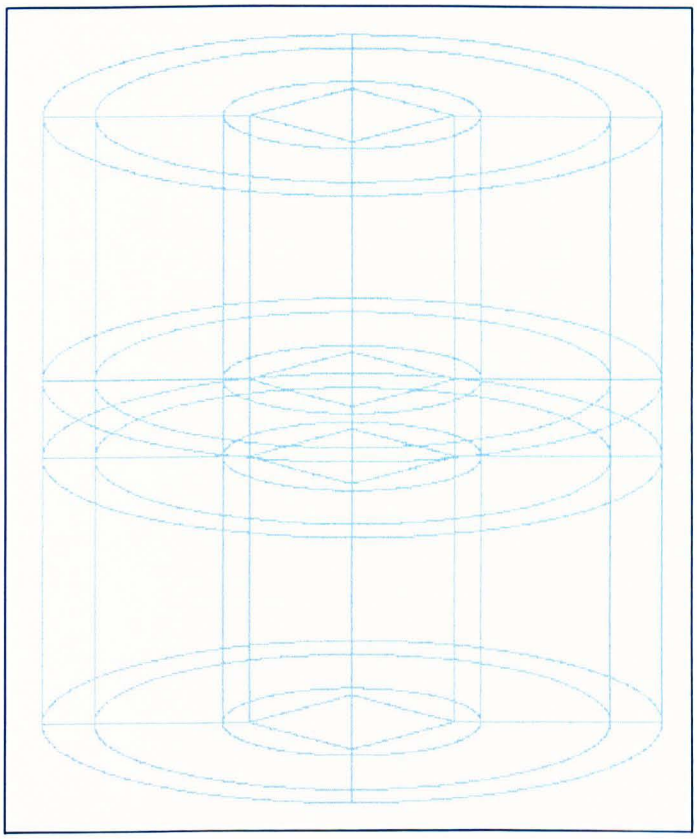

Figure (6.2): A view of the blocks from the CFD simulation.

The next step is the grid generation in which the volume of the liquid-phase is divided into a number of cells. The intensity of the grid depends on a number of factors which vary from problem to another. Figure (6.3) illustrates the surface grid, where most of the cells are concentrated at the interface and the impeller region. This is because dramatic changes are expected in these regions. The grid of the vessel, for both the paddle and the pitched impeller system, consists of 43,000 cells, see Appendix (3).

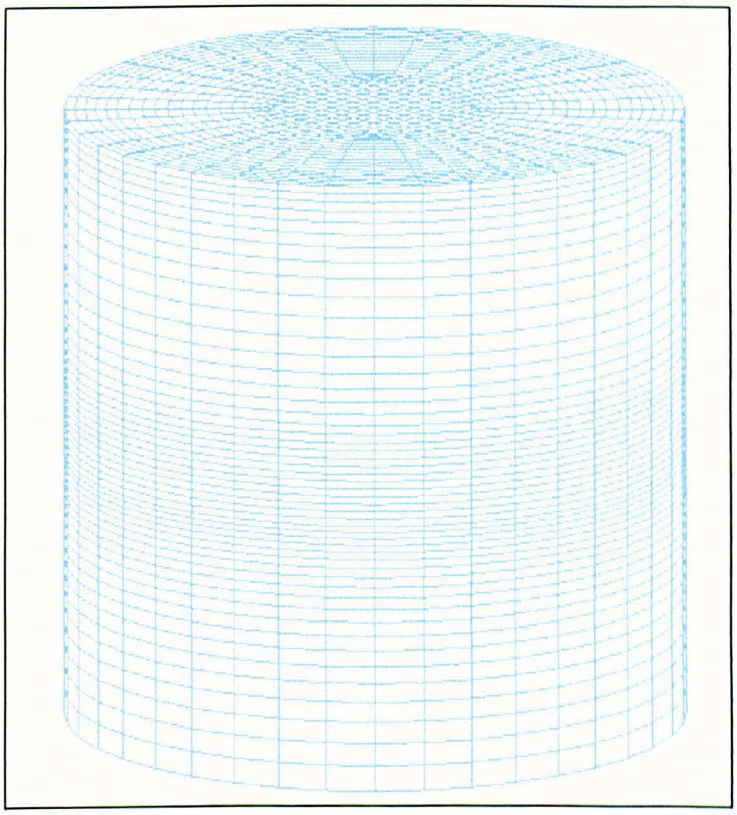

Figure (6.3): The surface grid of the vessel.

As it mentioned earlier that the impellers are presented as a momentum source, this is demonstrated in Figure (6.4)

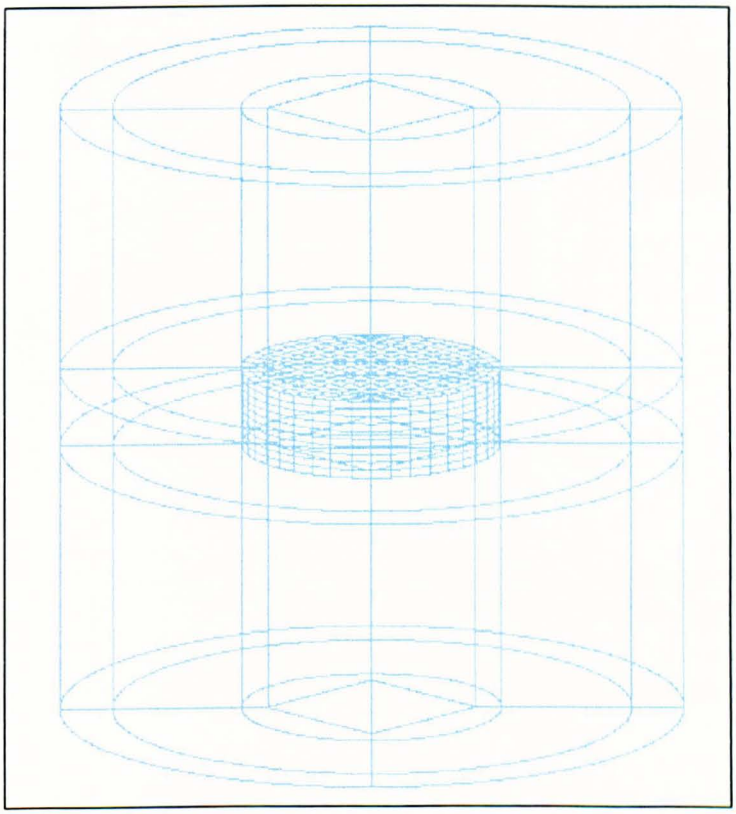

Figure (6.4): The impeller region mesh at the centre of the vessel where the momentum source is defined.

Figures (6.5) and (6.6) show the speed vectors and shaded contours of the flow, respectively, with a maximum value in the impeller tip region and two basic recirculation loops, one above the impeller mid-plane and one below. Pressure contours are shown in Figures (6.7) and (6.8), the high pressure regions are located in the stagnation zones, i.e., near the boundary walls and in the vicinity of the baffles.

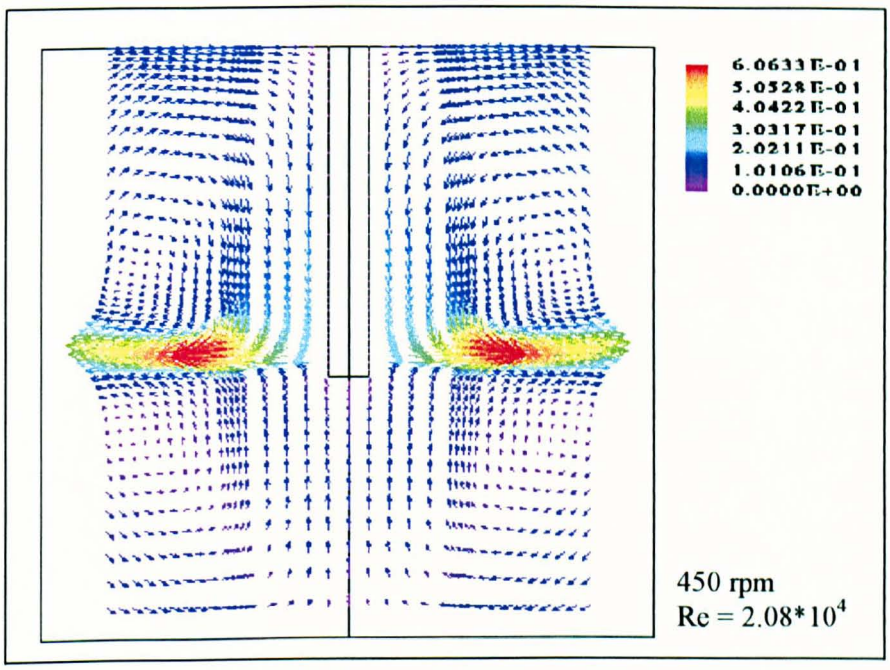

Figure (6.5): Speed (m/s) vectors at the axial central plane (y=0).

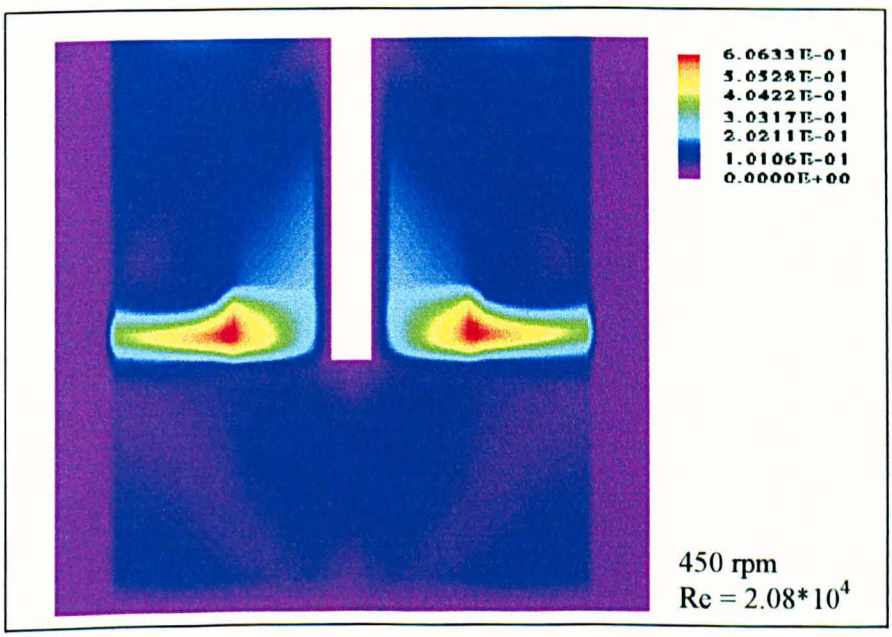

Figure (6.6): Speed (m/s) shaded contours at the axial central plane (y=0).

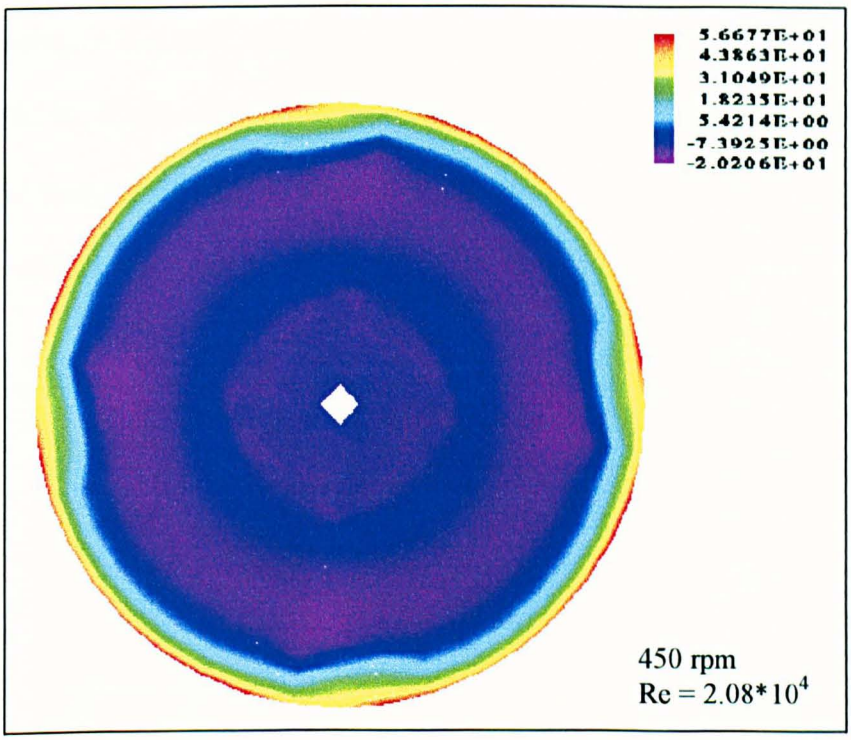

Figure (6.7): Pressure (Pa) shaded contours at the radial central plane (z = 0.06 m).

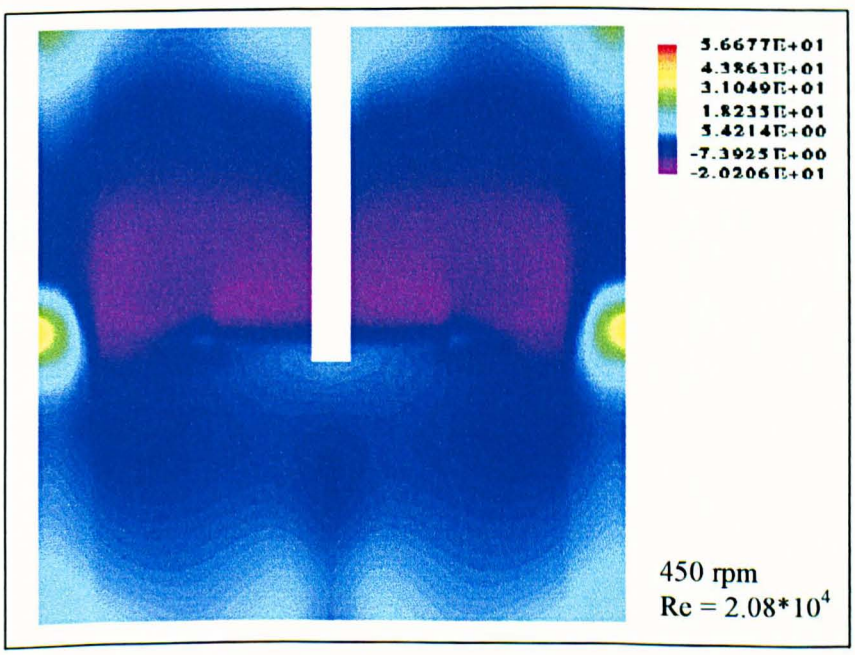

Figure (6.8): Pressure (Pa) shaded contours at the axial central plane (y = 0).

High turbulence levels are desired because it provides a good small scale (micro) mixing. It is found, however, to be highest in the impeller tip region, Figures (6.9) and (6.10). It should be noted that Figures (6.5), (6.6), (6.8) and (6.10) are taken for the axial plane, y=0.0 and Figures (6.7) and (6.9) represent the radial plane, z=0.06 m, i.e., the mid-plane.

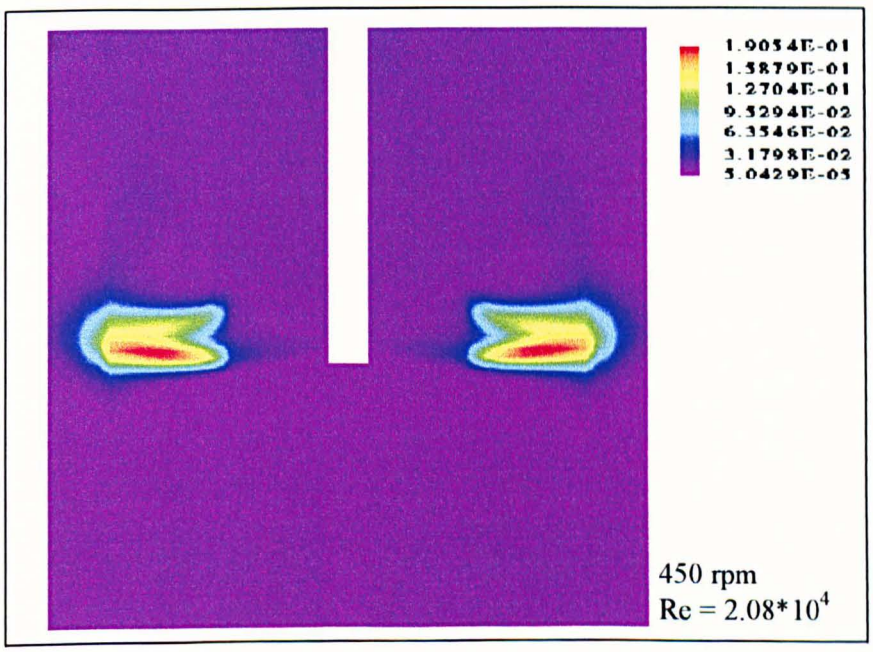

Figure (6.9): Turbulent energy (m^2/s^2) shaded contours at the axial central plane (y = 0).

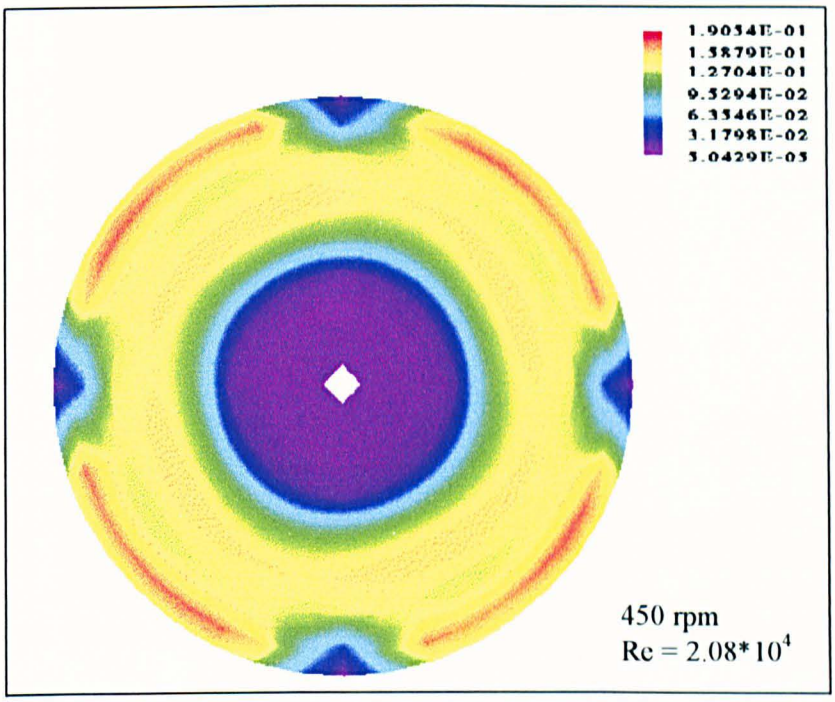

Figure (6.10): Turbulent energy (m^2/s^2) shaded contours at the axial central plane (y=0).

The hydrodynamic simulation of the six-blade 45° pitched impeller gives remarkable results and provides a good comparison tool with the first simulation (two-blade paddle). The comparison between Figures (6.6) and (6.11) shows the second system has better mixing characteristics than the first one. Also, the stagnation regions are smaller. Figure (6.12) shows the pressure shaded contours for the pitched blade impeller system.

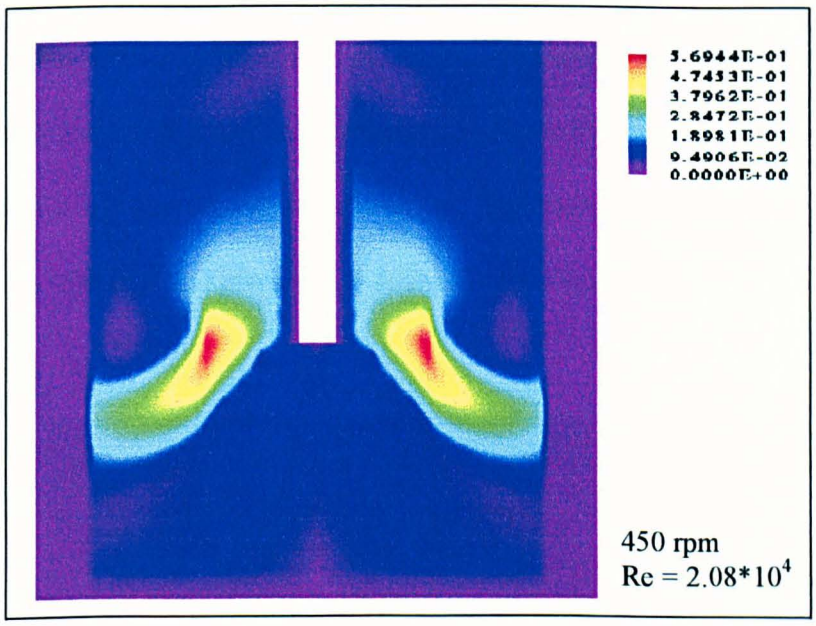

Figure (6.11): Speed (m/s) shaded contours at the axial central plane (y = 0), for 45° pitched-blade impeller system.

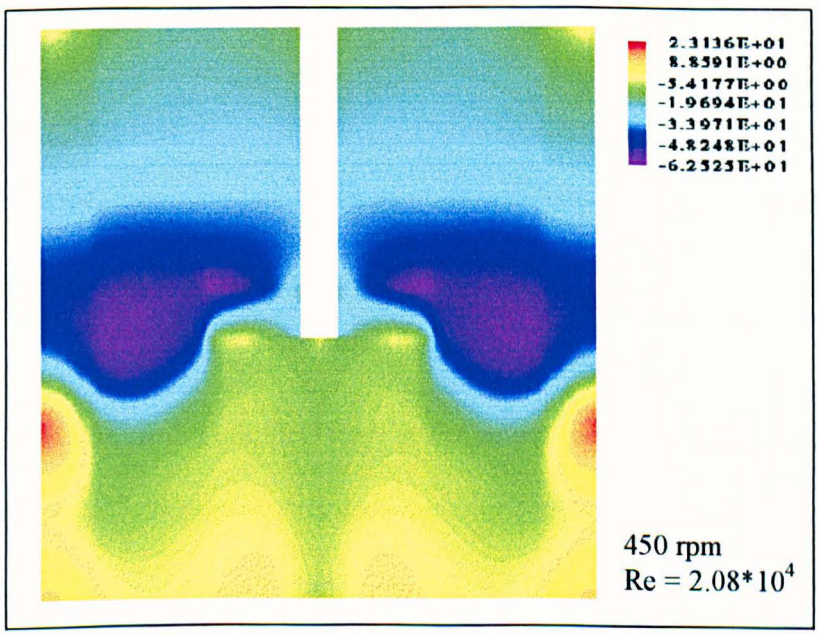

Figure (6.12): Pressure (Pa) shaded contours at the axial central plane (y = 0), for 45° pitched-blade impeller system.

In terms of turbulent energy, it is found to be higher in the impeller region only for the first system, but a larger region is covered by higher values in the second, Figure (6.13), which provides a more uniform mixing. Furthermore, the energy requirement for the pitched blade impeller system is lower. This behaviour proves that the second system is more efficient and gives better (overall) mixing results.

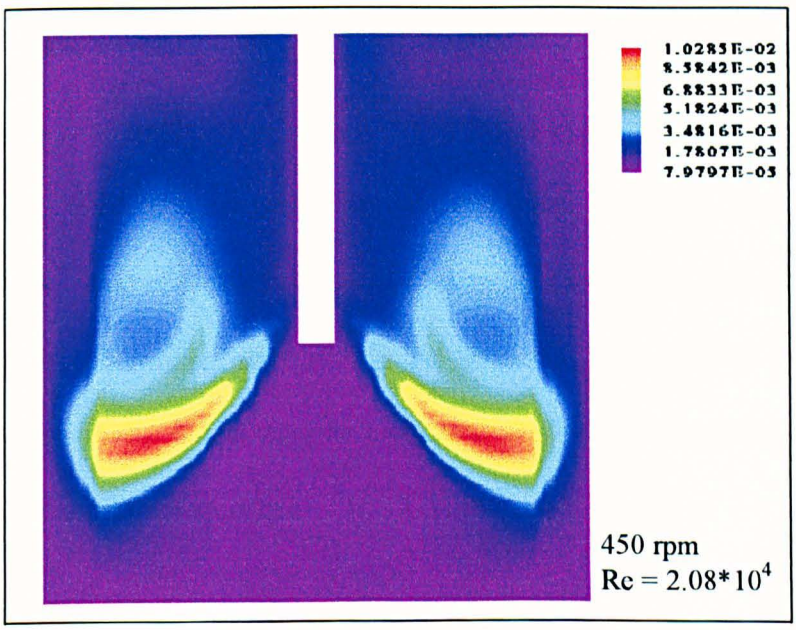

Figure (6.13): Turbulent energy (m^2/s^2) shaded contours at the axial central plane (y = 0), for 45° pitched-blade impeller system.

The direction of the pumped flow at the impeller region is ~40° (from the axial direction) and not 45°. However, this does not conflict with the experimental behaviour. It may be related to the geometry and internals of the vessel. However, Bakker *et al.* (1996) compared two CFD turbulent models, namely k-ε and k-ε RNG, with experimental results of Laser Doppler Velocimetry (LDV) and Digital Particle Image Velocimetry (DPIV) for 45° pitched blade impeller. The impeller discharge angle was

45° by the two turbulent models above, whereas the LDV and DPIV showed a significant deviation from the 45° direction. This conclusion supports the results of this project and demonstrates ability of the Reynolds differential stress model in predicting the swirling flows in the vessel. Rutherford *et al.* (1996) reported a similar agreement using different systems, where the discharge of a pitched blade impeller does not have a similar angle as the blades.

These results imply some of the CFX abilities in predicting the feasibility of the mixing process used in a particular application. Also, for semi-batch or continuous mixing vessels, feed or product streams can be positioned where the optimum performance of the mixing process can be achieved. The validity of the physical correlations used in the model may be examined as well by comparing the simulation results with the experimental data.

The accuracy of the simulation results is affected by the following:

1. The assumption of a rectangular and stagnant shaft can be a source of error.
2. The impeller representation as a momentum source, which could be improved by using the sliding grid method.
3. The limitation of the present technology to provide accurate turbulent models.
4. The baffles are assumed to be thin surfaces.
5. The intensity of the grid specially in the second system, where it needs to be finer in the central region. The disadvantage of this approach is the CPU time cost will be higher.

6.2. Hydrodynamic Simulation Validation

- **Qualitative experimental validation**

One of the essential steps in modelling is to the validation of the CFD simulation. This validation can be performed experimentally or by comparison with literature results. Still photographs of the flow pattern in the vessel is one way of quantitative experimental validation used in this study. To achieve this, the vessel is placed in a cubic container where the space between them and the vessel itself are filled with water. On the other hand, small beads (~1 mm diameter) of polystyrene are used instead of calcium carbonate precipitated particles because the latter are very small to display the flow pattern in a visible clear demonstration, see Figure (6.14). These beads are assumed to follow the water flow pattern in the vessel.

Figure (6.14) illustrates a white light source which produces a thin sheet of light through (approximately) the middle of the vessel. The light beams will be reflected by the beads which cross it. This visual behaviour is recorded by a video camera which is connected to a PC where the results are processed using an image analysis software to provide a selection of photographs.

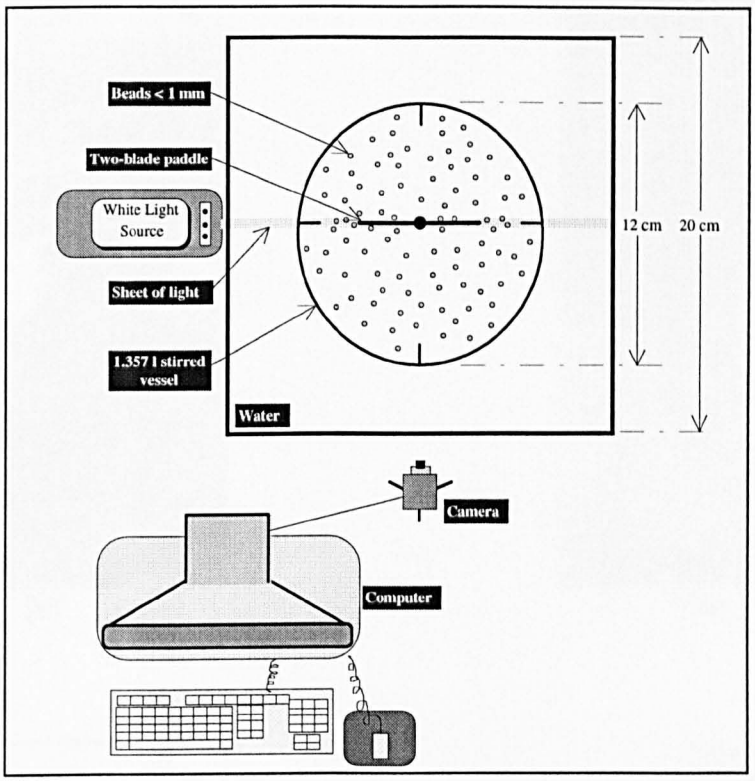

Figure (6.14): A schematic diagram of the hydrodynamic experimental validation set-up.

Figure (6.15) shows some pictures representing half of the vessel (Re = $2.08*10^4$). At the centre close to the impeller, two circulations are noticed above and below it. In some cases, however, the centre of this separation is shifted from the centre line of the impeller. This behaviour is due to the non-uniform mixing in the vessel. These picture are comparable with the CFD results, see Figure (6.5), where a similar estimation is predicted.

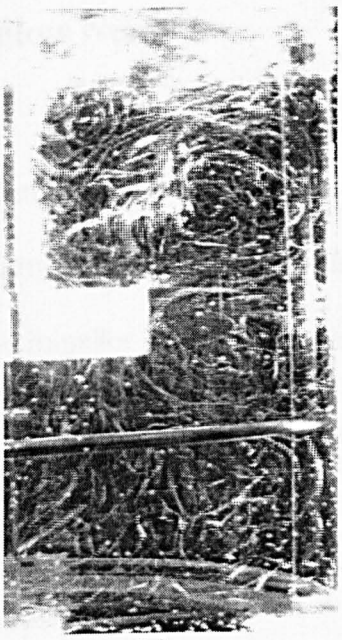

(a)

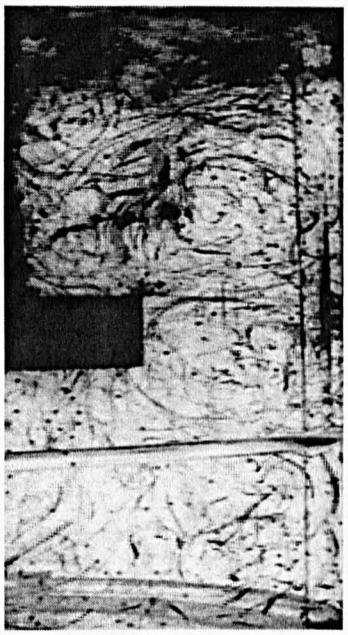

(b)

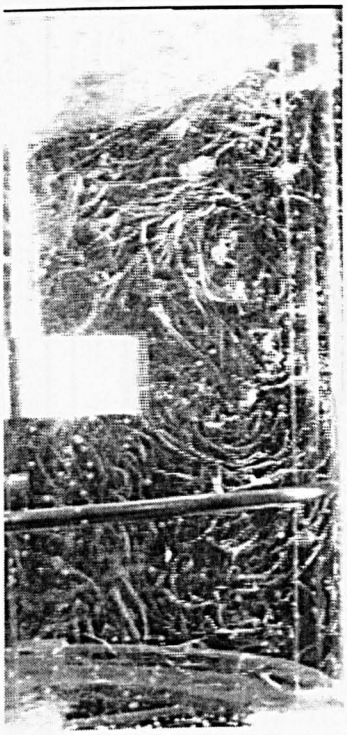

(c)

(d)

Figure (6.15): Experimental validation for the CFD simulation using image analysis software (two-blade paddle), Re = $2.08*10^4$, cf. Figure (6.5). Note that (b) is the negative of (a), to show more details.

- **Flow Number**

Dimensionless discharge or flow number (*Fl*) is another technique used to validate the CFD hydrodynamic results. The flow number is a measure of the pumping capacity of the impeller. In order to calculate the flow number, the radial velocity profile of the impeller is needed to calculate the discharge flow of the impeller as follows:

$$Q = 2\pi r_s \int_{Z_1}^{Z_2} v_r dZ \qquad (6.1)$$

the parameters of the above equation are defined in Figure (6.16).

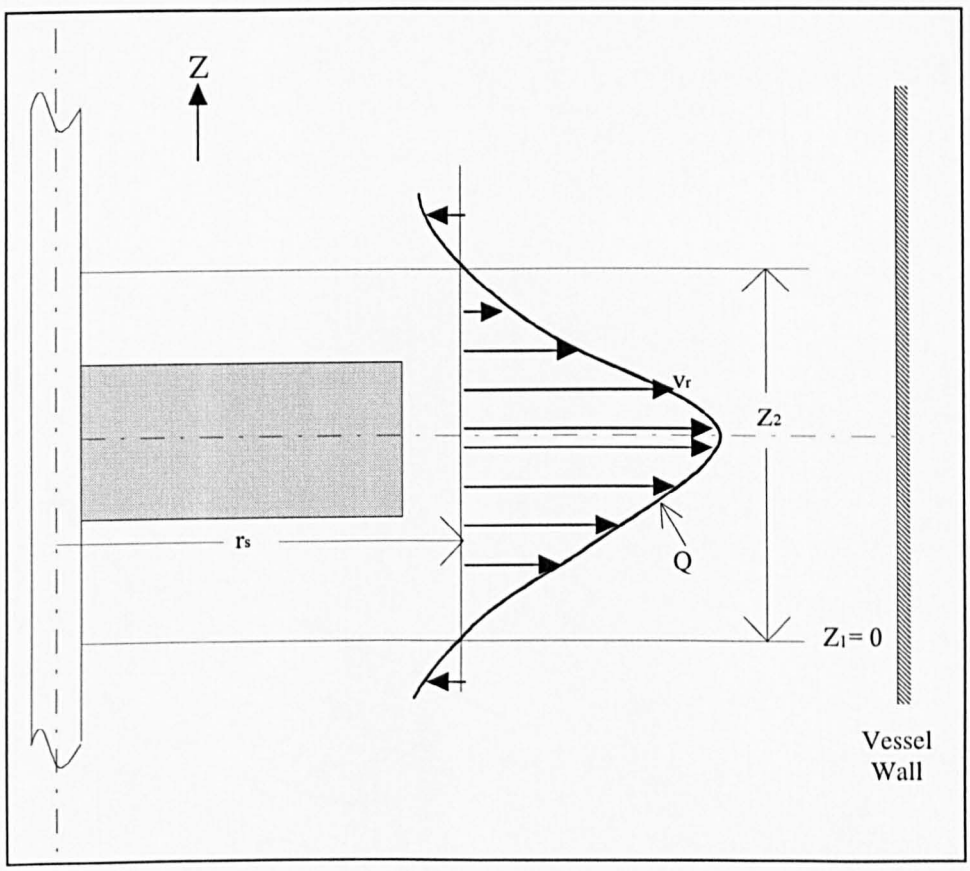

Figure (6.16): Schematic diagram to show the different parameters of equation (6.1).

However, there are some other correlations to estimate the Q values, e.g. Uhl and Gray (1966); Desouza and Pike (1972); Gunkel and Weber (1975) and Koutsakos *et al.* (1990).

Then, the flow number can be calculated as:

$$Fl = \frac{Q}{ND^3} \tag{6.2}$$

Figures (6.17) and (6.18) demonstrates the CFD results of the radial velocity 2 mm away from the tip of the impeller, in the radial direction. Different radial positions have no significant influence on the flow number. The integration on the right-hand side of equation (6.1) can be calculated subsequently as the area under the upper parts of the curves in Figures (6.17) and (6.18).

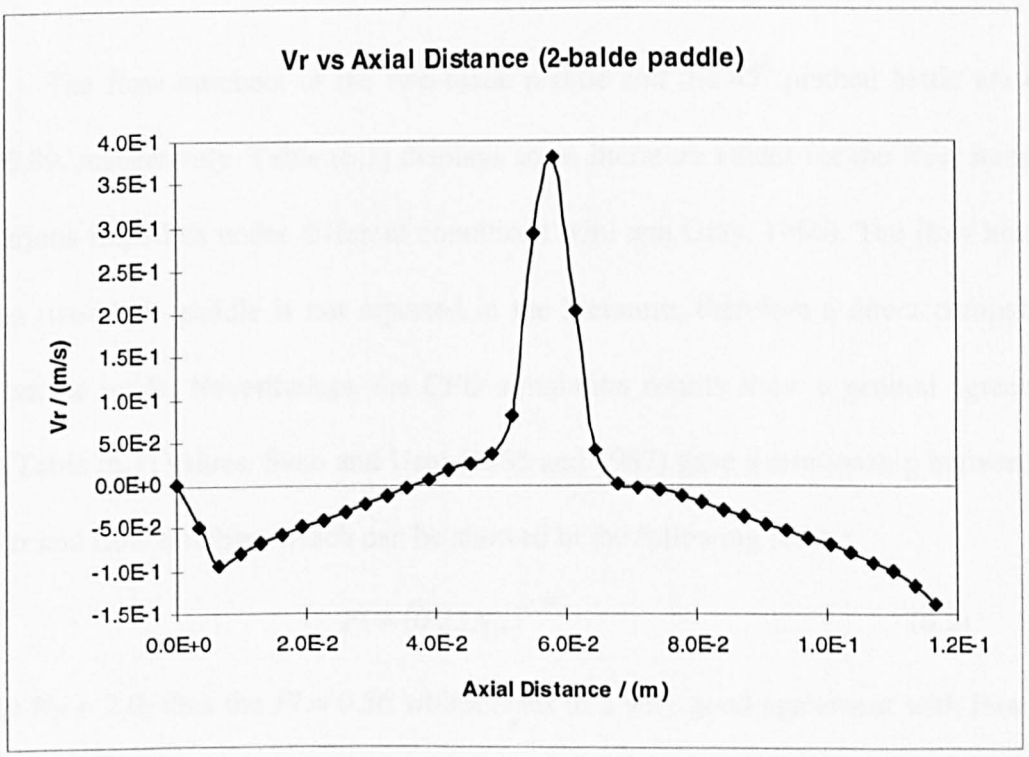

Figure (6.17): Radial velocity profile 2 mm away from the blade the two-blade paddle.

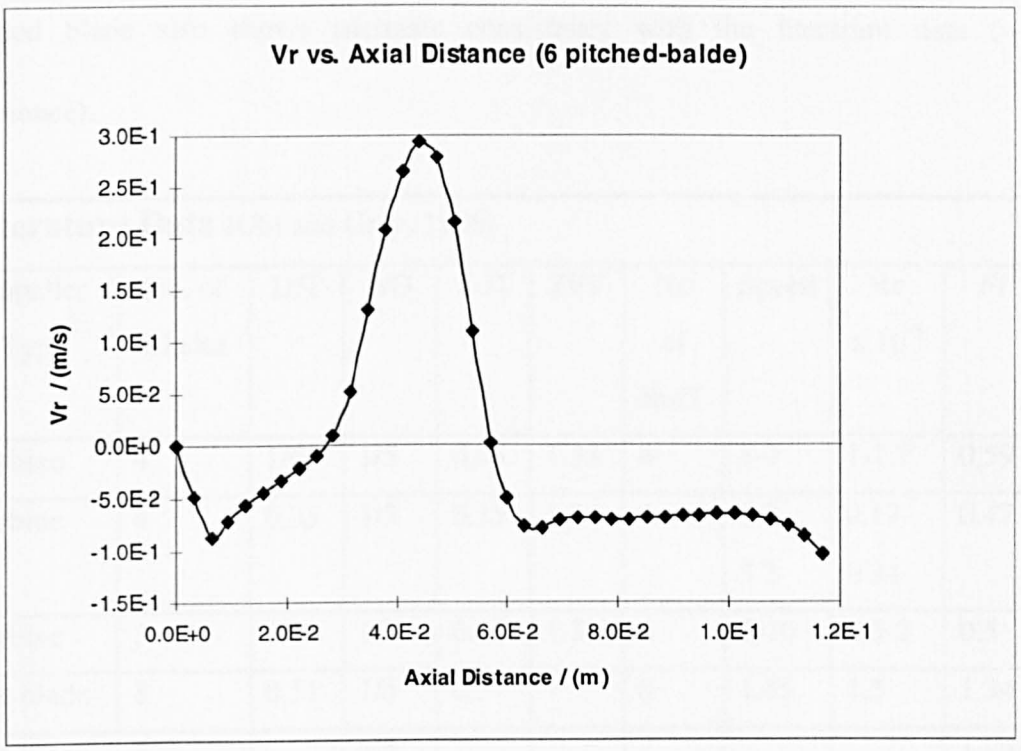

Figure (6.18): Radial velocity profile 2 mm away from the impeller blade of the 45° pitched blade.

The flow numbers of the two-blade paddle and the 45° pitched blade are 0.61 and 0.89, respectively. Table (6.1) displays some literature values for the flow numbers of various impellers under different conditions (Uhl and Gray, 1966). The flow number of the two-blade paddle is not reported in the literature, therefore a direct comparison can not be made. Nevertheless, the CFD simulation results show a general agreement with Table (6.1) values. Sano and Usui (1985 and 1987) gave a relationship between the power and flow numbers which can be showed in the following form:

$$Fl = \left(0.23 N_P\right)^{0.75} \qquad (6.3)$$

Since N_P = 2.0, thus the Fl = 0.56 which leads to a very good agreement with less than 9% difference between the CFD and literature results for the two blade paddle. The

pitched blade also shows adequate consistency with the literature data (≈12% difference).

Literature Data (Uhl and Gray, 1966)									
Impeller Type	No. of Blades	D/T	b/D	Zi/T	Zl/T	No of Baff'	Speed	Re x 10^{-5}	*Fl*
Turbine	4	1/6	1/5	0.45	1.33	4	5-7	1-1.7	0.59
Turbine	4	0.35	1/5	0.35	1.04	4	1.7-3.3	0.17-0.34	0.47
Turbine	3	1/6	1/5	0.45	1.33	4	6-10	1.5-2	0.5
Flat blade	8	0.51	1/5	0.5	1	8	1.45	1.3	1.34
Flat blade	8		1/5			?			1.25
Pitched blade	8	0.51	0.14	0.50	1	8		1.3	0.87
Pitched blade	8		0.14						1.0
CFD Simulation (this work)									
Flat blade	2	0.41	0.3	0.5	1	4	7.5	0.21	0.61
Pitched blade	6	0.41	0.21	0.5	1	4	7.5	0.21	0.89

Table (6.1): A comparison of flow numbers from the literature and CFD simulation.

6.3. Chemical Kinetics and Precipitation Process Simulation

This section describes a 2-D CFD simulation of the chemical kinetics and precipitation process. The 2-D representation (see Appendix 4) is chosen to test the validity of the model in a practical way, since the model has many parameters which make the 3-D option currently unfeasible with the presently provided computing facilities. The flow pattern of each 2-D case is shown in Appendix (5).

6.3.1. 1 rpm (Re = 46)

This laminar model is run for a real time of approximately 30 s and 200 hrs CPU time. Figures (6.19) to (6.22) illustrate the supersaturation shaded contours. (Note: the RHS of the C/L in the vessel is used in all illustrations). For computational reasons, this simulation considers 1 rpm (Re = 46) as an approximation to a stagnant flow, i.e. purely mass transfer.

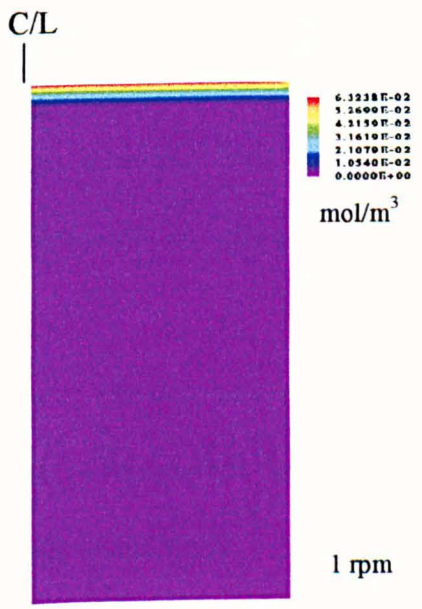

Figure (6.19): Supersaturation at t = 0.7 s.

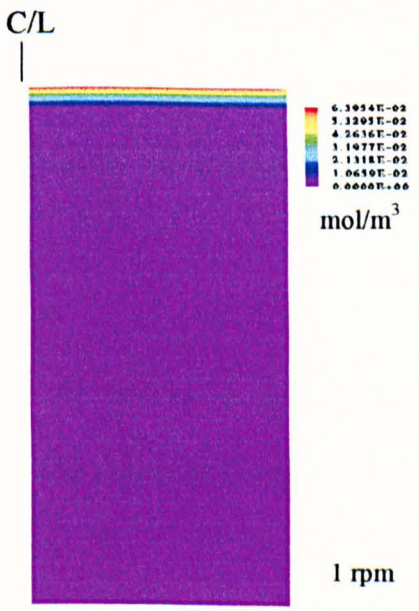

Figure (6.20): Supersaturation at t = 6.9 s.

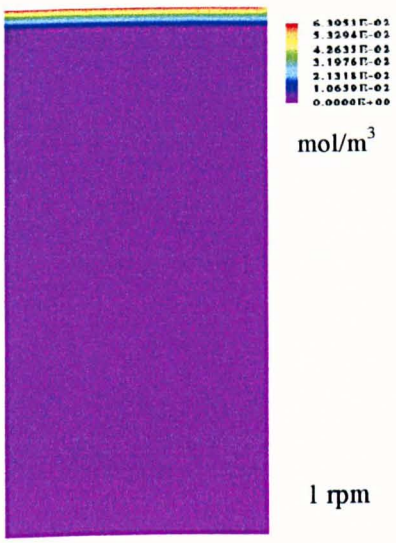

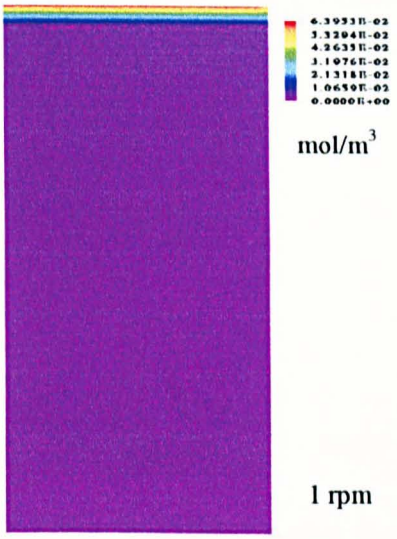

Figure (6.21): Supersaturation at t = 14.4 s. Figure (6.22): Supersaturation at t = 30.3 s.

As a result of the reaction, which *mainly* takes place in the interfacial region (i.e. the reaction not only can be initiated at the surface but also in the bulk of the vessel), calcium carbonate is produced and as the reaction proceeds and its concentration increases. Once the $CaCO_3$ concentration reaches the supersaturation region the simulation starts to calculate supersaturation. As shown above, the supersaturation stays at the interface for the whole given time. This explains that the process is mass diffusion controlled and possibly after a long time the supersaturation levels will gradually stretch out of the occupied region.

As the supersaturation comes into action, the nucleation will exist. Figures (6.23) to (6.26) present the mode of the nucleation rate which follows the same pattern of the supersaturation.

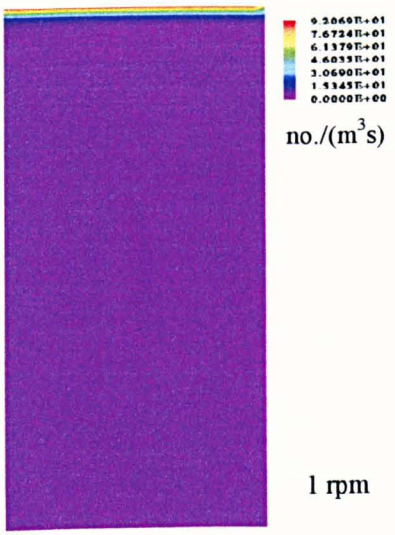

Figure (6.23): Nucleation rate at t = 0.7 s.

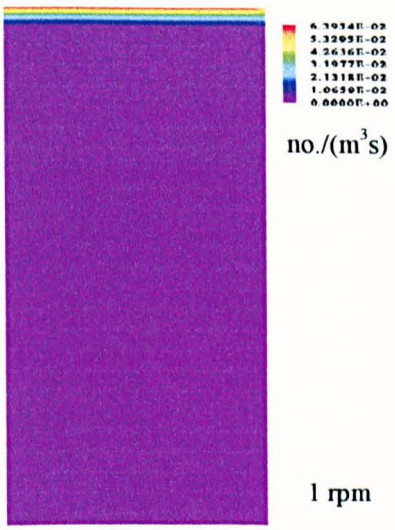

Figure (6.24): Nucleation rate at t = 6.9 s.

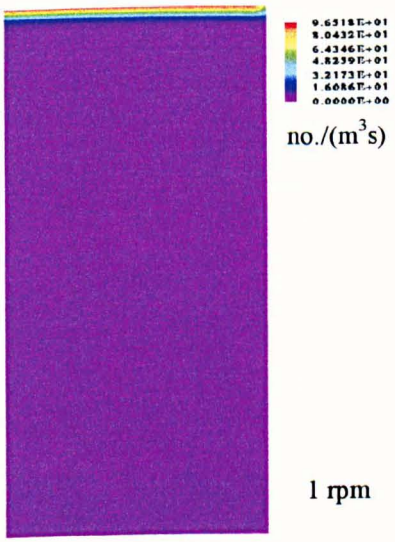

Figure (6.25): Nucleation rate at t = 14.4 s.

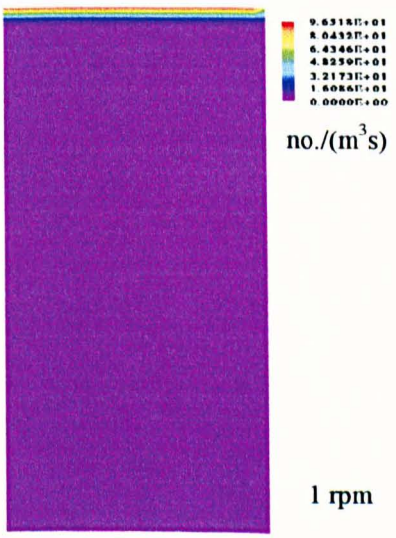

Figure (6.26): Nucleation rate at t = 30.3 s.

Similarly, the crystal growth rate also follows the supersaturation in same manner, which is illustrated by Figures (6.27) to (6.30).

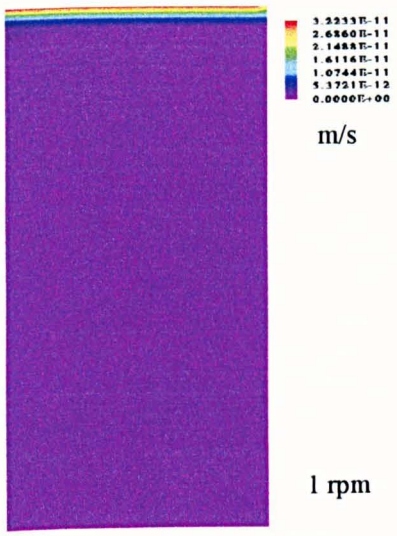

Figure (6.27): Growth rate at t = 0.7 s.

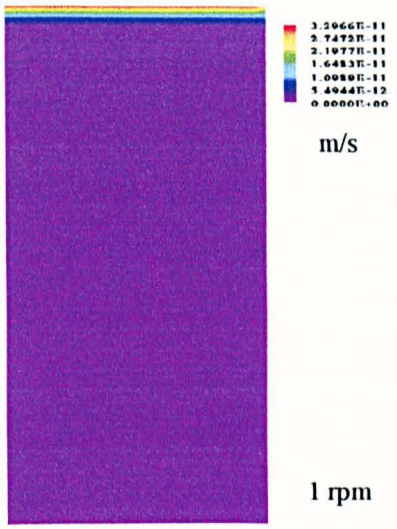

Figure (6.28): Growth rate at t = 6.9 s.

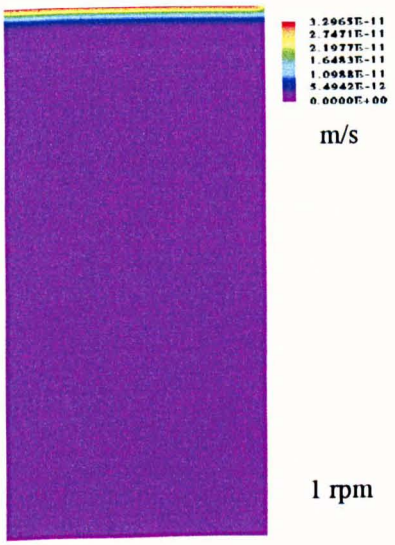

Figure (6.29): Growth rate at t = 14.4 s.

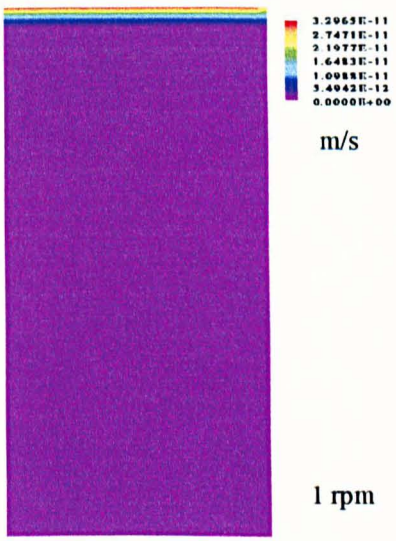

Figure (6.30): Growth rate at t = 30.3 s.

Since supersaturation, nucleation and growth rate are computed, moments can be introduced as explained earlier. The zeroth moment, which is a presentation of the total number of particles produced in the system, is displayed at different times in Figures (6.31) to (6.34).

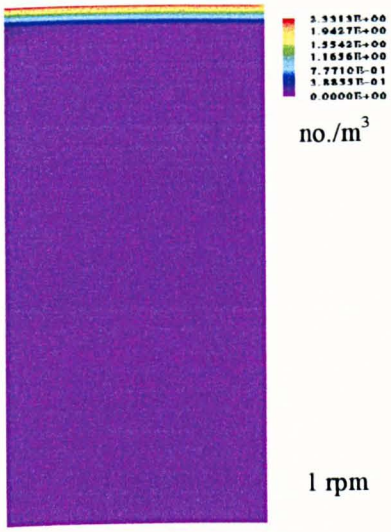

Figure (6.31): M_0 at t = 0.7 s.

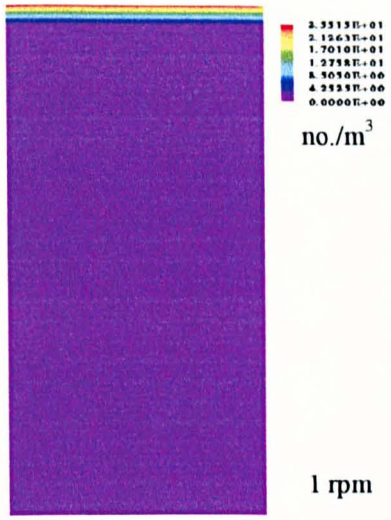

Figure (6.32): M_0 at t = 6.9 s.

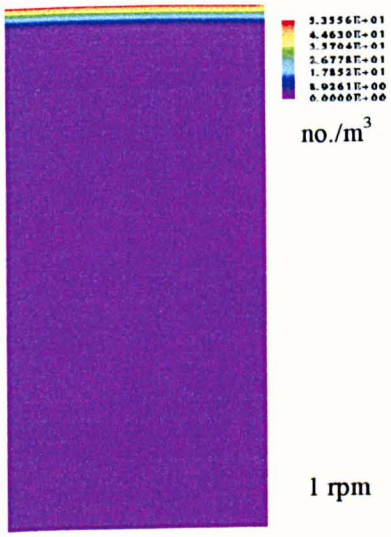

Figure (6.33): M_0 at t = 14.4 s.

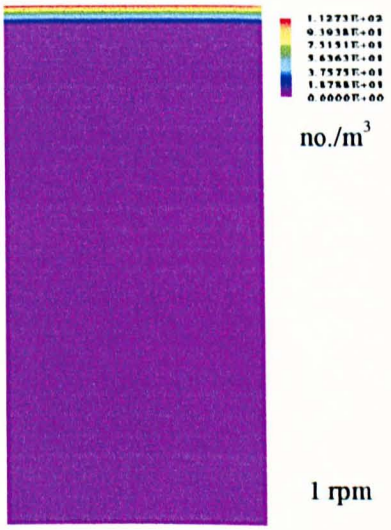

Figure (6.34): M_0 at t = 30.3 s.

Likewise, the trend of behaviour of the first and second moments, which are measures of the total length and surface area of the particles, respectively. Figures (6.35) to (6.38) manifest the first moment and Figures (6.39) and (6.40) reveal the second moment. On the other hand, the change of third moment values is too small, hence CFX does not show it in a graphical presentation.

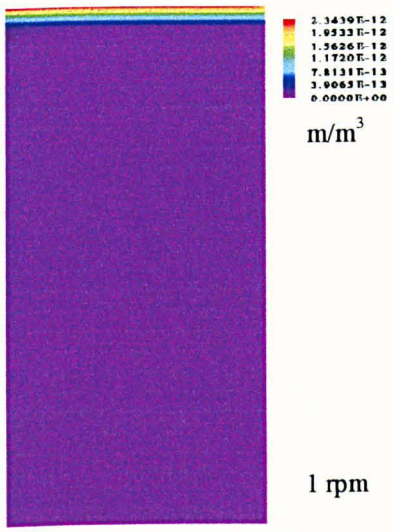

Figure (6.35): M_1 at t = 0.7 s.

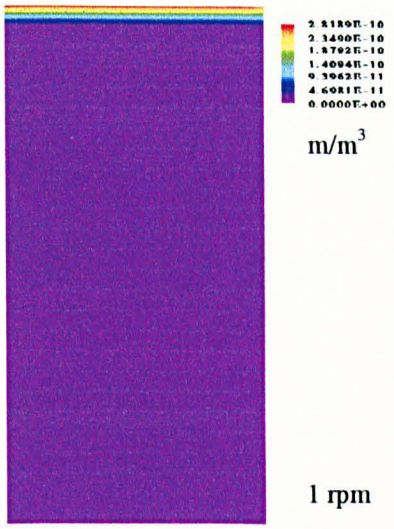

Figure (6.36): M_1 at t = 6.9 s.

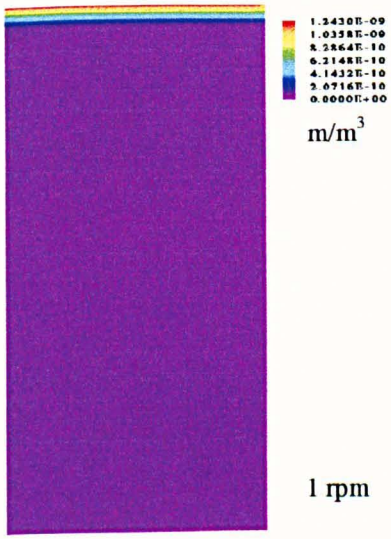

Figure (6.37): M_1 at t = 14.4 s.

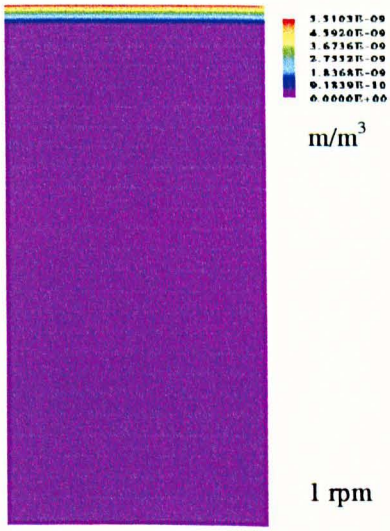

Figure (6.38): M_1 at t = 30.3 s.

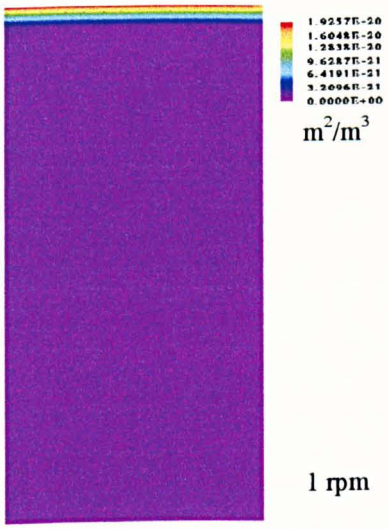

Figure (6.39): M_2 at t = 14.4 s.

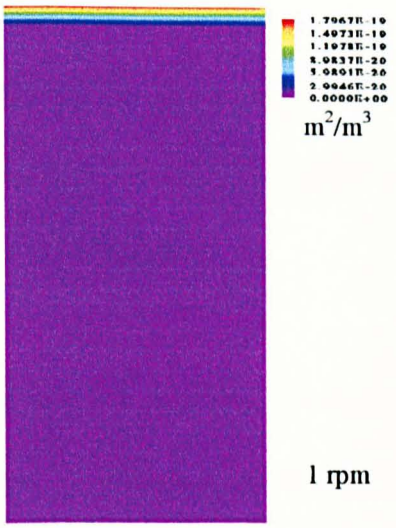

Figure (6.40): M_2 at t = 30.3 s.

6.3.2. 100 rpm (Re = $4.6*10^3$), Laminar Flow

This model applies a higher stirrer speed (100 rpm) to give a Re number $4.6*10^3$ which is neither fully developed laminar nor turbulent. To study the effect of both phenomena, the flow is defined as laminar and later as turbulent.

The laminar model gives a similar fashion as the 1 rpm (Re = 46) where the product stays at the interfacial region for a long time. Nevertheless, the values of all the parameters are higher than those of the previous stirrer speed. This declares the effect of the hydrodynamic represented by higher values of velocity vectors which remove (wash-out) the product from the interface in a faster rate. Hence, fresh reactants will be provided to allow further reaction. Figures (6.41) to (6.44) represent the supersaturation levels which reach a maximum local value of 0.101 mol/m^3 compared with 0.063 mol/m^3 from the previous system.

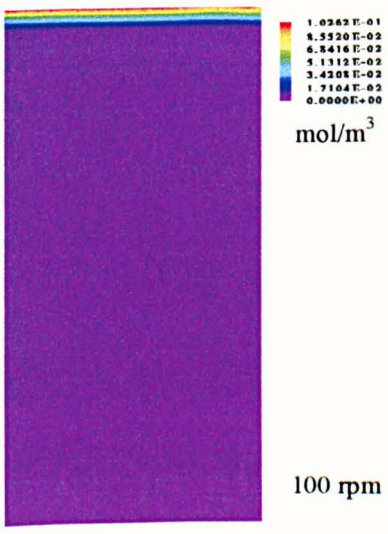

Figure (6.41): Supersaturation at t = 2.0 s.

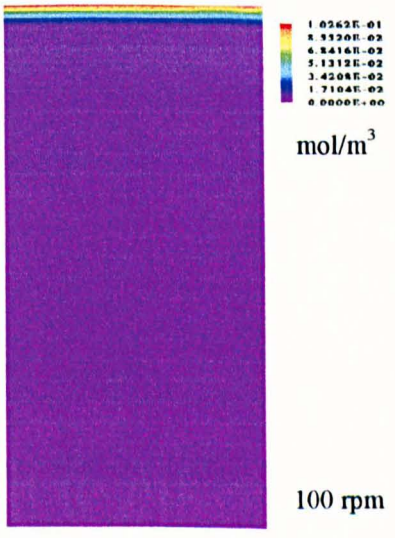

Figure (6.42): Supersaturation at t = 12.4 s.

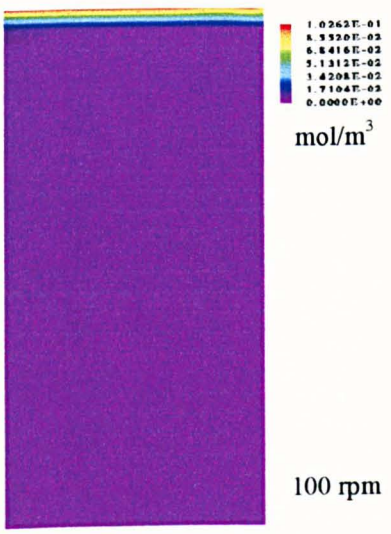

Figure (6.43): Supersaturation at t = 17.8 s.

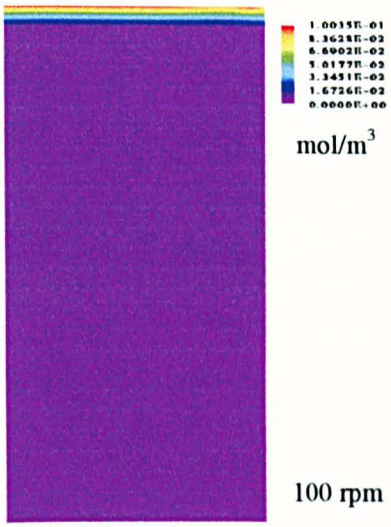

Figure (6.44): Supersaturation at t = 30.1 s.

Nucleation rate maximum local values also increases from ~96 (m^{-3} s^{-1}) for Re = 46 to ~700 (m^{-3} s^{-1}) or Re = $4.6*10^3$, Figures (6.45) to (6.48).

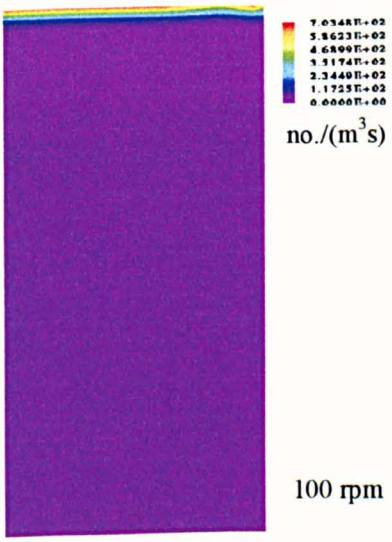

Figure (6.45): Nucleation rate at t = 2.0 s.

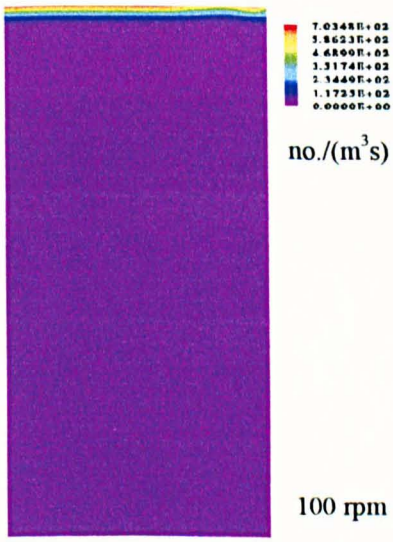

Figure (6.46): Nucleation rate at t = 12.4 s.

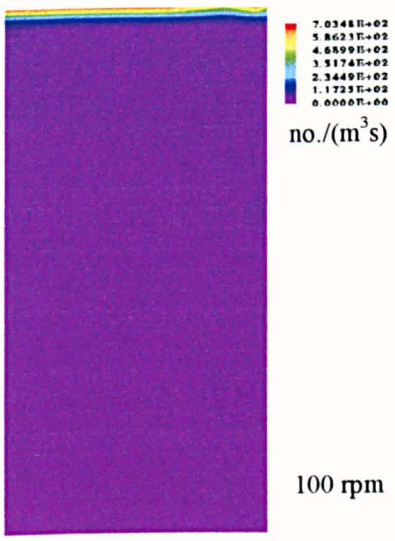

Figure (6.47): Nucleation rate at t = 17.8 s.

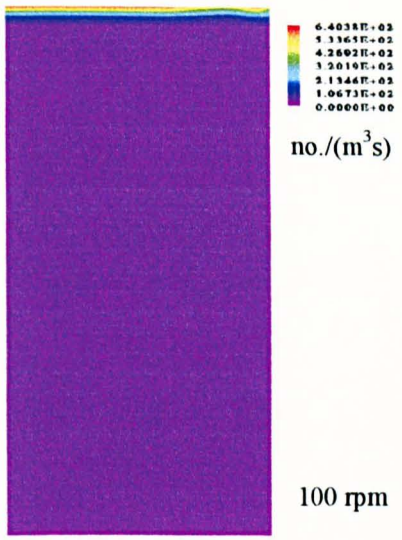

Figure (6.48): Nucleation rate at t = 30.1 s.

Crystal growth rate, Figures (6.49) to (6.52), is influenced by the supersaturation changes. CFD simulation local maximum values for the growth rate varies from ~3.2 $*10^{-11}$ (m/s) to 8.4$*10^{-11}$ (m/s) for Re = 46 and 4.6$*10^{3}$, respectively.

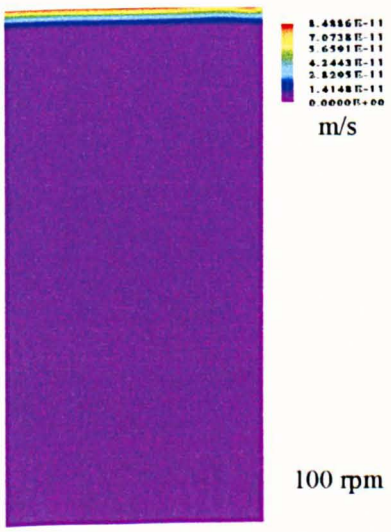

Figure (6.49): Growth rate at t = 2.0 s.

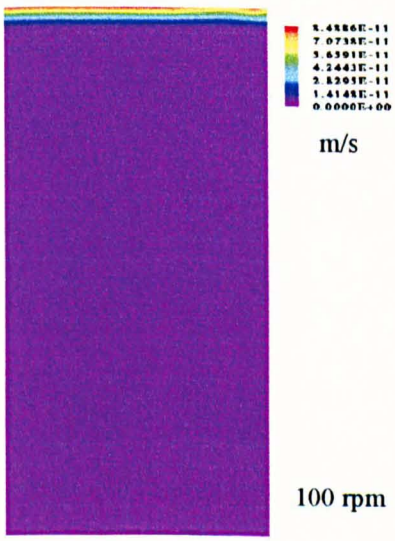

Figure (6.50): Growth rate at t = 12.4 s.

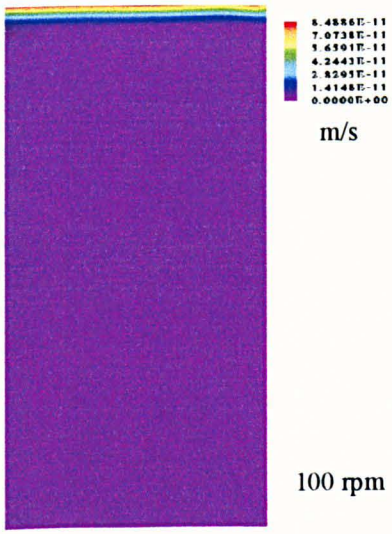

Figure (6.51): Growth rate at t = 17.8 s.

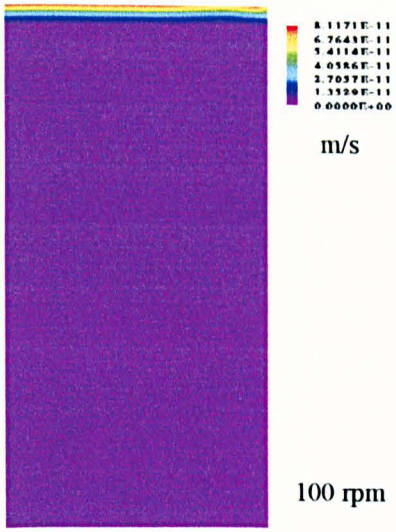

Figure (6.52): Growth rate at t = 30.1 s.

In the same way, M_0, M_1 and M_2 give higher local values for the higher Re number system, see Figures (6.53) to (6.64). The third moment however can not be displayed graphically because it has too small values.

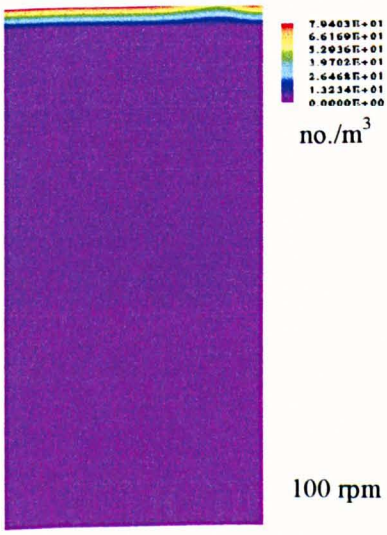

Figure (6.53): M_0 at t = 2.0 s.

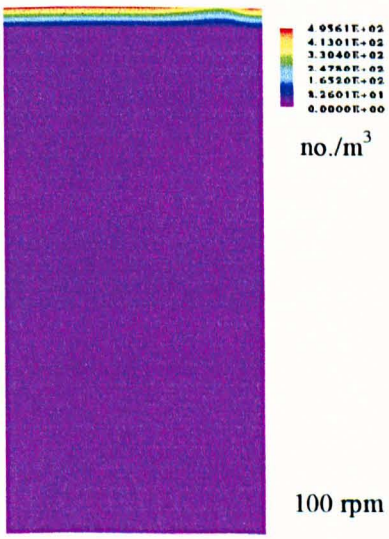

Figure (6.54): M_0 at t = 12.4 s.

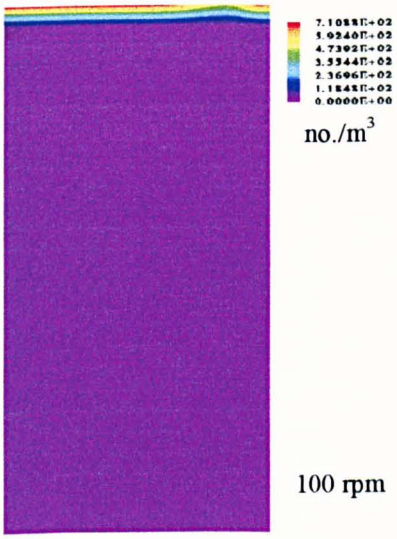

Figure (6.55): M_0 at t = 17.8 s.

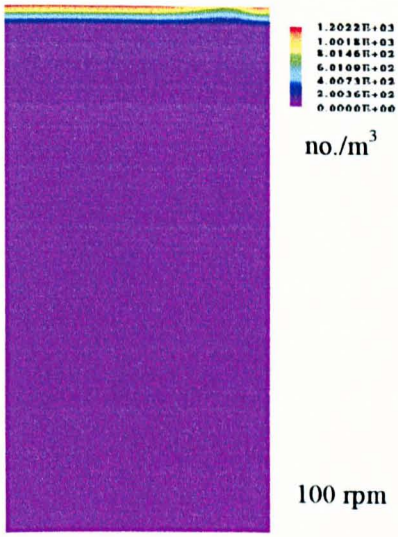

Figure (6.56): M_0 at t = 30.1 s.

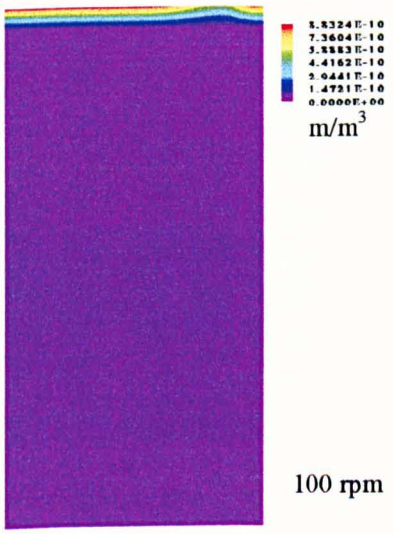

Figure (6.57): M_1 at t = 2.0 s.

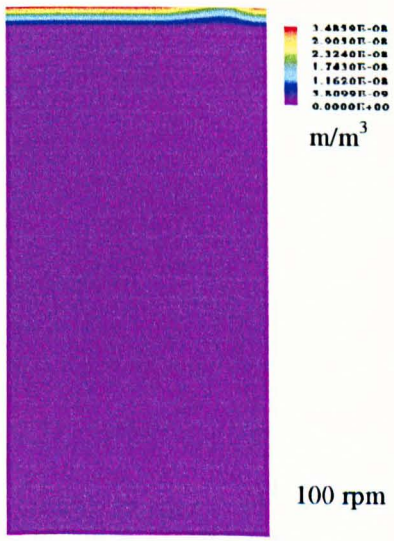

Figure (6.58): M_1 at t = 12.4 s.

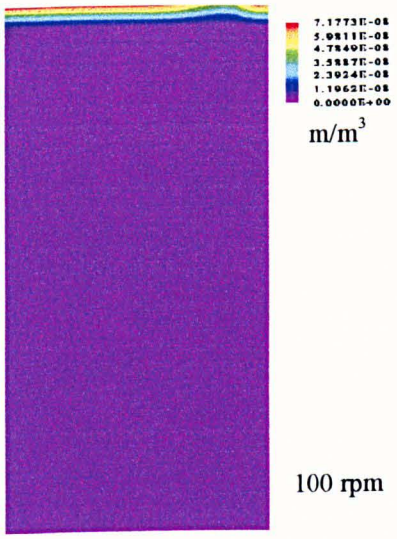

Figure (6.59): M_1 at t = 17.8 s.

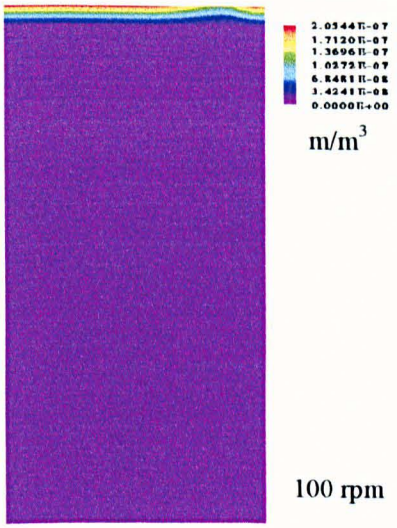

Figure (6.60): M_1 at t = 30.1 s.

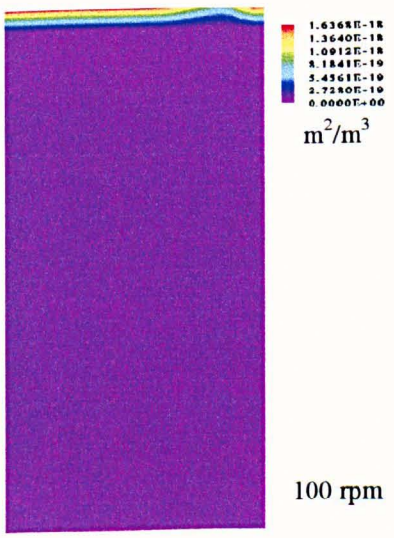

Figure (6.61): M_2 at t = 12.4 s.

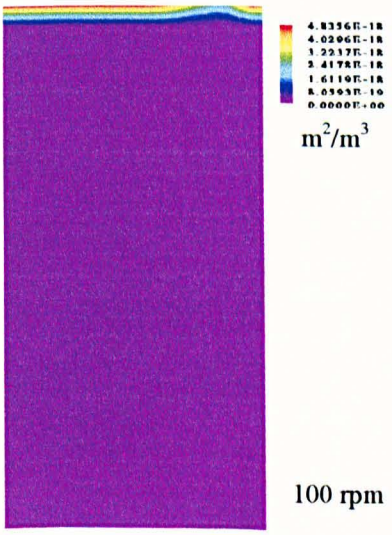

Figure (6.62): M_2 at t = 17.8 s.

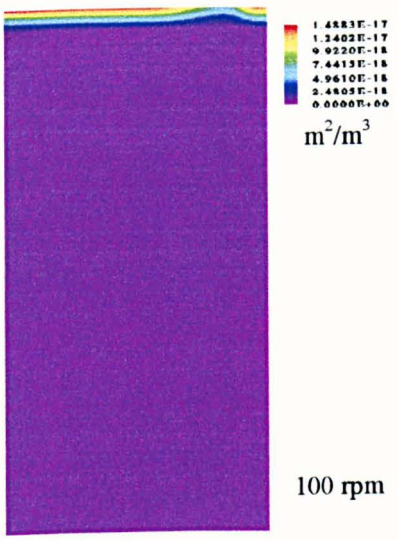

Figure (6.63): M_2 at t = 25.9 s.

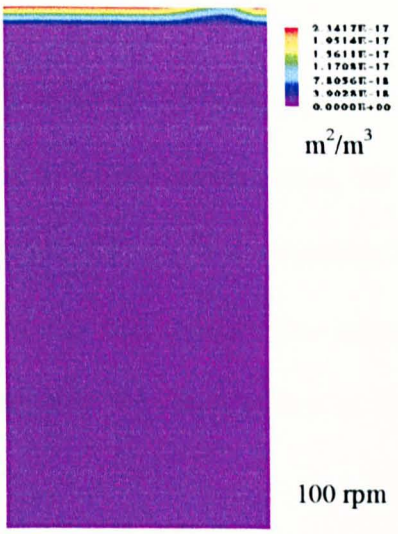

Figure (6.64): M_2 at t = 30.1 s.

At the interface, near the right top corner, there is a small region where the supersaturation, and therefore all the other parameters shown above, has lower local values than the other regions at the interface. Figure (6.65 b) shows speed vectors at that point where there is a very small reverse circulation loop at the top-right corner of the vessel and because of this split in the flow the speed reaches very small values. Hence, poor mixing is developed resulting in correspondingly lower levels of the supersaturation. A corresponding *inflection* is not seen at the C/L, however, there is only static point at the C/L axis.

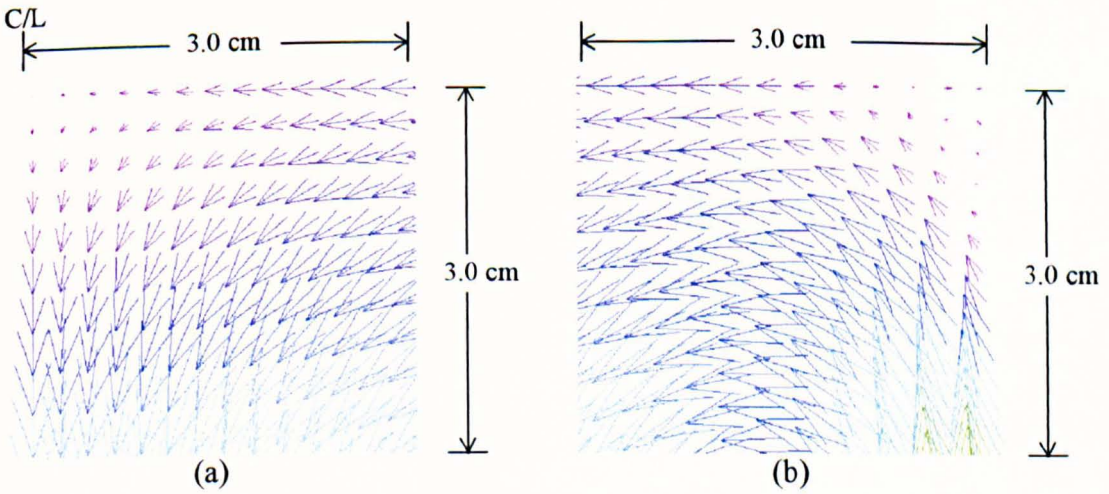

Figure (6.65): Speed vectors at the *top-left* and *right* corners of the vessel (100 rpm, laminar).

6.3.3. 100 rpm (Re = $4.6*10^3$), Turbulent Flow

In this simulation, the Reynolds differential stress model is utilised to describe the flow pattern behaviour in the vessel. In reactive precipitation processes, the extent of mixing is essential to bring the reactants in contact and enable the reaction to take place. Thus, introduction of turbulence in such systems will enhance the mixing and subsequently the precipitation process. The formation of the small eddies in the flow intensifies the micromixing process.

Altering the flow from laminar to turbulent in the CFD simulation influences the progress of the reaction significantly. Hence, the variation in the different parameters can be noticed in a short period of time, Figures (6.66) to (6.103).

The simulation is run for 500 hrs simulating approximately 5 s real time.

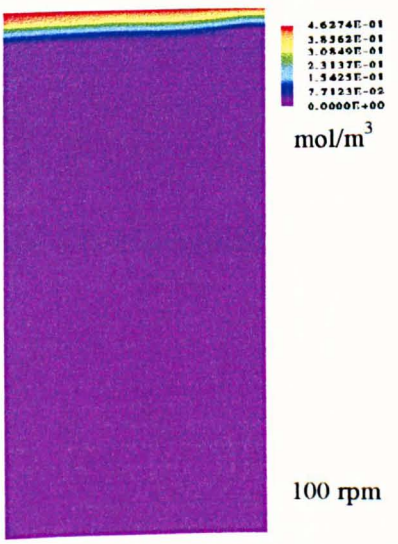

Figure (6.66): Supersaturation at t = 0.2 s.

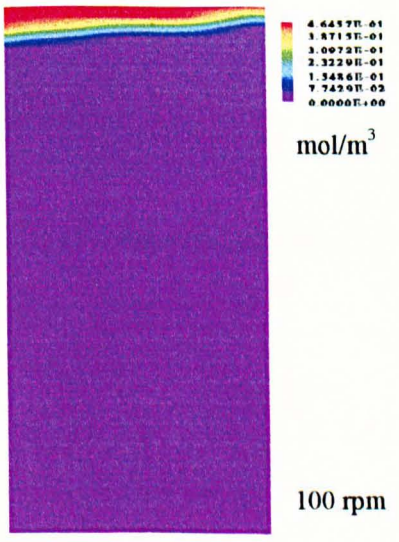

Figure (6.67): Supersaturation at t = 1.3 s.

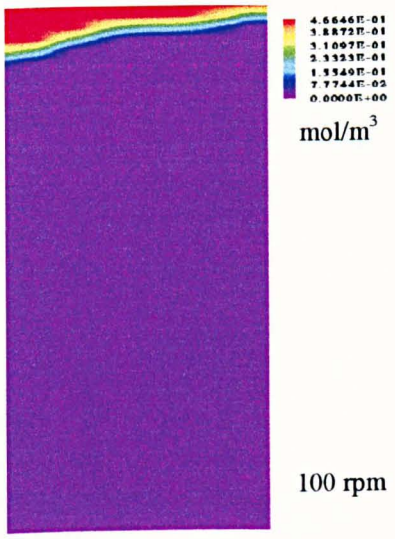

Figure (6.68): Supersaturation at t = 2.7 s.

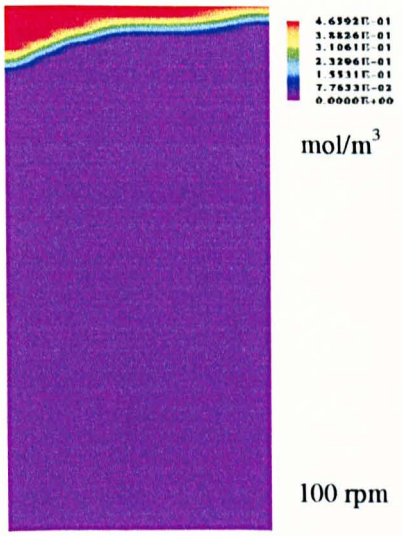

Figure (6.69): Supersaturation at t = 4.1 s.

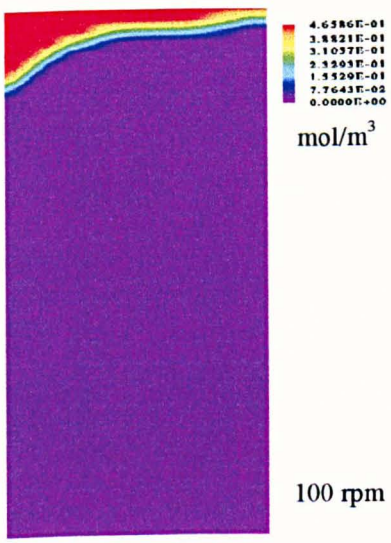

Figure (6.70): Supersaturation at t = 4.5 s.

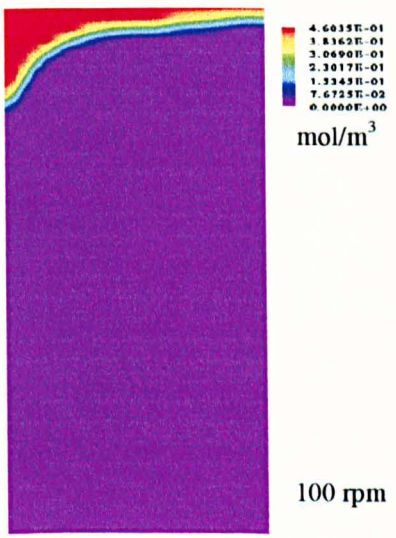

Figure (6.71): Supersaturation at t = 5.1 s.

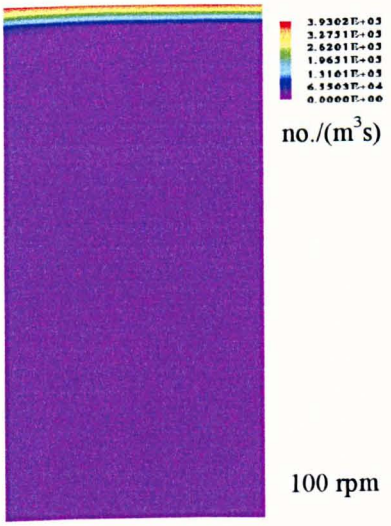

Figure (6.72): Nucleation rate at t = 0.2 s.

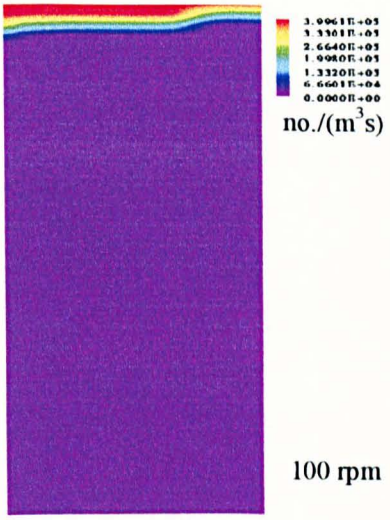

Figure (6.73): Nucleation rate at t = 1.3 s.

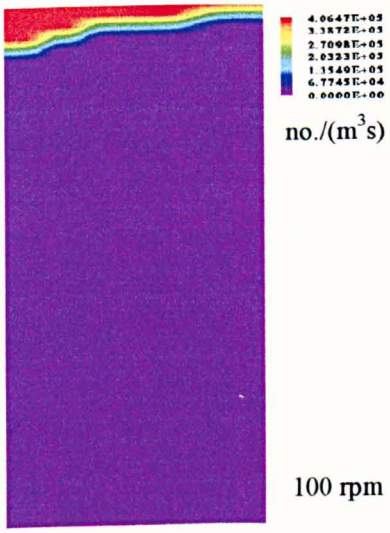

Figure (6.74): Nucleation rate at t = 2.7 s.

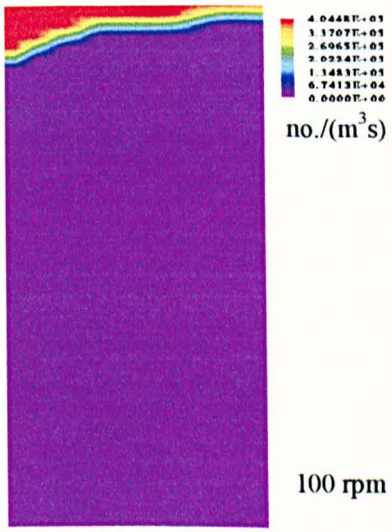

Figure (6.75): Nucleation rate at t = 4.1 s.

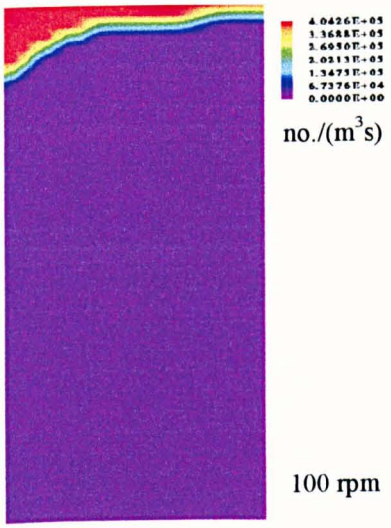

Figure (6.76): Nucleation rate at t = 4.5 s.

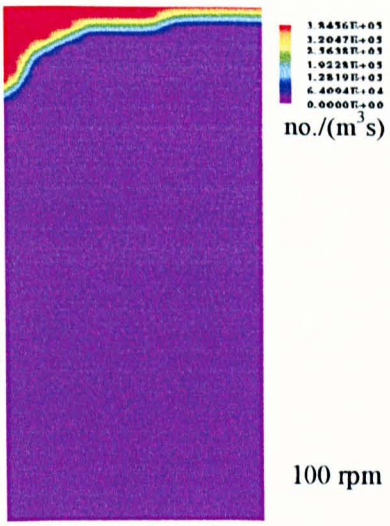

Figure (6.77): Nucleation rate at t = 5.1 s.

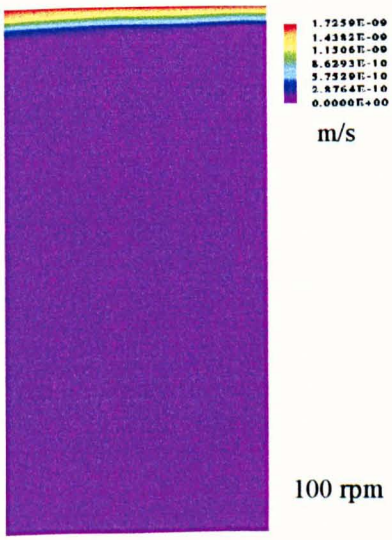

Figure (6.78): Growth rate at t = 0.2 s.

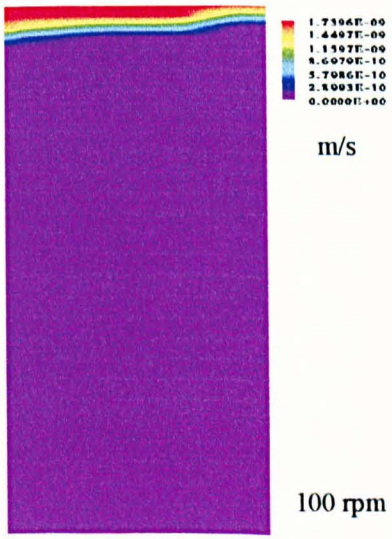

Figure (6.79): Growth rate at t = 1.3 s.

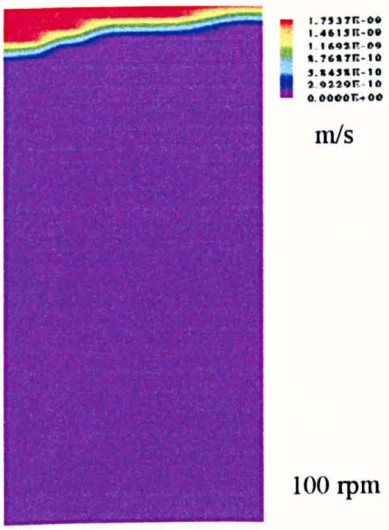

Figure (6.80): Growth rate at t = 2.7 s.

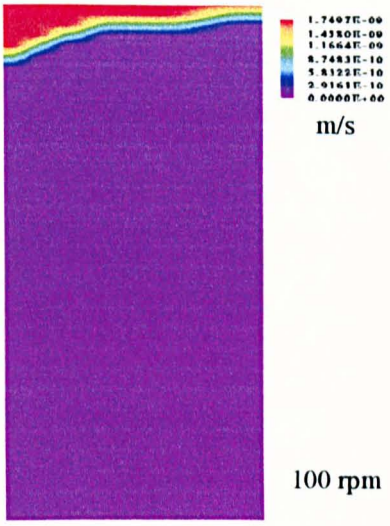

Figure (6.81): Growth rate at t = 4.1 s.

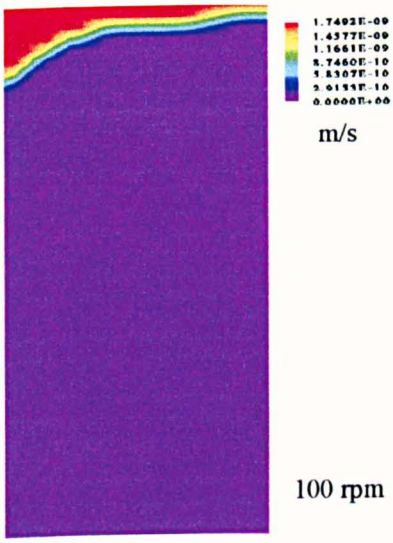

Figure (6.82): Growth rate at t = 4.5 s.

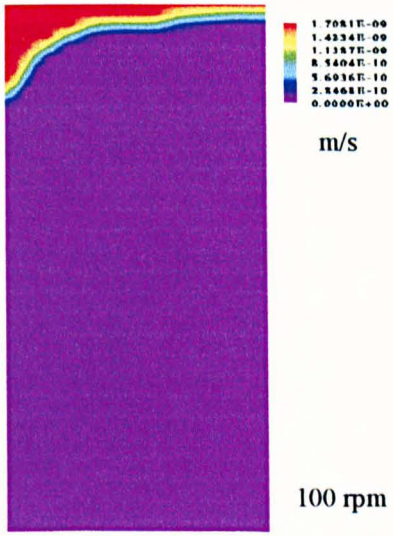

Figure (6.83): Growth rate at t = 5.1 s.

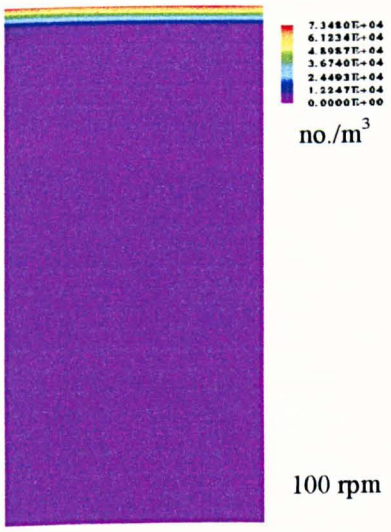

Figure (6.84): M_0 at t = 0.2 s.

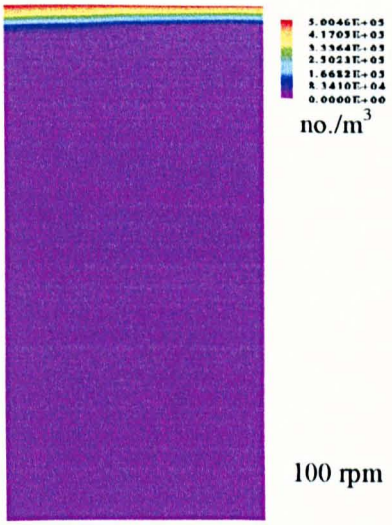

Figure (6.85): M_0 at t = 1.3 s.

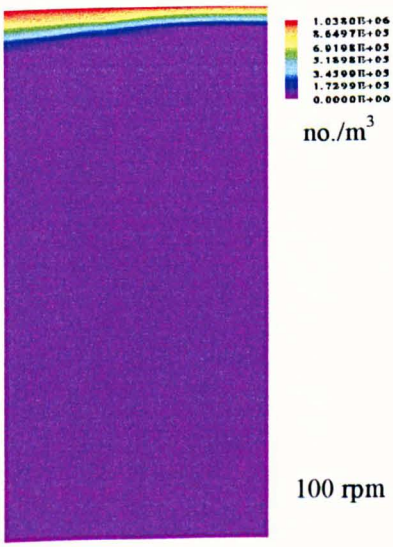

Figure (6.86): M_0 at t = 2.7 s.

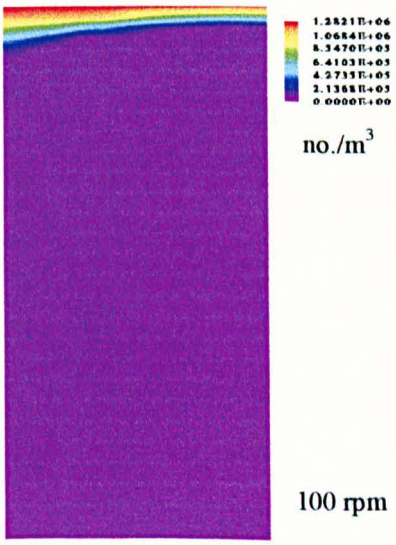

Figure (6.87): M_0 at t = 4.1 s.

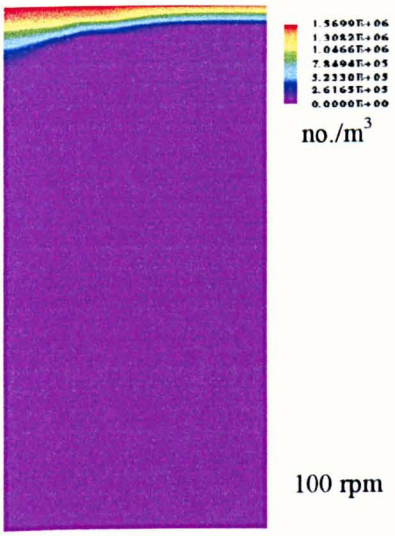

Figure (6.88): M_0 at t = 4.5 s.

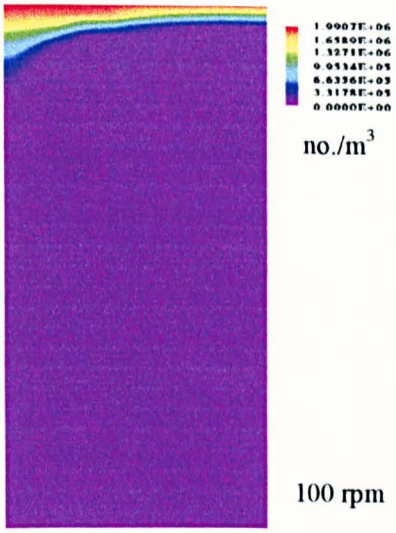

Figure (6.89): M_0 at t = 5.1 s.

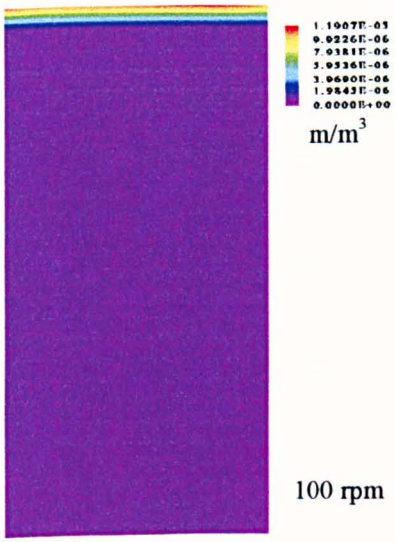

Figure (6.90): M_1 at t = 0.2 s.

Figure (6.91): M_1 at t = 1.3 s.

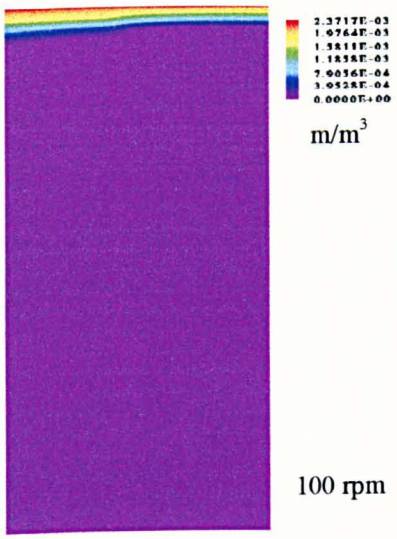

Figure (6.92): M_1 at t = 2.7 s.

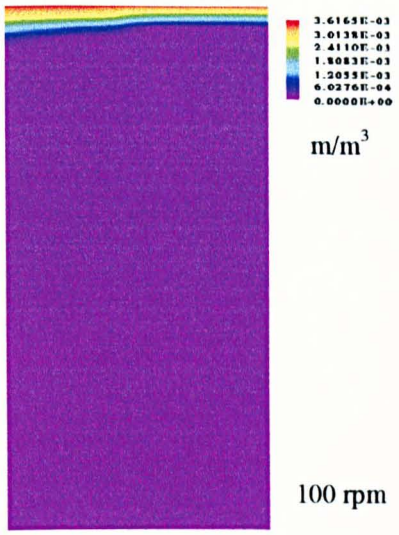

Figure (6.93): M_1 at t = 4.1 s.

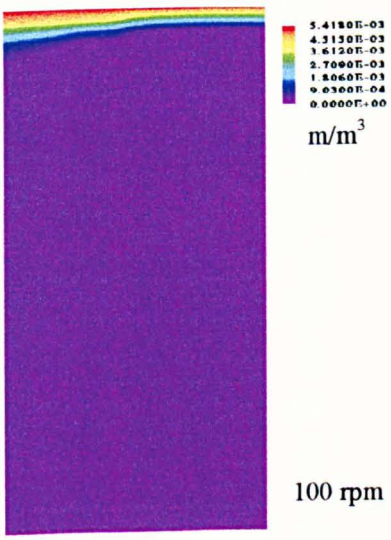

Figure (6.94): M_1 at t = 4.5 s.

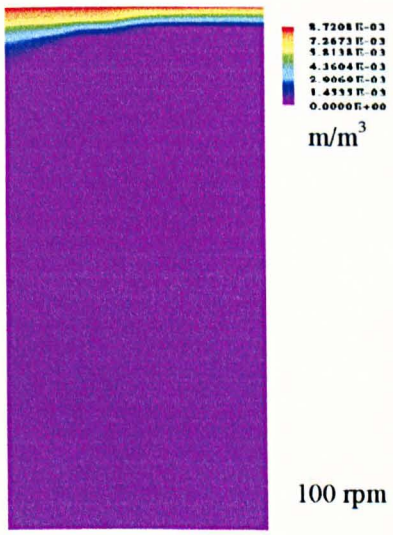

Figure (6.95): M_1 at t = 5.1 s.

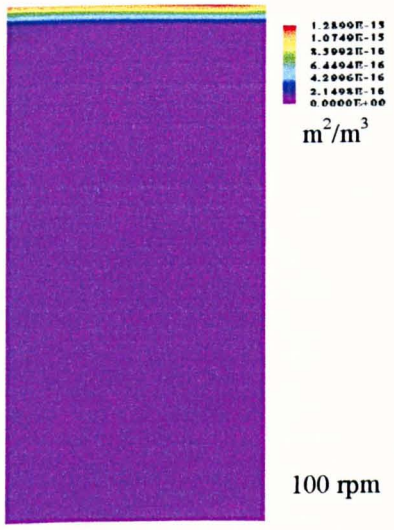

Figure (6.96): M_2 at t = 0.2 s.

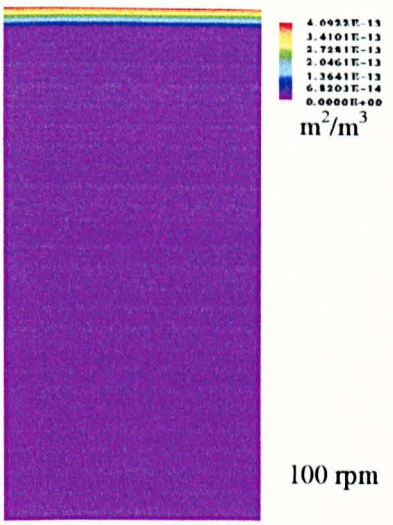

Figure (6.97): M_2 at t = 1.3 s.

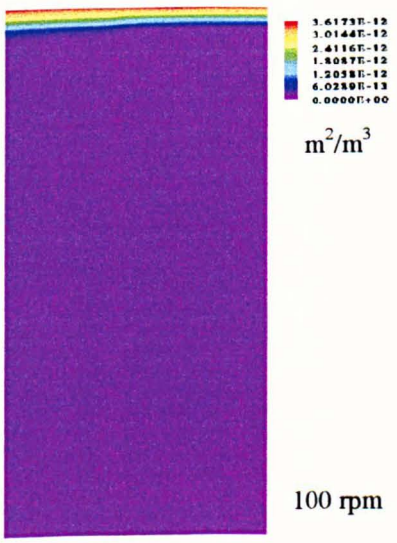

Figure (6.98): M_2 at t = 2.7 s.

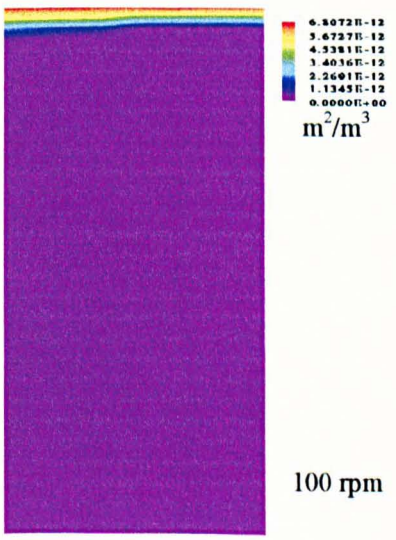

Figure (6.99): M_2 at t = 4.1 s.

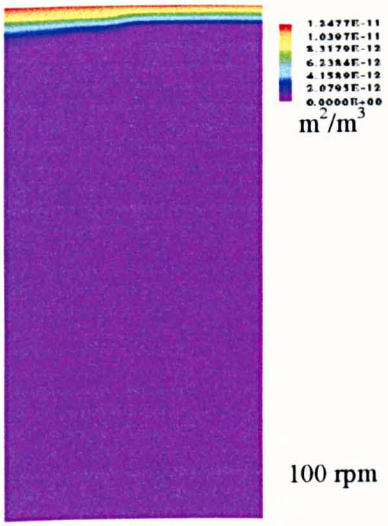

Figure (6.100): M_2 at t = 4.5 s.

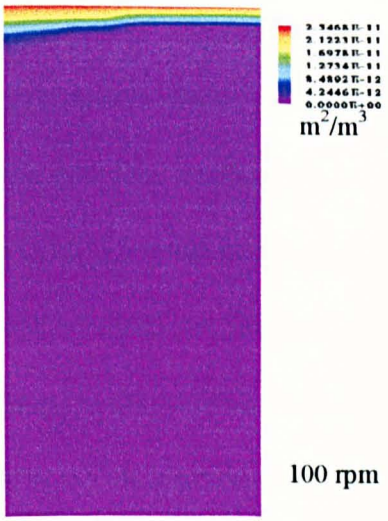

Figure (6.101): M_2 at t = 5.1 s.

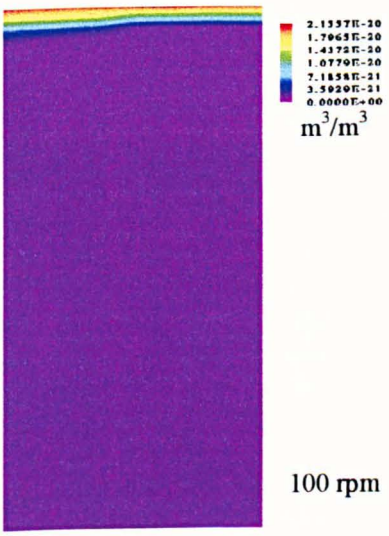

Figure (6.102): M_3 at t = 4.5 s.

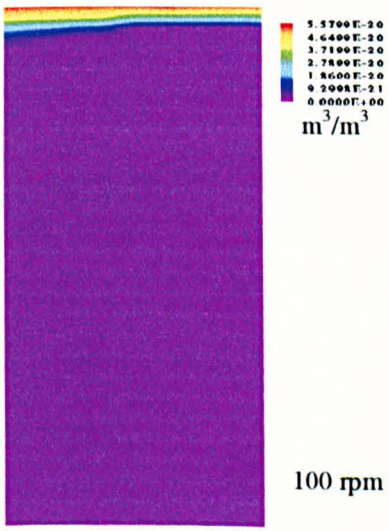

Figure (6.103): M_3 at t = 5.1 s.

The only difference between the previous simulation and this one is the presence of turbulence in the later. However, the change in the performance of the process is significant. The reaction is extended from the interface to the bulk of the liquid from the left hand side, which will be explained later.

6.3.4. 200 rpm (Re = $9.3*10^3$), Turbulent Flow

This system has an almost fully developed turbulent flow. As expected, the precipitation process proceeds even further than the previous systems (Re = 46 and $4.6*10^3$) for a given time. Nonetheless, the product ($CaCO_3$) tends to progress, into the bulk, from the left hand side following the speed vectors direction. Since the particles, under these conditions, are removed from (washed out of) the interface in a faster rate, the reaction will be supplied with more fresh reactants which improves the yield of the process. Figures (6.104) to (6.111) portray the supersaturation progress over time.

This model is run for 500 hrs to give real time of approximately 5 s.

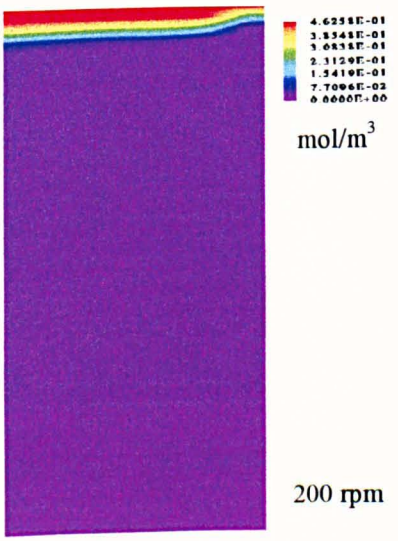

Figure (6.104): Supersaturation at t = 0.2 s.

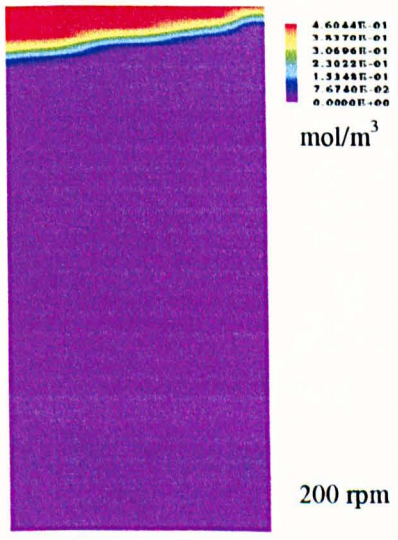

Figure (6.105): Supersaturation at t = 0.6 s.

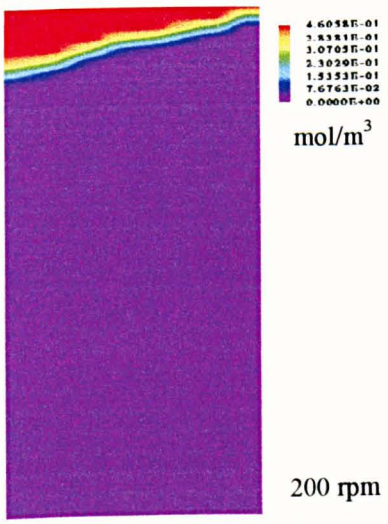

Figure (6.106): Supersaturation at t = 0.8 s.

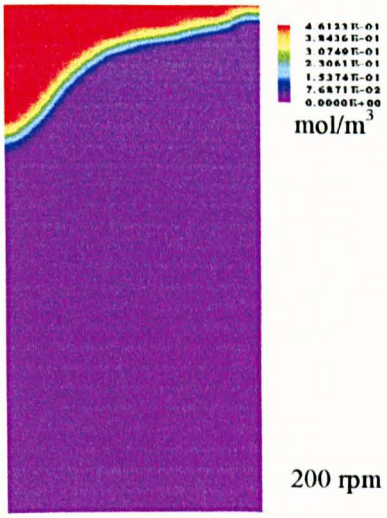

Figure (6.107): Supersaturation at t = 1.3 s.

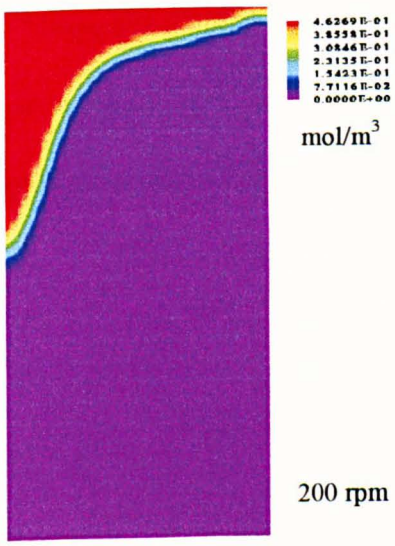

Figure (6.108): Supersaturation at t = 1.7 s.

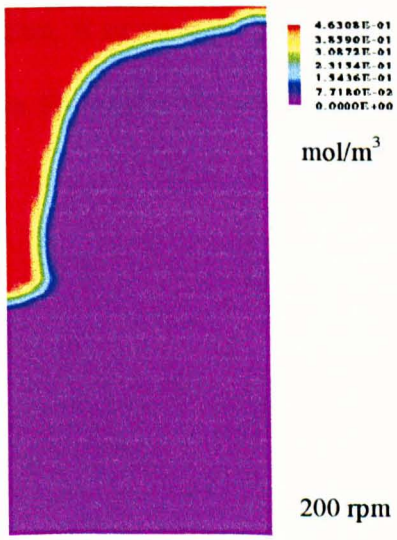

Figure (6.109): Supersaturation at t = 2.1 s.

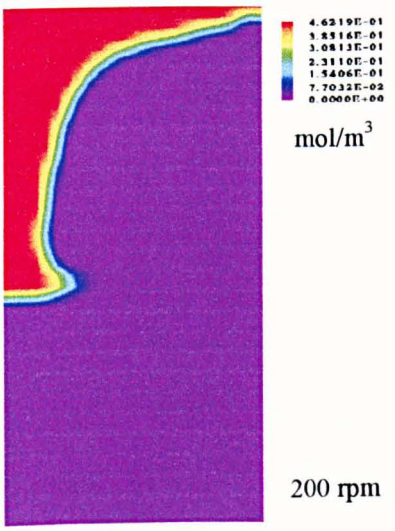

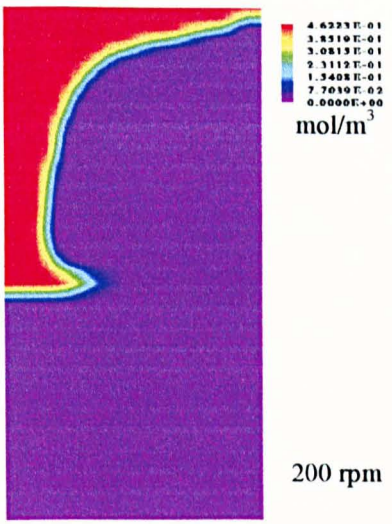

Figure (6.110): Supersaturation at t = 2.5 s. Figure (6.111): Supersaturation at t = 5.2 s.

When the product reaches the impeller region, it stops from progressing in the axial (downward) direction and starts to move in the radial direction following the outward flow pattern, Figure (6.112).

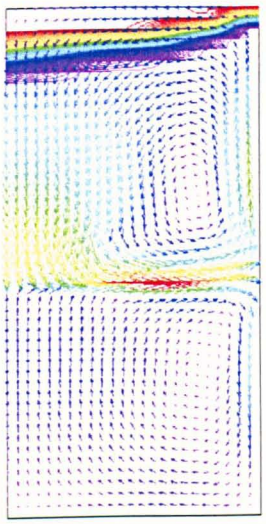

(a)

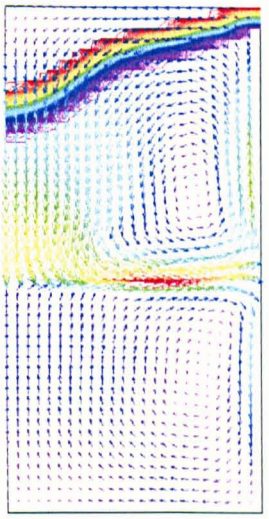

(b)

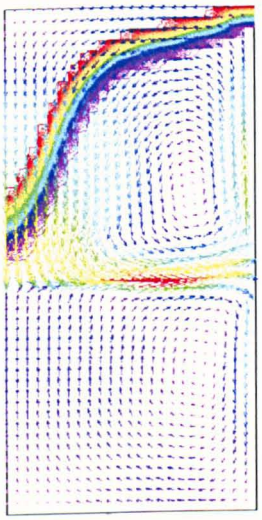

(c)

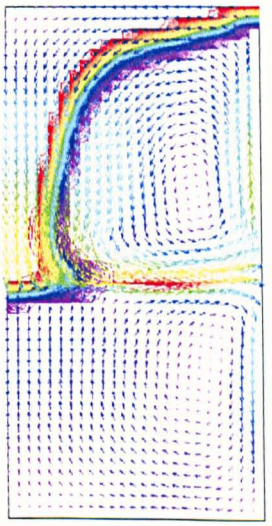

(d)

Figure (6.112): CFD images of speed vector (m/s) superimposed on supersaturation (mol/m^3) contours ($Re = 9.3*10^3$), for t = 0.6, 1.3, 1.7 and 5.2 s for a, b, c and d, respectively.

The nucleation rate local maximum value is ~ $3.9*10^5$ m^{-3} s^{-1} giving a higher rate than previous systems, see Figures (6.113) to (6.118).

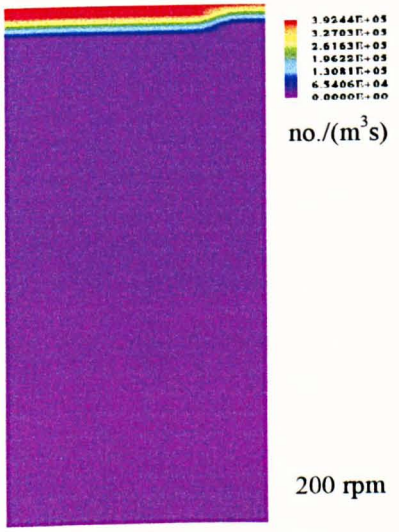

Figure (6.113): Nucleation rate at t = 0.2 s.

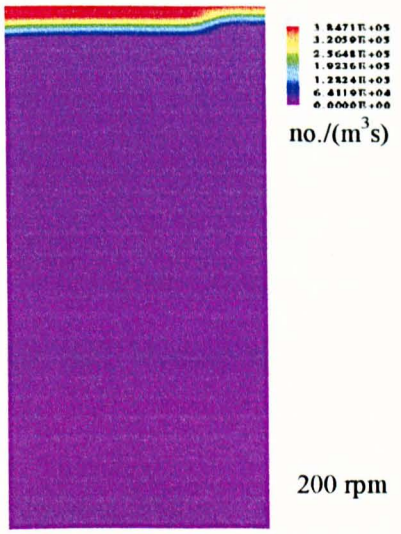

Figure (6.114): Nucleation rate at t = 0.3 s.

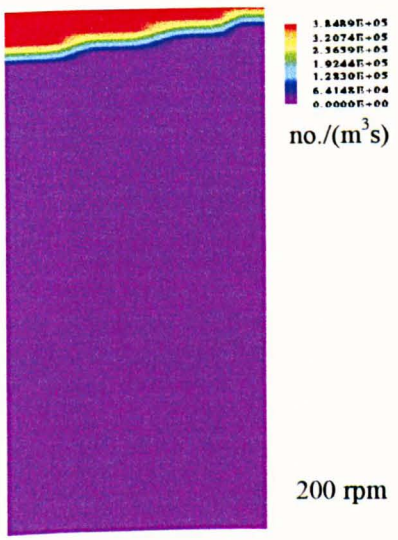

Figure(6.115): Nucleation rate at t = 0.6 s.

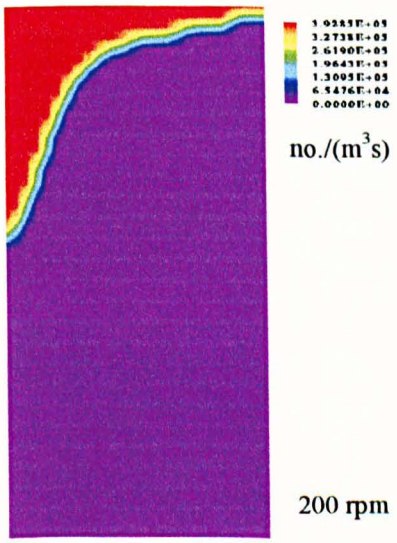

Figure(6.116): Nucleation rate at t = 1.7 s.

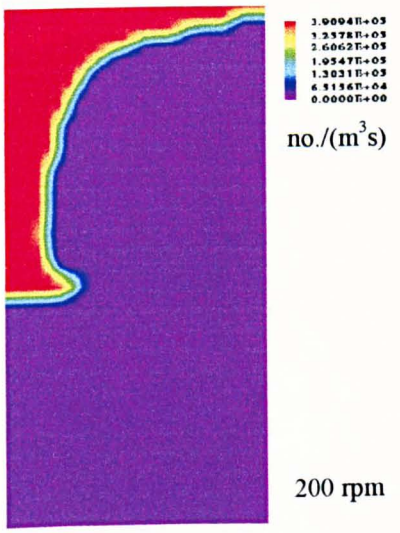

Figure(6.117): Nucleation rate at t = 3.5 s.

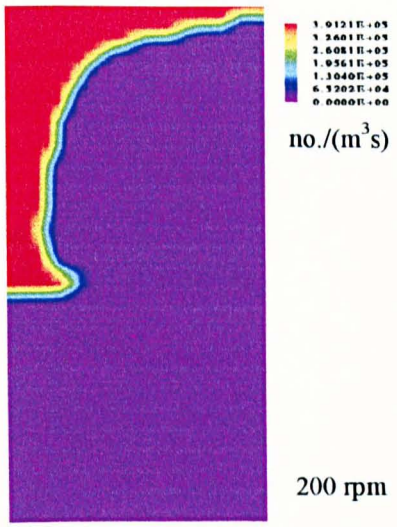

Figure(6.118): Nucleation rate at t = 5.2 s.

The crystal growth rate follows a similar pattern, Figures (6.119) to (6.124), with a maximum local value of ~ $1.7*10^{-9}$ m/s.

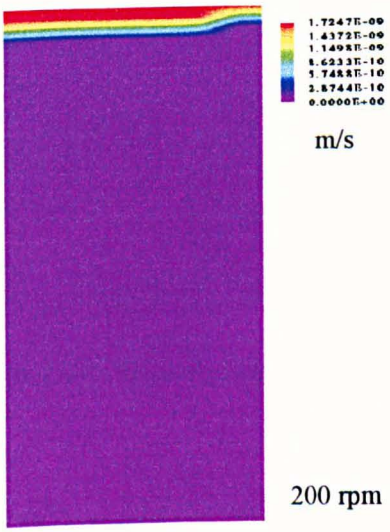

Figure(6.119): Growth rate at t = 0.2 s.

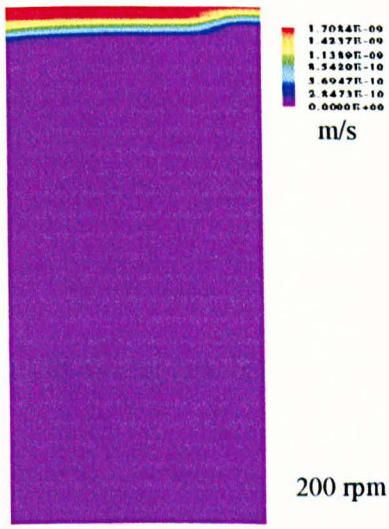

Figure(6.120): Growth rate at t = 0.3 s.

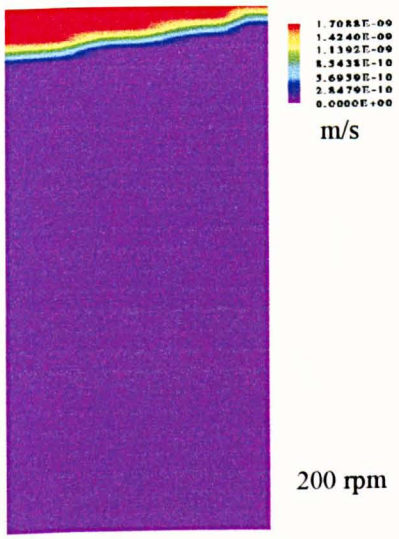

Figure(6.121): Growth rate at t = 0.6 s.

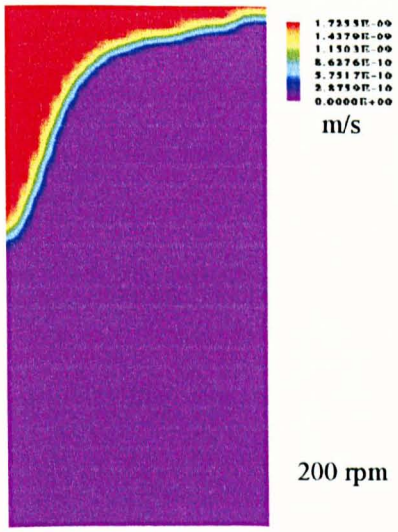

Figure(6.122): Growth rate at t = 1.7 s.

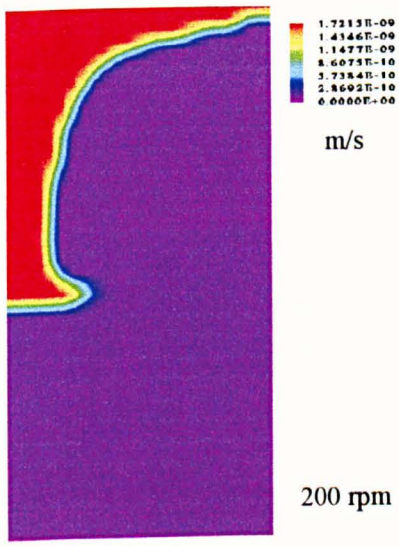

Figure(6.123): Growth rate at t = 3.5 s.

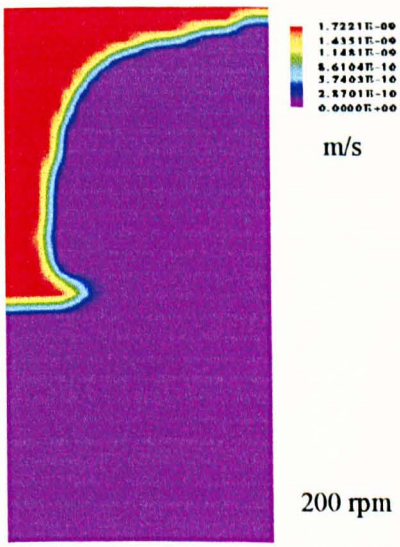

Figure(6.124): Growth rate at t = 5.2 s.

The variations of the M_0, M_1, M_2 and M_3 are shown in Figures (6.125) to (6.144).

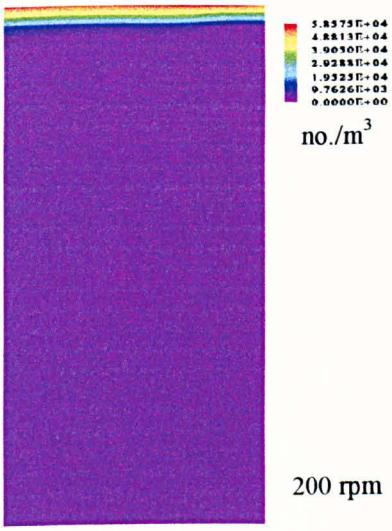

Figure(6.125): M_0 at t = 0.2 s.

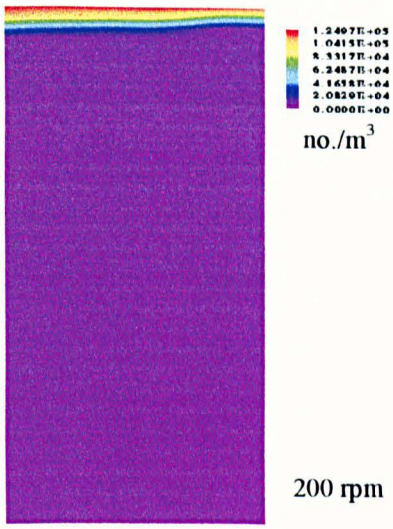

Figure(6.126): M_0 at t = 0.3 s.

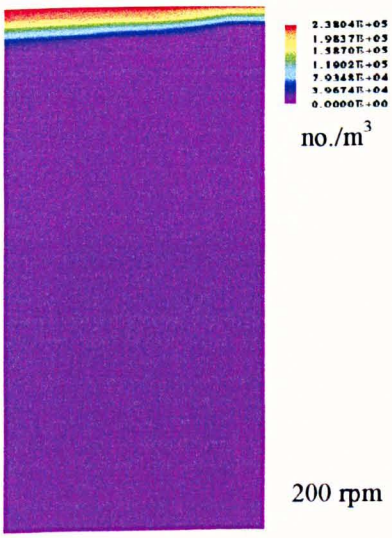

Figure(6.127): M_0 at t = 0.6 s.

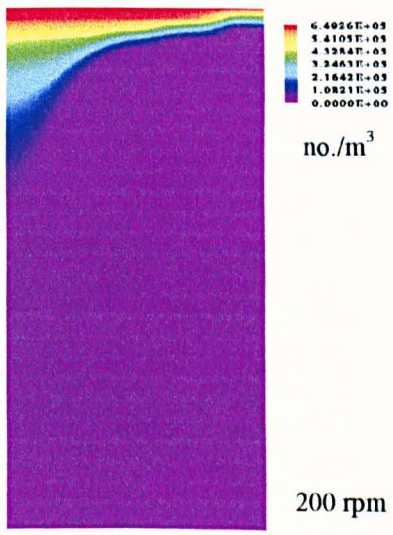

Figure(6.128): M_0 at t = 1.7 s.

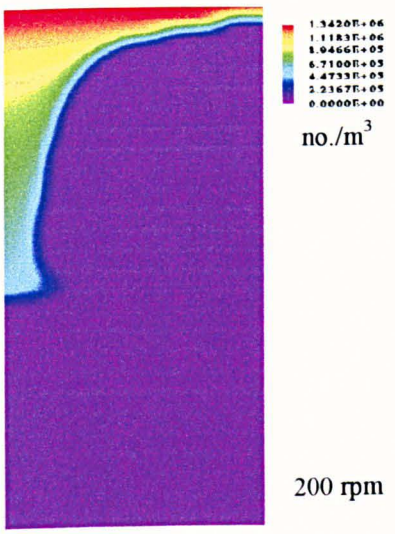

Figure(6.129): M_0 at t = 3.5 s.

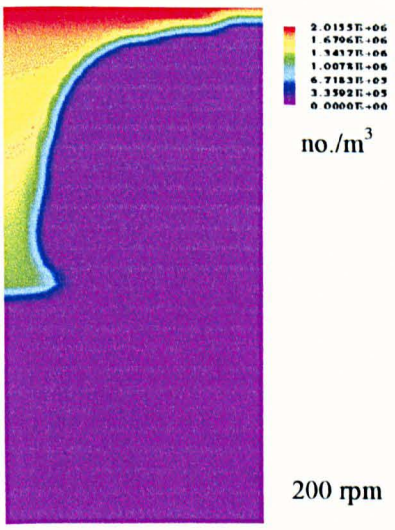

Figure(6.130): M_0 at t = 5.2 s.

M_0 results show that there are more particles at the interface where the reaction is taking place.

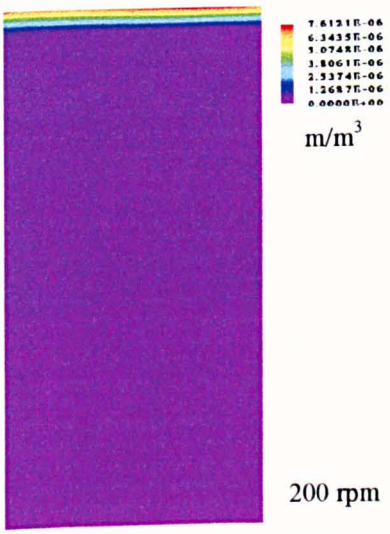

Figure(6.131): M_1 at t = 0.2 s.

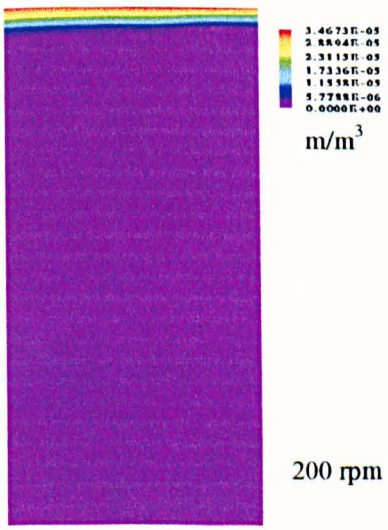

Figure(6.132): M_1 at t = 0.3 s.

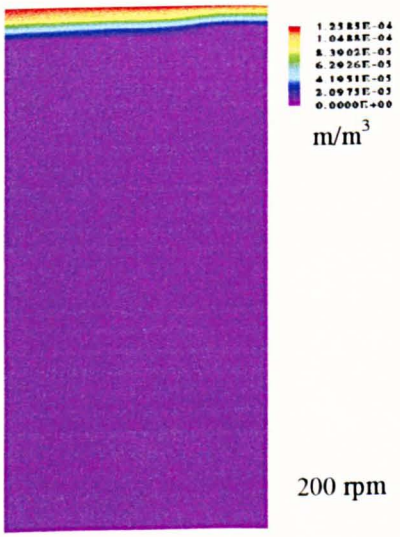

Figure(6.133): M_1 at t = 0.6 s.

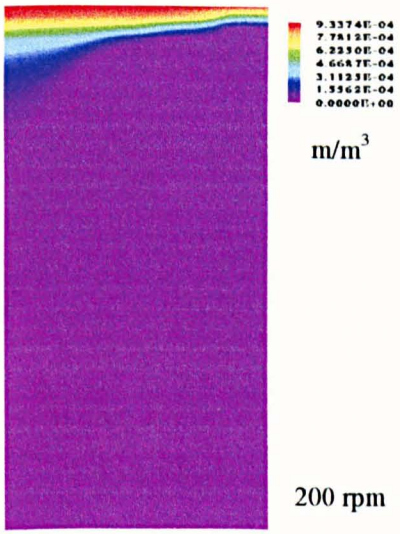

Figure(6.134): M_1 at t = 1.7 s.

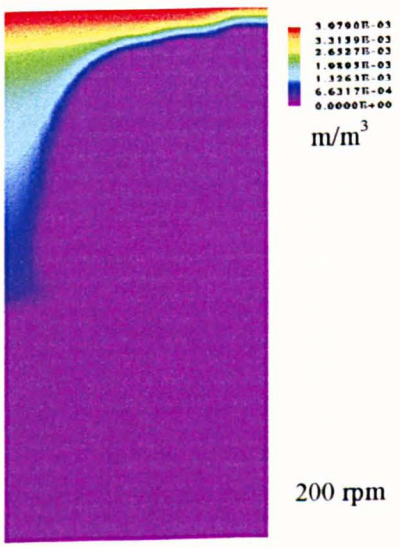

Figure(6.135): M_1 at t = 3.5 s.

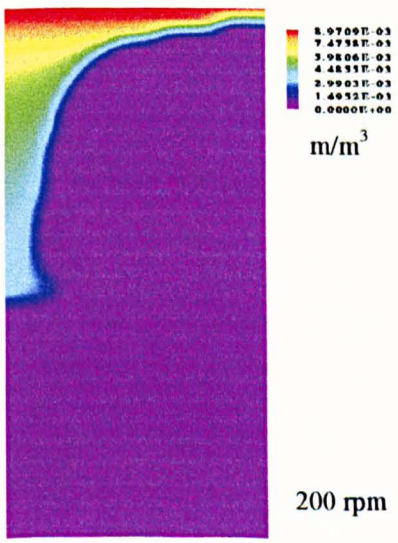

Figure(6.136): M_1 at t = 5.2 s.

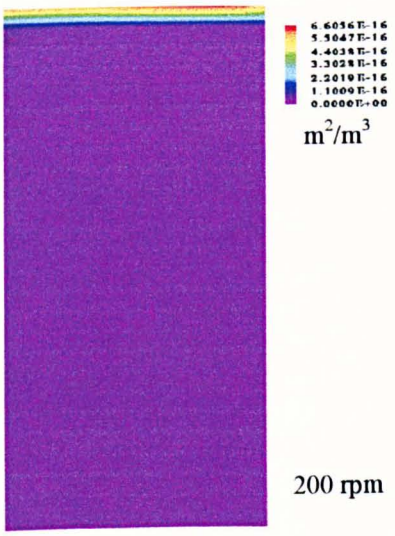

Figure(6.137): M_2 at t = 0.2 s.

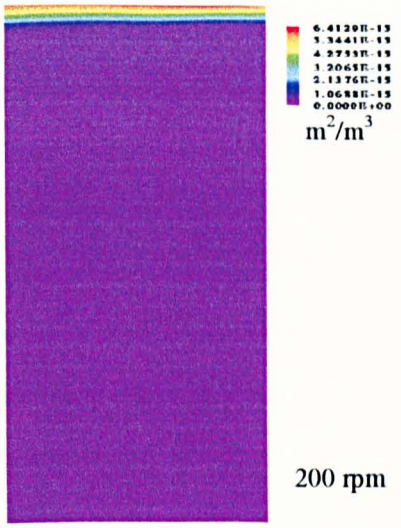

Figure(6.138): M_2 at t = 0.3 s.

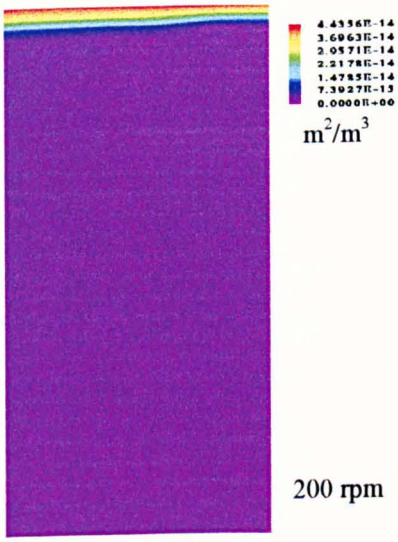

Figure(6.139): M_2 at t = 0.6 s.

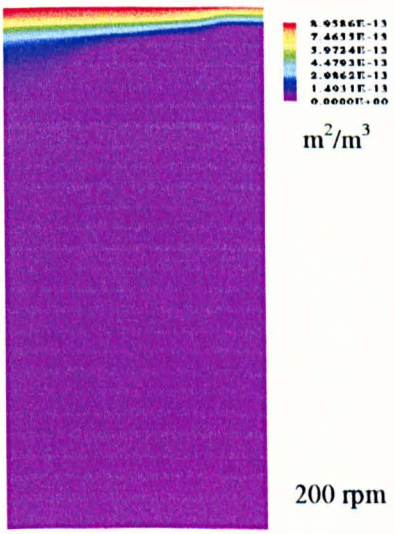

Figure(6.140): M_2 at t = 1.7 s.

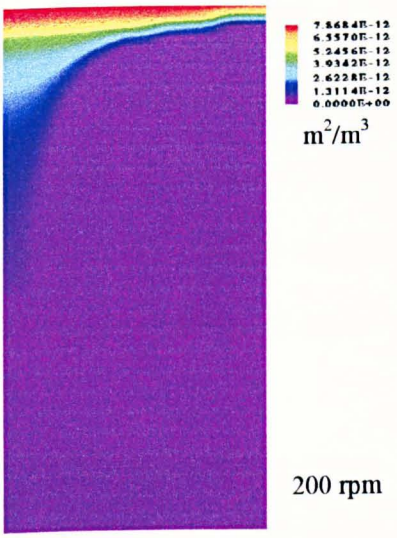

Figure(6.141): M_2 at t = 3.5 s.

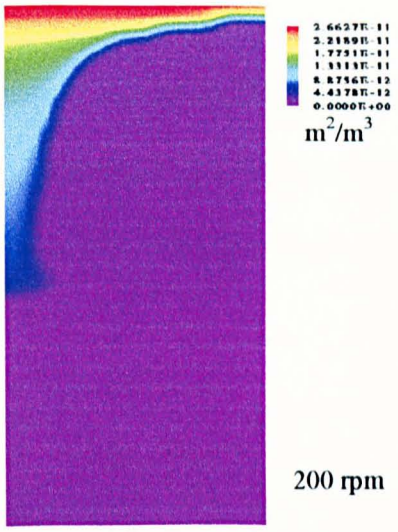

Figure(6.142): M_2 at t = 5.2 s.

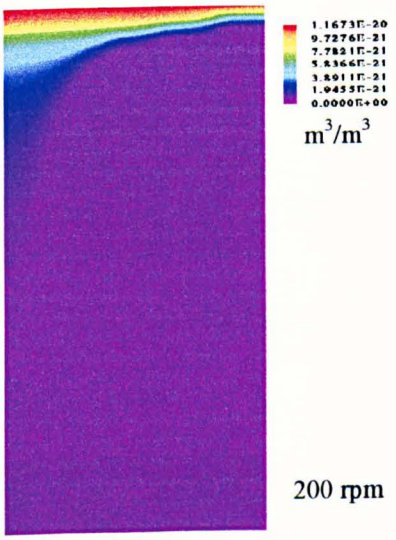

Figure(6.143): M_3 at t = 3.5 s.

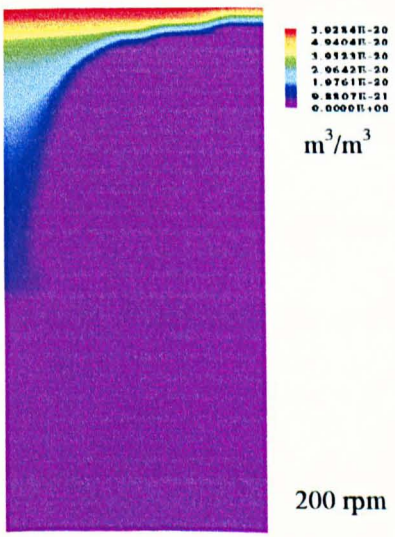

Figure(6.144): M_3 at t = 5.2 s.

6.3.5. 450 rpm (Re = $2.1*10^4$), Turbulent Flow

This simulation exploits the highest Re number in this study. The high resultant turbulent energy promotes a faster development of supersaturation levels in less time compared with the previous runs, Figures (6.145) to (6.154). The simulation time is ~ 960 hrs to give a real time of 10 s.

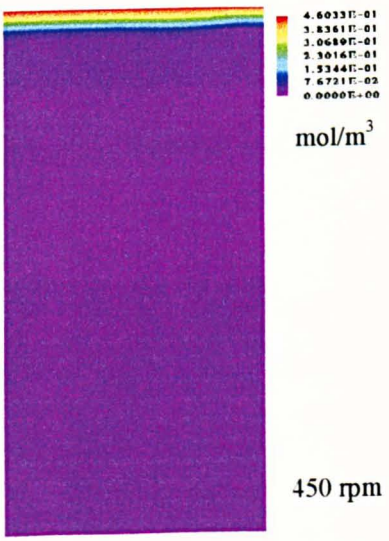

Figure (6.145): Supersaturation at t = 0.04 s.

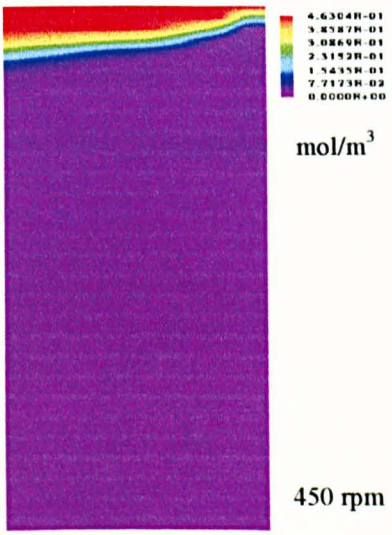

Figure (6.146): Supersaturation at t=0.13 s.

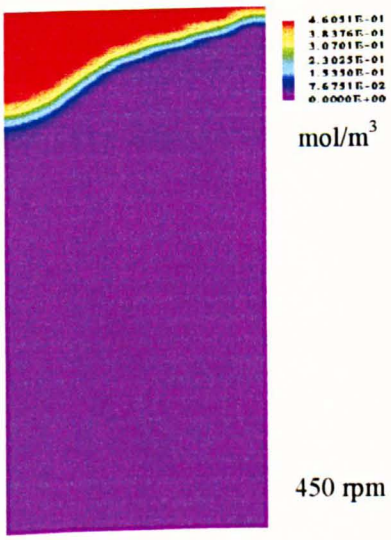

Figure (6.147): Supersaturation at t = 0.4 s.

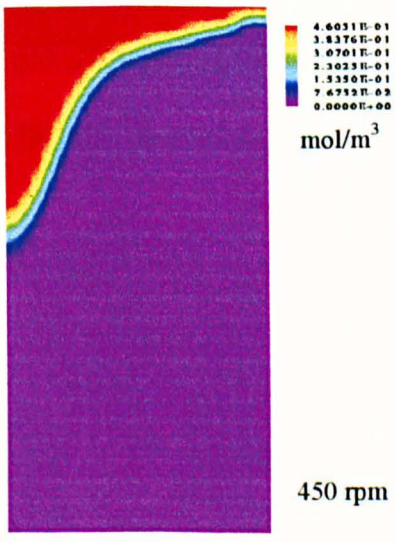

Figure (6.148): Supersaturation at t = 0.6 s.

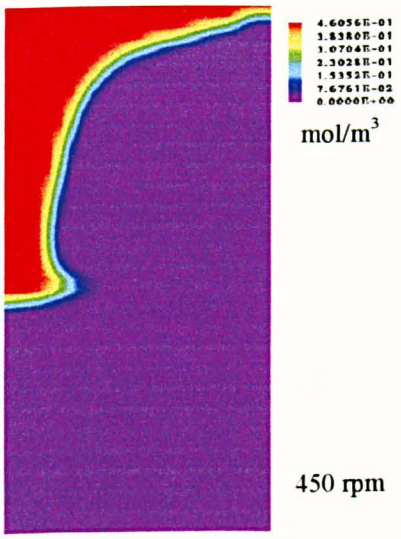

Figure (6.149): Supersaturation at t = 0.9 s.

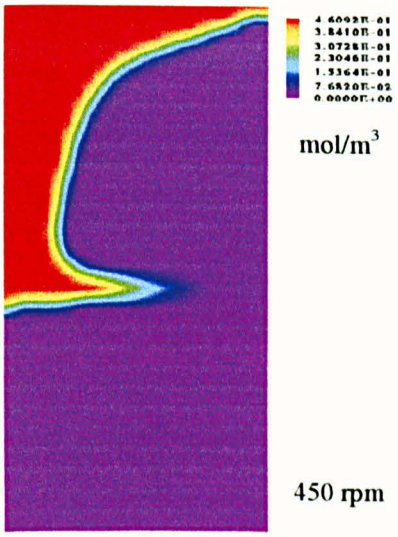

Figure (6.150): Supersaturation at t = 1.3 s.

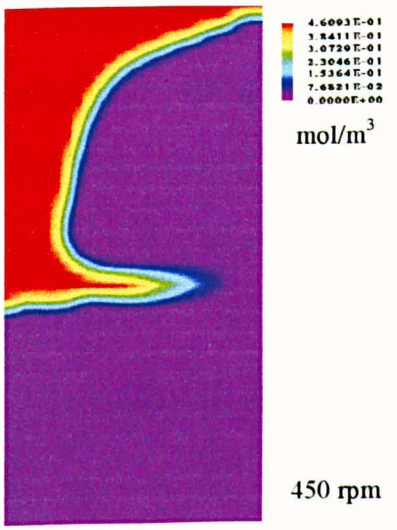

Figure (6.151): Supersaturation at t = 1.7 s.

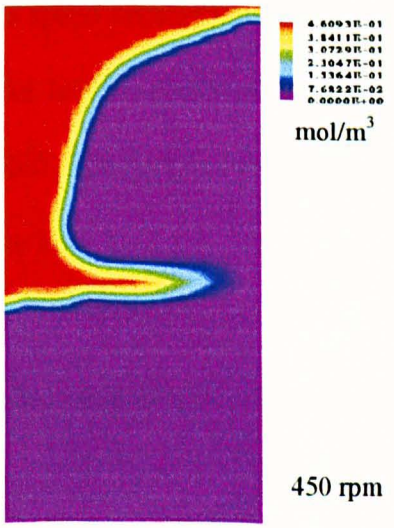

Figure (6.152): Supersaturation at t = 2.1 s.

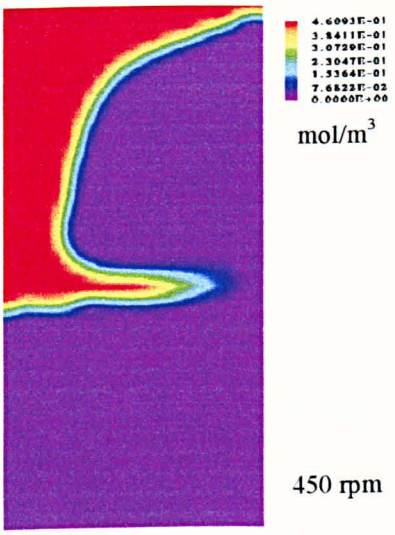

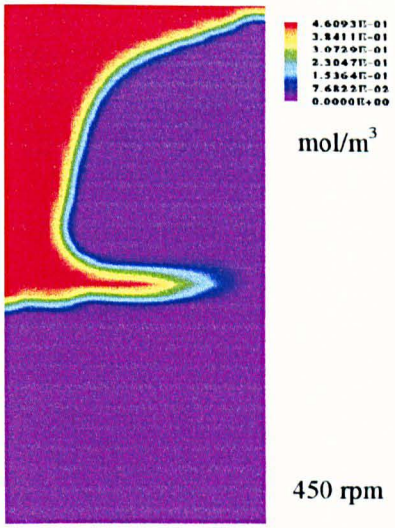

Figure (6.153): Supersaturation at t = 7.0 s. Figure (6.154): Supersaturation at t=10.0 s.

The product flow in the same pattern as the speed vectors where it comes from the interface into the bulk of the liquid from the left-hand side till it reaches the impeller region. Then, it starts to spread in the radial direction and retain this position for long (computing) time and does not complete the loop.

The nucleation and growth rate are extended accordingly, Figures (6.155) to (6.174).

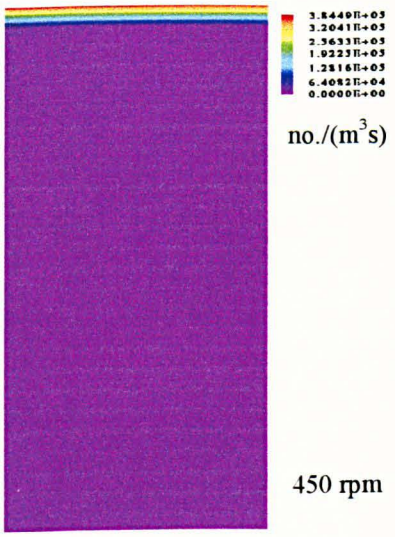

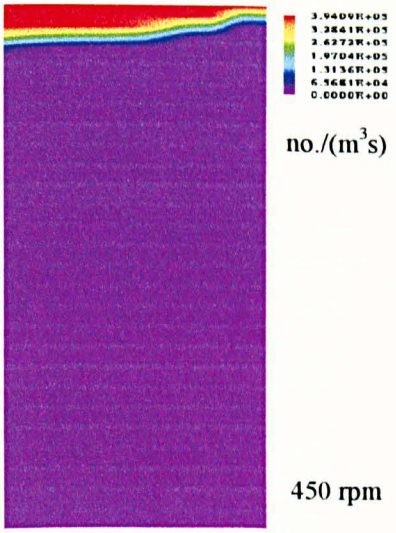

Figure (6.155): Nucleation rate at t = 0.04 s. Figure (6.156):Nucleation rate at t= 0.13 s.

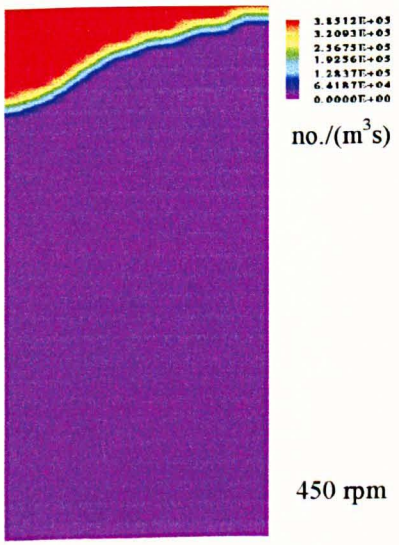

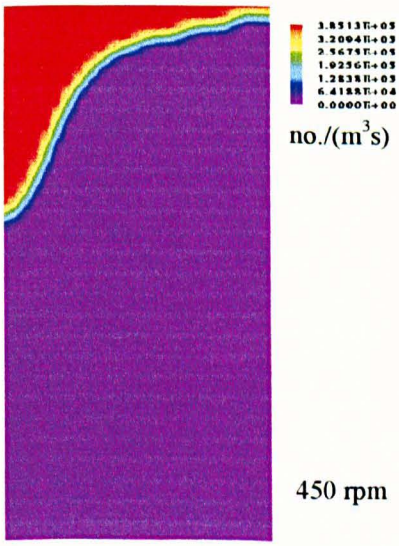

Figure (6.157): Nucleation rate at t = 0.4 s. Figure (6.158): Nucleation rate at t = 0.6 s.

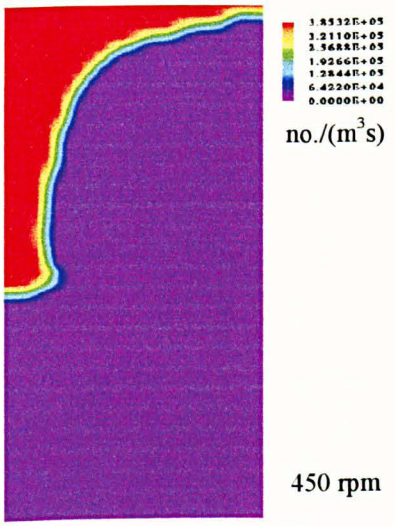

Figure (6.159): Nucleation rate at t = 0.9 s.

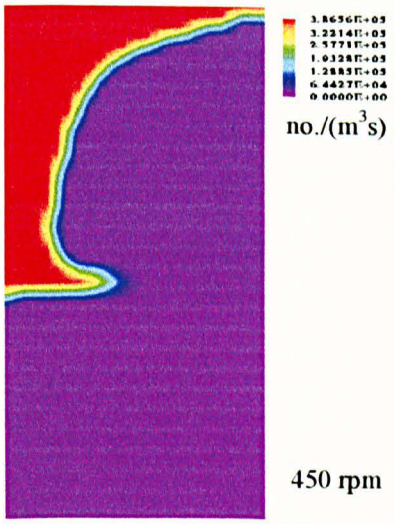

Figure (6.160): Nucleation rate at t = 1.3 s.

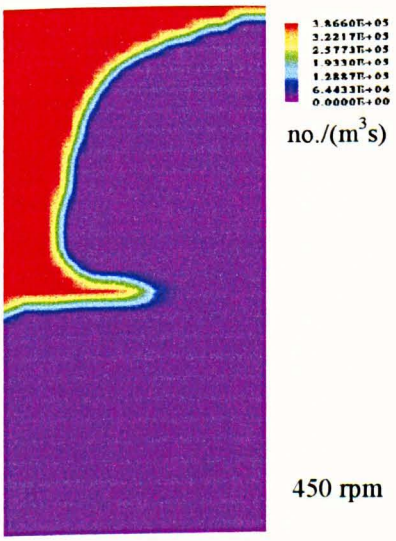

Figure (6.161): Nucleation rate at t = 1.7 s.

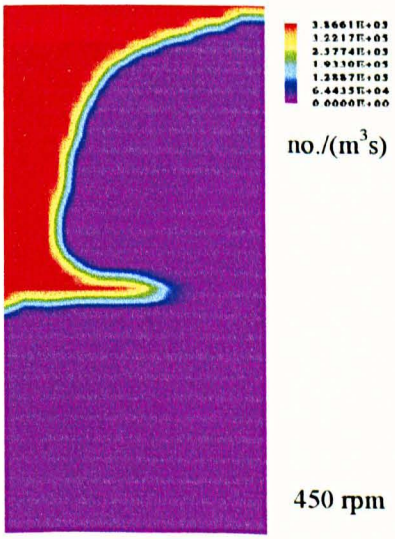

Figure (6.162): Nucleation rate at t = 2.1 s.

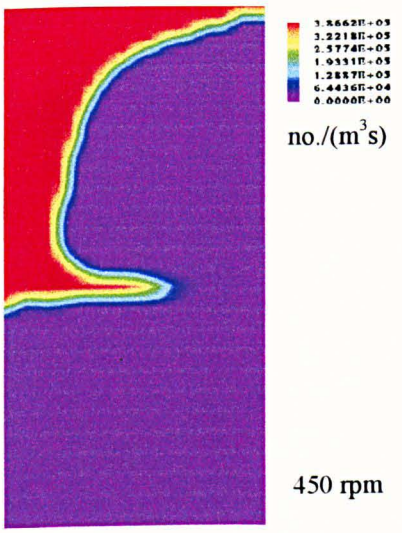

Figure (6.163): Nucleation rate at t = 7.0 s.

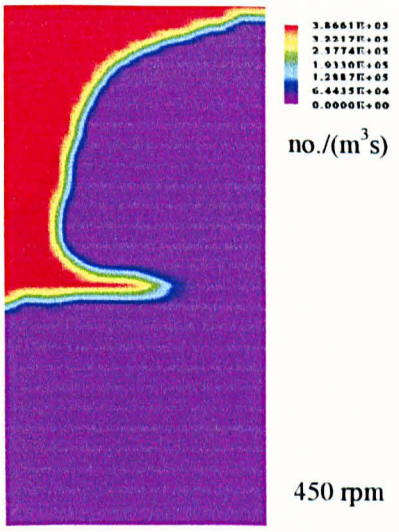

Figure (6.164): Nucleation rate at t=10.0 s.

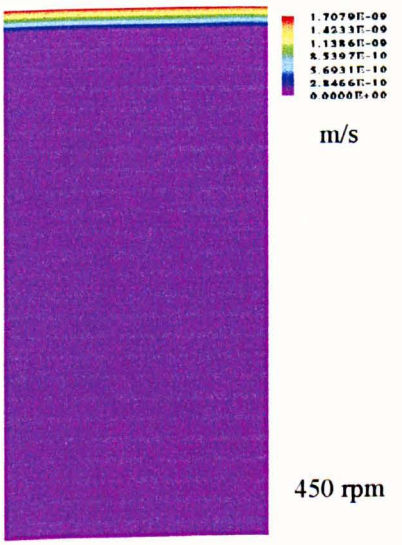

Figure (6.165): Growth rate at t = 0.04 s.

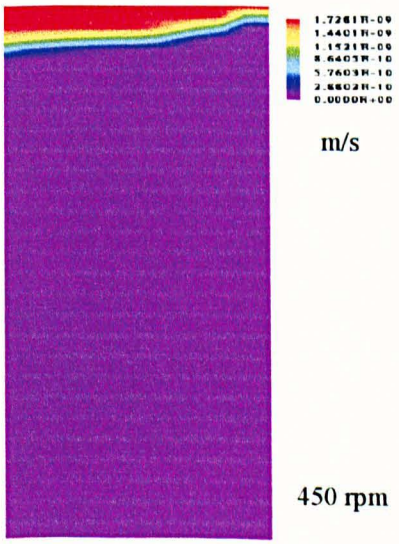

Figure (6.166): Growth rate at t = 0.13 s.

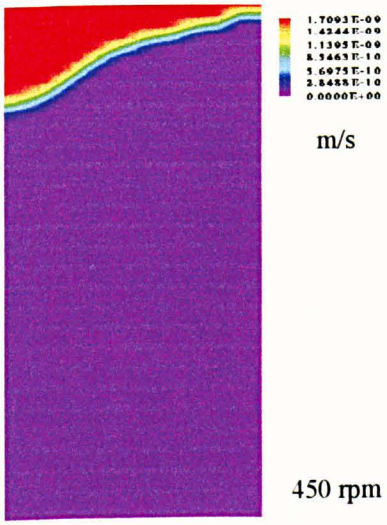

Figure (6.167): Growth rate at t = 0.4 s.

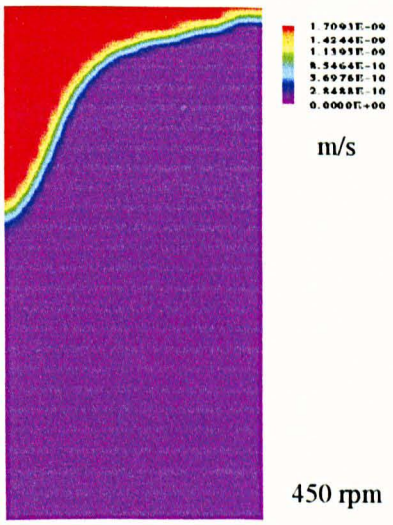

Figure (6.168): Growth rate at t = 0.6 s.

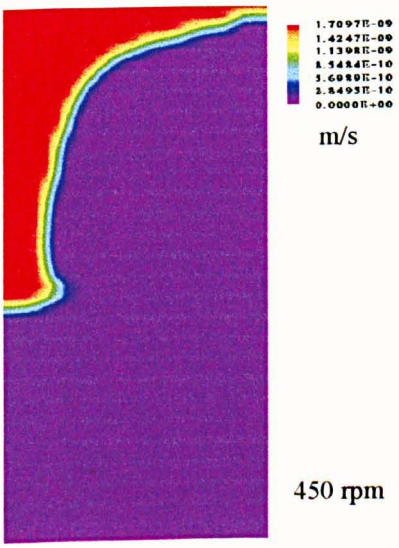

Figure (6.169): Growth rate at t = 0.9 s.

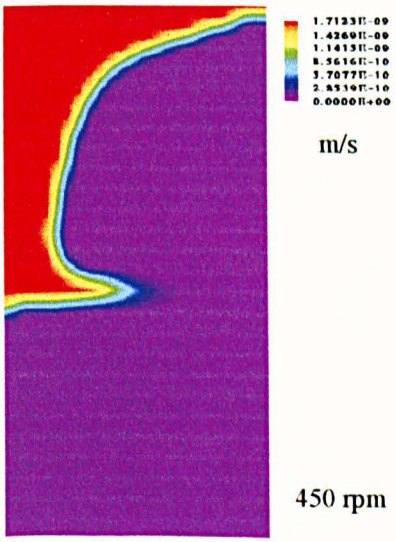

Figure (6.170): Growth rate at t = 1.3 s.

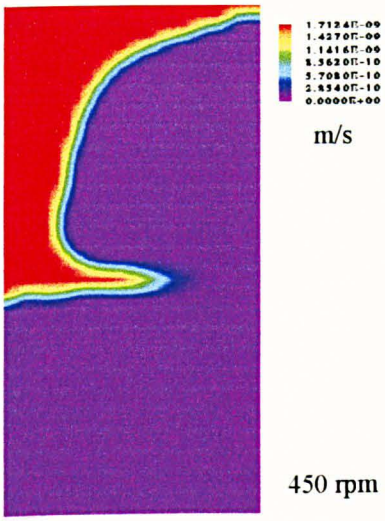

Figure (6.171): Growth rate at t = 1.7 s.

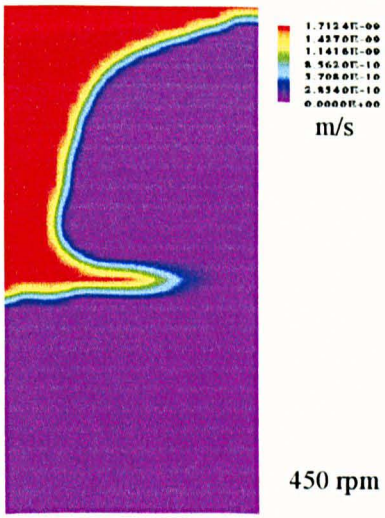

Figure (6.172): Growth rate at t = 2.1 s.

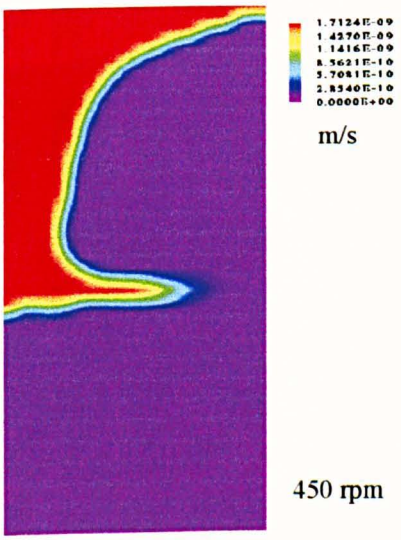

Figure (6.173): Growth rate at t = 7.0 s.

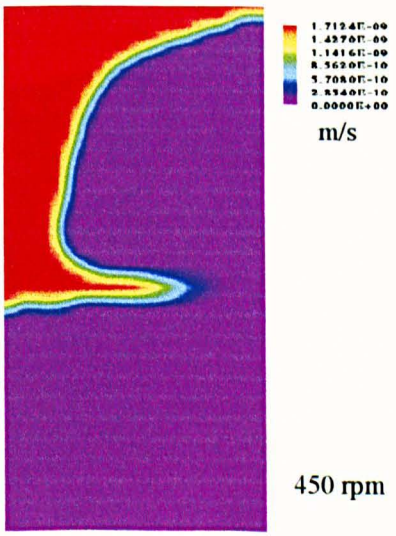

Figure (6.174): Growth rate at t = 10.0 s.

The moments (M_0, M_1, M_2 and M_3) are illustrated in Figures (6.175) to (6.207).

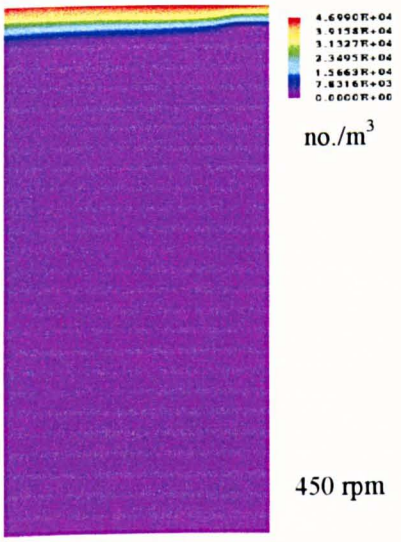

Figure(6.175): M_0 at t = 0.13 s.

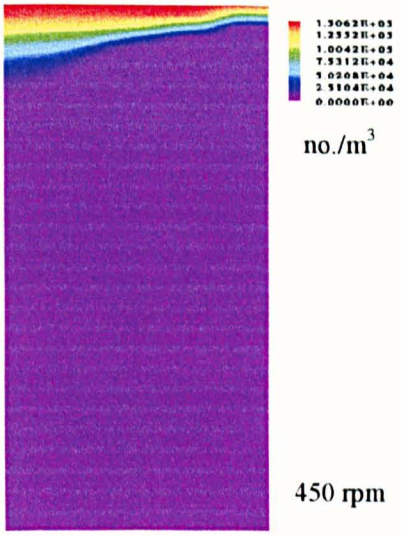

Figure(6.176): M_0 at t = 0.4 s.

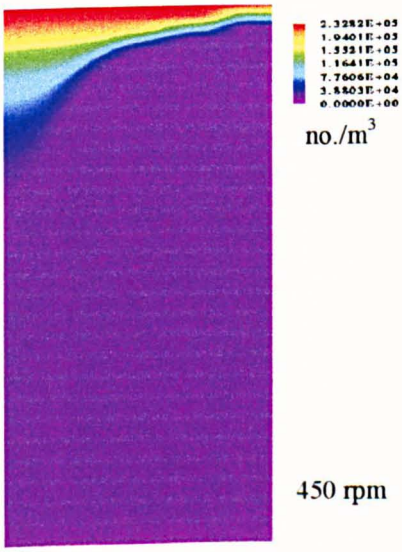

Figure(6.177): M_0 at t = 0.6 s.

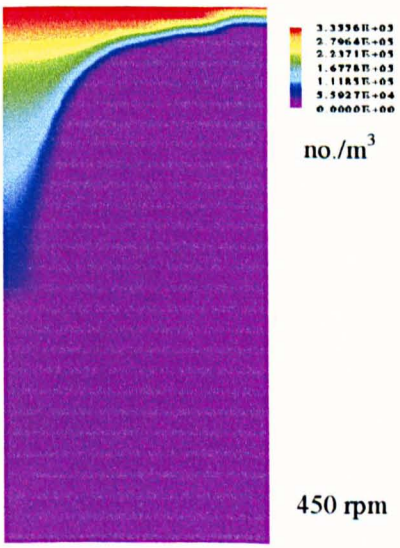

Figure(6.178): M_0 at t = 0.9 s.

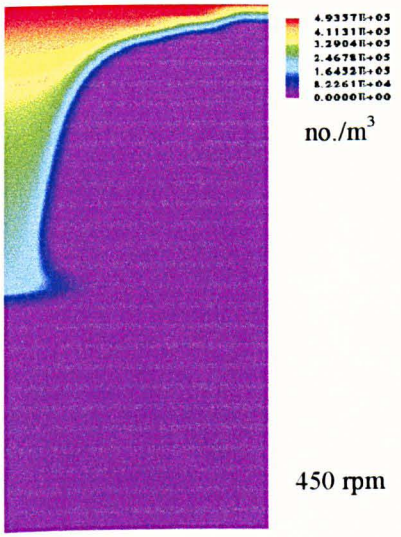

Figure(6.179): M_0 at t = 1.3 s.

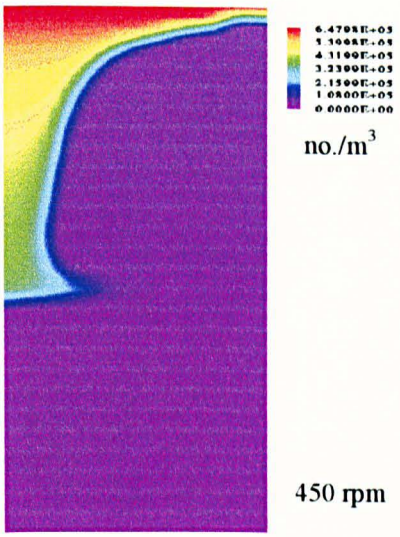

Figure(6.180): M_0 at t = 1.7 s.

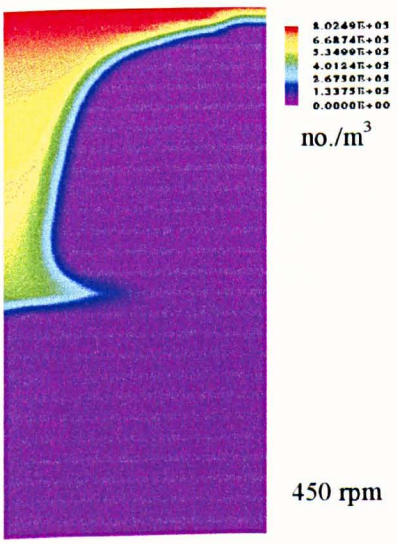

Figure(6.181): M_0 at t = 2.1 s.

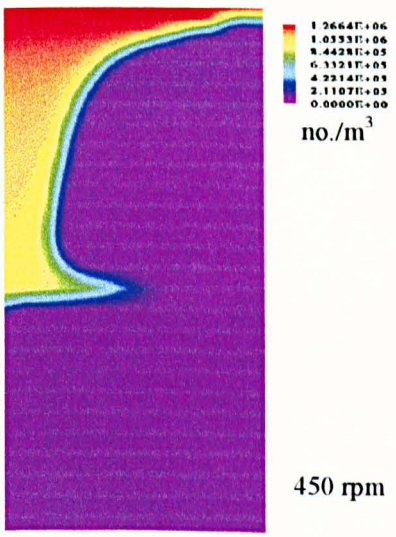

Figure(6.182): M_0 at t = 3.3 s.

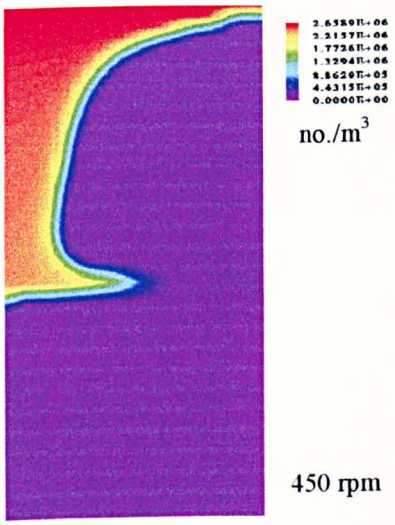

Figure(6.183): M_0 at t = 7.0 s.

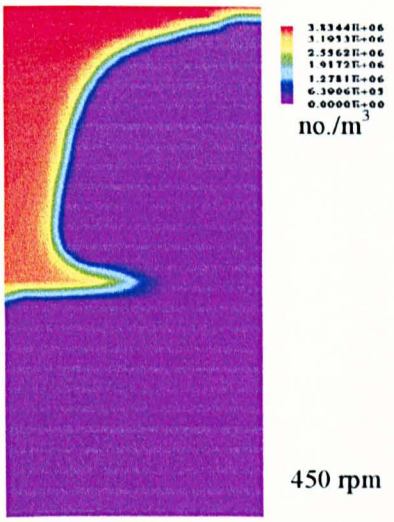

Figure(6.184): M_0 at t = 10.0 s.

The total number of particles is higher at the interfacial region and since the supersaturation is not going any further, the number of particles increases gradually at the interface and away from it as well.

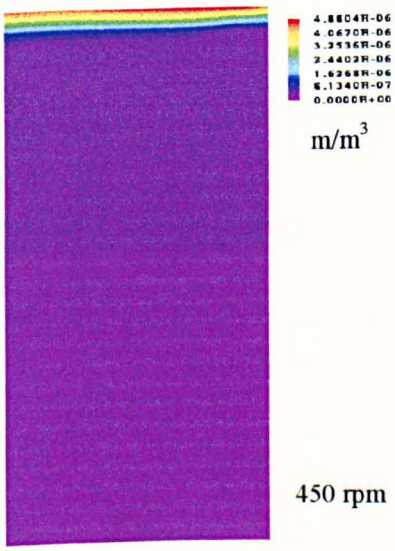

Figure(6.185): M_1 at t = 0.13 s.

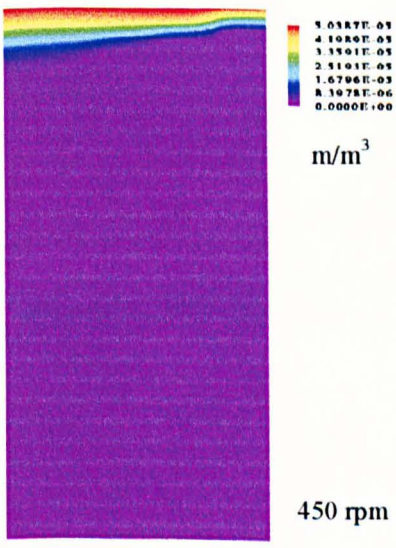

Figure(6.186): M_1 at t = 0.4 s.

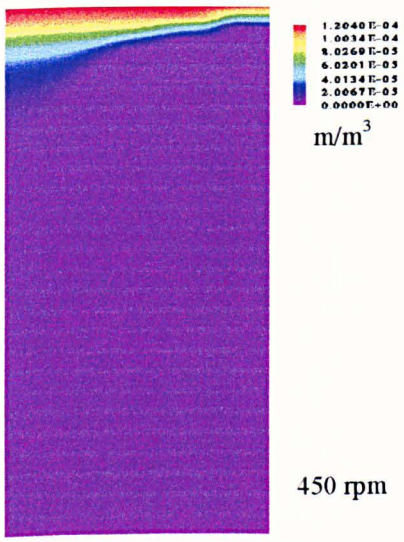

Figure(6.187): M_1 at t = 0.6 s.

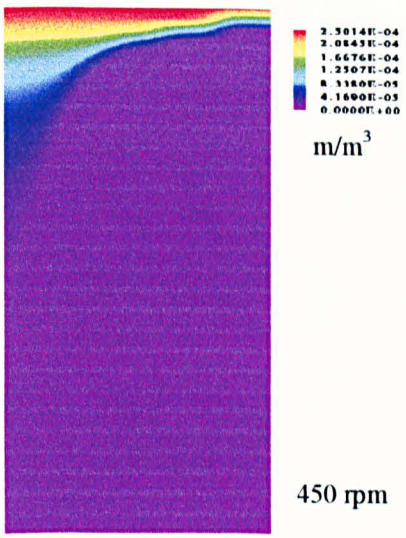

Figure(6.188): M_1 at t = 0.9 s.

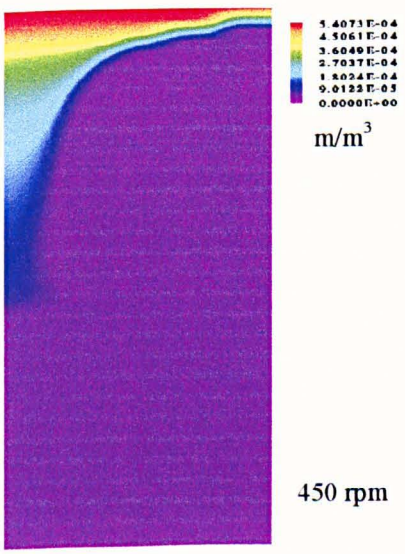

Figure(6.189): M_1 at t = 1.3 s.

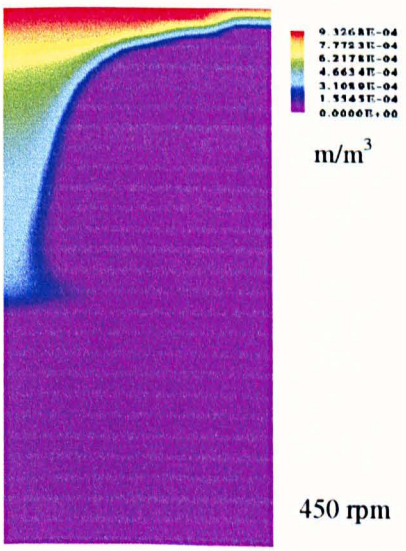

Figure(6.190): M_1 at t = 1.7 s.

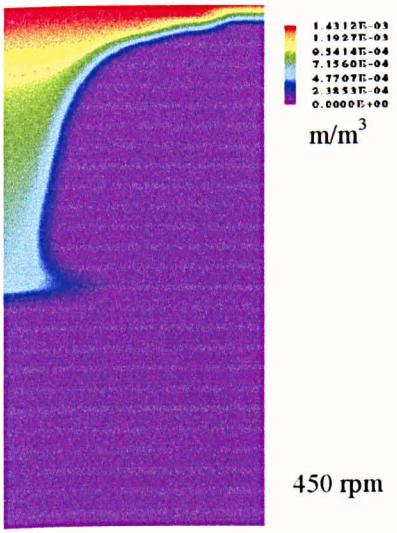

Figure(6.191): M_1 at t = 2.1 s.

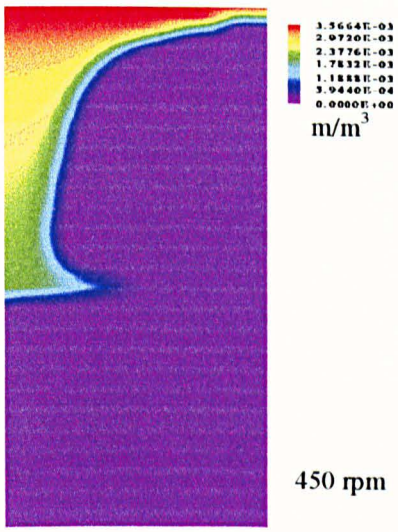

Figure(6.192): M_1 at t = 3.3 s.

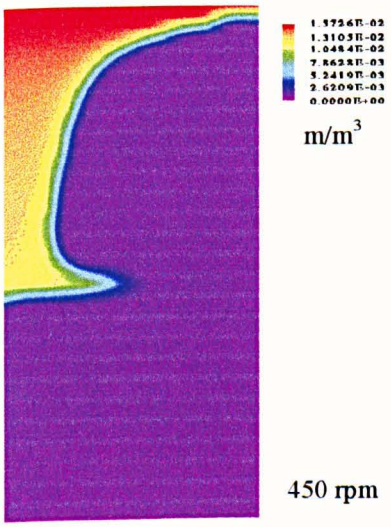

Figure(6.193): M_1 at t = 7.0 s.

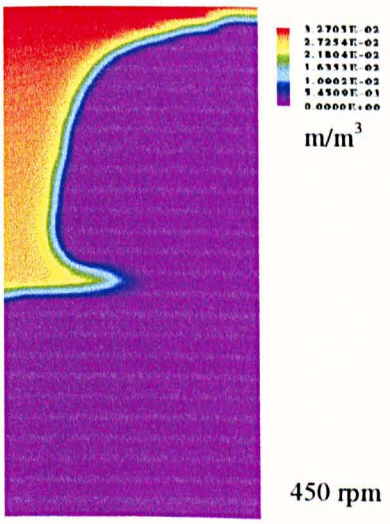

Figure(6.194): M_1 at t = 10.0 s.

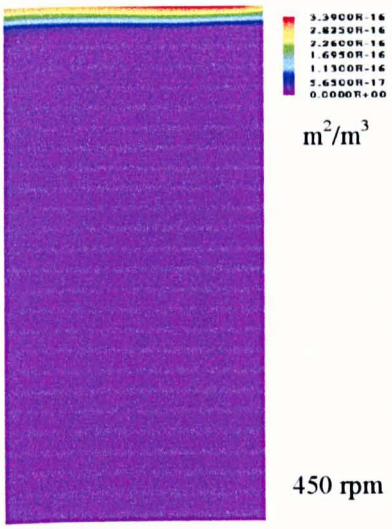

Figure(6.195): M_2 at t = 0.13 s.

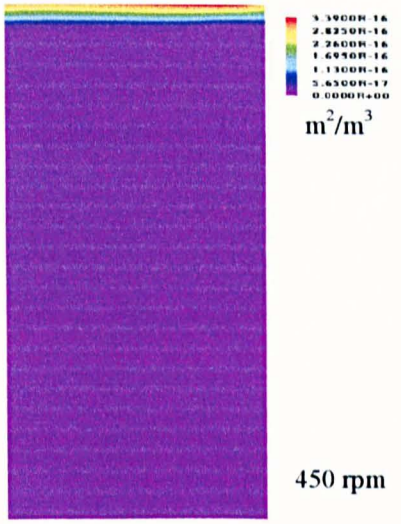

Figure(6.196): M_2 at t = 0.4 s.

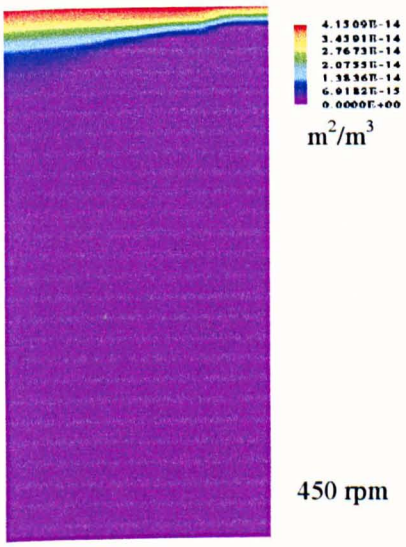

Figure(6.197): M_2 at t = 0.6 s.

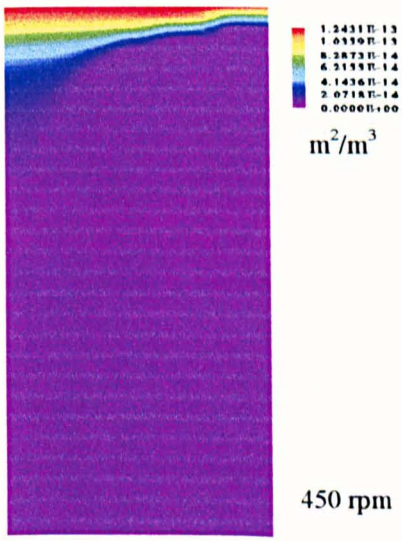

Figure(6.198): M_2 at t = 0.9 s.

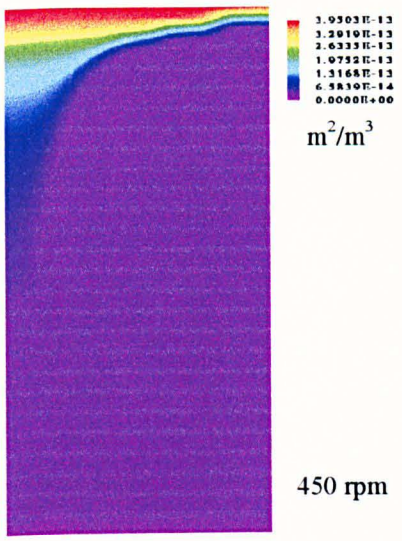

Figure(6.199): M_2 at t = 1.3 s.

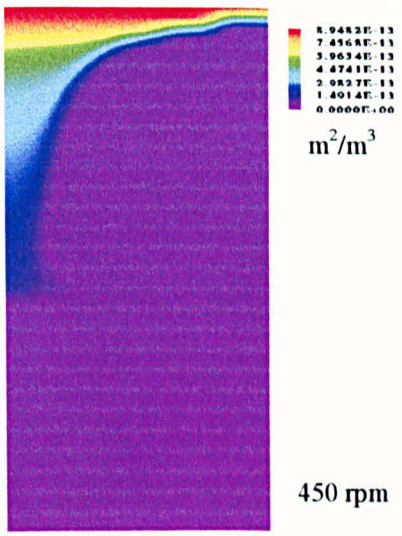

Figure(6.200): M_2 at t = 1.7 s.

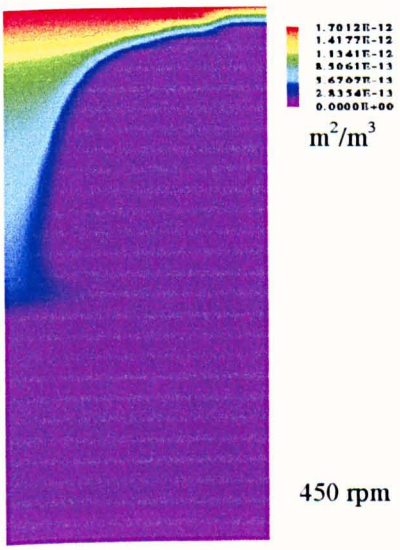

Figure(6.201): M_2 at t = 2.1 s.

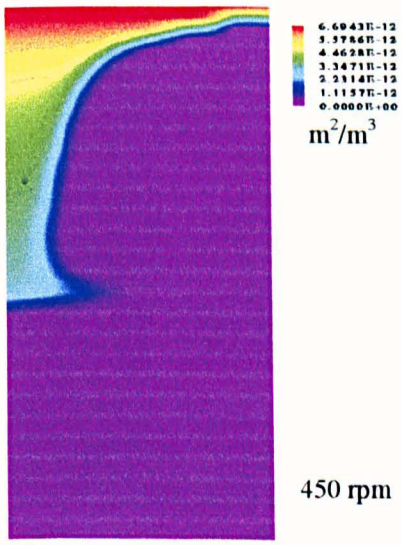

Figure(6.202): M_2 at t = 3.3 s.

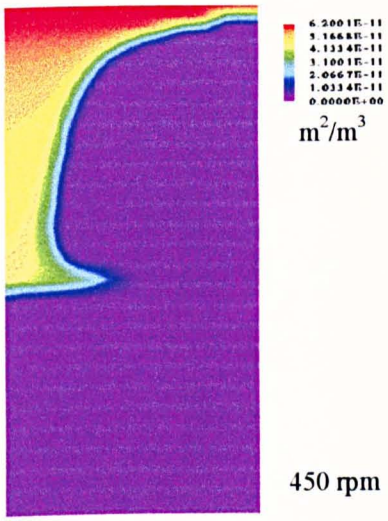

Figure(6.203): M_2 at t = 7.0 s.

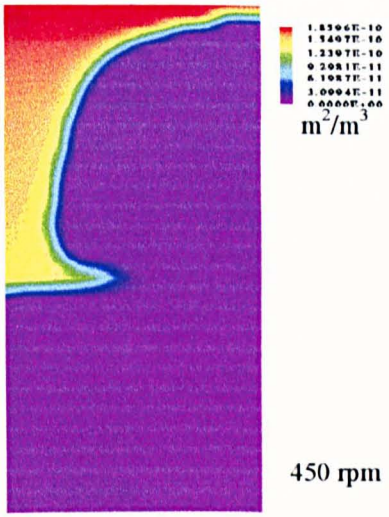

Figure(6.204): M_2 at t = 10.0 s.

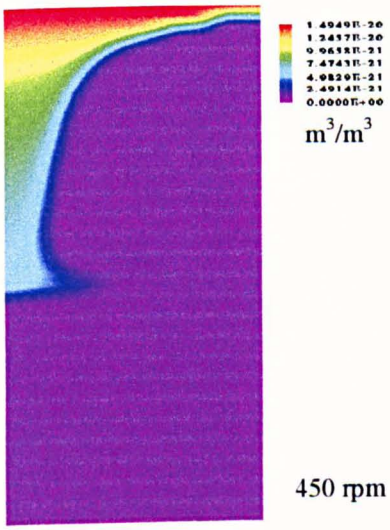

Figure(6.205): M_3 at t = 3.7 s.

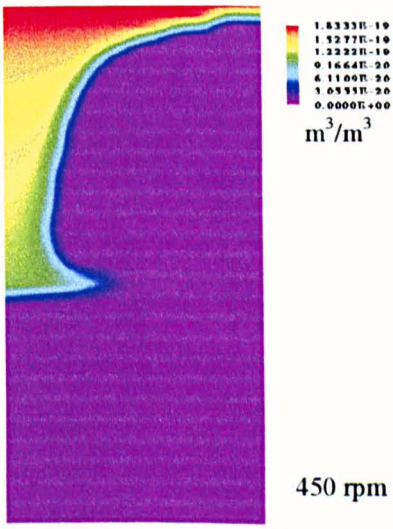

Figure(6.206): M_3 at t = 7.0 s.

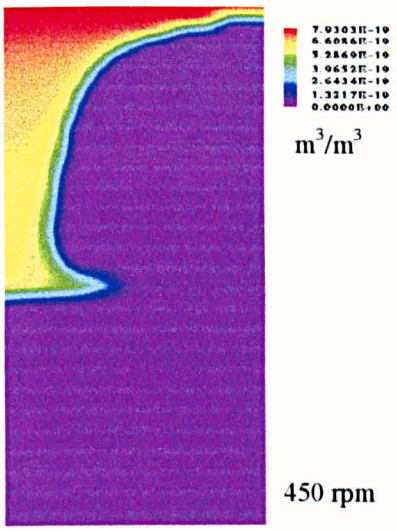

Figure(6.207): M_3 at t = 10.0 s.

6.4. CFD Simulations Data Analysis

- **Supersaturation**

The values of the supersaturation presented in the following tables, Table (6.2) to Table (6.6), are the average values over the whole vessel.

Figure (6.208) represents the progress of the supersaturation with time for 1 rpm (Re = 46) and 100 rpm (Re = $4.6*10^3$). Since the reaction is taking place at the interface only (for the given time), it is difficult to see a significant change in the average supersaturation levels. However, the average supersaturation is higher for higher Re number.

Time (s)	Sup. (mol/m^3)
0	0
0.68	0.00104
1.37	0.00104
2.05	0.00105
5.49	0.00105
7.63	0.00105
10.65	0.00105
12.85	0.00105
15.80	0.00105
19.94	0.00105
25.79	0.00105
30.27	0.00105

Table (6.2): Average supersaturation versus time for 1 rpm (Re = 46).

Time (s)	Sup. (mol/m^3)
0	0
0.09	0.00172
0.99	0.00171
1.98	0.00175
4.77	0.00171
6.11	0.00175
8.99	0.00175
10.34	0.00171
16.82	0.00171
19.15	0.00171
23.56	0.00175
30.13	0.00171

Table (6.3): Average supersaturation versus time for 100 rpm (Re = $4.6*10^3$) with laminar flow.

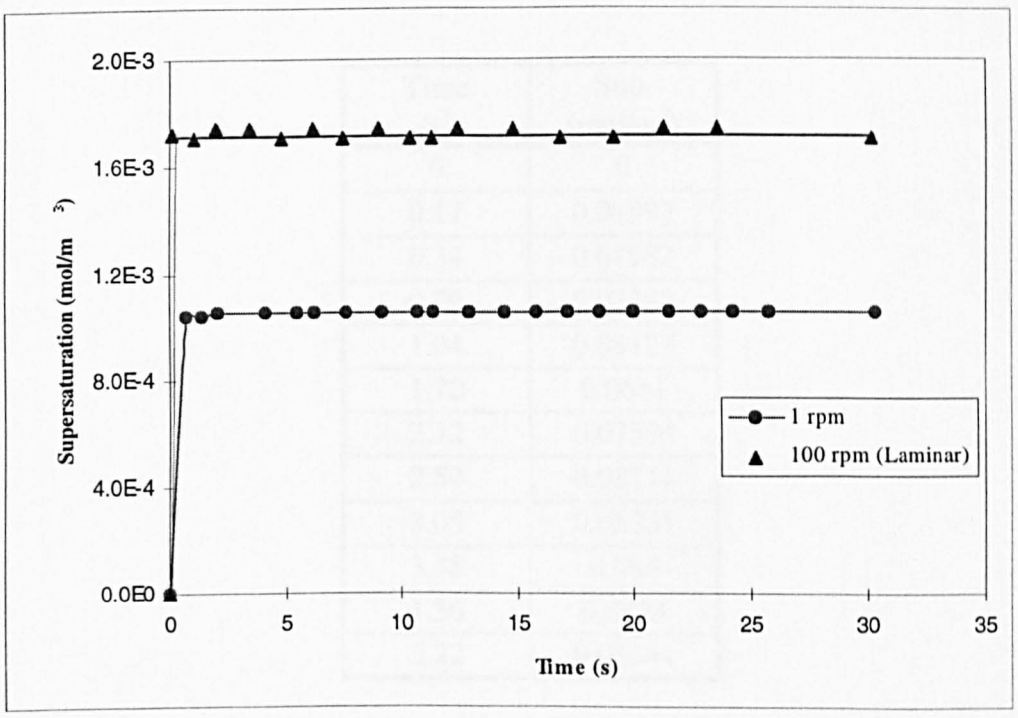

Figure (6.208): Average supersaturation versus time for 1 rpm (Re = 46) and 100 rpm (Re = $4.6*10^3$).

Time (s)	Sup. (mol/m^3)
0	0
0.22	0.01418
0.51	0.01307
0.91	0.01737
1.54	0.01754
2.01	0.02096
2.32	0.02158
2.92	0.02346
3.32	0.02452
4.05	0.02646
4.49	0.02671
5.13	0.02643

Table (6.4): Average supersaturation versus time for 100 rpm ($Re = 4.6*10^3$) with turbulent flow system.

Time (s)	Sup. (mol/m^3)
0	0
0.17	0.01993
0.34	0.01982
0.79	0.03383
1.04	0.04123
1.70	0.0641
2.12	0.07594
2.54	0.08111
3.05	0.08331
3.48	0.084
4.36	0.0824
5.22	0.08341

Table (6.5): Average supersaturation versus time for 200 rpm ($Re = 9.3*10^3$) system.

Time (s)	Sup. (mol/m^3)
0	0
0.13	0.0292
0.61	0.0669
1.29	0.1037
1.69	0.1121
2.10	0.1144
2.50	0.1148
3.30	0.1148
3.71	0.1149
4.11	0.1148
4.52	0.1148
5.33	0.1148

Table (6.6): Average supersaturation versus time for 450 rpm ($Re = 2.1*10^4$) system.

Figure (6.209) shows the change of the average supersaturation with time for the three turbulent models ($Re = 4.6*10^3$, $9.3*10^3$ and $2.1*10^4$). The higher the Re number the higher the supersaturation value. After 2 to 3 s, the change in the supersaturation is not significant because the progress of the reaction is too small, after this time.

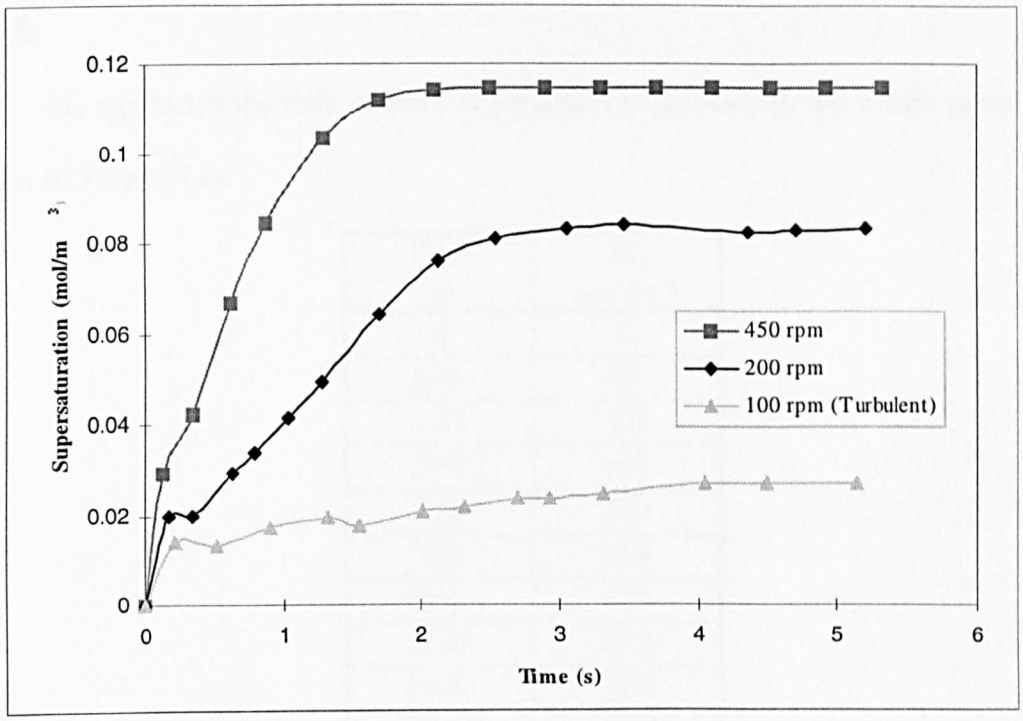

Figure (6.209): Average supersaturation versus time for 100 rpm (Re = $4.6*10^3$), 200 rpm (Re = $9.3*10^3$) and 450 rpm(Re = $2.1*10^4$).

- M_0

M_0 represents the total number of precipitated particles in the whole vessel, see Tables (6.7) to (6.11).

Time (s)	M_0 (no./m^3)
0	0
0.68	49
1.37	101
2.05	154
5.49	429
7.63	598
10.65	840
12.85	1015
15.80	1251
19.94	1580
25.79	2047
30.27	2400

Table (6.7): Total M_0 versus time, for 1 rpm (Re = 46).

Time (s)	M_0 (no./m^3)
0	0
0.09	71
0.99	795
1.98	1591
4.77	3818
6.11	4903
8.99	7207
10.34	8286
16.82	13466
19.15	15337
23.56	18880
30.13	24156

Table (6.8): Total M_0 versus time, for 100 rpm (Re = $4.6*10^3$) with laminar flow.

Figure (6.210) demonstrates the variation of the total number of particles in the system with time over the whole range of time (30 s). The second system has higher M_0 values than the first.

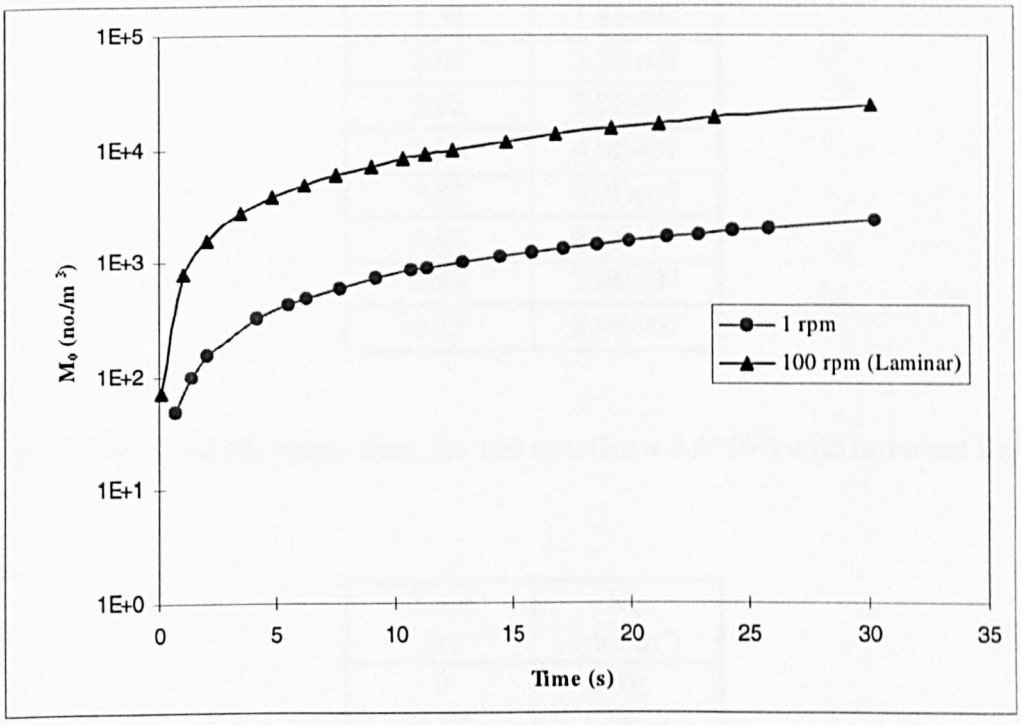

Figure (6.210): M_0 versus time for 1 rpm (Re = 46) and 100 rpm (Re = $4.6*10^3$).

Time (s)	M_0 (no./m^3)
0	0
0.22	1.7E+06
0.51	4.5E+06
0.91	8.8E+06
1.54	1.8E+07
2.01	2.5E+07
2.32	2.9E+07
2.92	4.0E+07
3.32	4.7E+07
4.05	6.1E+07
4.49	7.0E+07
5.13	8.4E+07

Table (6.9): Total M_0 versus time, for 100 rpm (Re = $4.6*10^3$) with turbulent flow.

Time (s)	M_0 (no./m^3)
0	0
0.17	1.7E+6
0.34	4.1E+6
0.79	1.3E+7
1.04	2.1E+7
1.70	4.9E+7
2.12	7.3E+7
2.54	1.0E+8
3.05	1.4E+8
3.48	1.7E+8
4.36	2.3E+8
5.22	2.8E+8

Table (6.10): Total M_0 versus time, for 200 rpm (Re = $9.3*10^3$).

Time (s)	M_0 (no./m^3)
0	0
0.13	1.7E+6
0.61	1.8E+7
1.29	6.6E+7
1.69	1.0E+8
2.10	1.4E+8
2.50	1.7E+8
3.30	2.5E+8
3.71	2.8E+8
4.11	3.2E+8
4.52	3.6E+8
5.33	4.3E+8

Table (6.11): Total M_0 versus time, for 450 rpm (Re = $2.1*10^4$).

Figure (6.211) displays the change in M_0 over the studied period of time (5 s). Also, it predicts higher values for higher Re numbers.

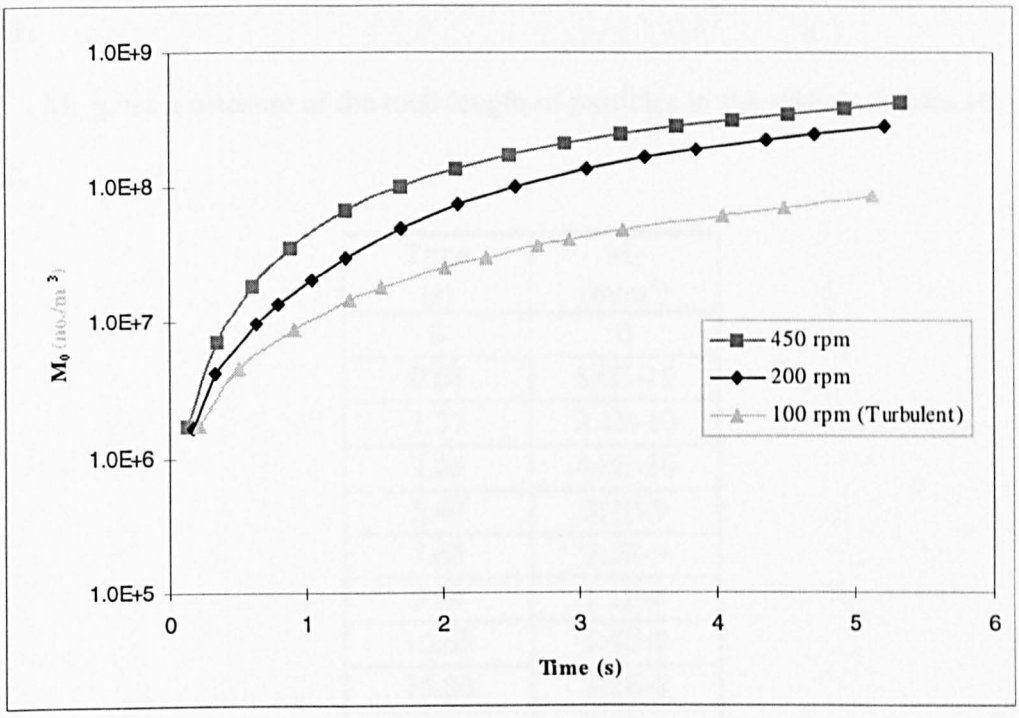

Figure (6.211): M_0 versus time for 100 rpm ($Re = 4.6*10^3$), 200 rpm ($Re = 9.3*10^3$) and 450 rpm ($Re = 2.1*10^4$).

- M_1

M_1 gives a measure of the total length of particles in the system, Tables (6.12) to (6.16).

Time (s)	M_1 (m/m^3)
0	0
0.68	5.0E-11
1.37	2.1E-10
2.05	4.9E-10
5.49	3.7E-9
7.63	7.3E-9
9.14	1.1E-8
10.65	1.4E-8
15.80	3.2E-8
19.94	5.1E-8
25.79	8.5E-8
30.27	1.2E-7

Table (6.12): Total M_1 versus time, for 1 rpm (Re = 46).

Time (s)	M_1 (m/m^3)
0	0
0.09	2.6E-11
0.99	4.3E-9
1.98	1.7E-8
4.77	1.0E-7
6.11	1.7E-7
8.99	3.6E-7
10.34	4.7E-7
16.82	1.3E-6
19.15	1.6E-6
23.56	2.5E-6
30.13	4.0E-6

Table (6.13): Total M_1 versus time, for 100 rpm (Re = $4.6*10^3$) with laminar flow.

Figure (6.212) shows the change in the total length of particles in the system with time. M_1 is proportional to the Re number.

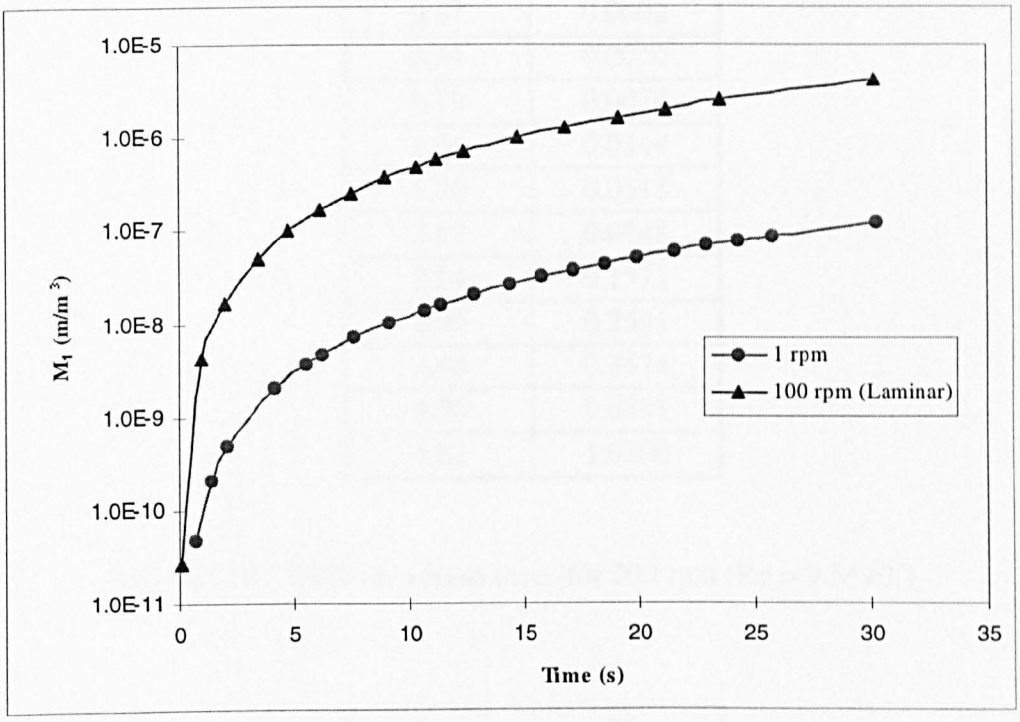

Figure (6.212): M_1 versus time for 1 rpm (Re = 46) and 100 rpm (Re = $4.6*10^3$).

Time (s)	M_1 (m/m^3)
0	0
0.22	0.0003
0.51	0.0018
0.91	0.0062
1.54	0.0202
2.01	0.0365
2.32	0.0502
2.92	0.0855
3.32	0.1139
4.05	0.1796
4.49	0.2271
5.13	0.3101

Table (6.14): Total M_1 versus time, for 100 rpm (Re = $4.6*10^3$) with turbulent flow.

Time (s)	M_1 (m/m^3)
0	0
0.17	0.0002
0.34	0.0010
0.79	0.0074
1.04	0.0144
1.70	0.0518
2.12	0.0948
2.54	0.1571
3.05	0.2591
3.48	0.3674
4.36	0.6581
5.22	1.0206

Table (6.15): Total M_1 versus time, for 200 rpm ($Re = 9.3*10^3$).

Time (s)	M_1 (m/m^3)
0	0
0.13	0.0001
0.61	0.0071
1.29	0.0536
1.69	0.1101
2.10	0.1906
2.50	0.2955
3.30	0.5782
3.71	0.7561
4.11	0.9583
4.52	1.1847
5.33	1.7110

Table (6.16): Total M_1 versus time, for 450 rpm ($Re = 2.1*10^4$).

Figure (6.213) gives the M_1 against time for the three turbulent systems. It can be noticed that M_1 is proportional to Re number.

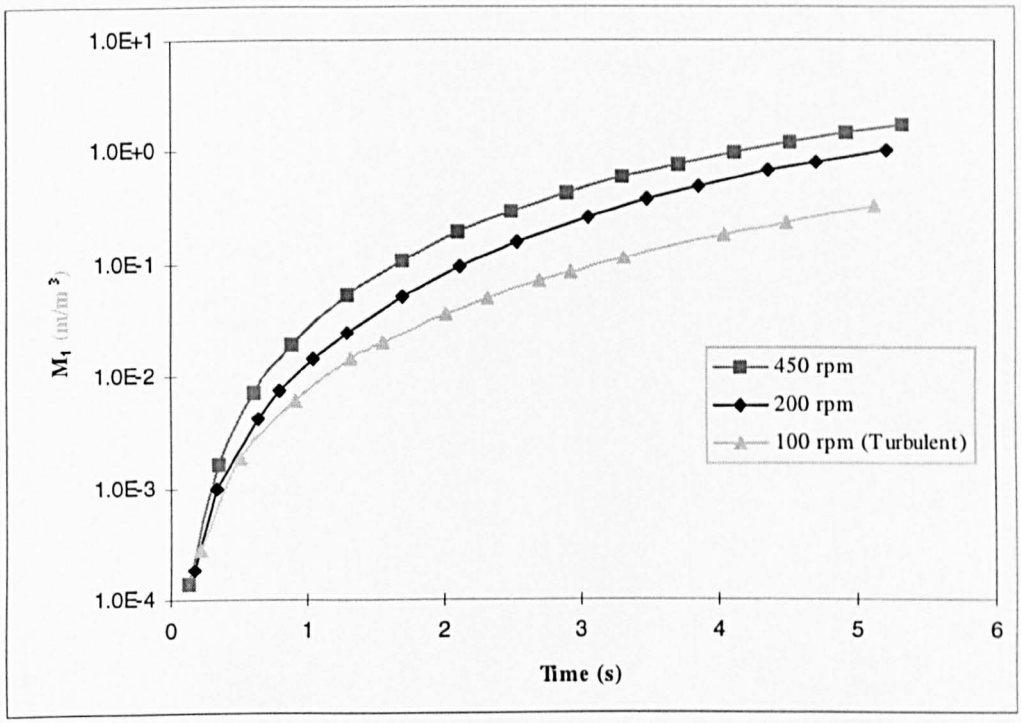

Figure (6.213): M_1 versus time for 100 rpm ($Re = 4.6*10^3$), 200 rpm ($Re = 9.3*10^3$) and 450 rpm ($Re = 2.1*10^4$).

- M_2

M_2 symbolise the total surface area of the particles in the system, Tables (6.17) to (6.21).

Time (s)	M_2 (m^2/m^3)
0	0
0.68	3.4E-23
1.37	2.9E-22
2.05	1.0E-21
5.49	2.2E-20
7.63	5.9E-20
10.65	1.6E-19
12.85	2.9E-19
15.80	5.4E-19
19.94	1.1E-18
25.79	2.4E-18
30.27	3.8E-18

Table (6.17): Total M_2 versus time, for 1 rpm (Re = 46).

Time (s)	M_2 (m^2/m^3)
0	0
0.09	7.3E-24
0.99	1.6E-20
1.98	1.3E-19
4.77	1.8E-18
6.11	3.7E-18
8.99	1.2E-17
10.34	1.8E-17
16.82	7.8E-17
19.15	1.2E-16
23.56	2.1E-16
30.13	4.5E-16

Table (6.18): Total M_2 versus time, for 100 rpm (Re = $4.6*10^3$) with laminar flow.

Figure (6.214) exhibits the change in the total surface area of the particles in the vessel with time. M_2 is proportional to Re number.

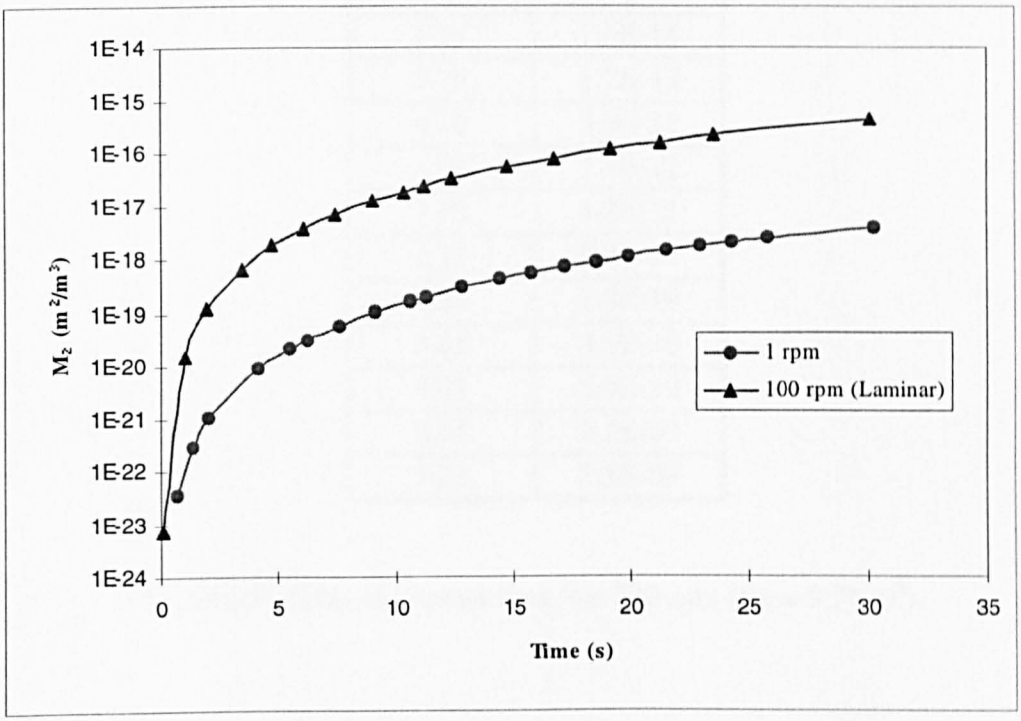

Figure (6.214): M_2 versus time for 1 rpm (Re = 46) and 100 rpm (Re = $4.6*10^3$).

Time (s)	M_2 (m^2/m^3)
0	0
0.22	2.9E-14
0.51	5E-13
0.91	3.1E-12
1.54	1.6E-11
2.01	3.9E-11
2.32	6.1E-11
2.92	1.3E-10
3.32	2E-10
4.05	3.8E-10
4.49	5.3E-10
5.13	8.2E-10

Table (6.19): Total M_2 versus time, for 100 rpm (Re = $4.6*10^3$) with turbulent flow.

Time (s)	M_2 (m^2/m^3)
0	0
0.17	1.5E-14
0.34	1.7E-13
0.79	3.0E-12
1.04	7.4E-12
1.70	4.2E-11
2.12	9.3E-11
2.54	1.8E-10
3.05	3.6E-10
3.48	5.9E-10
4.36	1.3E-09
5.22	2.5E-09

Table (6.20): Total M_2 versus time, for 200 rpm ($Re = 9.3*10^3$).

Time (s)	M_2 (m^2/m^3)
0	0
0.13	8.6E-15
0.61	2.1E-12
1.29	3.2E-11
1.69	8.6E-11
2.10	1.9E-10
2.50	3.5E-10
3.30	9.4E-10
3.71	1.4E-09
4.11	2.0E-09
4.52	2.7E-09
5.33	4.7E-09

Table (6.21): Total M_2 versus time, for 450 rpm ($Re = 2.1*10^4$).

Figure (6.215) reveals the change in M_2 with time where higher Re numbers give higher M_2 values.

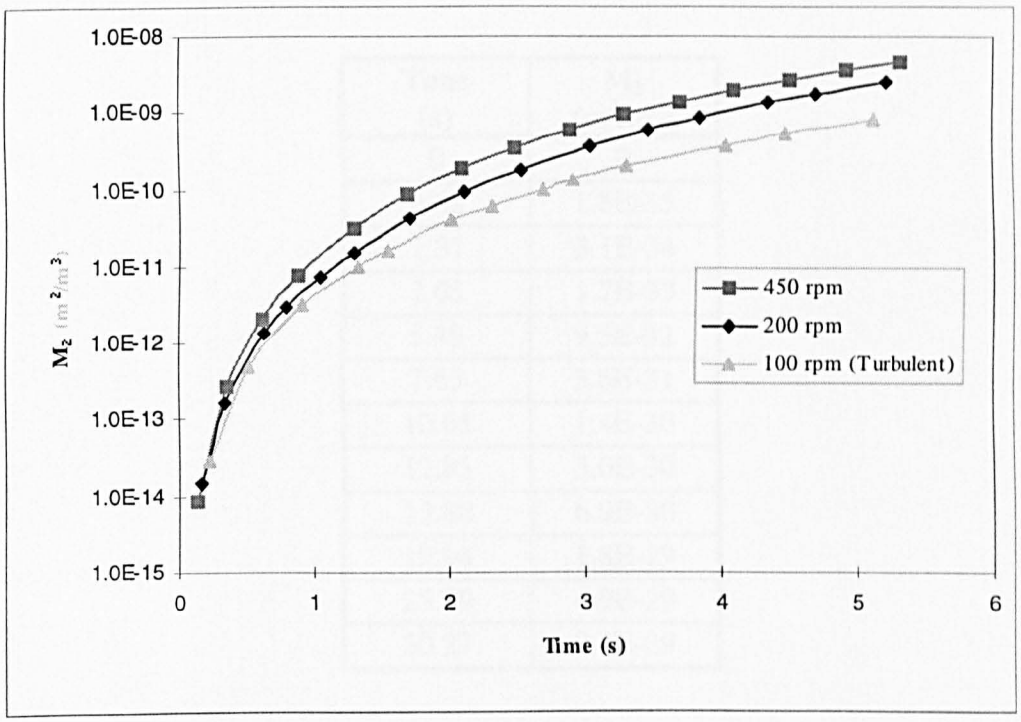

Figure (6.215): M_2 versus time for 100 rpm ($Re = 4.6*10^3$), 200 rpm ($Re = 9.3*10^3$) and 450 rpm ($Re = 2.1*10^4$).

- M_3

The third moment M_3 is a measure of the volume, and therefore the mass, of the particles in the vessel, Tables (6.22) to (6.26).

Time (s)	M_3 (m^3/m^3)
0	0
0.68	1.8E-35
1.37	3.1E-34
2.05	1.7E-33
5.49	9.5E-32
7.63	3.6E-31
10.65	1.4E-30
12.85	3.0E-30
15.80	6.9E-30
19.94	1.8E-29
25.79	4.9E-29
30.27	9.4E-29

Table (6.22): Total M_3 versus time, for 1 rpm (Re = 46).

Time (s)	M_3 (m^3/m^3)
0	0
0.09	1.6E-36
0.99	4.2E-32
1.98	6.9E-31
4.77	2.3E-29
6.11	6.4E-29
8.99	3.0E-28
10.34	5.2E-28
16.82	3.7E-27
19.15	6.1E-27
23.56	1.4E-26
30.13	3.8E-26

Table (6.23): Total M_3 versus time, for 100 rpm (Re = $4.6*10^3$) with laminar flow.

Figure (6.216) follows a similar trend of Figures (6.211) and (6.213) where M_3 is proportional to Re number.

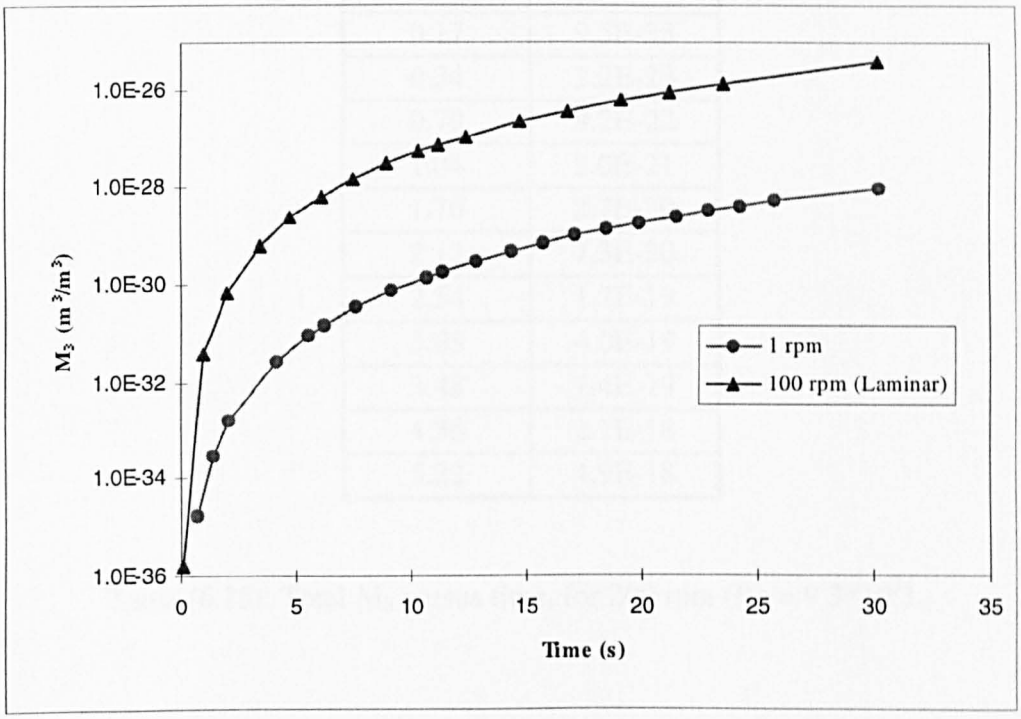

Figure (6.216): M_3 versus time for 1 rpm (Re = 46) and 100 rpm (Re = $4.6*10^3$).

Time (s)	M_3 (m^3/m^3)
0	0
0.22	2.3E-24
0.51	1.0E-22
0.91	1.2E-21
1.54	1.0E-20
2.01	3.1E-20
2.32	5.7E-20
2.92	1.5E-19
3.32	2.6E-19
4.05	6.1E-19
4.49	9.4E-19
5.13	1.7E-18

Table (6.24): Total M_3 versus time, for 100 rpm (Re = $4.6*10^3$) with turbulent flow.

Time (s)	M_3 (m^3/m^3)
0	0
0.17	9.5E-25
0.34	2.2E-23
0.79	9.2E-22
1.04	3.0E-21
1.70	2.7E-20
2.12	7.3E-20
2.54	1.7E-19
3.05	4.0E-19
3.48	7.4E-19
4.36	2.1E-18
5.22	4.9E-18

Table (6.25): Total M_3 versus time, for 200 rpm ($Re = 9.3*10^3$).

Time (s)	M_3 (m^3/m^3)
0	0
0.13	4.2E-25
0.61	4.8E-22
1.29	1.5E-20
1.69	5.3E-20
2.10	1.4E-19
2.50	3.3E-19
3.30	1.2E-18
3.71	2.0E-18
4.11	3.1E-18
4.52	4.7E-18
5.33	9.6E-18

Table (6.26): Total M_3 versus time, for 450 rpm ($Re = 2.1*10^4$).

Again Figure (6.217) shows $M_3 \propto Re$.

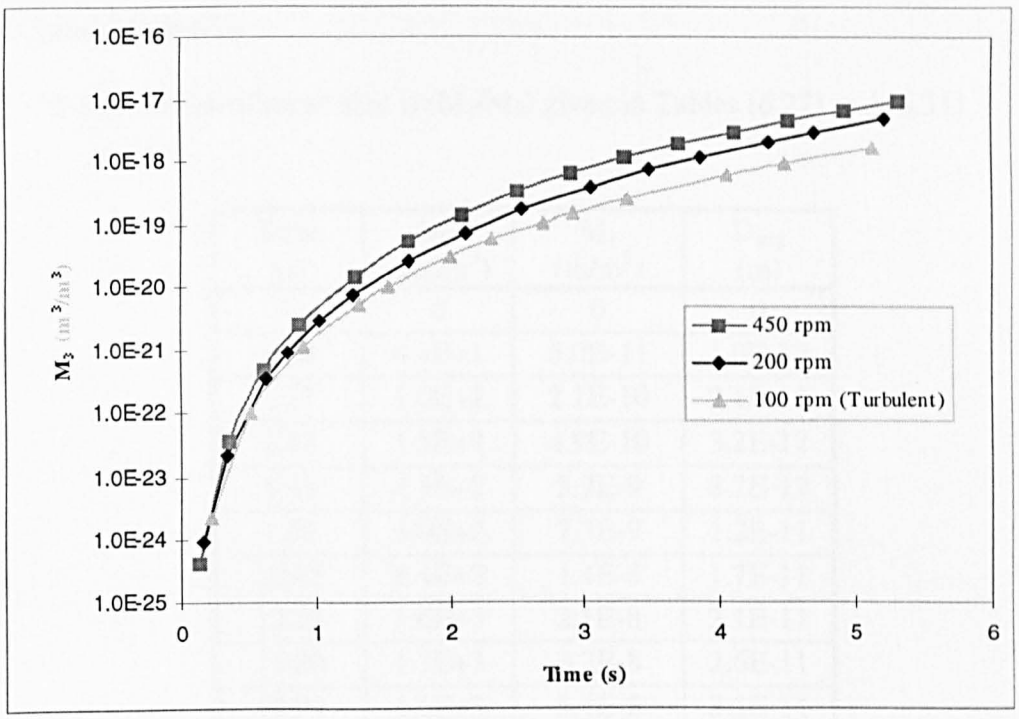

Figure (6.217): M_3 versus time for 100 rpm ($Re = 4.6*10^3$), 200 rpm ($Re = 9.3*10^3$) and 450 rpm ($Re = 2.1*10^4$).

- **Crystal Mean Size**

A number-based mean size is (M_1/M_0) given in Tables (6.27) and (6.31).

Time (s)	M_0 (no./m^3)	M_1 (m/m^3)	D_{avg} (m)
0	0	0	0
0.68	4.9E+1	5.0E-11	1.0E-12
1.37	1.0E+2	2.1E-10	2.1E-12
2.05	1.5E+2	4.9E-10	3.2E-12
5.49	4.3E+2	3.7E-9	8.7E-12
7.63	6.0E+2	7.3E-9	1.2E-11
10.65	8.4E+2	1.4E-8	1.7E-11
12.85	1.0E+3	2.1E-8	2.1E-11
15.80	1.3E+3	3.2E-8	2.6E-11
19.94	1.6E+3	5.1E-8	3.2E-11
25.79	2.0E+3	8.5E-8	4.2E-11
30.27	2.4E+3	1.2E-7	4.9E-11

Table(6.27): Average mean size calculated from M_0 and M_1, for 1 rpm (Re = 46).

Time (s)	M_0 (no./m^3)	M_1 (m/m^3)	D_{avg} (m)
0	0	0	0
0.09	7.1E+1	2.6E-11	3.7E-13
0.99	7.9E+2	4.3E-9	5.4E-12
1.98	1.6E+3	1.7E-8	1.1E-11
4.77	3.8E+3	1.0E-7	2.6E-11
6.11	4.9E+3	1.7E-7	3.4E-11
8.99	7.2E+3	3.6E-7	5.0E-11
10.34	8.3E+3	4.7E-7	5.7E-11
16.82	1.3E+4	1.3E-6	9.3E-11
19.15	1.5E+4	1.6E-6	1.1E-10
23.56	1.9E+4	2.5E-6	1.3E-10
30.13	2.4E+4	4.0E-6	1.7E-10

Table(6.28): Average mean size calculated from M_0 and M_1, for 100 rpm (Re = $4.6*10^3$), laminar flow.

Figure (6.218) indicates higher mean size for higher Re numbers following the same behaviour of the moments.

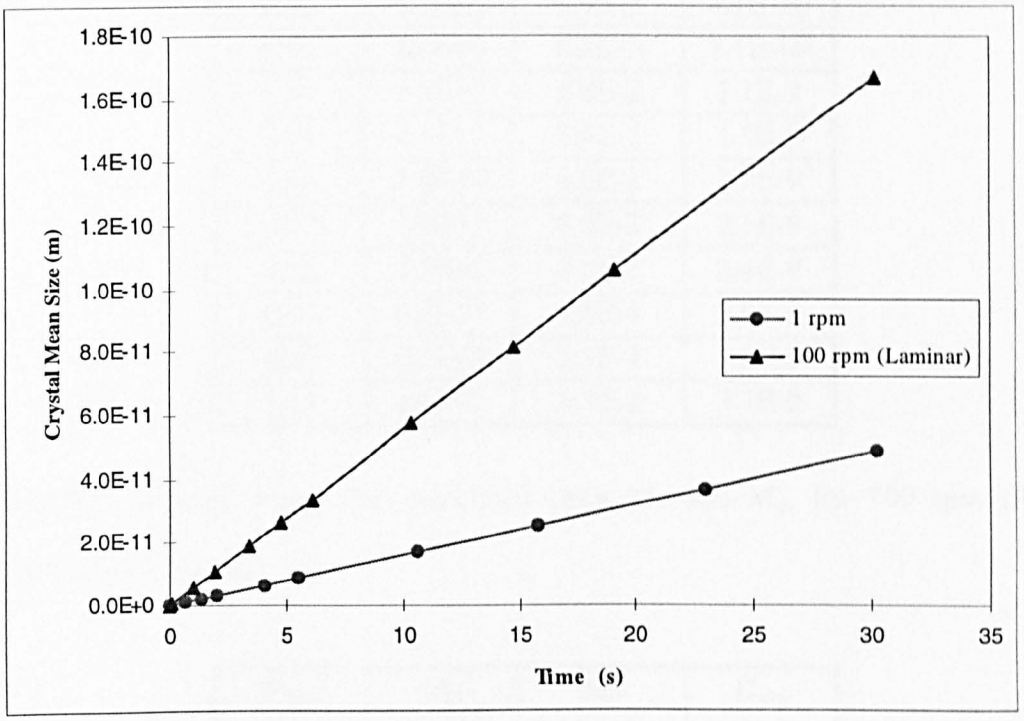

Figure (6.218): Average mean size versus time, for 1 rpm (Re = 46) and 100 rpm (Re = $4.6*10^3$).

Time (s)	M_0 (no./m^3)	M_1 (m/m^3)	D_{avg} (m)
0	0	0	0
0.22	1.7E+6	2.7E-4	1.6E-10
0.51	4.5E+6	1.8E-3	4.1E-10
0.91	8.8E+6	6.2E-3	7.1E-10
1.54	1.8E+7	2.0E-2	1.1E-9
2.01	2.5E+7	3.6E-2	1.5E-9
2.32	2.9E+7	5.0E-2	1.7E-9
2.92	4.0E+7	8.5E-2	2.1E-9
3.32	4.7E+7	1.1E-1	2.4E-9
4.05	6.1E+7	1.8E-1	2.9E-9
4.49	7.0E+7	2.3E-1	3.3E-9
5.13	8.4E+7	3.1E-1	3.7E-9

Table(6.29): Average mean size calculated from M_0 and M_1, for 100 rpm (Re = $4.6*10^3$), turbulent flow.

Time (s)	M_0 (no./m^3)	M_1 (m/m^3)	D_{avg} (m)
0	0	0	0
0.17	1.7E+6	1.9E-4	1.1E-10
0.34	4.1E+6	1.0E-3	2.4E-10
0.79	1.3E+7	7.4E-3	5.5E-10
1.04	2.1E+7	1.4E-2	7.0E-10
1.70	4.9E+7	5.2E-2	1.1E-9
2.12	7.3E+7	9.5E-2	1.3E-9
2.54	1.0E+8	1.6E-1	1.6E-9
3.05	1.4E+8	2.6E-1	1.9E-9
3.48	1.7E+8	3.7E-1	2.2E-9
4.36	2.3E+8	6.6E-1	2.9E-9
5.22	2.8E+8	1.0E+0	3.6E-9

Table(6.30): Average mean size calculated from M_0 and M_1, for 200 rpm (Re = $9.3*10^3$).

Time (s)	M_0 (no./m^3)	M_1 (m/m^3)	D_{avg} (m)
0	0	0	0
0.13	1.7E+6	1.4E-4	8.3E-11
0.61	1.8E+7	7.1E-3	3.9E-10
1.29	6.6E+7	5.4E-2	8.1E-10
1.69	1.0E+8	1.1E-1	1.1E-9
2.10	1.4E+8	1.9E-1	1.4E-9
2.50	1.7E+8	3.0E-1	1.7E-9
3.30	2.5E+8	5.8E-1	2.4E-9
3.71	2.8E+8	7.6E-1	2.7E-9
4.11	3.2E+8	9.6E-1	3.0E-9
4.52	3.6E+8	1.2E+0	3.3E-9
5.33	4.3E+8	1.7E+0	4.0E-9

Table(6.31): Average mean size calculated from M_0 and M_1, for 450 rpm (Re = $2.1*10^4$).

Figure (6.219) demonstrates the variation of the mean size with time. At the beginning of the process, low Re number systems give higher mean size values. This is because at that time, there is less number of particles which share a high supersaturation region. This would allow the particles to grow more. After a reasonable time the effect of the hydrodynamics comes into play, where the micromixing is enhanced and therefore high Re number systems give larger mean size for some time.

It can be noticed that the mean crystal sizes from the CFD simulations are too small compared with the molecular size (~ 2 Å) and the critical particle size (see Appendix 6) of $CaCO_3$. This is attributed to the fact that the initial crystal size is

assumed to be zero (as is common in MSMPR theory, for example) and the time of the simulation is not yet large enough to allow the crystals to grow to a realistic size.

Figures (6.220) and (6.221) provide another way of comparison between the different studied systems. The mean size is given in term of M_3 which is proportional to the mass of particles. In each figure, the lower the Re number, the larger the mean size.

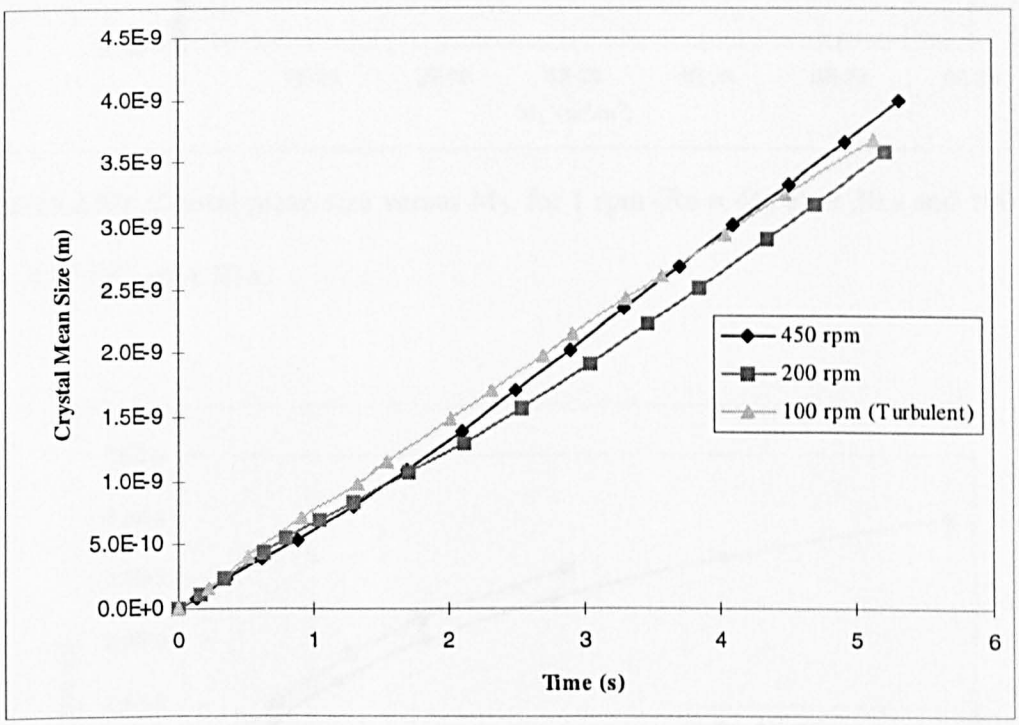

Figure (6.219): Average mean size versus time, for 100 rpm (Re = $4.6*10^3$), 200 rpm (Re = $9.3*10^3$) and 450 rpm (Re = $2.1*10^4$).

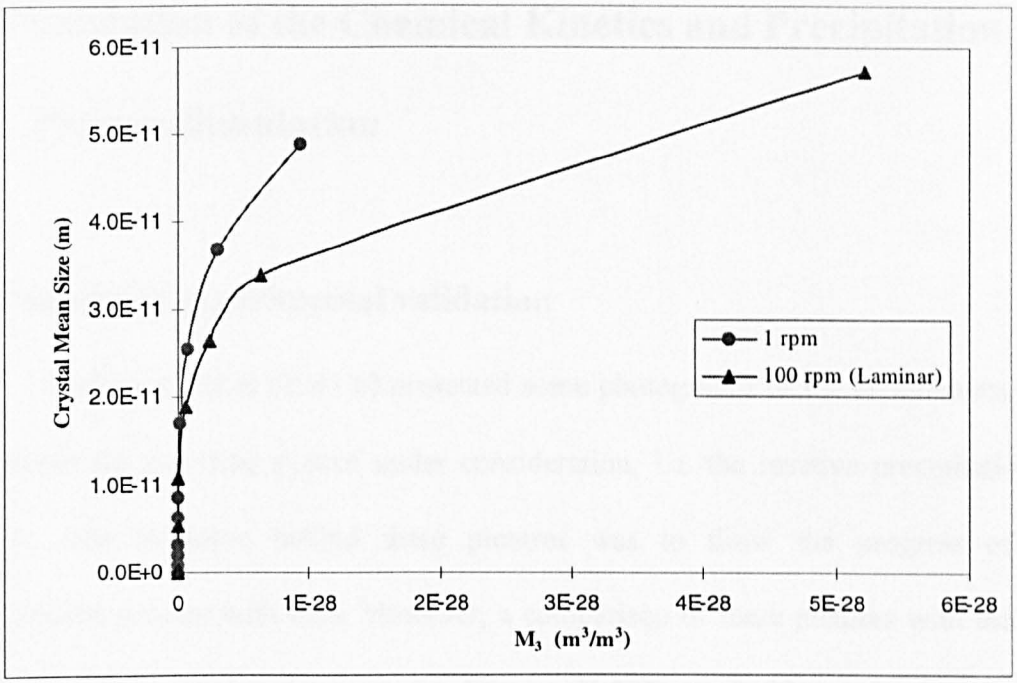

Figure (6.220): Crystal mean size versus M_3, for 1 rpm (Re = 46) after 30 s and 100 rpm (Re = $4.6*10^3$) after 10 s.

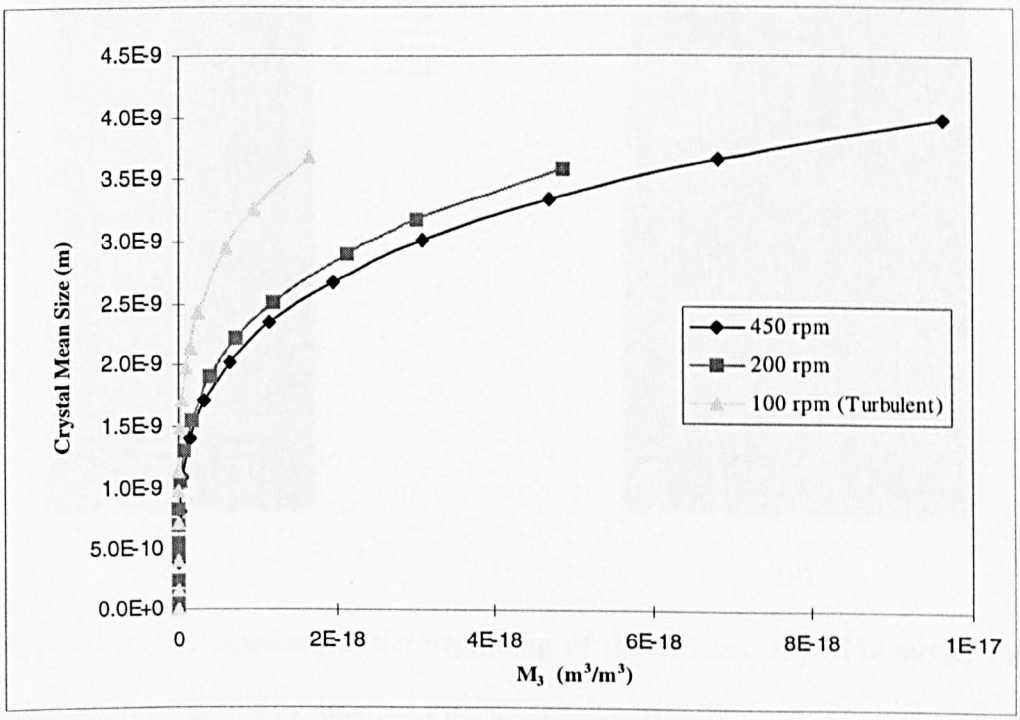

Figure (6.221): Crystal mean size versus M_3 after 5 s, for 100 rpm (Re = $4.6*10^3$), 200 rpm (Re = $9.3*10^3$) and 450 rpm (Re = $2.1*10^4$).

6.5. Validation of the Chemical Kinetics and Precipitation Process Simulation

- **Qualitative experimental validation**

Wachi and Jones (1991 b) presented some photographs of the experiments they performed for the same system under consideration, i.e. the reactive precipitation of $CaCO_3$. The objective behind these pictures was to show the progress of the precipitation process with time. However, a comparison of these pictures with the 2-D CFD simulation results, as given by Figures (6.222) to (6.224), proposes a good agreement.

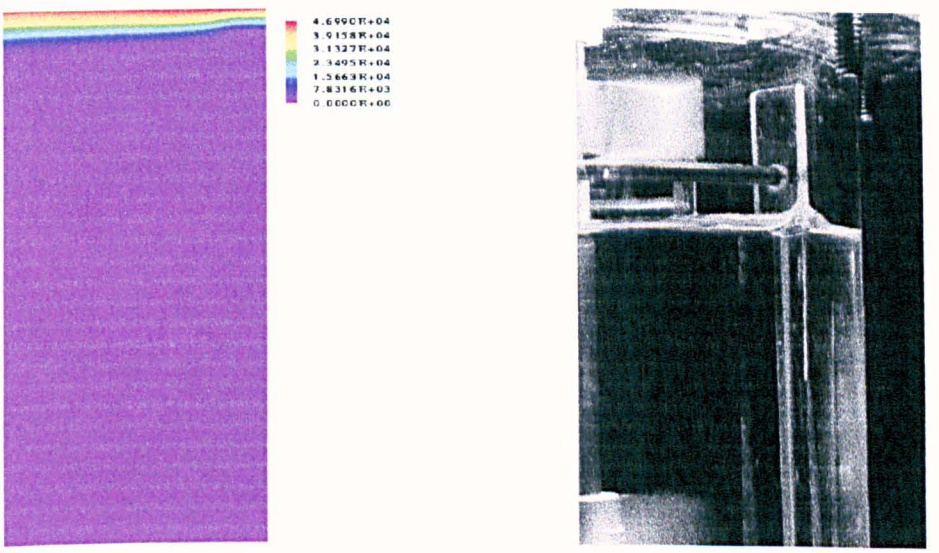

(a) (b)

Figure (6.222): The interface at the beginning of the process, (a) CFD model for M_0 (450 rpm, t = 0.1 s and (b) a picture of the experiment (t = 0).

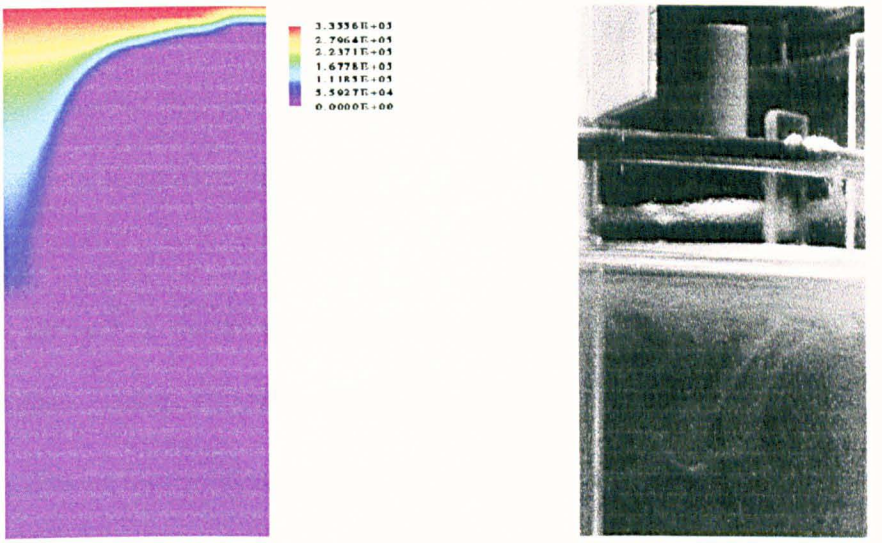

(a) (b)

Figure (6.223): Particles start to disperse into the bulk from the interface region, (a) M_0 from CFD model (450 rpm, t = 1 s) and (b) a picture of the experiment after 1 mins.

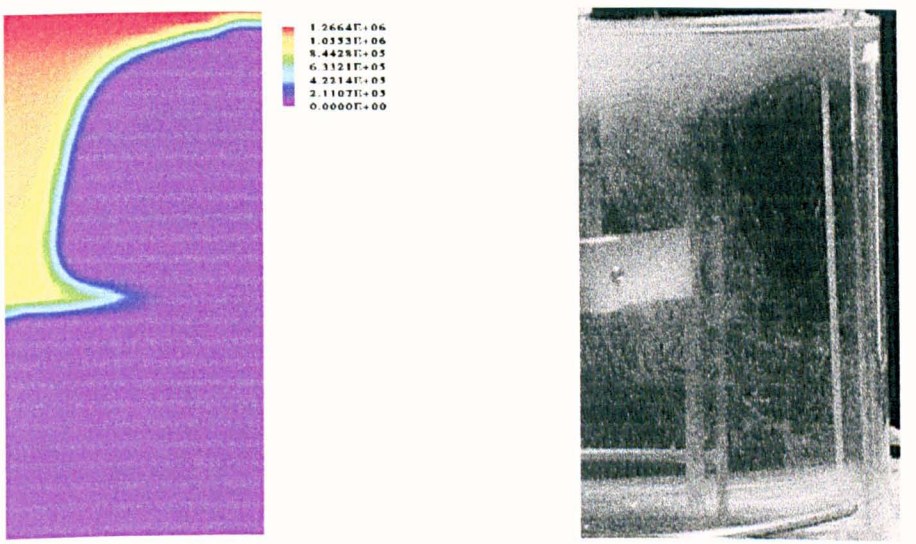

(a) (b)

Figure (6.224): More particles appear in the system following the flow pattern, (a) M_0 from CFD model (450 rpm, t = 10 s) and (b) a picture of the experiment after 3 mins.

Although the crystal mean size from the CFD simulation is too small to be seen it indicates, however, that once the particles reach the observable size, they will appear in the experimentally observed regions.

As implied in the above figures, the precipitated particles of $CaCO_3$ tends to follow the flow pattern. At the tip of the impeller the flow speed vectors proceed in the radial direction until they hit the wall of the vessel where they split into two circulations, above and below the mid-plane of the impeller. In the upper circulation, the speed vectors hit the interface at the right corner therefore the precipitated particles have less chance to disperse into the bulk from that side. However, the flow continues its journey from the right corner to be parallel to the interface for a short distance and then starts to come down to complete the circulation. The flow, on its way to the interface, brings fresh reactants and carries the precipitated particles into the bulk of the liquid. Figure (6.225) highlights the progress of this behaviour through CFD images of speed vectors superimposed on supersaturation contours .

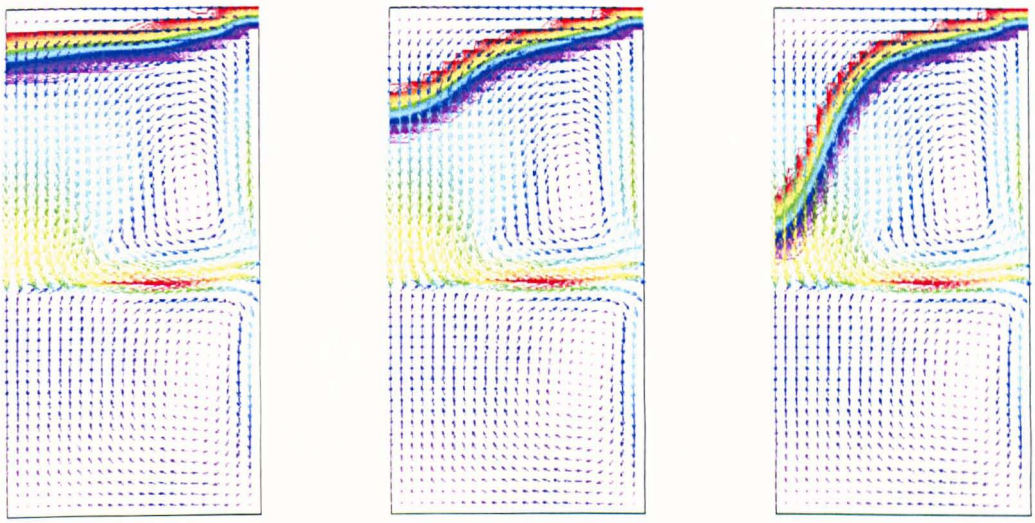

(a) (b) (c)

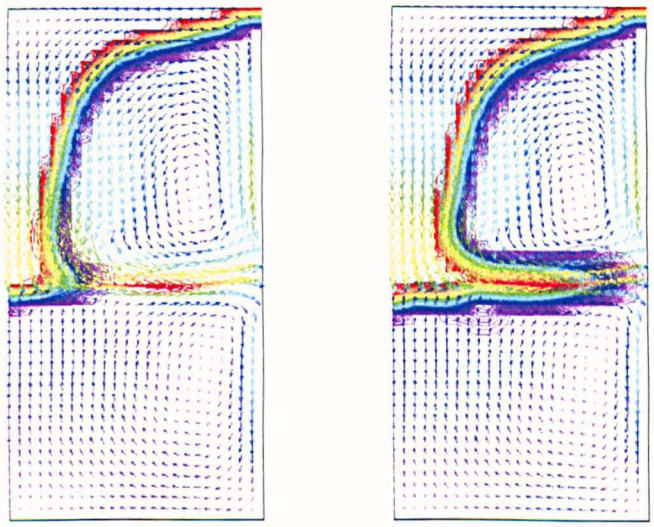

(d) (e)

Figure (6.225): CFD images of speed vector (m/s) superimposed on supersaturation (mol/m^3) contours ($Re = 2.1*10^4$), for t = 0.04, 0.4, 0.6, 0.9 and 10.0 s for a, b, c, d and e, respectively.

- **Mass Balance**

A mass balance check between the solid and liquid phases is performed in the CFD simulation. If there is significant change then the simulation does not converge. Water is specified as a background fluid which means that its concentration is not calculated from a transport equation but is estimated by setting the water mass fraction equal to the difference between unity and the sum of the mass fractions of the other species. The only addition to the system is the carbon dioxide flow rate, therefore the overall added mass to the system is unreacted CO_2 and produced $CaCO_3$. To carry out this calculations on a specific example, the last run of the 450 rpm (Re = $2.1*10^4$) system is selected, see Appendix (7). The concentrations of unreacted CO_2, unreacted $Ca(OH)_2$ and produced $CaCO_3$, are 11.480, 1.360 and 1.360 mol/m^3, respectively and H_2O concentration is 55.3 $kmol/m^3$. This gives an approximately error of 0.02% overall, which is negligible.

The atomic balance of Ca in the system also can be tested to check if there is any difference in the Ca atoms in the system, as follows:

Initial = Final

5.17 mol Ca / mol $Ca(OH)_2$ = 1.36 mol Ca / mol $CaCO_3$ + 3.81 mol Ca / mol $Ca(OH)_2$

Therefore, the system is conservative with respect to Ca atoms.

If the added mass to the system is significant, however, then a mass source should be included in the CFD simulation to account for that.

- **CFD Simulation and Film and Penetration Theories**

A comparison between the penetration and film theories is reported by Hostomský and Jones (1995). Their penetration theory model calculates the bulk supersaturation, bulk mean size and the number of crystals in the bulk and at the interface. Whereas only the mean size is accounted for from the film theory model, Figures (6.226) to (6.229).

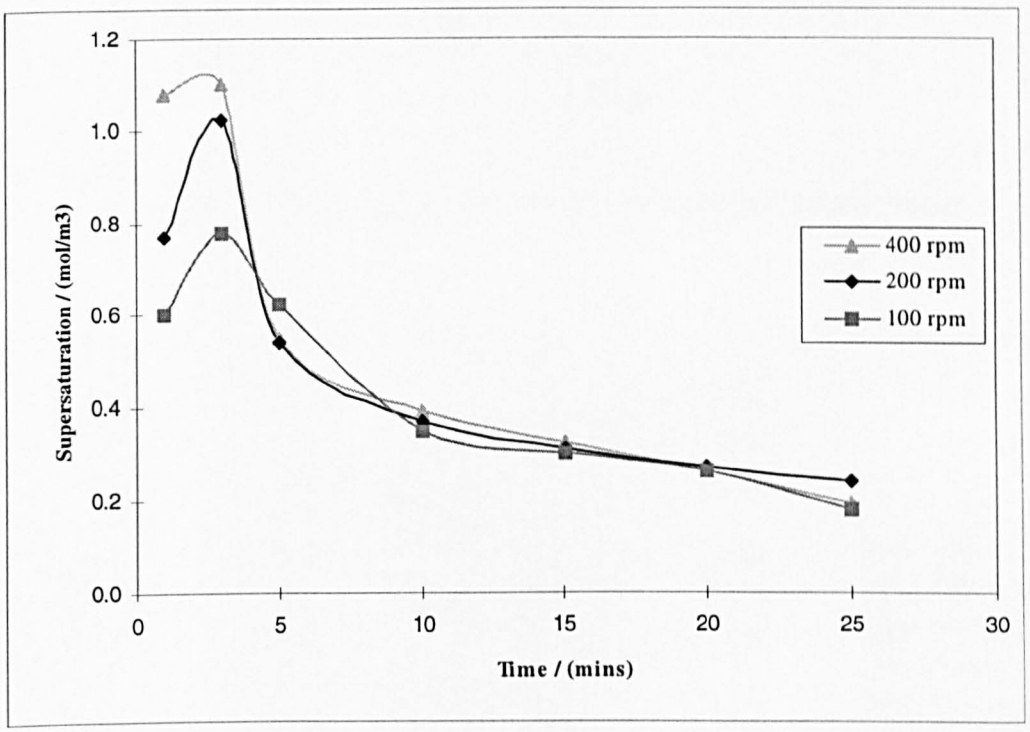

Figure (6.226): Bulk supersaturation versus time from the penetration theory (after Hostomský and Jones, 1995).

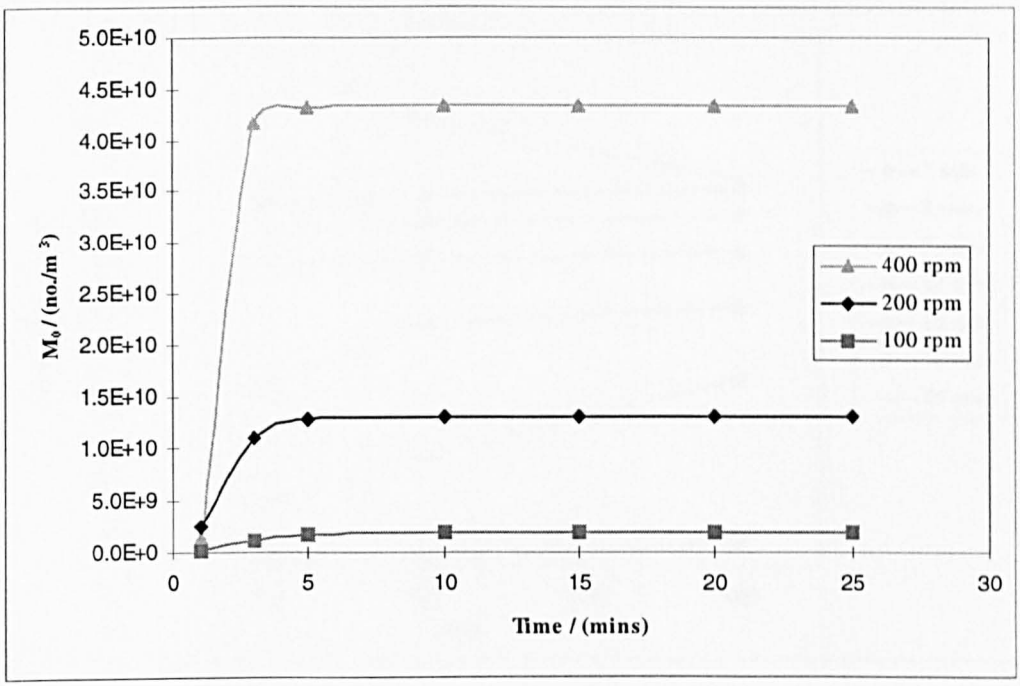

Figure (6.227): M_0 in the bulk versus time from the penetration theory.

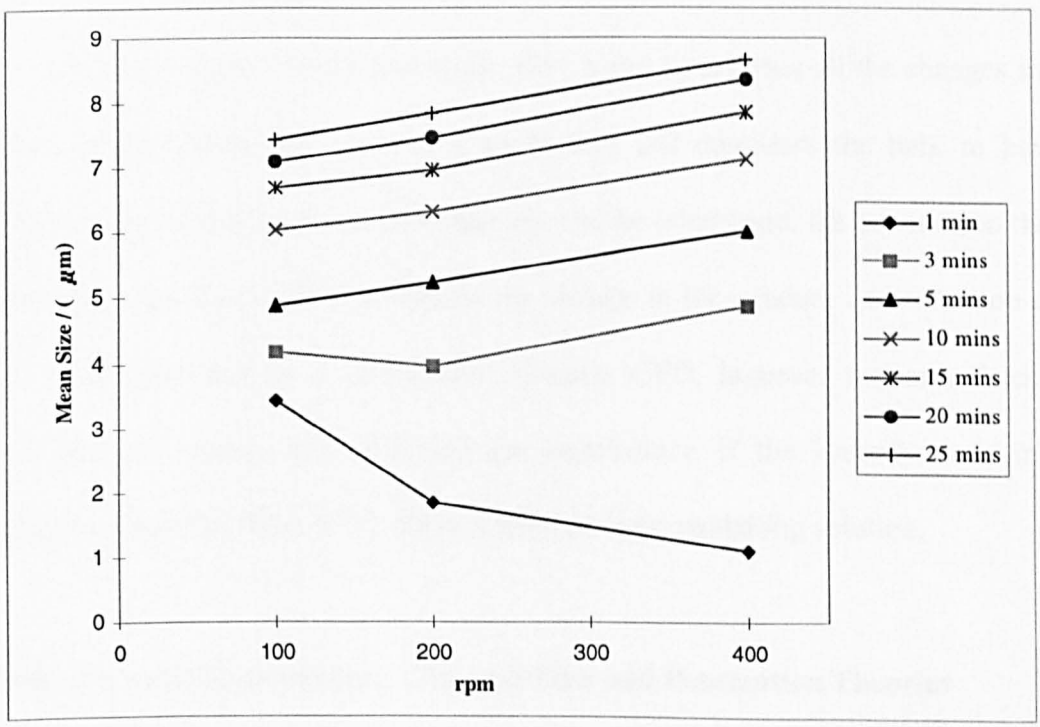

Figure (6.228): Crystal mean size versus stirrer speed from penetration theory.

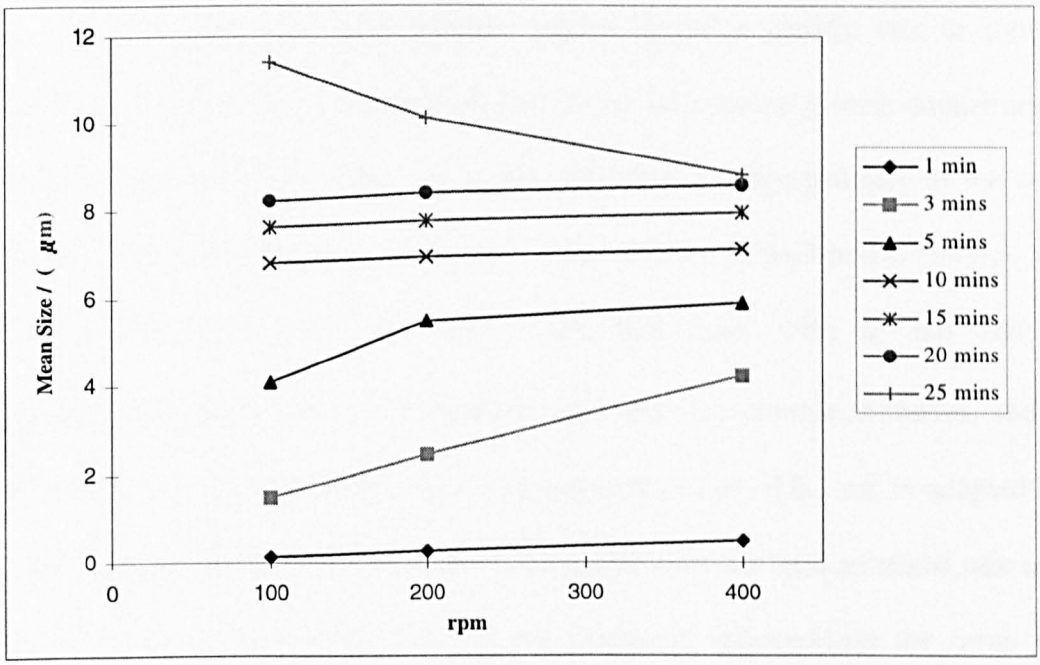

Figure (6.229): Crystal mean size versus stirrer speed from film theory (after Wachi and Jones, 1991 a and b).

The film theory (Wachi and Jones, 1991 a and b) assumes all the changes in the product concentration take place in a small film and considers the bulk to have a uniform concentration of the reaction species. On the other hand, the penetration theory (Hostomský and Jones, 1995) considers the change in the product concentration on a larger scale presented by a penetration distance. CFD, however accommodates the whole range of change and illustrates the significance of the hydrodynamic in the precipitation process. Thus, CFD offers a more realistic modelling solution.

- **Direct Comparison Between CFD and Film and Penetration Theories**

In order to compare the CFD results directly with the film and penetration theories, these theories need to be examined at the same (smaller) CFD time scale in this project.

The film and penetration theories require an initial particle size to start the calculations. The concept of the critical size where the particle growth commences is reported in literature. Nevertheless, it is not more than a rough estimate of the actual size. This value, for example, is calculated to be ~ 0.2 nm (from Mullin, 1993), ~ 0.25 μm (from Mersmann, 1995), 0.5 μm (Wachi and Jones, 1991 a) and 0.01 μm (Hostomský and Jones, 1995), see Appendix (6). For convenience, however, and not overestimating the critical particle size, a conservative value of 0.1 nm is adopted here for both theories. On the other hand, the CFD model does not need an initial size and a value in the range of 0 to 0.1 nm has no significant influence on the mean size, therefore, the initial size is taken as 0 for simplicity.

Figure (6.230) shows the results of the CFD simulation, film and penetration theories using the same reaction and precipitation kinetics, see Appendix (1 and 8). The film theory performance indicates that the mean size is dominated by the nucleation process in the film, i.e. high supersaturation. Therefore, the variation in the mean size is small, for the given time. The penetration theory on the other hand demonstrates the domination of growth process in the bulk. At the same time, the penetration theory utilises almost all the bulk region for the precipitation process. Consequently, it underestimates local supersaturation and hence nucleation and thereby overestimates the mean size of the particles over the model time. CFD simulation results, however, show only a portion of the bulk is used during the precipitation process, see Figure (6.154). Thus, it predicts an intermediate behaviour between the other two theories.

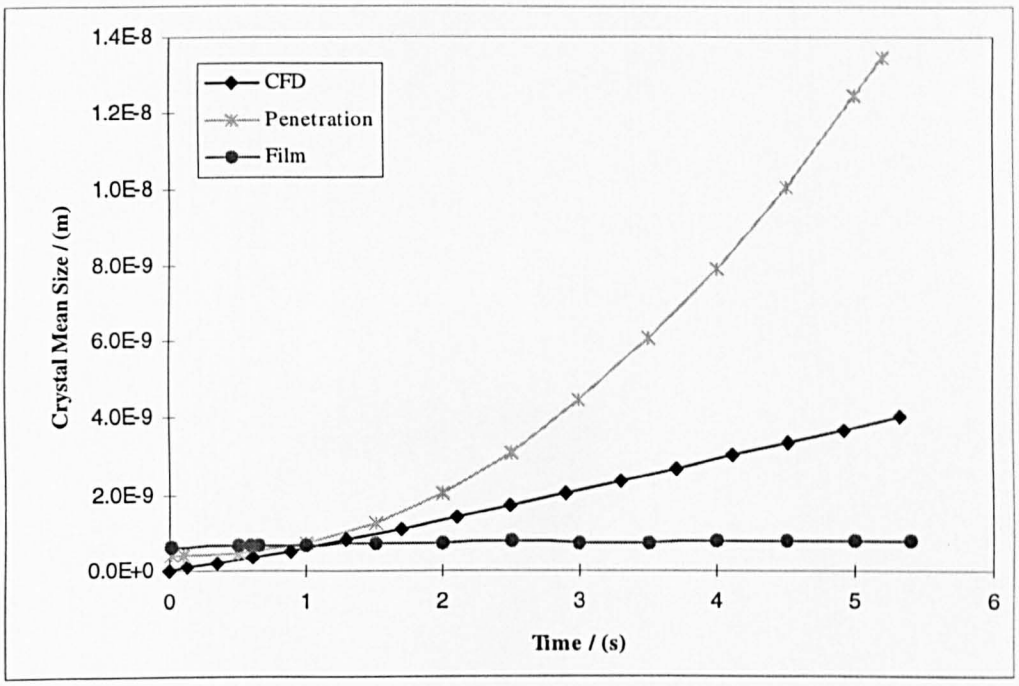

Figure (6.230): Crystal mean size against time for CFD simulation, film and penetration theories.

Although the CFD simulations presented here are for a few seconds only, they display the interactions between the chemical and precipitation kinetics and the hydrodynamics of the system. If sufficient computing resources are available, however, CFD can provide the proper alternative from any other up-to present theory.

7

CONCLUSIONS

7. CONCLUSIONS

This study adopts the CFD technique (using CFX package of AEA Technology) to model the batch carbonation of lime. A 3-D CFD hydrodynamic model is presented as a verification of the mixing process in the system. A 1.357 litre vessel with two types of impellers, namely two-blade paddle and 45° pitched blade impeller, is applied to investigate the performance of the mixing process and the reliability of the CFD solution. The CFD hydrodynamic simulations utilise the momentum source method in the modelling of the impellers. Reynolds differential stress model is employed to describe the turbulence in the system. This turbulent model accounts for the swirling flows in stirred tanks which makes it a preferred alternative to the traditional k-ε model.

The CFD hydrodynamic results, however, are validated qualitatively using an image analysis and quantitatively by applying Flow number calculations for both models. The image analysis and the CFD results show two circulation loops above and below the mid-plane of the two-blade paddle. Nevertheless, experimentally, the mid-plane is shifted from its central position which is may be caused by the imperfect mixing in the vessel and/or the different boundary conditions between the top and bottom of the vessel.

The pitched blade model shows the discharge taking an angle significantly different from the blades angle. The experimental data from the literature (e.g., Bakker *et al.*, 1996 and Rutherford *et al.*, 1996) support this behaviour which may be related to

the geometry and internals of the mixing vessel. Also, the Reynolds differential stress model performs better, in the stirred tanks, than the k-ε and k-ε RNG turbulence models as shown from the comparison with the literature.

A comparison is given between the CFD calculated Flow number and the literature values, see Table (6.1). A very good agreement with less than 9% difference between the CFD and literature results for the paddle, 0.61 and 0.56, respectively, is obtained. The pitched blade also shows adequate consistency with the literature data.

The precipitation process involves carbon dioxide which is supplied, at a constant rate, to the interfacial region of an aqueous solution of calcium hydroxide to produce calcium carbonate. The chemical and precipitation kinetics of this system are studied using a 2-D CFD model. This model accommodates two new CFD areas. First, the transient reactive precipitation process in a stirred tank. Second, the chemical kinetics which exposes the influence of micromixing on the precipitation processes. This simulation assumes single (liquid) phase process as the carbon dioxide is presented in the boundary condition of the problem. At the same time, it is proposed that there is no change in the interface level where the reaction is taking place.

The precipitation kinetics studied in this project are supersaturation, primary nucleation and size-independent crystal growth. Consequently, the first four moments, i.e. M_0, M_1, M_2 and M_3, are determined. Four different stirrer speeds (or Re numbers) are implemented in this project to study the effect of the hydrodynamics on the precipitation processes. Due to the limitation of the available equipment to run the CFD

package, the real time of the simulation is hampered to only 30 s and 5 s for laminar and turbulent cases, respectively.

The first system is taken as 1 rpm (Re = 46) as an approximation to stagnant flow because of computational reasons. If there is no flow in the system, then the CFD will have some problems in converging. Therefore, the CFD computations need to be triggered by some sort of a flow motion. The second is 100 rpm ($Re = 4.6*10^3$) which is neither laminar nor turbulent. Hence, it is modelled once as laminar and then as turbulent to demonstrate the predominance of turbulence on the mixing quality and then the precipitation kinetics. A critical difference is noticed by the presence of the turbulence in the system which enhances the micromixing. The CFD results reveal a better estimation of the process is provided by the turbulent model for this stirrer speed.

The CFD simulations of the laminar cases show the product ($CaCO_3$) stays at the interfacial region for the whole time of the simulations (30 s). Also, these simulations offer detailed information about supersaturation, nucleation rate, crystal growth rate, moments and crystal mean size.

The three turbulent simulations display different results where the product, after some time, continue its progress away from the interface. The velocity vectors as they approach the interface from the RHS, they bring new (fresh) reactant materials to the reaction zone, i.e. the interfacial region, and remove the product to the bulk of the liquid from the LHS. This behaviour coincides with the experimental pictures reported at longer times by Wachi and Jones (1991b), see Figure (6.224).

In addition, the number (as well as the surface area and the volume) of particles is higher at the interface and decreases as it proceeds into the bulk of the liquid. On the other hand, the crystal mean size from the CFD results is too small. Nonetheless when they reach the observable size, the particles will appear in the regions predicted by the CFD simulations. The overall mass balance estimates approximately 0.02% error which is negligible to affect the convergence of the problem. However, the atomic Ca balance shows no notable change in the Ca concentration in the system.

Adaptive time stepping is used because the reaction time scale is not completely defined. The time step is in the range of 0.4-0.425 ms for the laminar cases and 0.03-0.06 ms for turbulent problems.

A validation of the chemical kinetics and precipitation process CFD simulation is carried out by a comparison with the film and penetration theories for the same time period as the CFD simulation. These two theories demonstrate nucleation dominated and growth dominated processes, respectively. Therefore, the film theory predicts a very small change in the mean crystal size and penetration theory presents an overestimation of it for the given time. The CFD simulation on the other hand predicts an intermediate performance giving a more realistic behaviour than the two previous theories.

Although the CFD predictions are for only few seconds real time, they look encouraging and indicate the feasibility of CFD in modelling the reactive precipitation

processes. The presented chemical kinetics and precipitation process simulation builds the foundation link between the CFD and the reactive precipitation processes.

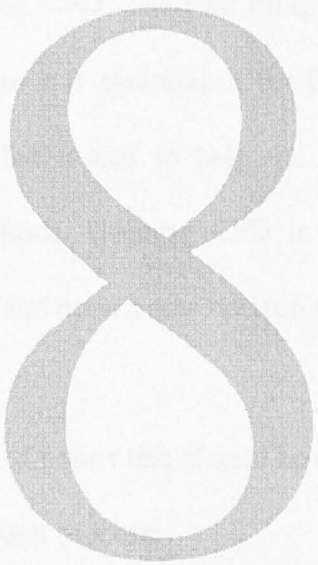

RECOMMENDATIONS & FUTURE WORK

8. RECOMMENDATIONS AND FUTURE WORK

• Recommendations

This section will highlight the main guidelines in the modelling of reactive precipitation processes using CFD. The first thing to remember is, to understand the problem beforehand because it is essential in the CFD modelling. As well as the fact that the CFD is nothing but a tool to help the researcher to visualise the details concerning the flows of fluids. Utilising CFD in the correct manner, however will improve our understanding and open a new horizon in the modelling approaches.

There are a number of points that should be considered in the CFD modelling of a specific reactive precipitation process:

- ➤ Make a literature survey on the system to be studied.
- ➤ Choose a simplified geometry and preferably a 2-D to start with.
- ➤ Collect the physical properties of the species involved in the reaction as well as the chemical kinetics of the reaction itself.
- ➤ Study the relevant CFD built-in subroutines and select the one which needs minimum alterations.
- ➤ Avoid impossible subroutine combinations which are usually listed in the manuals of the CFD package.
- ➤ Apply the minimum possible number of variables in the first run.
- ➤ Define the boundary conditions of the problem and use other alternatives if needed, e.g. specifying the free surface as a wall with zero shear stresses.

- If the flow is turbulent, introduce the proper turbulent model which depends on the application in hand.
- Run the hydrodynamic model only for the first instant and make sure that it gives reasonable results.
- Employ the chemical kinetics and precipitation process model on the basis of the previous hydrodynamic model and switch-off the hydrodynamic equations. This will save a lot of CFD computational time.
- Investigate the number of iterations, for steady-state. It is recommended not to start with high numbers, however 200 to 500 iterations are advisable. For unsteady-state, the knowledge of the time scale of the reaction is required. If the process is well defined, then use the fixed time stepping where the exact time step and the number of steps are to be specified. If not, then apply the adaptive time stepping in which the user should only give initial estimation for the time step. Also, the number of the time steps and number of iterations are necessary, typically 200 and 50, respectively.
- Utilise the on-line active convergence plot and mark the parameters which do not converge.
- Alter the equation solvers if it has an influence on the convergence. Nonetheless, always start with default solvers.
- Use the transient control option, in transient problems, if the model does not converge with respect to a specific parameter.
- change the time step and check how sensitive the system is with respect to it. Usually the time step has a great influence on the convergence of the problem.

• Future Work

Using better computation facilities, the model developed in this work can be run for a longer time and in 3-D to predict the behaviour of the system even better. The 2-D simulation is ready in its present state, with only few trivial changes, to be applied on the 3-D model or even on the draft baffled tube (DBT) crystallizer model of AEA Technology.

Agglomeration has a significant presence in the precipitation processes, therefore, the next development should incorporate the agglomeration kinetics. The model can be extended more to accommodate secondary nucleation and size-dependent crystal growth.

The model predicts the precipitation rate from a reaction commencing at an interfacial region. The same principle can be employed to study the bubble column systems where the reaction is also commencing at an interface, i.e. the bubble surface. This means that the present CFD simulation can be introduced on a microscale to predict the precipitation process.

Investigating the possibility of including multi-phase behaviour in the model, would be advantageous. Especially if the system has a considerable amount of particulate material with a large crystal mean size so that the particles do not follow the flow pattern of the fluid.

9

NOMENCLATURE

9. NOMENCLATURE

σ: Interfacial energy, standard deviation, turbulent Prandtl number.

ω: Mass fraction of solute in solution.

ω: Constant angular velocity.

α: Constant, coefficient of expansion, volume to length shape factor.

β: Constant, coefficient of expansion, surface to length shape factor.

θ: Dimensionless residence time.

δ: Film thickness.

ρ: Fluid density.

ρ_c: Crystal density.

μ: Chemical potential of the solute, fluid dynamic viscosity.

μ^*: Chemical potential at saturation.

μ_{eff}: Effective viscosity.

μ_T: Turbulent viscosity.

ν: Kinematic viscosity, number of ions formed from one mole of electrolyte.

γ: Parameter determined experimentally, interfacial tension of the solid in contact with the solution.

ϕ: A property.

ϕ: Pressure-strain correlation term.

ε:	Fraction of the available energy transmitted to the crystal, screw dislocation activity, stirrer energy dissipation rate.
τ:	Mean residence time, stress term, turbulent stress.
a:	Numerical constant
A:	pre-exponential constant, surface area, constant.
b:	Constant.
B:	Particle birth function, dimensionless driving force for mass transfer, constant.
B:	Body force vector.
B°:	Nucleation rate.
c:	Solute concentration.
c*:	Solute concentration at equilibrium.
cv:	Coefficient of variation.
C:	Constant, constant in Reynolds stress equations.
C_P:	Heat capacity.
D:	Particle death function, impeller diameter.
D_A:	Molecular diffusivity, diffusivity of dissolved gas A.
D_{avg}:	Crystal mean size.
D_B:	Diffusivity of reactant B.
D_c:	Diffusion coefficient.
E:	Impact energy.
E_G:	Activation energy.

F: Feed rate, azimuthal reaction force of the fluid on the impeller, volumetric body force.

F_x,F_y,F_z: Forces in the x, y and z directions respectively.

Fl: Flow number.

g: Growth rate parameter.

g: Gravity vector.

G: Growth rate, buoyancy stress production of turbulence kinetic energy.

G: Buoyancy stress production term.

$\mathbf{G}_{buoy}$: Production due to buoyancy.

$\mathbf{G}_{res}$: Production due to resistance.

$\mathbf{G}_{rot}$: Production due to rotation.

h: Height of nucleus, fluctuating total enthalpy.

H: Mean enthalpy.

$\hat{H}$: Specific enthalpy.

I: Primary nucleation parameter.

I: A dissipation component.

k: Shape factor, primary nucleation parameter, proportionality factor, turbulence kinetic energy.

k_1,k_2: Rate constants.

k_G: Growth rate coefficient, gas phase mass transfer coefficient.

k_L: Liquid-film mass transfer coefficient.

K: Boltzman constant, mass transfer coefficient.

K`,K``: First and second dissociation of H_2CO_3, respectively.

K_F: Volumetric force divided by the radial distance.

K_L^o: Physical absorption coefficient.

K_{sp}: Solubility product of calcite.

K_w: Equilibrium constant of the reaction $H_2O \rightarrow H^+ + OH^-$.

L: Characteristic crystal dimension, mother liquor flow rate, Prandtl mixing length.

L`: Arbitrary characteristic crystal dimension.

L: Cumulative length.

m: Mass (weight) density.

m_c : Mass of the impacting crystal.

m_j / M_j: jth moment.

M: Mass of crystals per unit volume, cumulative mass distribution function.

n: Population density.

n_t, n_o : Numbers of particles at t = t and t = 0, respectively.

N: Rotational speed, number of crystals per unit volume, absorption rate per unit surface.

N_p: Power number.

p: Pressure, partial pressure.

P: Crystal production rate, pressure, shaft power, production of turbulence kinetic energy.

P: Shear stress production term.

q: Stoichiometric factor.

Q: Required rate of heat transfer, discharge rate.

Q_i: Inlet volumetric flow rate.

Q_o: Outlet volumetric flow rate.

r: Radial distance.

r_1: Inner radius of the impeller.

r_2: Outer radius of the impeller.

R: Mass flux, gas constant, rate of reaction.

R_1,R_2: Rate of reactions.

Re: Reynolds number.

s: Relative supersaturation, fraction of surface renewed in unit time, fluctuating scalar concentration.

S: Relative supersaturation, mean scalar concentration, source term

Sc: Schmidt number.

Sh: Sherwood number.

t: Time, age.

t*: Half-time.

T: Temperature, impeller torque.

T*: Temperature at equilibrium.

u: Fluctuating velocity vector.

U: Fluid mean velocity vector, dependent variable.

u_L: Characteristic velocity of the liquid.

u_x: The velocity of the component normal to the gas-liquid interface.

v: Molar volume.

v: Velocity vector.

$\mathbf{v}_e$: External (spatial) particle velocity vector.

$\mathbf{v}_i$: Internal particle velocity vector.

v_r: Radial velocity.

V: Cell volume.

V: Suspension volume.

V_S: Volume swept by the impeller.

V_T: Constant slurry volume.

W: The axial depth of the impeller.

x: Distance from the interface.

x_F: Mass fraction of the feed.

x_L: Mass fractions of the mother liquor.

x_c: Mass fraction of the solute in the crystal.

x_P: Penetration distance.

X: Relative size.

Y: The mass ratio of solute to solvent in the solution.

10

LITERATURE CITED

10. LITERATURE CITED

- ✧ Al-Khayat, A. and Garside, J., Calcium carbonate precipitation: the role and importance of solution chemistry, In *Industrial Crystallization '90*, A. Mersmann, Garmisch, FRG (Ed.), 235-241, (1990).
- ✧ Al-Rashed, M. H., Jones, A. G., Hannan, M. and Price, C., CFD Modelling of a precipitation mixing vessel, *13th Symposium on Industrial Crystallization*, 419-424, Toulouse, (1996).
- ✧ Astarita, G., Mass transfer with chemical reaction, Elsevier Publishing Company, Amsterdam / London / New York, (1967).
- ✧ Bakker, A., Laroche, R. D., Wang, M. H. and Calabrese, R. V., Sliding mesh simulation of laminar flow in stirred reactors, *Trans IChemE*, Vol **75** Part A,42-44, (1997).
- ✧ Bakker, A., Myers, K. J., Ward, R. W. and Lee, C. K., The laminar and turbulent flow pattern of a pitched blade turbine, *Trans IChemE*, Vol **74** Part A, 485-491, (1996).
- ✧ Becker, G. W., Jr. and Larson, M. A., Mixing and fast chemical reaction III: Diffusion-reaction model for the CSTR, *Chemical Engineering Progress Symp. Ser.* No. 95, **65** (14), (1969).
- ✧ Bird, R. B., Stewart, W. E. and Lightfoot, E. N., Transport Phenomena, John Wiley & Sons, INC., (1960).
- ✧ Bode, J., Application of computational fluid dynamics in the chemical industry, *Chem. Eng. Technol.*, **17**, 145-148, (1994).

- Bourne, J. R. and Dell'ava, Micro- and macro-mixing in stirred tank reactors of different sizes, *Chemical Engineering Research Design*, Vol. **65**, 180-186, March (1987).
- Burton, W. K., Cabrera, N. and Frank, F. C., The growth of crystals and the equilibrium structure of their surfaces, *Philosophical Transactions*, **A243**, 299-358, (1951).
- Christoffersen, J. and Christoffersen, M. R., Kinetics of spiral growth of calcite crystals and determination of the absolute rate constant, *J. Crystal Growth*, **100**, 203-211, (1990).
- Clarke, D. S. and Wilkes, N. S., The calculation of turbulent flows in complex geometries using a differential stress model AERE-R 13428, (1989).
- Costa, P. and Trevissoi, C., Reactions with non-linear kinetics in partially segregated fluids, *Chem. Eng. Sci.*, **27**, 2041-2054, (1972).
- Danckwerts, P. V., Continuous-flow systems: distribution of residence times, *Chem. Eng. Sci.*, **2** (1), (1953).
- Danckwerts, P. V., Gas-liquid reactions, McGraw-Hill Book Company, (1970).
- David, R. and Marcant, B., Predictions of micromixing effects in precipitation: Case of double-jet precipitators, *AIChE*, Vol. **40** (3), 424-432, (1994).
- Desouza, A. and Pike, R. W., Fluid dynamics and flow patterns in stirred tanks with a turbine impeller, *Can. J. Chem. Eng.*, **50**, 15-23, (1972).
- Foumeny, E. A. and Sandhu, K. S., Computational modelling of the mixing characteristics in stirred tanks, The 1995 *IChemE Research Event / First European Conference*, 659-661, (1995).

✧ Garside, J. and Tavare, N. S., Mixing, reaction and precipitation in an MSMPR crystallizer: Effects on reaction kinetics on the limits of micromixing, In *Industrial Crystallisation* '84, S. J. Jancic and E. J. de Jong, Eds., Elsevier, Amsterdam, 131, (1984).

✧ Garside, J. and Tavare, N. S., Mixing, reaction and precipitation in an MSMPR crystallizer, *Chem. Eng. Sci.*, **40** (8), 1, 486, (1985).

✧ Garside, J. and Wei, H., Pumped, stirred and maybe precipitated: simulation of precipitation processes using CFD, *Acta Polytechnica Scandinavica, Chemical Technology and Metallurgy Series*, No. **244**, 9-15, (1997).

✧ Garside, J., Tailoring crystal products in precipitation processes and the role of mixing, *AIChE Symposium Series*, Vol **87** No. 284, 16-25, (1991).

✧ Glasscock, D. A. and Rochelle, G. T., Numerical simulation of theories for gas absorption with chemical reaction, *AIChE Journal*, Vol **35** No. 8, 1271-1281, (1989).

✧ Günkel, L. A. and Weber, M. E., Flow phenomena in stirred tanks, Part I: The impeller stream, *AIChE Journal*, Vol **21** No. 5, 931-939, (1975).

✧ Hallas, N. J. and Hannan, M. L., Measurement and computation of hydrodynamics for a draft tube baffled crystallizer, In *Industrial Crystallisation '90*, Ed. A. Mersmann, 107, (1990).

✧ Harvey III, A. D., Lee, C. and Rogers, S. E., Steady-state modelling and experimental measurement of a baffled impeller stirred tank, *AIChE Journal*, Vol **41** No. 10, 2177-2186, (1995).

✧ Hikita, H. and Ishikawa, H., Physical absorption in agitated vessels with a flat gas-liquid interface. *Bull. Univ. Osaka Perfect* **A18**, 427, (1969).

- Hostomský, J. and Jones, A. G., Modelling of calcium carbonate precipitation in the reaction between gaseous carbon dioxide and aqueous solution of calcium hydroxide. in: *Industrial Crystallization* '93, Rojkowski, Z. (Ed.), University of Warsaw, (1993).
- Hostomský, J. and Jones, A. G., A penetration model of the gas-liquid reactive precipitation of calcium carbonate crystals, *Trans. IChemE*, Vol. **73**, Part A, 241, (1995).
- Jones, A. G., Wachi, S. and Delannoy, C-C., Precipitation of calcium carbonate in a fluidized bed reactor, In *Fluidization VII*, Brisbane, O. E. Potter and D. J. Nicklin (Ed.), New York: Engineering Foundation), 407-414, (1992).
- Koutsakos, E., Nienow, A. W. and Dyster, K. N., Laser anemometry study of shear thinning fluids agitated by a Rushton turbine, *IChemE Symposium Series* No. **121**, 51-73, (1990).
- Kubota, N., Akazawa, K. and Shimizu, K., Kinetics of BaCO3 precipitation in an MSMPR crystallizer, *Industrial Crystallization '90*, Garmisch-Partenkirchen, Mersmann, A. (Ed.), 199-204, (1990).
- Levenspiel, O., Chemical Reaction Engineering, 2nd edn., Jonh Wiley & Sons, Inc., Singapore, (1972).
- Lewis, W. K. and Whitman, W. G., *Ind. Eng. Chem.*, **16**: 1215, (1924).
- McCabe, W. L. and Smith, J. C., Unit operations of chemical engineering, Third edn., 852-861, McGraw-Hill Kogakusha LTD., (1976).
- Mersmann, A., Crystallization technology handbook, Marcel Dekker, Inc., New York, (1995).
- Mersmann, A., Design of crystallizers, *Chem. Eng. Process.*, **23**, 213-228, (1988).

- Mersmann, A. and Angerhöfer, J. F., Controlled precipitation, *Chem. Eng. Technol.*, 17, 1-9, (1994).
- Mersmann, A. and Kind, M., Chemical engineering aspects of precipitation from solution, *Chem. Eng. Technol.*, **11**, 264-276, (1988).
- Mullin, J. W., Crystallisation, Third edn., 285-309, Butterworth-Heinemann, (1993).
- Murthy, J. Y., Mathur, S. R. and Choudhury, D., CFD simulation of flows in stirred tank reactors using a sliding mesh technique, *IChemE Symposium Series* No. **136**, 341-348, (1994).
- Nancollas, G. H. and Reddy, M. M., The crystallization of calcium carbonate: II. calcite growth mechanism, *Journal of Colloid and Interface Science*, **37** (4), 824-830, (1971).
- Nerst, W., *Z. Phys. Chem.*, **47**: 52, (1904).
- Patankar, S. V., Numerical heat transfer and fluid flow, Hemisphere (McGraw-Hill), New York, (1980).
- Pnueli, D. and Gutfinger, C., Fluid Mechanics, Cambridge: Cambridge University Press, (1992).
- Pohorecki, R. and Baldyga, J., The use of a new model of micromixing for determination of crystal size in precipitation, *Chem. Eng. Sci.*, **38** (1), 1, 79-83, (1983).
- Randolph, A. D. and Larson, M. A., Theory of particulate processes, 2nd edn., Academic Press, (1988).
- Randolph, A. D., Effect of crystal breakage on crystal size distribution in a mixed suspension crystallizer, *I & EC Fundamentals*, Vol 8 No. 1, 58-63, (1969).

- Reddy, J. N., An introduction to the finite element method, McGraw-Hill, New York, (1984).
- Rousseau, R. W., Crystallization, Kirk-Othmer Encyclopaedia of chemical engineering technology, Vol. **7**, Fourth edn., 683-716, Wiley-Interscience Publication, (1993).
- Rousseau, R. W., Li, K. K. and McCabe, W. L., The influence of seed crystal size on nucleation rates, AIChE Symposium Series No. **153**, 72, 48-52, (1976).
- Rutherford, K., Lee, K. C., Mahmoudi, M. S. and Yianneskis, M., Hydrodynamic characteristics of dual Rushton impeller stirred vessels, *AIChE Journal*, Vol. **42** No. 2, 332-346, (1996).
- Sada, E., Kumazawa, H. and Lee, C. H., *Chem. Engng. Sci.*, **32**, 1165-1170, (1977).
- Sada, E., Kumazawa, H. and Aoyama, M.,*Chem. Engng. Commun.*, **71**,73-82, (1988).
- Sano, Y. and Usui, H., Interrelations among mixing time, Power number and discharge flow rate number in baffled mixing vessels, *J. of Chemical Engineering of Japan*, Vol. 18 No. 1, 47-52, (1985).
- Sano, Y. and Usui, H., Effects of paddle dimensions and baffle conditions on the interrelations among discharge flow rate, mixing power and mixing time in mixing vessels, *J. Chem. Engng. Japan*, **20**(4), 399, (1987).
- Seckler, M. M., Bruinsma, O. S. L. and Van Rosmalen, G. M., Influence of hydrodynamic on the precipitation of calcium sulphate: a computational study, *Chem. Eng. Comm.*, Vol. **135**, 113, (1995).

- Seckler, M. M., Nijssen, S. J., Bruinsma, O. S. L. and Van Rosmalen, G. M., Influence of hydrodynamic conditions on the precipitation of calcium phosphate: a computational study, *In Industrial Crystallisation*, 2-085, (1993).
- Secor, R. M. and Beutler, J. A., Penetration theory for diffusion accompanied by a reversible chemical reaction with generalised kinetics, *AIChE Journal*, Vol **13** No. 2, 365-373, (1967).
- Sharratt, P. N., Computational fluid dynamics and its application in the process industries, *Trans. IChemE*, Vol. **68**, Part A, 13, (1990).
- Shaw, C. T., Using computational fluid dynamics, Prentice Hall International Ltd., U.K., (1992).
- Sherwood, T. K., Pigford, R. L. and Wilke, C. R., Mass transfer, Chemical Engineering Series, McGraw-Hill, Chapter 5, (1975).
- Smallwood, P. V., Some aspects of the surface chemistry of calcite and aragonite Part II: crystal growth, *Colloid & Polymer Sci.*, **255**, 994-1000, (1977).
- Smoluchowski, M., Versuch einer mathematischen theoric der koagulations kinetic kolloider Lösungen, Zeitschrift für Physikalische Chemie, **92**, 129-168, (1918).
- Söhnel, O. and Garside, J., Precipitation: basic principles and industrial applications, Oxford: Butterworth-Heinemann, (1992).
- Söhnel, O. and Mullin, J. W., Precipitation of calcium carbonate, *J. Crystal Growth*, **60**, 239-250, (1982).
- Söhnel, O., Chainese, A. and Jones, A. G., Theoretical approaches to design of precipitation systems: The present state of art, *Chem. Eng. Comm.*, Vol. **106**, 151-175, (1991).

- Tavare, N. S., Journal review: Mixing in continuous crystallizers", *AIChE*, Vol. **32** (5), 705-732, May (1986).
- Tavare, N. S., Micromixing limits in an MSMPR crystallizer, *Chem. Eng. Technol.*, **12**, 1-10, (1989).
- Tavare, N. S., Mixing, reaction and precipitation: environment micromixing models in continuous crystallizers-I Premixed feeds, *Computers Chemical Engineering*, Vol. **16**, No. 10/11, 923-936, (1992).
- Treybal, R. E., Mass transfer operations, 3rd edn., McGraw-Hill Book Co., Singapore, (1980).
- Uhl, V. W. and Gray, J. B., Mixing theory and practice, Vol. **I**, 1-4, Academic Press, New York and London, (1966).
- United States/National Bureau of Standards, Tables of the error function and its derivatives, Washington, D. C.: U. S. Govt. Printing Office, (1954).
- Van Leeuwen, M. L. J., Bruinsma, O. S. L. and Van Rosmalen, G. M., Influence of mixing on the product quality in precipitation, *Chem. Eng. Sci.*, Vol **51** No 11, 2595-2600, (1996).
- Versteeg, H. K. and Malalasekera, W., An introduction to computational fluid dynamics: the finite volume method, Longman Scientific & Technical, Malaysia, (1995).
- Wachi, S. and Jones, A. G., Effect of gas-liquid mass transfer on crystal size distribution during the batch precipitation of calcium carbonate, *Chem. Eng. Sci.*, **46**(12), 3293, (1991b).
- Wachi, S. and Jones, A. G., Mass transfer with chemical reaction and precipitation, *Chem. Eng. Sci.*, **46**(4), 1027, (1991a).

- Wachi, S. and Jones, A. G., Aspects of gas-liquid reaction systems with precipitate particle formation, *Reviews in Chemical Engineering*, Vol. **11** No. 1, (1995).
- Wachi, S. and Morikawa, H., Liquid-phase chloronation of ethylene and 1,2-dichloroethene, *J. Chem. Eng. Japan*, **19**, 437, (1986).
- Weetman, R. J., Development of an erosion resistant mixing impeller for large scale solid suspension applications with CFD comparisons, *IChemE Symposium Series* No. **136**, 49-56, (1994).
- Wei, H. and Garside, J., Application of CFD modelling to precipitation systems, *Trans. IChemE*, Vol. **75**, Part A, 219-227, (1997).
- Werner, F. and Mersmann, A. B., An engineering approach to turbulence, *IChemE Symposium Series* No. **136**, 129-136, (1994).
- White, F. M., Fluid Mechanics, Third edn., McGraw-Hill, New York, (1994).
- Whitman, W. G., *Chem. Met. Eng.*, **29**: 146, (1923).
- Xu, Y. and McGrath, G., CFD predictions of stirred tank flows, *Trans IChemE*, Vol **74** Part A, 471-475, (1996).
- Yagi, H., Design of habit of particles formed in gas-liquid reactors, *Proceedings of the International Symposium on crystallization*, Kyoto, Japan, 156-160, (1988).
- Zettlemoyer, A. C., Nucleation, Marcel and Dekker, Inc., New York, Chapter 5, (1969).
- Zienkiewicz, O. C. and Taylor, R. L., The finite element Method, Fourth edn., Volume 1: Basic formulation and linear problems, McGraw-Hill, New York, (1989).
- Zumstein, R. C. and Rousseau, R. W., Utilising of industrial data in the development of a model for crystallizer simulation, *AIChE Symposium Series*, Vol **83** No. 253, 130-139, (1987).

11

APPENDIX

Parameter	Value
α	1.0
β	6.0
μ	$8.967*10^{-4}$ kg m^{-1} s^{-1}
ρ (water)	996.6 mol m^{-3}
ρ_c (calcite)	27100 mol m^{-3}
c_{Ca+} (initial)	5.17 mol m^{-3}
H_{CO_2}	0.0346 bar m^3 mol^{-1}
k (eqn. 3.13)	12.4 m^3 s^{-1} mol^{-1}
k_1	12.4 m^3 s^{-1} mol^{-1}
k_2^*	1000 m^3 s^{-1} mol^{-1}
K`	$4.45*10^{-4}$ mol m^{-3}
K``	4.69 mol m^{-3}
K_{sp}	0.00347 mol^2 m^{-6}
K_w	$1.0*10^{-8}$ mol^2 m^{-6}
MW[5]: CO_2	44.01 g mol^{-1}
MW: $Ca(OH_2)$	74.10 g mol^{-1}
MW: $CaCO_3$	100.09 g mol^{-1}
MW: H_2O	18.02 g mol^{-1}
P_{CO_2}	0.25 bar

* Approximating equilibrium for reaction (3.3).
[5] MW is the Molecular Weight.

Table (A.1): The values of the parameters used in the simulation.

Parameter	Set A	Set B
k_n $mol^{-n}m^{3n-3}s^{-1}$	$1.0*10^{+7}$	$4.5*10^{+8}$
n	4.2	6.0
k_g $mol^{-g}m^{3g+1}s^{-1}$	$8.06*10^{-9}$	$2.2*10^{-8}$
g	2.0	2.0

Table (A.2): Precipitation kinetics; set A is used in the CFD simulation, film and penetration theories (~ 5 s.) and set B is used only for penetration theory (25 mins), Hostomský and Jones (1995).

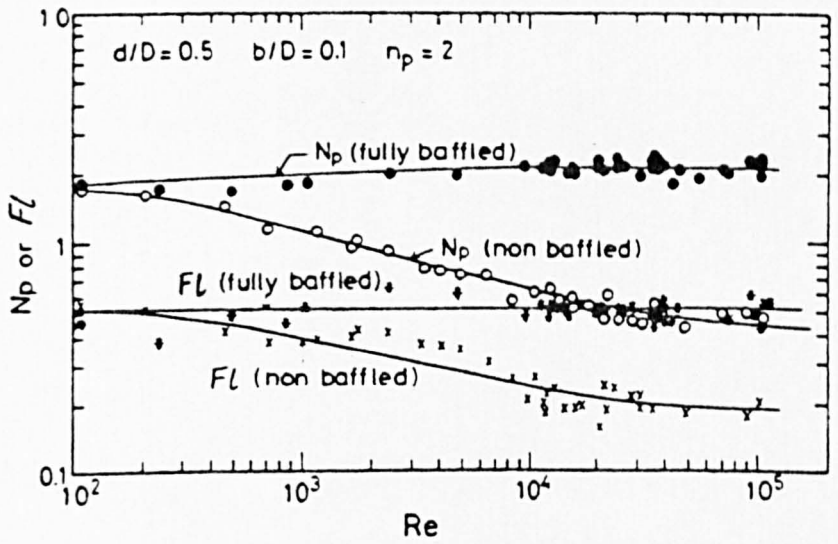

Figure (A.1): Variation of N_p and *Fl* with Re, Sano and Usui (1987).

Where b, d and n_p are the width of impeller blade, diameter of impeller and number of impeller blades, respectively. For the two blade paddle system in this project: d/D = 0.42 and b/D = 0.13.

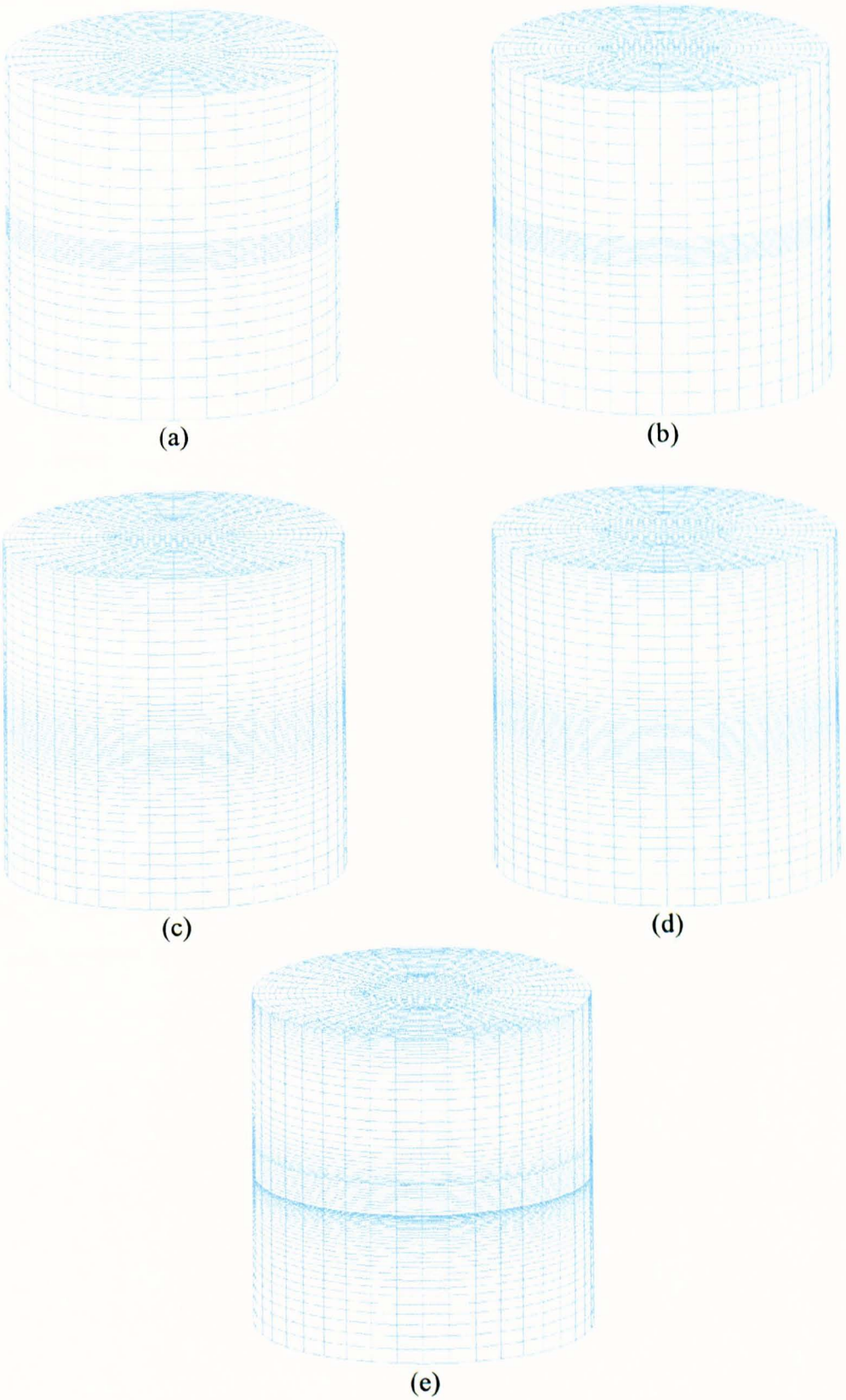

Figure (A.2): Different grid presentations; (a) 18,240 cells (b) 25,800 cells (c) 43,000 cells (d) 54,000 cells and (e) 63,000 cells.

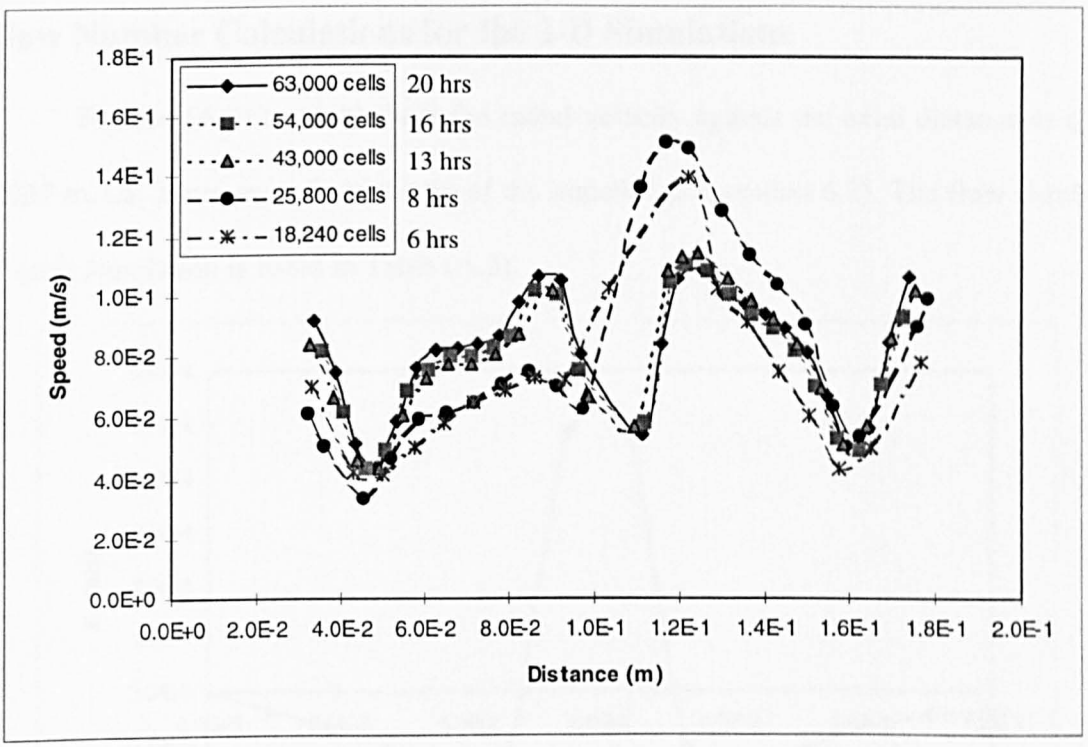

Figure (A.3): Speed versus Distance for a line (x = -0.06 to 0.06, y = -0.06 to 0.06 and z = 0 to 0.12 m) in the vessel.

Figure (A.3) shows the simulations of 43,000 cells and over have almost similar results, i.e. virtually grid-independent solution. Therefore, the simulation of 43,000 cells is chosen because it takes less time than the other higher grids, viz. 54,000 and 63,000 cells.

Flow Number Calculations for the 2-D Simulations

Figures (A.4) to (A.8) show the radial velocity against the axial distance at r_s = 0.027 m, i.e. 2 mm away from the tip of the impeller (c.f. section 6.2). The flow number of each simulation is listed in Table (A.3).

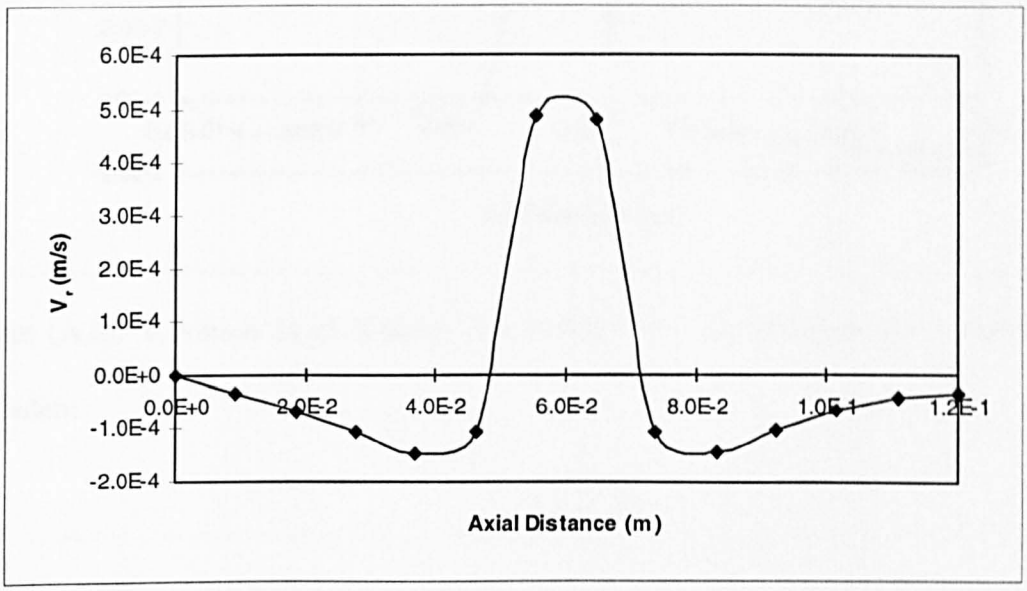

Figure (A.4): V_r versus axial distance at r_s = 0.027 m, for 1 rpm (Re = 46).

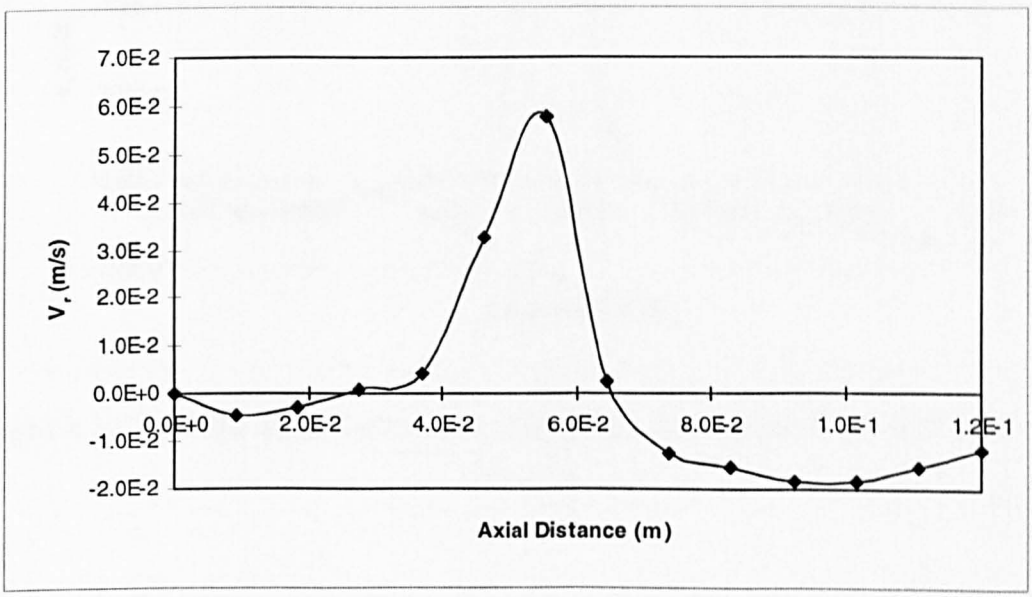

Figure (A.5): V_r versus axial distance at r_s = 0.027 m, for 100 rpm (Re = $4.6*10^3$), Laminar.

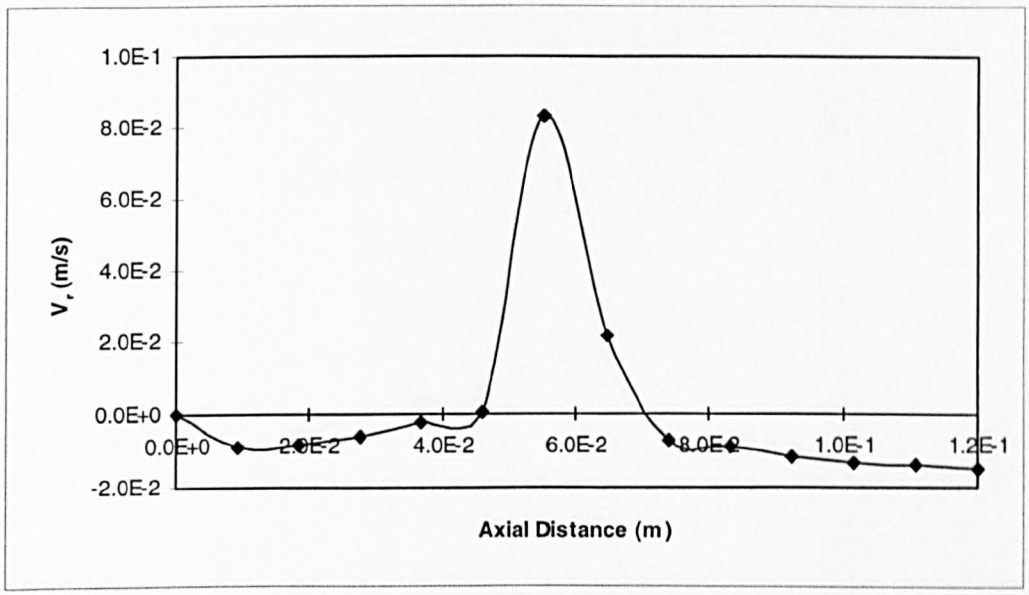

Figure (A.6): V_r versus axial distance at r_s = 0.027 m, for 100 rpm (Re = $4.6*10^3$), Turbulent.

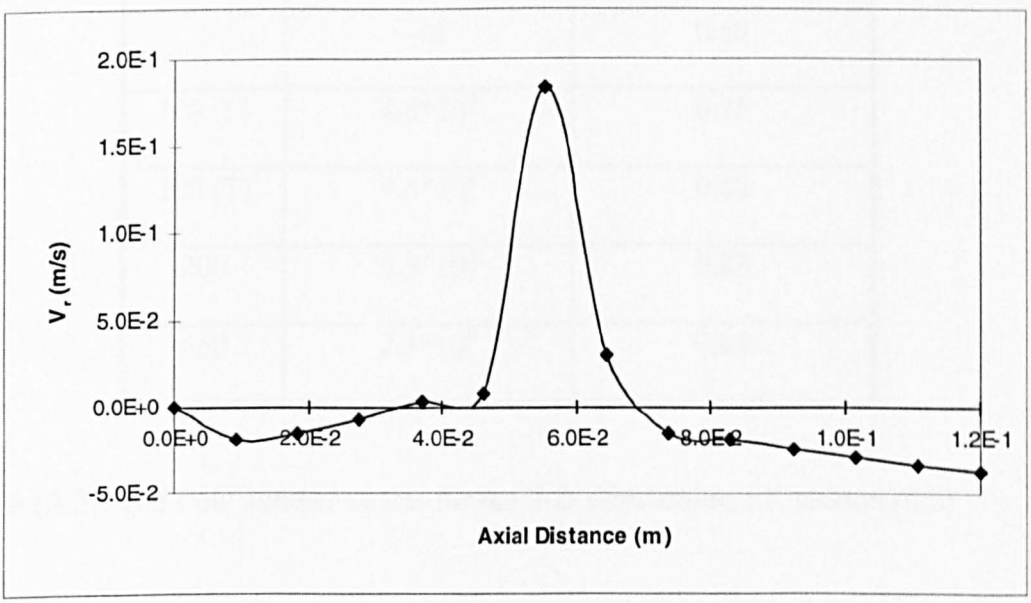

Figure (A.7): V_r versus axial distance at r_s = 0.027 m, for 200 rpm (Re = $9.3*10^3$).

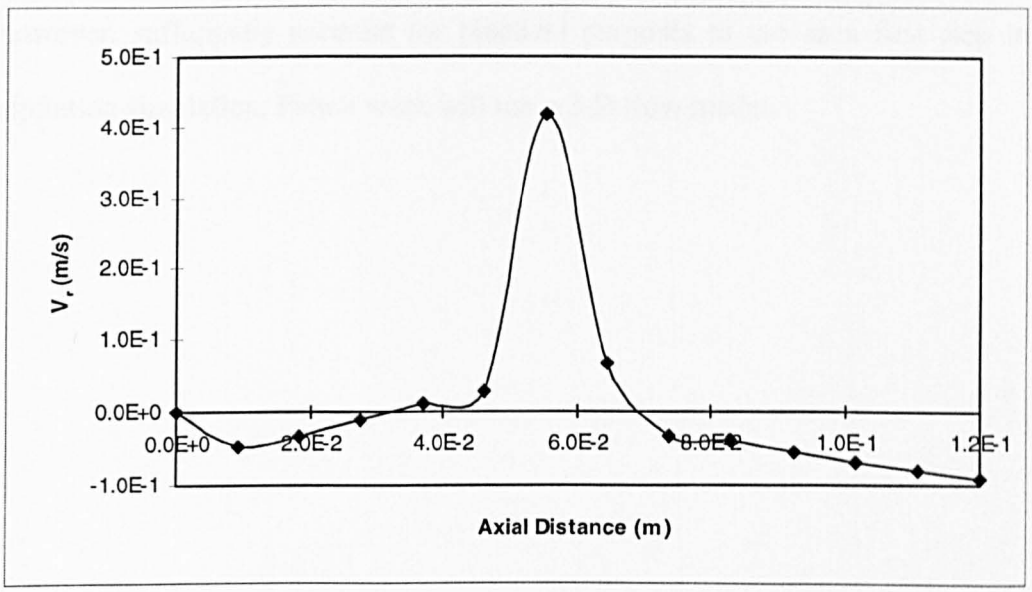

Figure (A.8): V_r versus axial distance at $r_s = 0.027$ m, for 450 rpm ($Re = 2.1*10^4$).

rpm	Re	*Fl*
1	46	0.69
100 (L)	$4.6*10^3$	0.75
100 (T)	$4.6*10^3$	0.82
200	$9.3*10^3$	0.83
450	$2.1*10^4$	0.85

Table (A.3): The flow number values for the 2-D simulations, c.f. section (6.2).

The flow number values for the 2-D simulations are of similar magnitude as the 3-D value (0.61) at 450 rpm, although a direct comparison is not strictly valid. The deviation is most likely due to the essential absence of baffles from the 2-D geometry which has a considerable influence on the hydrodynamics of the system. The 2-D model

is, however, sufficiently accurate for practical purposes to use as a first step in the precipitation simulation. Future work will use a 3-D flow model.

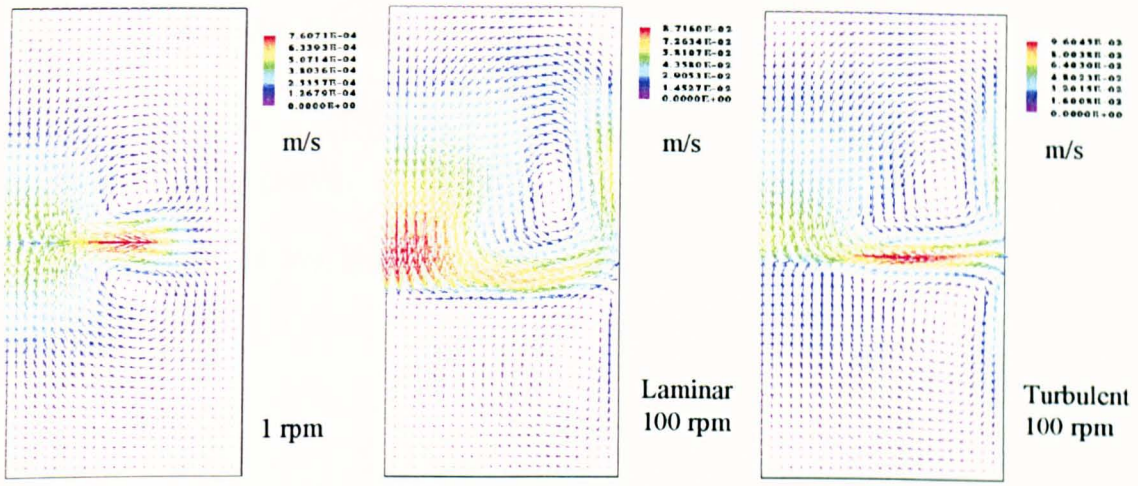

(a) Re = 46 (b) Re = $4.6*10^3$ (c) Re = $4.6*10^3$

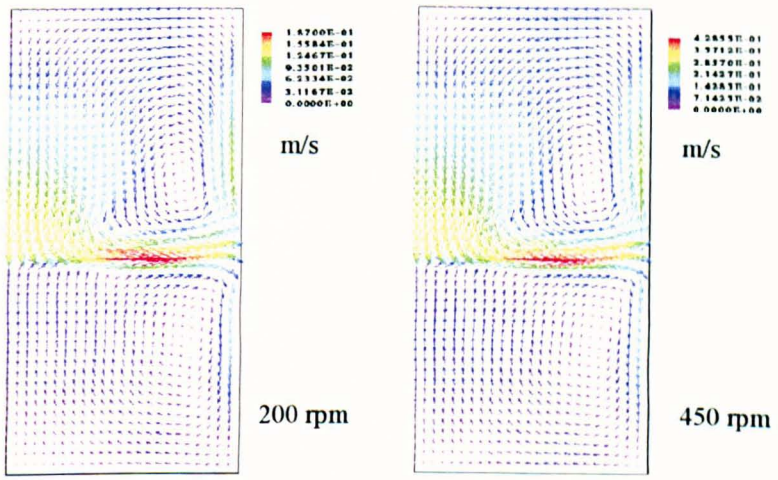

(d) Re = $9.3*10^3$ (e) Re = $2.1*10^4$

Figure (A.9): Speed vectors of the 2-D CFD simulations.

Critical Particle Size Estimation

- Source: Mullin (1993)

Equation (1.29) gives the size-solubility (Gibbs-Thomson) relationship as follows:

$$r = \frac{2\gamma v c^*}{\nu R T (c - c^*)}$$

the values of the parameters are; $\gamma = 0.12$ J/m^2 (Söhnel and Mullin, 1982), $v = 3.7*10^{-5}$ m^3/mol (Christoffersen and Christoffersen, 1990), $c^* = 0.0589$ mol/m^3 (Hostomský and Jones, 1995), $\nu = 2$, $R = 8.314$ J/mol K, $T = 298.15$ K, $c = 0.956$ mol/m^3 (from penetration model). Hence, $r = 1.17*10^{-10}$ m, i.e. 0.23 nm diameter.

- Source: Mersmann (1995)

In order to calculate the critical particle size the molecular diameter and the interfacial tension are needed. The molecular diameter can be estimated from the following equation:

$$d_m \approx \sqrt[3]{\frac{M}{\rho_c N_A}}$$

where M and N_A are the molecular mass and Avogadro's number (= $6.023*10^{23}$ mol^{-1}), respectively. Therefore, $d_m \approx 1.8$ nm. Then, solving the following equation for L_{crit}:

$$\frac{L_{crit}}{d_m} = \frac{4 d_m^2 \gamma}{kT \ln S}$$

where k is Boltzmann constant (= $1.381*10^{-23}$ J/K). L_{crit}, hence, equal to 0.25 μm.

Appendix (7)

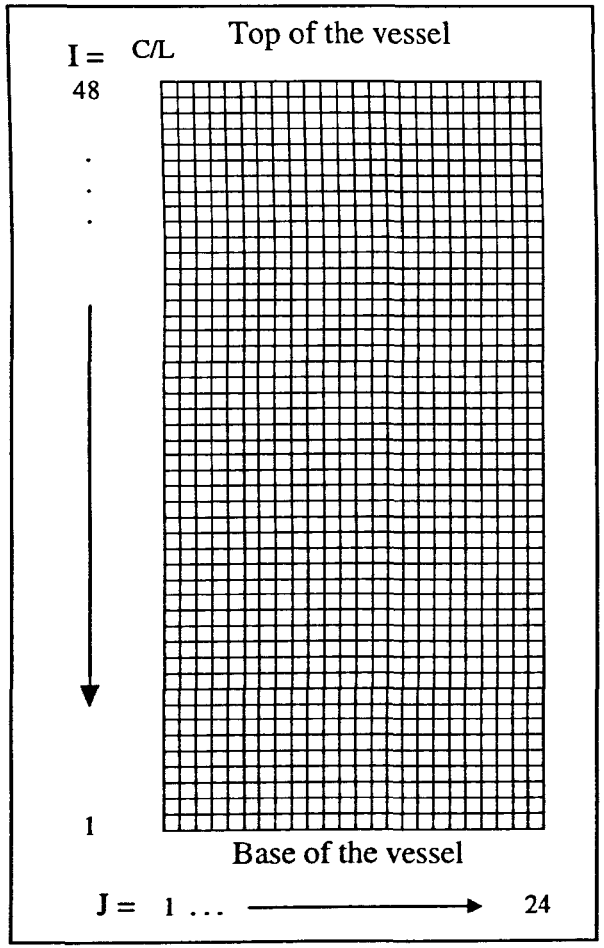

Figure (A.10): 2-D model grid (48 x 24 cells) 0.12 x 0.06 m.

Table (A.4): **CO_2 (aq) Concentration (kmol/m^3):** The average $[CO_2]_{(aq)}$ over the whole vessel is 0.01148 kmol/m^3.

J =												
24	2.87E-33	2.09E-31	1.46E-29	9.74E-28	6.30E-26	4.00E-24	2.53E-22	1.66E-20	9.42E-19	2.28E-17	1.72E-18	1.75E-19
23	1.42E-34	8.88E-33	4.63E-31	1.55E-29	0.00E+00	0.00E+00	0.00E+00	0.00E+00	8.30E-17	2.35E-15	1.64E-16	1.66E-17
22	6.63E-36	2.53E-34	0.00E+00	0.00E+00	0.00E+00	0.00E+00	0.00E+00	4.34E-17	5.47E-15	1.37E-13	9.31E-15	8.53E-16
21	0.00E+00	0.00E+00	0.00E+00	0.00E+00	0.00E+00	0.00E+00	0.00E+00	2.98E-15	2.15E-13	5.89E-12	4.15E-13	3.49E-14
20	0.00E+00	0.00E+00	0.00E+00	0.00E+00	0.00E+00	0.00E+00	5.06E-16	9.50E-14	6.09E-12	1.98E-10	1.41E-11	1.05E-12
19	0.00E+00	0.00E+00	0.00E+00	0.00E+00	0.00E+00	2.01E-17	1.23E-14	1.80E-12	1.32E-10	5.33E-09	3.67E-10	2.34E-11
18	0.00E+00	0.00E+00	0.00E+00	2.42E-22	3.86E-19	3.34E-16	1.30E-13	2.23E-11	2.16E-09	1.12E-07	7.30E-09	3.87E-10
17	3.70E-30	2.54E-27	2.00E-24	1.72E-21	1.66E-18	1.51E-15	7.33E-13	1.83E-10	2.61E-08	1.76E-06	1.11E-07	4.76E-09
16	2.02E-30	1.45E-27	1.28E-24	1.47E-21	2.37E-18	3.79E-15	2.54E-12	9.36E-10	2.13E-07	1.97E-05	1.28E-06	4.37E-08
15	3.70E-31	2.53E-28	2.02E-25	1.66E-22	1.22E-18	6.55E-15	5.88E-12	2.99E-09	1.06E-06	1.41E-04	1.16E-05	2.98E-07
14	4.05E-32	2.39E-29	0.00E+00	0.00E+00	8.81E-19	8.70E-15	9.61E-12	6.10E-09	3.08E-06	5.47E-04	8.11E-05	1.42E-06
13	1.89E-33	0.00E+00	0.00E+00	2.32E-20	5.22E-17	2.47E-14	1.54E-11	8.64E-09	5.42E-06	1.16E-03	3.99E-04	4.22E-06
12	0.00E+00	0.00E+00	7.70E-23	2.67E-18	3.18E-15	1.08E-12	6.91E-11	1.27E-08	6.62E-06	1.83E-03	1.18E-03	7.81E-06
11	2.00E-30	1.63E-25	1.60E-20	1.14E-16	1.48E-13	5.17E-11	2.82E-09	3.04E-08	6.96E-06	2.48E-03	2.36E-03	1.02E-05
10	0.00E+00	0.00E+00	1.17E-21	1.10E-15	4.57E-12	1.46E-09	5.67E-08	7.73E-07	5.06E-06	3.09E-03	3.92E-03	1.09E-05
9	0.00E+00	0.00E+00	0.00E+00	0.00E+00	3.61E-11	2.42E-08	3.89E-07	1.30E-06	5.52E-06	3.96E-03	5.97E-03	2.26E-05
8	0.00E+00	0.00E+00	0.00E+00	0.00E+00	0.00E+00	7.97E-11	7.43E-08	8.71E-07	9.25E-06	5.55E-03	8.72E-03	3.31E-04
7	0.00E+00	0.00E+00	0.00E+00	0.00E+00	0.00E+00	0.00E+00	3.01E-09	4.53E-07	4.55E-05	7.54E-03	1.25E-02	2.63E-03
6	0.00E+00	0.00E+00	8.76E-31	0.00E+00	0.00E+00	0.00E+00	0.00E+00	6.88E-07	1.77E-04	9.89E-03	1.79E-02	7.37E-03
5	0.00E+00	0.00E+00	0.00E+00	5.23E-26	9.82E-24	0.00E+00	0.00E+00	1.09E-07	1.25E-04	1.36E-02	2.53E-02	1.50E-02
4	0.00E+00	0.00E+00	0.00E+00	0.00E+00	3.81E-21	6.13E-19	0.00E+00	2.11E-07	1.87E-04	1.77E-02	3.50E-02	2.61E-02
3	0.00E+00	0.00E+00	0.00E+00	0.00E+00	0.00E+00	3.60E-16	2.48E-14	0.00E+00	4.98E-05	2.32E-02	4.65E-02	4.08E-02
2	0.00E+00	0.00E+00	0.00E+00	0.00E+00	0.00E+00	0.00E+00	5.03E-11	2.95E-07	1.21E-04	2.82E-02	5.93E-02	5.78E-02
1	0.00E+00	0.00E+00	0.00E+00	0.00E+00	0.00E+00	0.00E+00	0.00E+00	4.79E-06	1.67E-03	3.10E-02	7.13E-02	7.23E-02
I =	13	14	15	16	17	18	19	20	21	22	23	24

Table (A.4): CO_2 (aq) concentration, continued

J =												
24	1.40E-20	7.83E-22	2.96E-23	8.02E-25	1.89E-26	4.42E-28	1.02E-29	2.31E-31	5.10E-33	1.12E-34	6.55E-35	0.00E+00
23	1.29E-18	6.09E-20	1.40E-21	9.59E-24	9.44E-26	1.83E-27	3.55E-29	6.82E-31	1.29E-32	5.30E-33	2.46E-31	1.20E-29
22	6.65E-17	3.12E-18	6.76E-20	2.11E-22	0.00E+00	0.00E+00	0.00E+00	3.15E-32	3.93E-33	1.47E-31	7.68E-30	4.09E-28
21	2.44E-15	1.08E-16	2.27E-18	9.18E-21	0.00E+00	0.00E+00	0.00E+00	0.00E+00	4.18E-32	2.28E-30	1.25E-28	7.09E-27
20	6.40E-14	2.54E-15	5.32E-17	4.49E-19	0.00E+00	0.00E+00	0.00E+00	0.00E+00	4.25E-31	2.51E-29	1.40E-27	8.12E-26
19	1.19E-12	3.95E-14	7.51E-16	7.79E-18	3.59E-20	0.00E+00	0.00E+00	0.00E+00	1.58E-30	2.08E-28	1.16E-26	6.78E-25
18	1.58E-11	4.19E-13	6.92E-15	7.44E-17	5.44E-19	2.47E-21	3.46E-25	0.00E+00	0.00E+00	1.50E-27	8.16E-26	4.67E-24
17	1.51E-10	3.14E-12	4.35E-14	4.38E-16	3.44E-18	2.18E-20	1.12E-22	4.39E-25	1.22E-27	1.11E-26	5.47E-25	2.99E-23
16	1.04E-09	1.64E-11	1.85E-13	1.64E-15	1.21E-17	7.58E-20	4.16E-22	2.07E-24	1.44E-26	1.19E-25	4.34E-24	2.04E-22
15	4.98E-09	5.69E-11	5.13E-13	3.93E-15	2.57E-17	1.44E-19	7.08E-22	3.23E-24	2.47E-25	2.87E-24	6.23E-23	1.96E-21
14	1.51E-08	1.21E-10	8.68E-13	5.70E-15	3.25E-17	1.56E-19	6.40E-22	8.21E-24	2.38E-23	1.65E-22	2.01E-21	4.05E-20
13	2.68E-08	1.42E-10	7.84E-13	4.41E-15	2.21E-17	9.13E-20	6.30E-22	1.14E-21	3.96E-21	1.80E-20	1.38E-19	1.69E-18
12	2.70E-08	7.36E-11	2.52E-13	1.21E-15	6.22E-18	5.45E-20	7.15E-20	2.43E-19	9.10E-19	3.11E-18	1.69E-17	1.42E-16
11	1.34E-08	0.00E+00	0.00E+00	0.00E+00	4.08E-18	8.62E-18	2.03E-17	5.70E-17	2.28E-16	8.57E-16	2.98E-15	2.07E-14
10	3.17E-09	2.08E-11	3.14E-15	2.69E-16	1.24E-15	3.28E-15	7.77E-15	1.74E-14	5.79E-14	2.67E-13	9.95E-13	3.72E-12
9	8.67E-08	1.91E-11	6.76E-14	8.48E-14	4.66E-13	1.41E-12	3.65E-12	7.80E-12	1.82E-11	7.79E-11	4.05E-10	1.49E-09
8	1.04E-06	0.00E+00	1.78E-11	0.00E+00	1.41E-10	5.72E-10	1.83E-09	4.37E-09	8.83E-09	2.41E-08	1.41E-07	7.96E-07
7	5.03E-05	5.70E-07	5.24E-08	1.45E-10	3.73E-08	1.93E-07	8.50E-07	2.52E-06	5.26E-06	1.07E-05	3.70E-05	2.95E-04
6	1.74E-03	1.07E-04	2.29E-05	5.99E-06	1.46E-05	5.01E-05	2.88E-04	1.11E-03	2.26E-03	3.62E-03	5.19E-03	7.03E-03
5	8.71E-03	5.16E-03	3.59E-03	3.39E-03	4.77E-03	6.33E-03	8.03E-03	9.85E-03	1.18E-02	1.39E-02	1.62E-02	1.88E-02
4	2.04E-02	1.69E-02	1.51E-02	1.51E-02	1.72E-02	1.96E-02	2.20E-02	2.46E-02	2.72E-02	3.00E-02	3.29E-02	3.61E-02
3	3.69E-02	3.46E-02	3.33E-02	3.39E-02	3.67E-02	3.97E-02	4.27E-02	4.59E-02	4.91E-02	5.24E-02	5.58E-02	5.94E-02
2	5.69E-02	5.63E-02	5.65E-02	5.82E-02	6.16E-02	6.51E-02	6.87E-02	7.24E-02	7.62E-02	8.00E-02	8.40E-02	8.82E-02
1	7.30E-02	7.41E-02	7.60E-02	7.88E-02	8.27E-02	8.67E-02	9.09E-02	9.51E-02	9.95E-02	1.04E-01	1.09E-01	1.14E-01
I =	25	26	27	28	29	30	31	32	33	34	35	36

Table (A.4): CO_2 (aq) concentration, continued

J =												
24	0.00E+00	0.00E+00	0.00E+00	0.00E+00	0.00E+00	0.00E+00	0.00E+00	0.00E+00	0.00E+00	0.00E+00	0.00E+00	2.88E-02
23	5.98E-28	3.15E-26	1.88E-24	1.38E-22	1.31E-20	1.54E-18	2.18E-16	3.39E-14	5.13E-12	7.08E-10	1.12E-06	4.23E-02
22	2.23E-26	1.27E-24	7.85E-23	5.61E-21	5.07E-19	6.02E-17	9.26E-15	1.82E-12	4.35E-10	1.26E-07	5.88E-05	4.82E-02
21	4.17E-25	2.56E-23	1.68E-21	1.21E-19	1.04E-17	1.13E-15	1.66E-13	3.28E-11	8.89E-09	3.29E-06	1.45E-03	5.26E-02
20	4.95E-24	3.20E-22	2.20E-20	1.63E-18	1.34E-16	1.31E-14	1.62E-12	2.70E-10	6.08E-08	1.74E-05	4.65E-03	5.67E-02
19	4.17E-23	2.75E-21	1.96E-19	1.51E-17	1.27E-15	1.19E-13	1.28E-11	1.68E-09	2.80E-07	5.70E-05	7.92E-03	6.07E-02
18	2.82E-22	1.83E-20	1.30E-18	1.02E-16	8.98E-15	8.86E-13	9.87E-11	1.25E-08	1.82E-06	2.81E-04	1.13E-02	6.50E-02
17	1.75E-21	1.10E-19	7.46E-18	5.64E-16	4.84E-14	4.83E-12	5.69E-10	7.84E-08	1.21E-05	1.64E-03	1.48E-02	6.97E-02
16	1.11E-20	6.71E-19	4.43E-17	3.20E-15	2.56E-13	2.30E-11	2.40E-09	2.96E-07	3.98E-05	3.69E-03	1.85E-02	7.48E-02
15	8.55E-20	4.60E-18	2.90E-16	2.08E-14	1.67E-12	1.49E-10	1.47E-08	1.54E-06	1.56E-04	6.13E-03	2.27E-02	8.05E-02
14	1.12E-18	4.48E-17	2.34E-15	1.52E-13	1.17E-11	1.05E-09	1.10E-07	1.25E-05	1.18E-03	9.08E-03	2.74E-02	8.68E-02
13	3.40E-17	8.59E-16	3.28E-14	1.63E-12	1.06E-10	8.24E-09	7.18E-07	6.06E-05	3.33E-03	1.27E-02	3.29E-02	9.38E-02
12	1.79E-15	3.84E-14	9.30E-13	3.56E-11	1.70E-09	1.10E-07	8.57E-06	6.66E-04	6.28E-03	1.72E-02	3.93E-02	1.02E-01
11	1.86E-13	2.45E-12	5.94E-11	1.39E-09	5.49E-08	2.35E-06	1.24E-04	3.33E-03	1.03E-02	2.28E-02	4.70E-02	1.10E-01
10	3.45E-11	3.29E-10	4.46E-09	1.26E-07	2.60E-06	1.00E-04	2.41E-03	7.54E-03	1.59E-02	3.00E-02	5.59E-02	1.18E-01
9	6.26E-09	7.99E-08	7.92E-07	9.78E-06	3.11E-04	2.89E-03	7.18E-03	1.36E-02	2.34E-02	3.89E-02	6.59E-02	1.26E-01
8	2.73E-06	1.28E-05	2.19E-04	1.91E-03	4.77E-03	8.74E-03	1.42E-02	2.19E-02	3.29E-02	4.95E-02	7.69E-02	1.35E-01
7	1.46E-03	3.24E-03	5.55E-03	8.52E-03	1.24E-02	1.74E-02	2.40E-02	3.27E-02	4.46E-02	6.18E-02	8.91E-02	1.44E-01
6	9.23E-03	1.18E-02	1.50E-02	1.88E-02	2.35E-02	2.94E-02	3.68E-02	4.62E-02	5.86E-02	7.59E-02	1.02E-01	1.54E-01
5	2.17E-02	2.51E-02	2.89E-02	3.34E-02	3.87E-02	4.50E-02	5.28E-02	6.26E-02	7.51E-02	9.20E-02	1.17E-01	1.65E-01
4	3.96E-02	4.35E-02	4.78E-02	5.27E-02	5.83E-02	6.48E-02	7.25E-02	8.22E-02	9.43E-02	1.10E-01	1.34E-01	1.79E-01
3	6.33E-02	6.75E-02	7.21E-02	7.72E-02	8.29E-02	8.93E-02	9.68E-02	1.06E-01	1.17E-01	1.32E-01	1.54E-01	1.96E-01
2	9.26E-02	9.73E-02	1.02E-01	1.08E-01	1.13E-01	1.20E-01	1.27E-01	1.35E-01	1.45E-01	1.59E-01	1.79E-01	2.17E-01
1	1.19E-01	1.24E-01	1.30E-01	1.36E-01	1.43E-01	1.50E-01	1.58E-01	1.67E-01	1.79E-01	1.92E-01	2.11E-01	2.49E-01
I =	37	38	39	40	41	42	43	44	45	46	47	48

Table (A.5): **$Ca(OH)_2$ Concentration ($kmol/m^3$):** The average $[Ca(OH)_2]$ over the whole vessel is 0.0036 $kmol/m^3$.

J =												
24	0.00E+00	0.00E+00	0.00E+00	0.00E+00	1.00E-05	2.00E-05	4.00E-05	9.00E-05	1.80E-04	3.30E-04	3.80E-04	2.60E-04
23	0.00E+00	0.00E+00	0.00E+00	0.00E+00	0.00E+00	1.00E-05	4.00E-05	1.00E-04	2.90E-04	7.20E-04	7.90E-04	5.50E-04
22	0.00E+00	0.00E+00	0.00E+00	0.00E+00	0.00E+00	1.00E-05	2.00E-05	9.00E-05	3.60E-04	1.11E-03	1.23E-03	8.40E-04
21	0.00E+00	0.00E+00	0.00E+00	0.00E+00	0.00E+00	0.00E+00	1.00E-05	8.00E-05	4.00E-04	1.51E-03	1.65E-03	1.14E-03
20	0.00E+00	0.00E+00	0.00E+00	0.00E+00	0.00E+00	0.00E+00	1.00E-05	8.00E-05	4.70E-04	1.97E-03	2.05E-03	1.34E-03
19	0.00E+00	0.00E+00	0.00E+00	0.00E+00	0.00E+00	0.00E+00	1.00E-05	1.00E-04	6.30E-04	2.50E-03	2.42E-03	1.47E-03
18	0.00E+00	0.00E+00	0.00E+00	0.00E+00	0.00E+00	0.00E+00	2.00E-05	1.20E-04	8.40E-04	3.07E-03	2.78E-03	1.55E-03
17	0.00E+00	0.00E+00	0.00E+00	0.00E+00	0.00E+00	0.00E+00	2.00E-05	1.50E-04	1.10E-03	3.67E-03	3.14E-03	1.60E-03
16	0.00E+00	0.00E+00	0.00E+00	0.00E+00	0.00E+00	0.00E+00	2.00E-05	1.80E-04	1.37E-03	4.28E-03	3.52E-03	1.64E-03
15	0.00E+00	0.00E+00	0.00E+00	0.00E+00	0.00E+00	0.00E+00	3.00E-05	2.10E-04	1.63E-03	4.80E-03	3.97E-03	1.67E-03
14	0.00E+00	0.00E+00	0.00E+00	0.00E+00	0.00E+00	1.00E-05	5.00E-05	2.50E-04	1.83E-03	5.06E-03	4.47E-03	1.70E-03
13	0.00E+00	0.00E+00	0.00E+00	0.00E+00	0.00E+00	2.00E-05	1.10E-04	3.20E-04	1.92E-03	5.13E-03	4.88E-03	1.75E-03
12	0.00E+00	0.00E+00	0.00E+00	0.00E+00	0.00E+00	8.00E-05	2.70E-04	4.70E-04	1.87E-03	5.15E-03	5.05E-03	1.84E-03
11	0.00E+00	0.00E+00	0.00E+00	0.00E+00	0.00E+00	2.30E-04	5.30E-04	6.60E-04	1.64E-03	5.15E-03	5.11E-03	2.04E-03
10	0.00E+00	0.00E+00	0.00E+00	0.00E+00	1.00E-05	4.70E-04	7.50E-04	9.00E-04	1.27E-03	5.15E-03	5.14E-03	2.44E-03
9	0.00E+00	0.00E+00	0.00E+00	0.00E+00	6.00E-05	6.30E-04	8.10E-04	8.70E-04	9.20E-04	5.14E-03	5.15E-03	3.21E-03
8	0.00E+00	0.00E+00	0.00E+00	0.00E+00	0.00E+00	3.10E-04	7.40E-04	8.80E-04	1.01E-03	5.15E-03	5.17E-03	4.52E-03
7	0.00E+00	0.00E+00	0.00E+00	0.00E+00	0.00E+00	1.00E-05	4.50E-04	8.60E-04	2.74E-03	5.16E-03	5.17E-03	5.10E-03
6	0.00E+00	0.00E+00	0.00E+00	0.00E+00	0.00E+00	0.00E+00	5.00E-05	8.60E-04	3.96E-03	5.16E-03	5.17E-03	5.17E-03
5	0.00E+00	0.00E+00	0.00E+00	0.00E+00	0.00E+00	0.00E+00	0.00E+00	4.80E-04	3.99E-03	5.17E-03	5.17E-03	5.17E-03
4	0.00E+00	0.00E+00	0.00E+00	0.00E+00	0.00E+00	0.00E+00	0.00E+00	4.80E-04	4.19E-03	5.17E-03	5.17E-03	5.17E-03
3	0.00E+00	0.00E+00	0.00E+00	0.00E+00	0.00E+00	0.00E+00	0.00E+00	8.00E-05	3.37E-03	5.17E-03	5.17E-03	5.17E-03
2	0.00E+00	0.00E+00	0.00E+00	0.00E+00	0.00E+00	0.00E+00	0.00E+00	2.80E-04	4.05E-03	5.17E-03	5.17E-03	5.17E-03
1	0.00E+00	0.00E+00	0.00E+00	0.00E+00	0.00E+00	0.00E+00	0.00E+00	1.38E-03	5.05E-03	5.17E-03	5.17E-03	5.17E-03
I =	13	14	15	16	17	18	19	20	21	22	23	24

Table (A.5): $Ca(OH)_2$ concentration, continued

J =												
24	1.80E-04	1.10E-04	7.00E-05	4.00E-05	2.00E-05	1.00E-05	0.00E+00	0.00E+00	0.00E+00	0.00E+00	0.00E+00	0.00E+00
23	3.60E-04	2.10E-04	1.20E-04	6.00E-05	3.00E-05	1.00E-05	1.00E-05	0.00E+00	0.00E+00	0.00E+00	0.00E+00	0.00E+00
22	5.20E-04	2.80E-04	1.40E-04	6.00E-05	3.00E-05	1.00E-05	0.00E+00	0.00E+00	0.00E+00	0.00E+00	0.00E+00	0.00E+00
21	6.50E-04	3.20E-04	1.40E-04	6.00E-05	2.00E-05	1.00E-05	0.00E+00	0.00E+00	0.00E+00	0.00E+00	0.00E+00	0.00E+00
20	7.10E-04	3.20E-04	1.30E-04	5.00E-05	2.00E-05	1.00E-05	0.00E+00	0.00E+00	0.00E+00	0.00E+00	0.00E+00	0.00E+00
19	7.10E-04	3.00E-04	1.10E-04	4.00E-05	1.00E-05	0.00E+00	0.00E+00	0.00E+00	0.00E+00	0.00E+00	0.00E+00	0.00E+00
18	6.90E-04	2.70E-04	1.00E-04	3.00E-05	1.00E-05	0.00E+00	0.00E+00	0.00E+00	0.00E+00	0.00E+00	0.00E+00	0.00E+00
17	6.50E-04	2.40E-04	8.00E-05	3.00E-05	1.00E-05	0.00E+00	0.00E+00	0.00E+00	0.00E+00	0.00E+00	0.00E+00	0.00E+00
16	6.10E-04	2.00E-04	7.00E-05	2.00E-05	1.00E-05	0.00E+00	0.00E+00	0.00E+00	0.00E+00	0.00E+00	0.00E+00	0.00E+00
15	5.50E-04	1.70E-04	5.00E-05	1.00E-05	0.00E+00	0.00E+00	0.00E+00	0.00E+00	0.00E+00	0.00E+00	0.00E+00	0.00E+00
14	4.70E-04	1.20E-04	3.00E-05	1.00E-05	0.00E+00	0.00E+00	0.00E+00	0.00E+00	0.00E+00	0.00E+00	0.00E+00	0.00E+00
13	3.80E-04	8.00E-05	2.00E-05	0.00E+00	0.00E+00	0.00E+00	0.00E+00	0.00E+00	0.00E+00	0.00E+00	0.00E+00	0.00E+00
12	3.10E-04	5.00E-05	1.00E-05	0.00E+00	0.00E+00	0.00E+00	0.00E+00	0.00E+00	0.00E+00	0.00E+00	1.00E-05	1.00E-05
11	2.90E-04	3.00E-05	1.00E-05	0.00E+00	0.00E+00	0.00E+00	0.00E+00	0.00E+00	1.00E-05	1.00E-05	2.00E-05	4.00E-05
10	3.80E-04	4.00E-05	0.00E+00	0.00E+00	0.00E+00	1.00E-05	1.00E-05	2.00E-05	3.00E-05	5.00E-05	9.00E-05	1.50E-04
9	7.10E-04	1.10E-04	2.00E-05	1.00E-05	3.00E-05	4.00E-05	7.00E-05	1.00E-04	1.50E-04	2.20E-04	3.40E-04	5.30E-04
8	1.46E-03	3.80E-04	1.30E-04	9.00E-05	1.60E-04	2.30E-04	3.40E-04	4.80E-04	6.70E-04	9.20E-04	1.28E-03	1.79E-03
7	3.11E-03	1.30E-03	7.00E-04	5.90E-04	8.30E-04	1.13E-03	1.51E-03	1.97E-03	2.52E-03	3.21E-03	4.05E-03	4.89E-03
6	5.09E-03	3.91E-03	2.87E-03	2.69E-03	3.37E-03	4.15E-03	4.86E-03	5.10E-03	5.14E-03	5.16E-03	5.17E-03	5.17E-03
5	5.17E-03	5.17E-03	5.16E-03	5.15E-03	5.16E-03	5.17E-03	5.17E-03	5.17E-03	5.17E-03	5.17E-03	5.17E-03	5.17E-03
4	5.17E-03	5.17E-03	5.17E-03	5.17E-03	5.17E-03	5.17E-03	5.17E-03	5.17E-03	5.17E-03	5.17E-03	5.17E-03	5.17E-03
3	5.17E-03	5.17E-03	5.17E-03	5.17E-03	5.17E-03	5.17E-03	5.17E-03	5.17E-03	5.17E-03	5.17E-03	5.17E-03	5.17E-03
2	5.17E-03	5.17E-03	5.17E-03	5.17E-03	5.17E-03	5.17E-03	5.17E-03	5.17E-03	5.17E-03	5.17E-03	5.17E-03	5.17E-03
1	5.17E-03	5.17E-03	5.17E-03	5.17E-03	5.17E-03	5.17E-03	5.17E-03	5.17E-03	5.17E-03	5.17E-03	5.17E-03	5.17E-03
I =	25	26	27	28	29	30	31	32	33	34	35	36

Table (A.5): $Ca(OH)_2$ concentration, continued

J =												
24	0.00E+00	0.00E+00	0.00E+00	0.00E+00	0.00E+00	0.00E+00	0.00E+00	0.00E+00	0.00E+00	0.00E+00	-3.00E-05	5.17E-03
23	0.00E+00	0.00E+00	0.00E+00	0.00E+00	0.00E+00	0.00E+00	0.00E+00	0.00E+00	0.00E+00	0.00E+00	1.80E-04	5.17E-03
22	0.00E+00	0.00E+00	0.00E+00	0.00E+00	0.00E+00	0.00E+00	0.00E+00	0.00E+00	3.00E-05	2.90E-04	3.16E-03	5.17E-03
21	0.00E+00	0.00E+00	0.00E+00	0.00E+00	0.00E+00	0.00E+00	0.00E+00	3.00E-05	1.60E-04	1.01E-03	5.08E-03	5.17E-03
20	0.00E+00	0.00E+00	0.00E+00	0.00E+00	0.00E+00	1.00E-05	2.00E-05	1.00E-04	4.40E-04	2.06E-03	5.16E-03	5.17E-03
19	0.00E+00	0.00E+00	0.00E+00	0.00E+00	1.00E-05	2.00E-05	7.00E-05	2.40E-04	9.00E-04	3.36E-03	5.17E-03	5.17E-03
18	0.00E+00	0.00E+00	0.00E+00	0.00E+00	1.00E-05	5.00E-05	1.40E-04	4.70E-04	1.52E-03	4.70E-03	5.17E-03	5.17E-03
17	0.00E+00	0.00E+00	0.00E+00	1.00E-05	3.00E-05	9.00E-05	2.70E-04	8.00E-04	2.31E-03	5.13E-03	5.17E-03	5.17E-03
16	0.00E+00	0.00E+00	1.00E-05	2.00E-05	7.00E-05	1.80E-04	4.70E-04	1.25E-03	3.30E-03	5.16E-03	5.17E-03	5.17E-03
15	0.00E+00	1.00E-05	2.00E-05	5.00E-05	1.20E-04	3.00E-04	7.60E-04	1.88E-03	4.48E-03	5.17E-03	5.17E-03	5.17E-03
14	1.00E-05	1.00E-05	4.00E-05	9.00E-05	2.10E-04	5.00E-04	1.18E-03	2.74E-03	5.13E-03	5.17E-03	5.17E-03	5.17E-03
13	1.00E-05	3.00E-05	7.00E-05	1.60E-04	3.60E-04	8.20E-04	1.82E-03	3.92E-03	5.17E-03	5.17E-03	5.17E-03	5.17E-03
12	3.00E-05	6.00E-05	1.30E-04	2.90E-04	6.30E-04	1.35E-03	2.81E-03	5.08E-03	5.17E-03	5.17E-03	5.17E-03	5.17E-03
11	8.00E-05	1.60E-04	3.20E-04	6.40E-04	1.25E-03	2.41E-03	4.45E-03	5.17E-03	5.17E-03	5.17E-03	5.17E-03	5.17E-03
10	2.60E-04	4.60E-04	8.20E-04	1.46E-03	2.56E-03	4.34E-03	5.16E-03	5.17E-03	5.17E-03	5.17E-03	5.17E-03	5.17E-03
9	8.30E-04	1.32E-03	2.09E-03	3.30E-03	4.89E-03	5.16E-03	5.17E-03	5.17E-03	5.17E-03	5.17E-03	5.17E-03	5.17E-03
8	2.51E-03	3.54E-03	4.79E-03	5.14E-03	5.17E-03	5.17E-03	5.17E-03	5.17E-03	5.17E-03	5.17E-03	5.17E-03	5.17E-03
7	5.13E-03	5.16E-03	5.17E-03	5.17E-03	5.17E-03	5.17E-03	5.17E-03	5.17E-03	5.17E-03	5.17E-03	5.17E-03	5.17E-03
6	5.17E-03	5.17E-03	5.17E-03	5.17E-03	5.17E-03	5.17E-03	5.17E-03	5.17E-03	5.17E-03	5.17E-03	5.17E-03	5.17E-03
5	5.17E-03	5.17E-03	5.17E-03	5.17E-03	5.17E-03	5.17E-03	5.17E-03	5.17E-03	5.17E-03	5.17E-03	5.17E-03	5.17E-03
4	5.17E-03	5.17E-03	5.17E-03	5.17E-03	5.17E-03	5.17E-03	5.17E-03	5.17E-03	5.17E-03	5.17E-03	5.17E-03	5.17E-03
3	5.17E-03	5.17E-03	5.17E-03	5.17E-03	5.17E-03	5.17E-03	5.17E-03	5.17E-03	5.17E-03	5.17E-03	5.17E-03	5.17E-03
2	5.17E-03	5.17E-03	5.17E-03	5.17E-03	5.17E-03	5.17E-03	5.17E-03	5.17E-03	5.17E-03	5.17E-03	5.17E-03	5.17E-03
1	5.17E-03	5.17E-03	5.17E-03	5.17E-03	5.17E-03	5.17E-03	5.17E-03	5.17E-03	5.17E-03	5.17E-03	5.17E-03	5.17E-03
I =	37	38	39	40	41	42	43	44	45	46	47	48

Table (A.6): **$CaCO_3$ Concentration ($kmol/m^3$):** The average [$CaCO_3$] over the whole vessel is 0.0036 $kmol/m^3$.

J =												
24	1.06E-07	3.51E-07	1.07E-06	2.99E-06	7.76E-06	1.87E-05	4.24E-05	9.06E-05	1.82E-04	3.33E-04	3.79E-04	2.63E-04
23	2.75E-08	1.04E-07	3.67E-07	1.23E-06	3.91E-06	1.20E-05	3.59E-05	1.04E-04	2.92E-04	7.16E-04	7.92E-04	5.54E-04
22	7.23E-09	2.94E-08	1.13E-07	4.15E-07	1.51E-06	5.58E-06	2.17E-05	9.01E-05	3.58E-04	1.11E-03	1.23E-03	8.43E-04
21	1.75E-09	7.46E-09	3.05E-08	1.24E-07	5.32E-07	2.52E-06	1.35E-05	7.64E-05	3.96E-04	1.51E-03	1.65E-03	1.14E-03
20	3.92E-10	1.78E-09	8.19E-09	4.11E-08	2.41E-07	1.65E-06	1.20E-05	7.98E-05	4.73E-04	1.97E-03	2.05E-03	1.34E-03
19	8.72E-11	4.85E-10	3.12E-09	2.38E-08	2.06E-07	1.83E-06	1.44E-05	9.79E-05	6.31E-04	2.50E-03	2.42E-03	1.47E-03
18	2.52E-11	2.05E-10	1.91E-09	1.93E-08	2.03E-07	2.07E-06	1.71E-05	1.23E-04	8.45E-04	3.07E-03	2.78E-03	1.55E-03
17	7.68E-12	7.55E-11	8.09E-10	9.61E-09	1.34E-07	1.95E-06	1.93E-05	1.53E-04	1.10E-03	3.67E-03	3.14E-03	1.60E-03
16	1.67E-12	1.69E-11	1.89E-10	2.76E-09	7.07E-08	1.96E-06	2.21E-05	1.84E-04	1.37E-03	4.28E-03	3.52E-03	1.64E-03
15	2.32E-13	2.22E-12	2.28E-11	1.70E-10	4.48E-08	2.89E-06	2.89E-05	2.15E-04	1.63E-03	4.80E-03	3.97E-03	1.67E-03
14	2.35E-14	2.00E-13	0.00E+00	7.55E-11	9.90E-08	6.72E-06	4.98E-05	2.51E-04	1.83E-03	5.06E-03	4.47E-03	1.70E-03
13	1.72E-15	0.00E+00	0.00E+00	1.85E-09	4.12E-07	2.14E-05	1.14E-04	3.16E-04	1.92E-03	5.13E-03	4.88E-03	1.75E-03
12	8.55E-18	0.00E+00	1.80E-11	9.87E-09	1.57E-06	7.63E-05	2.71E-04	4.69E-04	1.87E-03	5.15E-03	5.05E-03	1.84E-03
11	3.96E-17	6.78E-14	1.21E-10	3.78E-08	5.12E-06	2.30E-04	5.27E-04	6.59E-04	1.64E-03	5.15E-03	5.11E-03	2.04E-03
10	0.00E+00	0.00E+00	0.00E+00	1.29E-07	1.51E-05	4.72E-04	7.53E-04	9.04E-04	1.27E-03	5.15E-03	5.14E-03	2.44E-03
9	0.00E+00	0.00E+00	0.00E+00	0.00E+00	6.38E-05	6.33E-04	8.14E-04	8.70E-04	9.20E-04	5.14E-03	5.16E-03	3.21E-03
8	9.42E-24	0.00E+00	0.00E+00	0.00E+00	0.00E+00	3.07E-04	7.41E-04	8.85E-04	1.01E-03	5.15E-03	5.17E-03	4.52E-03
7	6.15E-25	3.04E-22	0.00E+00	0.00E+00	0.00E+00	1.09E-05	4.53E-04	8.59E-04	2.74E-03	5.16E-03	5.17E-03	5.11E-03
6	0.00E+00	0.00E+00	3.60E-19	0.00E+00	0.00E+00	0.00E+00	4.78E-05	8.65E-04	3.96E-03	5.17E-03	5.17E-03	5.18E-03
5	3.06E-28	0.00E+00	0.00E+00	4.24E-16	0.00E+00	0.00E+00	0.00E+00	4.82E-04	3.99E-03	5.17E-03	5.17E-03	5.18E-03
4	1.45E-29	0.00E+00	0.00E+00	0.00E+00	5.32E-13	3.83E-11	0.00E+00	4.85E-04	4.19E-03	5.17E-03	5.17E-03	5.17E-03
3	4.44E-31	0.00E+00	0.00E+00	0.00E+00	0.00E+00	7.55E-10	0.00E+00	8.21E-05	3.37E-03	5.17E-03	5.17E-03	5.17E-03
2	1.09E-32	1.51E-33	0.00E+00	0.00E+00	0.00E+00	0.00E+00	1.28E-06	2.75E-04	4.05E-03	5.17E-03	5.17E-03	5.17E-03
1	3.10E-34	7.12E-35	0.00E+00	0.00E+00	0.00E+00	0.00E+00	0.00E+00	1.38E-03	5.05E-03	5.17E-03	5.17E-03	5.17E-03
I =	13	14	15	16	17	18	19	20	21	22	23	24

Table (A.6): $CaCO_3$ concentration, continued

J =												
24	1.77E-04	1.12E-04	6.75E-05	3.83E-05	2.05E-05	1.04E-05	5.01E-06	2.27E-06	9.62E-07	3.82E-07	1.41E-07	4.81E-08
23	3.57E-04	2.12E-04	1.16E-04	5.98E-05	2.90E-05	1.33E-05	5.79E-06	2.38E-06	9.25E-07	3.37E-07	1.14E-07	3.57E-08
22	5.17E-04	2.84E-04	1.41E-04	6.50E-05	2.82E-05	1.17E-05	4.67E-06	1.78E-06	6.45E-07	2.20E-07	7.01E-08	2.07E-08
21	6.52E-04	3.24E-04	1.42E-04	5.69E-05	2.17E-05	8.06E-06	2.93E-06	1.04E-06	3.58E-07	1.17E-07	3.65E-08	1.13E-08
20	7.11E-04	3.23E-04	1.30E-04	4.84E-05	1.72E-05	5.90E-06	1.97E-06	6.45E-07	2.06E-07	6.40E-08	2.05E-08	1.02E-08
19	7.14E-04	2.97E-04	1.12E-04	4.03E-05	1.38E-05	4.55E-06	1.43E-06	4.33E-07	1.28E-07	3.86E-08	1.74E-08	2.37E-08
18	6.89E-04	2.66E-04	9.64E-05	3.36E-05	1.12E-05	3.55E-06	1.06E-06	3.01E-07	8.44E-08	3.02E-08	3.08E-08	7.25E-08
17	6.53E-04	2.37E-04	8.20E-05	2.75E-05	8.74E-06	2.61E-06	7.34E-07	1.97E-07	5.82E-08	3.79E-08	7.53E-08	2.00E-07
16	6.08E-04	2.04E-04	6.66E-05	2.09E-05	6.21E-06	1.72E-06	4.46E-07	1.17E-07	4.94E-08	7.18E-08	1.81E-07	4.85E-07
15	5.47E-04	1.65E-04	4.95E-05	1.44E-05	3.93E-06	9.89E-07	2.38E-07	7.32E-08	6.96E-08	1.58E-07	4.11E-07	1.07E-06
14	4.67E-04	1.22E-04	3.30E-05	8.85E-06	2.21E-06	5.06E-07	1.28E-07	8.12E-08	1.52E-07	3.67E-07	9.13E-07	2.28E-06
13	3.79E-04	8.08E-05	1.95E-05	4.89E-06	1.13E-06	2.67E-07	1.36E-07	2.10E-07	4.37E-07	9.64E-07	2.19E-06	5.05E-06
12	3.09E-04	5.03E-05	1.05E-05	2.54E-06	6.39E-07	3.22E-07	4.53E-07	8.37E-07	1.61E-06	3.19E-06	6.47E-06	1.34E-05
11	2.90E-04	3.37E-05	5.57E-06	1.50E-06	9.02E-07	1.28E-06	2.25E-06	3.92E-06	6.91E-06	1.24E-05	2.29E-05	4.32E-05
10	3.79E-04	3.99E-05	4.11E-06	2.35E-06	4.11E-06	7.08E-06	1.19E-05	1.94E-05	3.16E-05	5.20E-05	8.73E-05	1.50E-04
9	7.14E-04	1.15E-04	2.00E-05	1.38E-05	2.54E-05	4.13E-05	6.51E-05	9.88E-05	1.48E-04	2.23E-04	3.41E-04	5.29E-04
8	1.46E-03	3.84E-04	1.28E-04	9.46E-05	1.56E-04	2.33E-04	3.39E-04	4.79E-04	6.65E-04	9.21E-04	1.28E-03	1.79E-03
7	3.12E-03	1.30E-03	6.97E-04	5.88E-04	8.31E-04	1.13E-03	1.51E-03	1.97E-03	2.52E-03	3.21E-03	4.05E-03	4.89E-03
6	5.09E-03	3.91E-03	2.87E-03	2.69E-03	3.37E-03	4.15E-03	4.86E-03	5.10E-03	5.14E-03	5.16E-03	5.16E-03	5.17E-03
5	5.18E-03	5.18E-03	5.16E-03	5.15E-03	5.16E-03	5.17E-03	5.17E-03	5.17E-03	5.17E-03	5.17E-03	5.17E-03	5.17E-03
4	5.17E-03	5.17E-03	5.17E-03	5.17E-03	5.17E-03	5.17E-03	5.17E-03	5.17E-03	5.17E-03	5.17E-03	5.17E-03	5.17E-03
3	5.17E-03	5.17E-03	5.17E-03	5.17E-03	5.17E-03	5.17E-03	5.17E-03	5.17E-03	5.17E-03	5.17E-03	5.17E-03	5.17E-03
2	5.17E-03	5.17E-03	5.17E-03	5.17E-03	5.17E-03	5.17E-03	5.17E-03	5.17E-03	5.17E-03	5.17E-03	5.17E-03	5.17E-03
1	5.17E-03	5.17E-03	5.17E-03	5.17E-03	5.17E-03	5.17E-03	5.17E-03	5.17E-03	5.17E-03	5.17E-03	5.17E-03	5.17E-03
I =	25	26	27	28	29	30	31	32	33	34	35	36

Table (A.6): $CaCO_3$ concentration, continued

J =												
24	1.51E-08	4.31E-09	1.12E-09	2.60E-10	4.85E-11	0.00E+00	0.00E+00	0.00E+00	0.00E+00	0.00E+00	0.00E+00	5.18E-03
23	1.03E-08	2.75E-09	7.74E-10	5.08E-10	1.20E-09	4.68E-09	2.35E-08	1.54E-07	1.09E-06	4.88E-06	1.90E-04	5.17E-03
22	5.86E-09	2.17E-09	2.61E-09	7.20E-09	2.47E-08	1.05E-07	5.15E-07	3.12E-06	2.67E-05	2.95E-04	3.16E-03	5.17E-03
21	5.22E-09	7.77E-09	2.19E-08	7.22E-08	2.65E-07	1.10E-06	5.08E-06	2.67E-05	1.59E-04	1.02E-03	5.08E-03	5.17E-03
20	1.55E-08	4.19E-08	1.29E-07	4.26E-07	1.51E-06	5.73E-06	2.30E-05	9.82E-05	4.44E-04	2.06E-03	5.16E-03	5.17E-03
19	6.06E-08	1.75E-07	5.26E-07	1.65E-06	5.48E-06	1.87E-05	6.59E-05	2.40E-04	8.97E-04	3.36E-03	5.17E-03	5.17E-03
18	2.00E-07	5.65E-07	1.63E-06	4.84E-06	1.47E-05	4.58E-05	1.45E-04	4.67E-04	1.52E-03	4.70E-03	5.17E-03	5.17E-03
17	5.48E-07	1.50E-06	4.16E-06	1.17E-05	3.31E-05	9.46E-05	2.73E-04	7.95E-04	2.31E-03	5.13E-03	5.17E-03	5.17E-03
16	1.30E-06	3.45E-06	9.20E-06	2.46E-05	6.57E-05	1.76E-04	4.69E-04	1.25E-03	3.30E-03	5.16E-03	5.17E-03	5.17E-03
15	2.78E-06	7.16E-06	1.84E-05	4.72E-05	1.20E-04	3.03E-04	7.58E-04	1.88E-03	4.48E-03	5.17E-03	5.17E-03	5.17E-03
14	5.69E-06	1.41E-05	3.50E-05	8.60E-05	2.09E-04	5.00E-04	1.18E-03	2.74E-03	5.13E-03	5.17E-03	5.17E-03	5.17E-03
13	1.18E-05	2.79E-05	6.61E-05	1.55E-04	3.59E-04	8.16E-04	1.82E-03	3.92E-03	5.17E-03	5.17E-03	5.17E-03	5.17E-03
12	2.85E-05	6.16E-05	1.35E-04	2.94E-04	6.35E-04	1.35E-03	2.81E-03	5.08E-03	5.17E-03	5.17E-03	5.17E-03	5.17E-03
11	8.30E-05	1.62E-04	3.21E-04	6.37E-04	1.25E-03	2.41E-03	4.45E-03	5.17E-03	5.17E-03	5.17E-03	5.17E-03	5.17E-03
10	2.61E-04	4.61E-04	8.19E-04	1.46E-03	2.56E-03	4.34E-03	5.16E-03	5.17E-03	5.17E-03	5.17E-03	5.17E-03	5.17E-03
9	8.30E-04	1.32E-03	2.09E-03	3.30E-03	4.89E-03	5.16E-03	5.17E-03	5.17E-03	5.17E-03	5.17E-03	5.17E-03	5.17E-03
8	2.51E-03	3.54E-03	4.79E-03	5.14E-03	5.17E-03	5.17E-03	5.17E-03	5.17E-03	5.17E-03	5.17E-03	5.17E-03	5.17E-03
7	5.13E-03	5.16E-03	5.17E-03	5.17E-03	5.17E-03	5.17E-03	5.17E-03	5.17E-03	5.17E-03	5.17E-03	5.17E-03	5.17E-03
6	5.17E-03	5.17E-03	5.17E-03	5.17E-03	5.17E-03	5.17E-03	5.17E-03	5.17E-03	5.17E-03	5.17E-03	5.17E-03	5.17E-03
5	5.17E-03	5.17E-03	5.17E-03	5.17E-03	5.17E-03	5.17E-03	5.17E-03	5.17E-03	5.17E-03	5.17E-03	5.17E-03	5.17E-03
4	5.17E-03	5.17E-03	5.17E-03	5.17E-03	5.17E-03	5.17E-03	5.17E-03	5.17E-03	5.17E-03	5.17E-03	5.17E-03	5.17E-03
3	5.17E-03	5.17E-03	5.17E-03	5.17E-03	5.17E-03	5.17E-03	5.17E-03	5.17E-03	5.17E-03	5.17E-03	5.17E-03	5.17E-03
2	5.17E-03	5.17E-03	5.17E-03	5.17E-03	5.17E-03	5.17E-03	5.17E-03	5.17E-03	5.17E-03	5.17E-03	5.17E-03	5.17E-03
1	5.17E-03	5.17E-03	5.17E-03	5.17E-03	5.17E-03	5.17E-03	5.17E-03	5.17E-03	5.17E-03	5.17E-03	5.17E-03	5.17E-03
I =	37	38	39	40	41	42	43	44	45	46	47	48

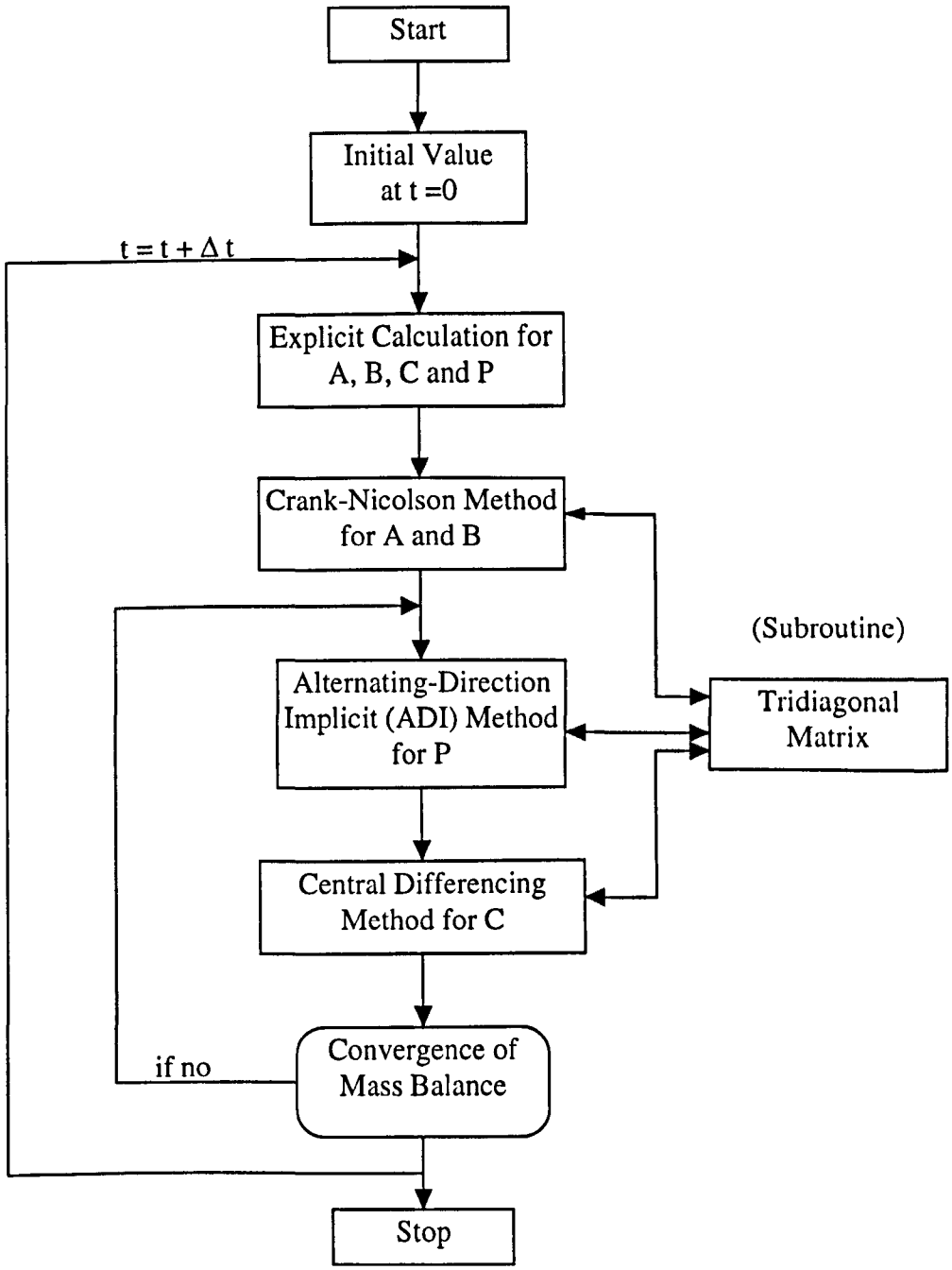

Figure (A.11): Film theory model computational flow chart, Wachi and Jones (1991 a).

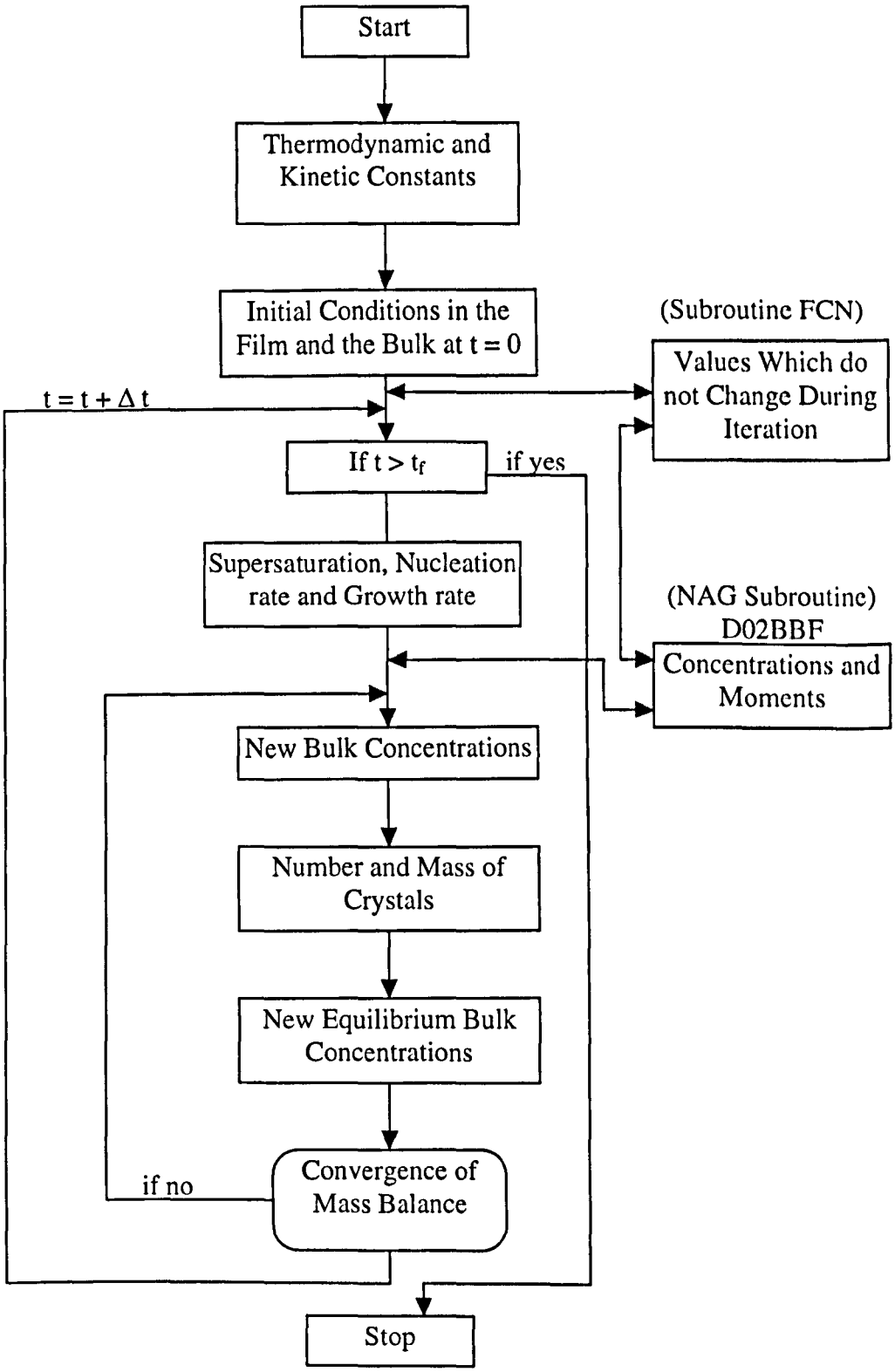

Figure (A.12): Penetration theory model computational flow chart, Hostomský and Jones (1995).